AN APPROACH TO SURFACE MODIFICATIONS WITH POLYMER BRUSHES USING AQUEOUS SYNTHETIC TECHNIQUES AND CHARACTERIZATION

A Dissertation

Presented to the Faculty of the Graduate School

of Cornell University

In Partial Fulfillment of the Requirements for the Degree of

Doctor of Philosophy

by

Roselynn Cordero

December 2018

AN APPROACH TO SURFACE MODIFICATIONS WITH POLYMER BRUSHES USING AQUEOUS SYNTHETIC TECHNIQUES AND CHARACTERIZATION

Roselynn Cordero, Ph. D.

Cornell University 2018

This thesis introduces a new emulsion polymerization technique called mini monomer encapsulated emulsion polymerization (mini ME emulsion) using activators regenerated by electron transfer (ARGET) atom transfer radical polymerization (ATRP) to form narrow dispersity poly(methyl methacrylate), PMMA and polystyrene, PS. Subsequent chapters discuss use of this method to create polymer brushes on silica nanoparticles to form "hairy" nanoparticles, and the use of polymer brushes on silica and cellulose substrates to serve as an antibody sensor. "Hairy nanoparticles" use a combination of a polymer brush and an inorganic nanoparticle core to improve the mechanical and thermal properties of a film.

Mini ME emulsion polymerization was created for the controlled polymerization of PMMA and PS in an aqueous medium. By guiding reaction localization with a phase transfer agent, tetrabutylammonium bromide (TBAB) and with acetone to control their diffusion rate, continuous feeding of the reaction loci with monomer was employed to keep a constant concentration of propagating radicals. This reaction process leads to low dispersity polymers with a predetermined molecular weight in an emulsion polymerization.

Once mini ME emulsion polymerization was established in aqueous media, the polymerization method was modified to grow polymer chains on a nanoparticle surface to obtain hairy nanoparticles. Within recent years, the study of polymer brushes, which

is broadly defined as polymer chains bound to a surface, has enabled ground-breaking materials with tailored interfaces, finding applications in nonfouling biosurfaces and creating novel mechanical and optical nanocomposite materials. The particles were functionalized with a hydrophobic initiator to control the polymerization loci forcing initiation to occur only within the organic phase surrounding the nanoparticle and minimizing reaction in the aqueous medium. Results of the new reaction route are described.

This technique was also employed to generate polymer brushes on surfaces such as those suitable for biosensing devices and is discussed. Reaction conditions and the results of preliminary testing to these new structures for antibody sensing are described. A poly(oligoethylene glycol) methacrylate (POEGMA) polymer brush, which is used to prevent non-specific adsorption of biomolecules, was grown from cellulose or silica microparticles under aqueous conditions. These brushes were then post-modified with a model antigen, dinitrophenyl (DNP) to increase the specificity of the sensor via specific antibody-antigen recognition. Preliminary results suggest that polymer brushes are needed to increase the sensitivity of the sensor by repelling molecules that would lead to a false positive result. A sensor based on the antibody catalyzed water oxidation pathway (ACWOP) eliminates the need for a secondary antibody, thus further increasing both the specificity and sensitivity of the device and is described in this thesis.

BIOGRAPHICAL SKETCH

Roselynn Cordero was born on the fourth of July in New York City, Manhattan. She is the daughter of NYPD detective, Javier Cordero and Rosa Cárdenas. In May 2012, she graduated *cum laude* from John Jay College of Criminal Justice in Manhattan, NY with her B.S. degree in forensic chemistry. During her years as an undergraduate student she studied inorganic synthetic techniques for a semester through an international REU program in Perugia, Italy, under the supervision of Professor Alceo Macchioni. She also worked closely with the Koji Nakanishi group in Columbia University for several years before publishing her first paper in 2011 with them. She was awarded outstanding undergraduate researcher in 2011, 2nd place and 2012, 1st place and was inducted to the Alpha Phi Sigma honor society.

Since the Fall of 2013, Roselynn has pursued her Ph.D. in the Department of Chemistry and Chemical Biology at Cornell University under the supervision of Professor Christopher K. Ober in the Department of Material Science and Engineering. As a graduate researcher, she interned at the Air Force Research Laboratory in Dayton, Ohio under Dr. Richard A. Vaia's supervision for two semesters.

Roselynn was awarded a blue ribbon at the 253rd American Chemical Society in San Francisco, CA for distinguished poster nominee and has traveled to Cairns, Australia to present her work on mini ME emulsions at the MACRO2018 World Polymer Conference. The topic of her thesis includes the synthesis of polymer brushes via novel aqueous polymerizations on spherical and flat surfaces for applications in biosensing and flexible electronics. After graduation, she will work as a senior research scientist at 3M based in Woodbury, MN.

Dedicated to Irving

for the love, support and comfort

throughout my years in graduate school

ACKNOWLEDGMENTS

Success is never achieved alone. Although a large portion of our Ph.D. work is done independently, it is through the help, assistance and support of others that allows us to achieve the goals we have in sight. I would like to take this opportunity to acknowledge and thank those who have helped me throughout my years at Cornell University.

First, I would like to whole-heartedly express my gratitude to my advisor, Christopher K. Ober. Although we may have had differences in opinion when it came to how we would approach a problem within the project, you were still there to guide me and encouraged my creativeness allowing me to grow as a scientist. Thank you for your advice, support and friendship.

Second, I would like to thank my co-chair Professor Barbara A. Baird and committee member Professor Héctor D. Abruña. Professor Baird has been an incredible mentor and supporter of my ideas throughout the years. She is the most patient person I have ever met and is always there when I need her. This is also true of Professor Abruña who, on several occasions, has had the ability to calm my nerves with his joyful and funny nature right before a big talk or job interview.

I would also like to express my deepest gratitude to Dr. Richard A. Vaia and his team Ali Jawaid, Lawrence Drummy and Justin Che for all their help and support with my research. Dr. Vaia was the catalyst for bringing mini ME emulsions to fruition and I am extremely grateful for our discussions and his advice throughout the years.

I would like to thank Professor Brian Kirby and his team Pranav Sundaram and Andrew Sanchez. We were able to reinvent the ACWOP biosensor within a year and have pivoted this biosensor towards its new generation. We have struggled together and as a team we have been able to conquer any problems that came our way. Thank you for all our discussions and brainstorming sessions.

I gratefully acknowledge the funding support from the Air Force Office of Scientific

Research (AFOSR) in which much of this work was made possible. I would also like to acknowledge the Cornell Nanofabrication Facility (CNF) and Cornell Center for Materials Research (CCMR).

Finally, I am so grateful to all my friends and family. I have made friendships here at Cornell that I will cherish for a life time. The laughter and silliness got me through some very frustrating periods in graduate school and I am extremely thankful for it.

TABLE OF CONTENTS

BIOGRAPHICAL SKETCH…..……....v

DEDICATION…….……..vi

ACKNOWLEDGEMENTS……..……vii

TABLE OF CONTENTS……..….ix

LIST OF FIGURES……...……..xiv

LIST OF TABLES.……xviii

ABBREVIATIONS..……..…….xix

CHAPTER 1: POLYMER BRUSHES ON FLAT AND CURVED SURFACES: AQUEOUS SYNTHETIC TECHNIQUES AND APPLICATIONS

Abstract……..…….…...1

Introduction……..…….2

Polymer Brushes on Flat Surfaces……..…….2

Key Applications of Polymer Brushes on Flat Surfaces

Antifouling Brush Surfaces and Resistance to Nonspecific Binding

Neutral Hydrophilic Brush Surfaces

Biosensors

Cell Adhesive Surfaces

Thermoresponsive Brush Surfaces

Polymer Brushes on Spherical Surfaces……..……...….…….16

Aqueous Synthetic Approaches to HNP system

Emulsion Polymerization

ATRP in Emulsion Polymerization

Conclusions…….…….30

References……..……..31

CHAPTER 2: MINI MONOMER ENCAPSULATED EMULSION POLYMERIZATION OF PMMA USING AQUEOUS ARGET ATRP

Abstract……..…….….45

Introduction……..……...45

Experimental……..…….49

Materials

Instrumentation

Synthesis of OBr ATRP Initiator

Synthesis of PMMA Homopolymer using Mini ME Emulsion ARGET ATRP

Results and Discussion…….……...51

Conclusions……..……63

Acknowledgements…….65

References……..……..66

CHAPTER 3: SYNTHESIS OF POLYSTYRENE USING MINI MONOMER ENCAPSULATED EMULSION POLYMERIZATION WITH AQUEOUS ARGET ATRP

Abstract……..…….….68

Introduction……..……...68

Experimental……..……..……...71

Materials

Instrumentation

Procedure for Synthesis of Polystyrene using Mini ME Emulsion ARGET ATRP

Results and Discussion…….……...74

Effect of Initiator

Effect of Monomer Concentration

Effect of Ligand

Compartmentalization Effects

Utilizing TPMA as Ligand

Conclusions…..……..……92

Acknowledgements……....97

References……..……...…….98

CHAPTER 4: MINI MONOMER ENCAPSULATED EMULSION POLYMERIZATION FOR THE STRAIGHT-FORWARD SYNTHESIS OF HAIRY NANOPARTICLES

Abstract…….….97

Introduction……..…….....97

Experimental……..……...101

Materials

Instrumentation

Synthesis of EDMP ATRP Initiator

Adding EDM Initiator to Ludox-TM 40 Particles

Synthesis of PMMA-SiO_2 HNPs using Mini ME Emulsion Polymerization

Results and Discussion…….……105

Effect of Surfactant Concentration

XRD Characterization

Effect of Monomer Concentration

Conclusions…..……..……119

Acknowledgements……....122

References……..……...…….123

CHAPTER 5: SYNTHESIS OF SILICA-POLYSTYRENE HAIRY NANOPARTICLES USING MINI MONOMER ENCAPSULATED EMULSION POLYMERIZATION

Abstract…….….124

Introduction……..…….....124

Experimental……..……...126

Materials

Instrumentation

Synthesis of PS-SiO_2 HNPs using Mini ME Emulsion Polymerization

Results and Discussion…….…….129

Conclusions…..……..……139

Acknowledgements……..…..143

References……..……...…….144

CHAPTER 6: A NOVEL BIOSENSOR FOR DIRECT ANTIBODY DETECTION BASED ON THE ANTIBODY-CATALYZED WATER OXIDATION PATHWAY

Abstract…….….143

Introduction……..…….....144

Experimental……..……...146

Materials

Instrumentation

Detection of Singlet Oxygen

Functionalization of Rose Bengal on Silica Microparticles

Proof of Concept ACWOP Assay

Detection with Ascorbic Acid

Functionalization of Silica Microparticles with DNP

Results and Discussion…….…….154

Conclusions…..……..……166

Acknowledgments……..…167

References……..……...…….168

CHAPTER 7: FUTURE DIRECTIONS.....……...……171

Iron-Mediated Mini ME Emulsion Polymerization

Metal-Free Mini ME Emulsion ATRP

HNP Array

Hydrogen Bonding HNPs

Hidden/latent Hydrogen Bonding

Phase Separated Mixed Brush Canopies

ACWOP Biosensor

APPENDIX A……...…….…193

APPENDIX B……...……..198

APPENDIX C…… 204

APPENDIX D…….207

SUPPLEMENTARY INFORMATION……...……..210

LIST OF FIGURES

CHAPTER 1

Figure 1: Illustration of neutral brushes on a flat surface 5

Figure 2: Illustration of polymer brushes on a flat surface at different graft densities 11

Figure 3: Schematic depiction of biosensor platform based on AWOP process 12

Figure 4: Illustration of a cell-repellent surface 18

Figure 5: Structure of HNPs at different graft densities 20

Figure 6: Illustration of HNP arrays and superlattice structure 21

Figure 7: Two-step Ugelstad seeded emulsion polymerization process 26

CHAPTER 2

Scheme 1: Depiction of proposed mechanism for mini ME emulsions 47

Figure 1: Graph depicting effect of halide salt concentration 53

Figure 2: FTIR of PMMA via mini ME emulsions using TBAB or NaCl 57

Figure 3: DLS of PMMA particle size distribution 59

Figure 4: Optical microscope image of MMA mini ME emulsion at T=0 60

Figure 5: Conversion vs. Time of PMMA using 100 mM TMAB, TBAC, and TBAB 61

Figure 6: First-order kinetic plot of PMMA using 100 mM and 300 mM TBAB and TBAC 62

CHAPTER 3

Figure 1: Graph of effect of Cu: Me_6TREN and ascorbic acid on M_n and dispersity of PS 76

Figure 2: Graph showing effect of Cu: Me_6TREN on M_n and dispersity

using HEBIB ATRP initiator 78

Figure 3: GPC curves of PMMA when EBIB or HEBIB was used at $[M]_\circ$ = 518 mM 79

Figure 4: Optical microscope images of monomer droplets at T=0 for PS mini ME emulsion polymerization 81

Figure 5: GPC of PMMA when EBIB or HEBIB was used At $[M]_\circ$ = 260 mM 83

Figure 6: GPC of PMMA using either PMDETA, TPMA, or Me_6TREN 85

Figure 7: DLS of PS particles using PMDETA, Me_6TREN, or TPMA 87

Figure 8: GPC and DLS of PS at $[M]_\circ$=260 mM using either EBIB or HEBIB as initiators 88

Figure 9: Graph of effect Cu: TPMA and ascorbic acid feed rate on M_n and dispersity 90

Figure 10: GPC of PS at $[M]_\circ$ = 518 mM and $[M]_\circ$ = 260 mM with TPMA as ligand 91

CHAPTER 4

Figure 1: Schematic of two-step synthetic procedure for SiO_2-PMMA HNPs 100

Figure 2: TGA of SiO_2-PMMA HNPs with varied surfactant concentration 107

Figure 3: SEM images of SiO_2-PMMA HNPs with varied surfactant concentration 109

Figure 4: TEM images of SiO_2-PMMA HNPs with varied surfactant Concentration 110

Figure 5: FTIR and TGA of Sample A SiO_2-PMMA HNPs 112

Figure 6: XRD of Sample A SiO_2-PMMA HNPs 114

Figure 7: TGA of SiO_2-PMMA HNPs with varied $[M]_\circ$ 116

Figure 8: SEM of SiO_2-PMMA HNPs with varied $[M]_\circ$ 117

Figure 9: TEM of SiO_2-PMMA HNPs with varied $[M]_\circ$ 118

CHAPTER 5

Figure 1: FTIR and TGA of SiO_2-PS HNPs 131

Figure 2: XRD of SiO_2-PS HNPs 132

Figure 3: SEM of SiO_2-PS HNPs 134

Figure 4: TEM of SiO_2-PS HNPs 135

Figure 5: SEM of time study from T=0 hr. to T=4 hr. 136

Figure 6: SEM of time study from T=12 hr. to T=28 hr. 137

Figure 7: SEM of time study from T=44 hr. to T=48 hr. 138

CHAPTER 6

Figure 1: Singlet oxygen generation in solution 155

Figure 2: Graph demonstrating proof-of-concept ACWOP assay 158

Figure 3: Depiction of functionalized silica microparticles with RB 161

Figure 4: Singlet oxygen generation on a surface 162

Figure 5: Capture of primary anti-DNP antibodies on DNP-silica 164

Figure 6: Demonstration of surface-based ACWOP biosensor 165

CHAPTER 7

Scheme 1: Proposed mechanism of metal-free ATRP 175

Figure 1: General research pathway 177

Figure 2: Depiction of strategies for controlling superlattice structures 179

Figure 3: Illustration of superlattice film coating strategy 182

Figure 4: Phase separated NP canopies 183

Figure 5: Depiction of Brush synthesis on paper substrate 185

Figure 6: Illustration of specific binding and non-specific repellence of anti-DNP antibodies. 186

Figure 7: Graph of fluorescence intensities on paper substrate 187

APPENDIX A

Figure A1: TEM image of micelles after polymerization using 100 mM NaCl 193

Figure A2: Graph of phase transfer agents against molecular weight and dispersity 194

Figure A3: Comparing the effects of varying $CuBr_2$ concentrations and ascorbic acid feeding rate on molecular weight of PMMA when using either TBAB or TBAC 195

Figure A4: Conversion of PMMA versus time using mini ME emulsion polymerization with TBAB and TBAC at 100 and 300 mM 196

Figure A5: ^1H NMR spectra of OBr ATRP initiator in its ammonium form in $DMSOd_6$ 197

APPENDIX B

Figure B1: Optimization of [HRP] to obtain maximum colorimetric H_2O_2 detection signal 198

Figure B2: Optimization of [TMB] to obtain maximum colorimetric H_2O_2 detection signal 199

Figure B3: H_2O_2 standard curve for the proof-of-concept assay 200

Figure B4: H_2O_2 standard curve for surface-based sensor experiments 201

Figure B5: Analysis of LOD of H_2O_2 for different [RB] in solution 202

APPENDIX D

Figure D: Comparison between photosensitization reactions in solution and on a surface 208

LIST OF TABLES

CHAPTER 2

Table 1: Data table of control MMA polymerizations with halide salts at 100 mM and 300 mM 54

Table 2: Data table of control MMA polymerization with halide salts at 100 mM 56

CHAPTER 7

Table 1: Iron-mediated mini ME emulsion of PMMA 173

LIST OF ABBREVIATIONS

1,3,5-trimethylbenzene (TMB)

2,4-dinitrophenyl (DNP)

Activators regenerated by electron transfer (ARGET)

Antibody-catalyzed water oxidation pathway (ACWOP)

Atom transfer radical polymerization (ATRP)

Bovine serum albumin (BSA)

Concentration polymer brush (CPB)

Dichloromethane (DCM)

Dimethyl formamide (DMF)

Enzyme-linked immunosorbent assay (ELISA)

Fourier transform infrared spectroscopy (FTIR)

Horseradish peroxidase (HRP)

Hydrofluoric (HF)

Hydrogen peroxide (H_2O_2)

Mini monomer encapsulated emulsion polymerization (mini ME emulsion)

N-hydroxysuccinimide (NHS)

Nitroxide-mediated polymerization (NMP)

Phosphate-buffered saline solution (PBS)

Poly(2-hydroxyethyl methacrylate) (PHEMA)

Poly(glycidyl methacrylate) (PGMA)

Poly(methyl methacrylate) (PMMA)

Poly(propylene glycol) methacrylate (POEGMA)

Polystyrene (PS)

Radius of gyration (R_g)

Reversible addition-fragmentation chain transfer (RAFT)

Semi-dilute polymer brush (SDPB)

Scanning electron microscopy (SEM)

Silicon oxide (SiO_2)

Tetrahydrofuran (THF)

Transmission electron microscopy (TEM)

CHAPTER 1

POLYMER BRUSHES ON FLAT AND CURVED SURFACES: AQUEOUS SYNTHETIC TECHNIQUES AND APPLICATIONS

Abstract

Polymer brushes have become a significant focus of polymer research with the need for straightforward and versatile surface modification. With the development of controlled radical polymerization from surfaces, new theoretical models and sophisticated characterization tools, the resulting ability to control brush density and brush thickness gives unparalleled control over surface properties and functionality. By increasing brush density, a stretched brush conformation results by constraining the cross-sectional area of that brush strand which thereby influences the interactions of molecules with the brush surface. Polymer brushes have produced many desired surface architectures for applications in fouling resistant medical devices, biosensing, and medical implant materials.[1] Their stability in relatively harsh biological environments makes them good candidates for low fouling applications. In particular, polymer brushes are advantageous due to their chemical versatility, which allows tuning of interfacial properties such as hydrophilicity and surface energy, adsorption of biological molecules, and cell adhesion.[2] This chapter will provide a literature review of the use of brush surfaces in biology relevant applications and include resistance to non-specific binding, cell bioadhesion, their use as platforms for

---

*Portions are excerpted from WL. Chen, R. Cordero, H. Tran, and C.K. Ober. *Macromolecules* **2017** *50* (11), 4089-4113. DOI 10.1021/acs.macromol.7b00450.

biosensors, and thermoresponsive surfaces. Furthermore, to expand on their multifaceted functionality, polymer brushes that are grafted onto spherical surfaces such as inorganic metal oxide nanoparticles provide films with enhanced thermal, optical, and mechanical properties for applications such as gradient index optical material (GRIN) for midwave-IR photonics, faraday rotators, as well as "nano-inks" for flexible hybrid electronics packaging. The focus of this thesis is on the synthesis of polymer brushes on spherical surfaces to manufacture polymer-grafted nanoparticles (PGNs) or "hairy nanoparticles" (HNPs) in an aqueous dispersed system for applications in not only biology but in opto-electronics, owing to their chemical diversity and microstructure.

1.1.Introduction

1.1.1. Polymer Brushes on Flat Surfaces

Polymer brushes are thin films of polymer chains covalently anchored to surfaces. Recent development of new theory to describe polymer brushes combined with new synthetic and characterization tools have led to a better understanding of their unique features and this, in turn, has triggered a significant growth of interest in the application of these important polymeric materials. Polymerization methods now permit the formation of complex polymer brush architectures with uniform molecular sizes, following growth from initiator sites bound to surfaces. The appropriate surface initiator coupled to controlled radical polymerization methods such as ATRP, NMP and RAFT[3–5] also enables control of brush density and, thus, brush chain conformation from the substrate surface. In a typical dense polymer brush, the number of attachment or tethering points is sufficiently high that the crowded polymer chains are forced to stretch

normal to a planar surface. This leads to residual tension in polymer brushes and may produce mechanochemical effects, influence location of brush chain ends in planar regions in the brush layer, and affects access by solvent and other molecules to the brush.[6]

Covalently attached brushes may also be prepared by other methods in addition to "grafting from" surface initiation. "Grafting to" techniques have been extensively studied and may involve attachment of polymer chains to a substrate by exposing photo radical surface-bound initiators in the presence of a polymer film.[7] The polymers become chemically linked to the surface and form the brush, enabling brush formation from polymers of extraordinarily high molecular weight. Alternatively, end functional chains have been tethered to surfaces using a simple thermal process to end link polymer chains to form a brush layer and create a neutral surface for the directed self-assembly of block copolymers for high resolution patterning.[8] These methods cannot readily form the dense, extended brush possible when using initiation from uniform arrays of initiator groups.

Stretched conformations, which require neither a confining geometry nor an external field, produce both extension of the chains and restricted mobility. The behavior of polymer brushes can, therefore, be quite different from the typical behavior of flexible polymer chains in solution or the melt where chains adopt a random walk.[9] The thickness of the polymer brush (h) may be obtained by using the equation below, as w is the excluded volume and σ is the graft density (number of chains per area), N is degree of polymerization:

$$h \sim N(\sigma w)^{1/3} \quad (1)$$

Assuming that in a dense brush the polymer chain is confined to a cylinder centered around its surface attachment point, the increase in brush thickness (L) scales with the degree of polymerization (N). The brush is then said to lie within the "concentrated brush" regime. In contrast, a sparsely packed brush chain behaves more like a random coil whose radius of gyration (R_g) ~ $N^{1/2}$. In this case, the brush is considered to be in the "mushroom" regime, whereas the "semi-dilute brush" (SDPB) regime is dominated by excluded volume repulsion, thus lies in a region between "mushroom" and "concentrated brush" (CPB) regimes (Fig. 1). The stretching or lack of it provides polymer brushes with properties that can be tuned and exploited in a variety of surface applications.

Brush stretching can lead to interesting mechanical properties in the solid state, including the ability to span channels and gaps over surprising distances because of the residual stress. If brush layers are removed from the substrate, this stiffness enables them to form robust thin films even if not crosslinked.[10] De Gennes among others was responsible for recognizing these differences[11,12] and the seminal work by Milner[13] has led to a greater understanding of these materials and the resulting interest in brushes as unique surface modifiers.

Polymer brushes are well known for transforming the nature of a surface with a layer just a few nanometers thick. Control of wetting properties, prevention of non-specific binding of biomolecules, colloidal stabilization and resistance to fouling are all examples of successful application of polymer brushes. Other uses include polymer compatibilizers[14], new adhesive materials[2,15], chromatographic devices[16], and etch

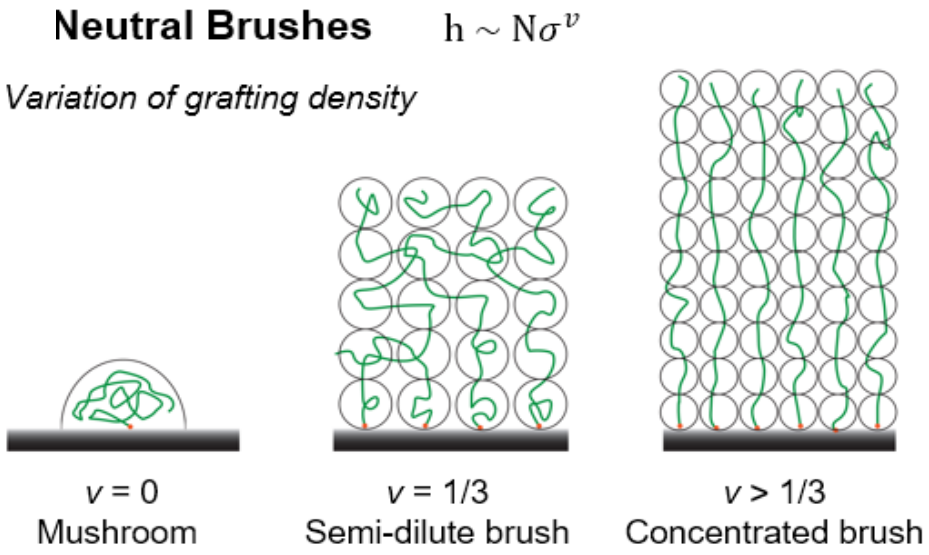

Figure 1. Schematic depiction of neutral brushes with general scaling law $h \sim N\sigma^{v}$ with variation of *v* at different conditions.

barriers.[17] Responsive polymer brushes can be used to change wettability and binding properties, act as valves in microfluidics, control transport of ions and transduce chemical and biochemical signals.[18] Synthetic polymer brushes are increasingly important as interfaces between materials and biological environments, as stimuli responsive surfaces, in drug delivery[19], as surfaces for cell growth and for bioseparation.[20] For example, charged brushes are used in lubrication and wetting and as antimicrobial coatings. Charge controls adsorption of molecules, enables attachment of specific molecules and living cells to surfaces and greatly influences such factors as non-specific binding on these surfaces. Nature uses brushes on interfaces to control surface wetting in the cartilage in joints[21] or the surfaces of lung tissue, for lubrication[22], or to limit deposition of macromolecules (polysaccharides, proteins) onto surfaces.

1.1.2 Key Applications of Polymer Brushes on Flat Surfaces

Polymer brushes have become an effective tool for surface modification producing many desired surface architectures for applications in antifouling medical devices, biosensing, antibacterial coatings, cell culture substrates, stem cell expansion and implant material.[1] Their stability in relatively harsh biological environments makes them good candidates for low fouling applications. In particular, polymer brushes are advantageous due to their chemical versatility, which allows tuning of interfacial properties such as hydrophilicity and surface energy, adsorption of biological molecules, and cell adhesion.[2] This section will focus on recent advances and applications of polymer brushes for the biomedical field, with a particular emphasis on brush surfaces that resist fouling and non-specific binding, serve as biosensing

platforms, or cell adhesive surfaces.

1.1.3 Antifouling Brush Surfaces and Resistance to Non-specific Binding

Materials that resist non-specific binding and that have antifouling surface properties are a fundamental component of several biological applications as they prevent the uncontrolled adsorption of proteins, cells or other biological species that can lower the sensitivity and reliability of biosensors as well as certain medical devices (i.e., heart valves, catheters, coronary stents).[23,24] Principally, antifouling surfaces minimize the intermolecular forces between extracellular biomolecules and an interface so that an adhered biological unit is easily released under low shear stresses.[25] While hydrophobic surfaces[26,27] exhibit protein adsorption, hydrophilic polymers show resistance to protein and cell adhesion.[28] There are two major classes of hydrophilic antifouling brushes: neutral and zwitterionic polymer brushes.[28]

In theory the antifouling ability of both neutral and zwitterionic polymers is associated with a hydration layer near the surface. This results from a tightly bound water layer which forms a physical and energetic barrier to prevent undesired protein adsorption. Aside from surface hydration, chain flexibility plays a role in protein resistance.[27–29] When a protein molecule approaches a surface, the compressed polymer brush chains cause steric repulsion and as a result the brush chains resist adsorption due to an unfavorable decrease in entropy. When surface hydration and steric repulsion come together, it produces optimal conditions for protein resistance, leading to "stealth surfaces". These surfaces remain entirely undetected in a biological setting, producing a true antifouling surface.[25]

1.1.4. Neutral Hydrophilic Brush Surfaces

Commonly, neutral antifouling polymer brushes are prepared from monomers such as HEMA or poly(ethylene glycol) methacrylate (PEGMA).[30] These monomers are appealing, since they behave similarly to polyethylene glycol (PEG), a well-known biocompatible polymer.[31] Furthermore, such monomers contain hydroxyl end groups, providing opportunity for post-modification to further tailor properties for devices and applications such as those highlighted in this section.[32]

A means of brush modification is through active ester chemistry that has been utilized to post-modify neutral brushes via amide coupling reactions.[33,34] Many researchers in recent years have demonstrated successful coupling of specific molecules on nonfouling neutral hydrophilic brush surfaces[35–37] Lavanant *et al.*[38] modified low density polyethylene (LDPE) surfaces with $PEGMA_{10}$ brushes where the brush coating was then modified with a peptide ligand, GGGRGDS. Murata *et al.*[39] synthesized polymers with succinimide side chains and then subsequently coupled numerous functional amines. Unfortunately, this approach relied on succinimide substituted monomers which involved specially tailored reagents, complicating the reaction synthesis. On the other hand, Diamanti *et al.*[40] post-functionalized PHEMA brushes via activation with N,N'-disuccinimidyl carbonate (DSC) with a subsequent coupling of molecules containing α-amine moieties.

Several others have employed neutral brushes to demonstrate fouling resistance for various platforms. Andruzzi *et al.*[41] exploited SI-NMP to polymerize styrene derivatives containing semi-fluorinated alkyl side groups or oligo(ethylene glycol)(OEGn) side groups to tune surface properties. In the study of fluorinated styrene-based polymer brushes, a second block in the diblock copolymer brushes was

always exposed at the air-polymer interface due to stretching of the polymer brushes at high grafting density. Moreover, NEXAFS measurements showed that thicker brushes had more oriented fluorinated side chains, therefore increasing the surface stability toward reconstruction upon long time contact with water.[41] The OEGn-containing styrene based polymer brushes significantly resisted protein adsorption and were also effective in preventing nonspecific cell adhesion. Surman *et al.*[42] compared polymer brushes of poly[oligo (ethylene glycol) methyl ether methacrylate], PHEMA, poly[N-(2-hydroxypropyl) methacrylamide] (PHPMA) and poly(carboxybetaine acrylamide) and their resistance to fouling when exposed to blood plasma. They were able to demonstrate that PHPMA brush surfaces had the best combination of hemocompatibility and stability. More recently, Rastogi *et al.*[43] used electrochemical methods to demonstrate that poly(acrylic) acid brushes grown from OEG containing ATRP initiators were extremely effective in suppressing non-specific adsorption of antibodies on gold surfaces. They used CV and QCM experiments to demonstrate that protein fouling can be significantly reduced while using gold electrodes coated with PEG polymer brushes.

Grafting densities and brush thicknesses have an immense impact on the non-fouling behavior of polymer brushes.[44–47] Zhao *et al.*[48] studied PDMA brushes and found that relative fouling significantly decreased when the grafting density was above 0.27 chains/nm^2 and brushes were strongly stretched. In fact, several studies show that such stretching is ideal for protein repellence, while brushes in the low density "mushroom" regime show nonspecific adsorption of protein and other biomolecules (See Figure 2).[49–51] Moreover, other research with PHPMA and PHEMA have shown that brush thickness

alters surface antifouling properties, changing the amount of protein adsorption when exposed to blood serum. An increase in protein resistance was observed as the brush length increased until ~20 nm in thickness, followed by a plateau, with subsequent increase above 40 nm.[48] Yandi and colleagues[52] have attributed reduced antifouling at thicknesses below the optimum range (20-40 nm) for poly(HEMA-*b*-PEG_{10}MA) brushes to a lower hydration capacity of the block copolymer. At chain lengths above an optimum range, the reduced antifouling properties were attributed to entanglement and crowding in the film reducing conformational freedom and hydration capacity.[52]

Although PEG polymer brushes show incredible fouling resistance, it was revealed that PEG decomposes in the presence of transition metal ions and oxygen, which are present in biochemically relevant solutions.[31,53] This has led to the search for alternatives to PEG leading to the increase of studies employing zwitterionic brushes for their antifouling purposes.[54]

1.1.5. Biosensors

Antifouling surfaces are crucial for the production of medical devices and biosensors as they increase their effectiveness.[24] Many biological systems have the capacity to exhibit intricate receptor-recognition; however, they tend to physically adsorb onto solid substrates without specific receptor-recognition interactions, causing high background noise or "false positives" in sensing applications.[1,23] This introduces several limitations of such technology especially at low analyte concentrations.[1] Antifouling brush systems have been widely investigated for their purpose in receptor-

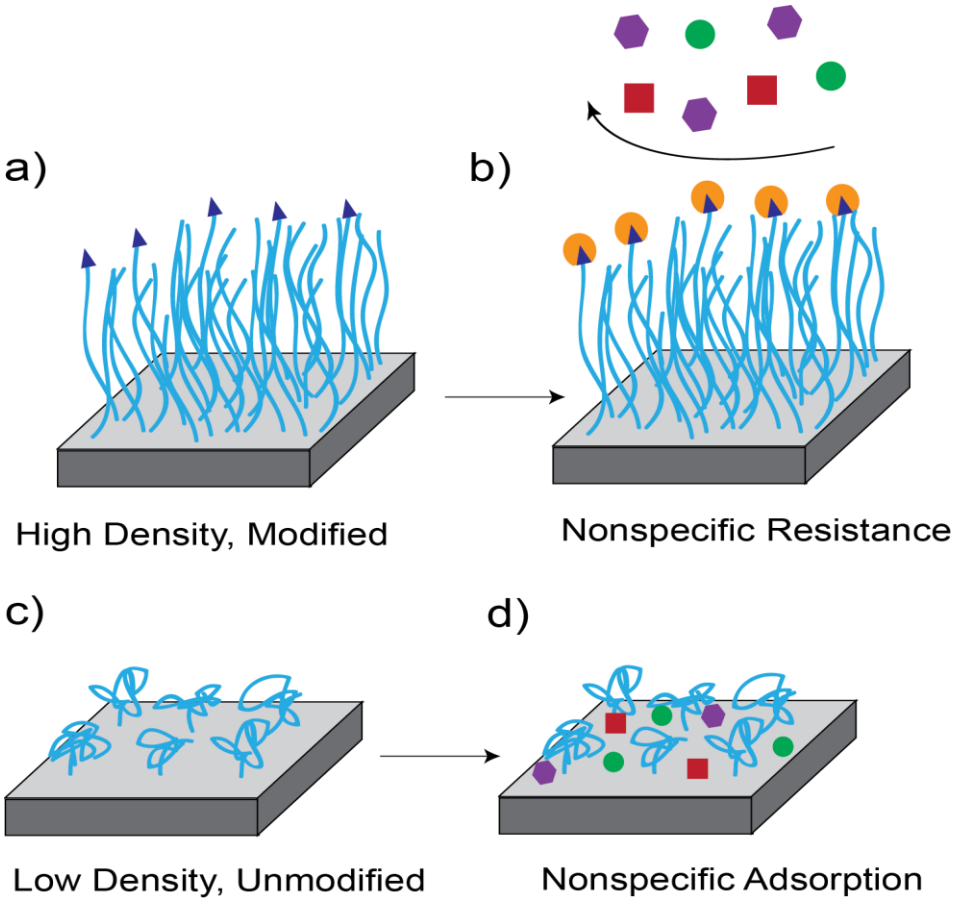

Figure 2. Schematic depiction of (a) A high density brush (light blue lines) modified with a functional molecule (dark blue triangles); (b) Nonspecific resistance of biomolecules allowing for the selective binding of the target molecule from a solution. (c) A low-density brush in the "mushroom" regime that allows for (d) nonspecific adsorption of biomolecules from a solution.

recognition interactions, i.e. biosensors.[55] This type of detection method offers many advantages as it affords a three-dimensional platform providing a higher density of functional groups for biomolecular ligand conjugation per surface area, leading to higher sensitivity of the sensor itself.[56] Polymer brush platforms have had widespread use in biosensor applications ranging from clickable protein modified surfaces[57] to the use of diblock copolymer interfaces with dual purposes.[57,58] Vaisocherova and coworkers[59] investigated a copolymer brush system with ultra-low fouling, poly[N-(2-hydroxy propyl) methacrylamide] (PHMAA) and poly(carboxybetaine methacrylamide) (PCBMAA), as a surface bio-recognition platform for analysis of a variety of complex food samples. The same group also introduced a biosensor capable of quantifying very high concentrations of anti-Epstein Barr Virus (EBV) antibodies in buffer or blood serum; nonetheless, diagnosis with this technique remained uncertain.[60] Riedel *et al.* [61] developed a label-free SPR biosensor assay capable of real-time recognition of different stages of EBV infection in blood serum. The use of brushes offered significant advantages not only in fouling resistance, but post-modification of the brushes tailored the brush properties for specific bio-recognition. The surface was prepared by coating an SPR chip with a poly(HOEGMA) antifouling brush, with successive attachment of streptavidin, biotinylated oligonucleotides (ON), and complementary oligonucleotide (CON)-antigen conjugates.

In an effort to reduce the complications of battling diabetes, a glucose biosensor was developed in 1962 paving the way for modern glucose sensors. Recently, Welch *et al.*[62] used a PGMA-ran-PHEMA brush tethered to the surface of conducting polymer, poly(3,4-ethylenedioxythiophene) doped with poly(styrene sulfonate) (PEDOT: PSS)

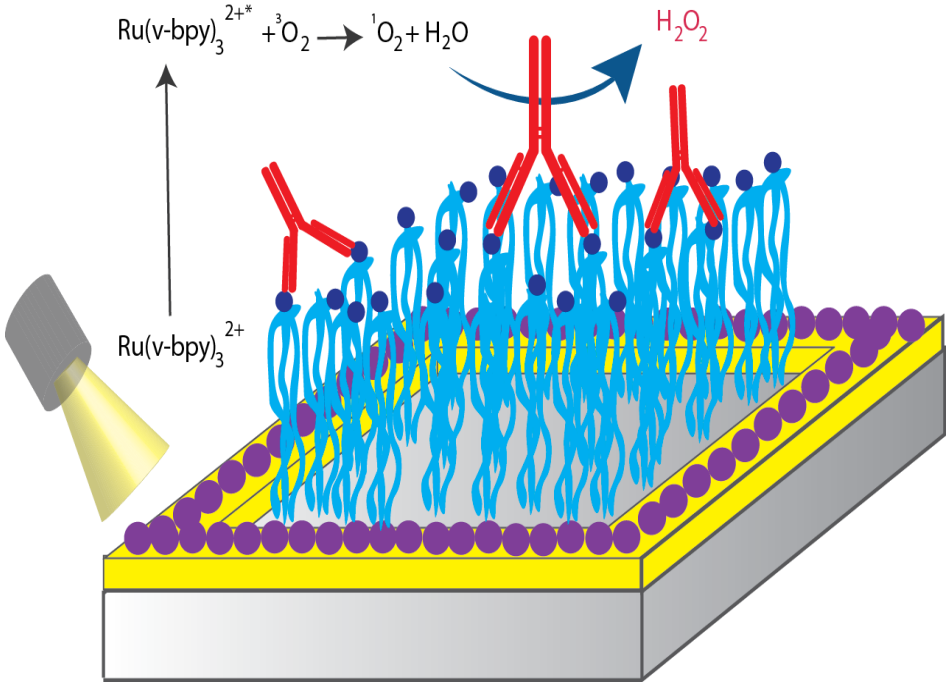

Figure 3. Schematic depiction of biosensor platform based on the ACWOP process. POEGMA polymer brushes (light blue lines) are functionalized with DNP (dark blue circles) molecules to specifically bind anti-DNP IgG antibodies. Photosensitizer (purple circles) is excited via UV irradiation generating singlet oxygen. Hydrogen peroxide is then generated in the presence of singlet oxygen. Reproduced with permission from C.K.Ober.

for the covalent sequestration of glucose oxidase (GOx). The PHEMA copolymer imparted resistance against non-specific protein adsorption, thus increasing the sensitivity and selectivity of glucose detection. PHEMA also served as a means to achieve a much higher loading capacity by helping to expose more functional groups within the system. Results indicated that without the incorporation of PHEMA, homogeneous PGMA brushes were likely to be in a glassy state and too rigid to react with glucose oxidase, thereby decreasing the efficiency of the system.

The detection of hydrogen peroxide is another important analyte of measurement in industrial and environmental analysis.[56] Most recently, Welch *et al.*[63] developed an immunosensor platform based on the antibody-catalyzed water oxidation pathway (ACWOP), a process inherent in all antibodies that catalyzes the conversion of singlet oxygen ($^1O_2$) and water to hydrogen peroxide (H_2O_2).[64] POEGMA polymer brushes were conjugated with small dinitrophenyl (DNP) molecules that specifically bind to anti-DNP IgG antibodies. Ruthenium (v-bipyridine)$_3^{2+}$ served as a photosensitizer and when excited it reacts with ambient oxygen generating $^1O_2$ (see Figure 3). Hydrogen peroxide levels generated through this pathway were measured as low as 0.33 nM using electrochemical methods. This demonstrates great sensitivity via receptor-recognition interactions due to the POEGMA polymer brush patterns on its interface.

1.1.6. Cell Adhesive Surfaces

The incorporation of specific cell or protein interactions is a fundamental factor for advanced materials such as “smart surfaces”. “Smart surfaces” that possess reversible properties in response to diverse environmental stimuli are pivotal in tailoring and controlling biological interactions. Polymer brushes have a plethora of capacities not

only in antifouling or prevention of non-specific binding, but in guiding and directing cellular behavior and function for applications such as regenerative medicine and tissue engineering. The topic below will focus on thermoresponsive polymer brushes that can be thermally triggered to change from a hydrophobic state to a hydrophilic antifouling state.

1.1.7. Thermoresponsive Brush Surfaces

Thermoresponsive polymer brushes exhibit a volume phase transition from a solvated state to non-solvated state under a certain critical temperature. This transition temperature, the lower critical solution temperature (LCST), happens when the polymers are heated above a critical value. Polymer brushes made from such polymers typically switch from a hydrated, extended conformation state into a dehydrated collapsed state through heating (see Figure 4). Polymers with LCST behavior are based on N-isopropylacrylamide (NIPAM), N, N-diethylacrylamide (DEAM), methylvinylether (MVE), poly(poly(ethylene glycol) methyl ether methacrylate) (PPEGMEMA), and N-vinylcaprolactam (NVCl) as monomers.[65] By utilizing a thermoresponsive polymer as a substrate for cell growth, a small change in ambient temperature can be applied to induce cell detachment.[66]

Several fundamental features must be possessed by a thermoresponsive polymer in order to be conducive to cell culture studies. First, the polymer must be responsive in a physiologically relevant temperature range as too high a temperature can cause cell degradation. Furthermore, the interface should be able to switch from cell-compliant to cell-repulsive over a small temperature range.[66] PNIPAM is one of the most studied thermoresponsive polymers for cell culture and biological platforms. In solution,

PNIPAM shows a sharp LCST at 32 ˚C, while the LCST transitions observed for PNIPAM polymer brushes are much broader, start at a lower temperature, and occur over a wider temperature range (from ~ 29 ˚C to ~ 49˚C).[66,67] In 1990, Yamada and coworkers[68] studied the behavior of cells on temperature-responsive PNIPAM polymer surfaces in order to control cell attachment and detachment. They found that the cells adhered completely to the surface of the plates at 37˚C, nevertheless, when the temperature was cooled to 4˚C, nearly 100% of the hepatocytes were detached and recovered. Similarly, others observed cell detachment at 20˚C when using a PNIPAM polymer brush surface.[69,70] This interesting discovery led to more extensive research and use of this particular polymer brush to implement biological "smart" platforms.

Tissue engineering has become a highly studied field in bioengineering due to its significant impact on the development of biological substitutes that restore and improve tissue function. The manufacture of these thermoresponsive polymeric interfaces is of significant importance as topology and architecture provide additional knowledge in cell response. Recently, SI-ATRP has been the most employed method of preparation for these thermoresponsive polymeric surfaces.[71] Xiao and Wirth[72] prepared polyacrylamide brush surfaces on either silica or poly(dimethyl siloxane) and observed a resistance to irreversible protein adsorption. Balamurugan *et al.* [73] prepared PNIPAM brush surfaces on gold and examined the hydration transition behavior of the polymer brush. Xu *et al.*[74] prepared the same polymer brush on silicon surfaces and observed the adhesion or detachment of 3T3 cells when temperatures were increased or decreased, respectively.

One major obstacle to using substrates fabricated from PNIPAM is that this polymer

generally does not promote cell adhesion. Nevertheless, a number of approaches have been reported applying PNIPAM as a platform for cell growth.[69,75] Various reports acknowledge that the thickness of a film is critical in the properties of PNIPAM regenerative platforms.[70,76] Previously, Okano and colleagues[77] prepared PNIPAM brushes on poly(4-vinylbenzyl chloride) coated polystyrene surfaces using SI-ATRP. They found that thicker PNIPAM layers with high grafting density exhibited negligible fibronectin (FN) adsorption, thus providing insignificant cell adhesion, supporting the claim that thick films are simply poor cell hosts. They also prepared endothelial cell sheets using PNIPAM brush surfaces grafted by electron beam (EB) radiation polymerization. It was observed that confluent endothelial cells (EC) monolayers detached as contiguous cell sheets from EB-grafted PNIPAM brush surfaces at reduced temperatures.[77] According to their studies, an effective thickness of a grafted PNIPAM layer should be between 15 nm and 20 nm to obtain optimal cell attachment and detachment in response to temperature changes.[69]

1.2 Polymer Brushes on Spherical Surfaces

Interestingly, as curvature increases in a substrate, the brush confinement and resulting chain stretching of planar substrates fades and a more relaxed brush is formed. Typically, curvature must be rather high (a radius of a few nm) to observe this effect and it is often associated with brushes on nanoparticles. A new family of materials, PGNs, which are also called "hairy" nanoparticles (HNPs), has been developed based on this effect in which the tight curvature permits entanglement of the pendent brushes. HNPs consist of a central core surrounded by a polymeric corona and their dispersion into a matrix strongly depends on their graft density and the

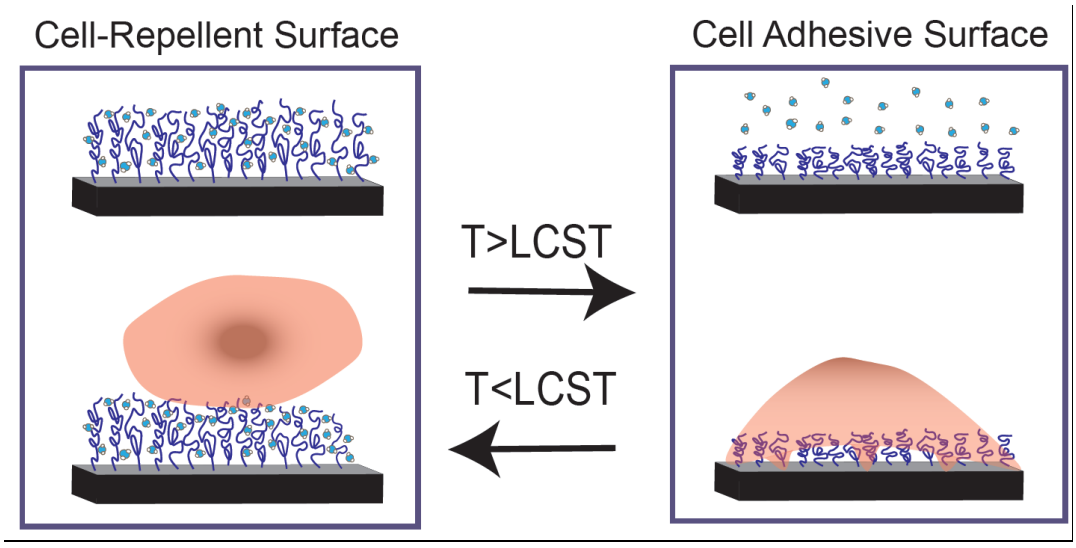

Figure 4. Schematic depiction of a cell-repellent surface (Left) with PNIPAM brushes in the hydrated state below its lowest critical solution temperature (LCST). As the temperature increases above the LCST, the brushes dehydrate and collapse allowing for cells to adhere to the surface (Right).

degree of polymerization of the corona. While these materials are relatively new, significantly improved thermomechanical, optical, and electrical properties[78] have already been observed. HNPs combine the properties connected with the inorganic core (i.e. band gap, dielectric properties, optical, etc.) with the processability and mechanical properties of the organic/polymeric component in one unified platform.[78]

Hairy nanoparticles are categorized depending on the DP and grafting density (σ) of the surface grafted chains, like brushes on flat surfaces, into the different brush regions "mushroom", "semi-dilute brush" (SDPB), and "concentrated brush" (CPB) (Fig. 5). At low molecular weights or grafting densities, the radius of gyration (R_g), does not exceed the interchain spacing. This results in adjacent chains not interacting, thus adopting the mushroom-like conformation. At high grafting densities, interchain interactions give rise to extended chain conformations, thus are in the CPB regime.[79] When the segmental interactions are reduced from those on the CPB region, a more relaxed chain conformation is observed and the chain density decreases leading to the SDPB regime. This relaxed chain conformation suggests that the mechanical properties of HNP brush assemblies may very well be enhanced if the segment length of the polymer chains, in the SDPB regime, form chain entanglements and lead to HNP assemblies.[79–81] These corona entanglements lead to enhanced mechanical properties, that are otherwise not present in dispersed HNPs. The critical radius R_c determines whether a transition from the CPB regime to the SDPB regime will occur as:[79]

$$R_c = R_0 \, (\sigma*)^{1/2} \, (\nu*)^{-1} \qquad (1.1)$$

where R_0 is the radius of the core, σ* is the reduced grafting density, and ν* is the

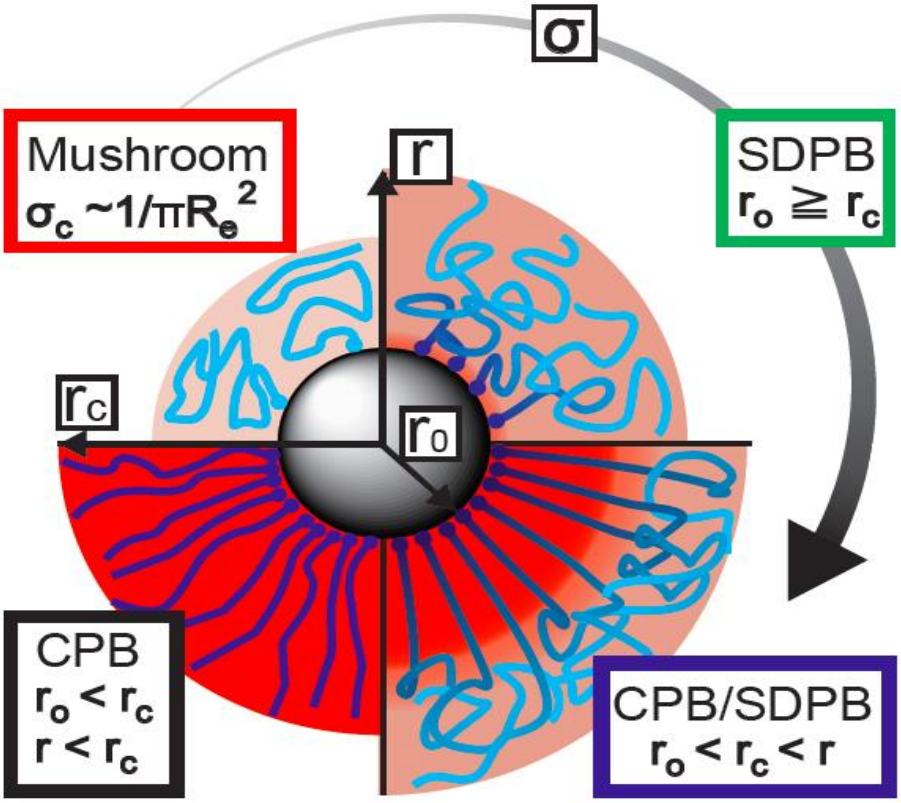

Figure 5. Structure of hairy nanoparticles (HNPs) at different grafting densities. (From upper-left going clockwise) At grafting densities (σ) less than R_g^{-2}, the corona is in the "mushroom" conformation. As the grafting density increases, the chains are forced to extend into a semi-dilute polymer brush (SDPB), and then into a concentrated polymer brush (CPB). Particle curvature implies that the area per chain increases with distance from the surface, and thus the outer ends of the chain are less crowded and may transition to the SDPB regime.

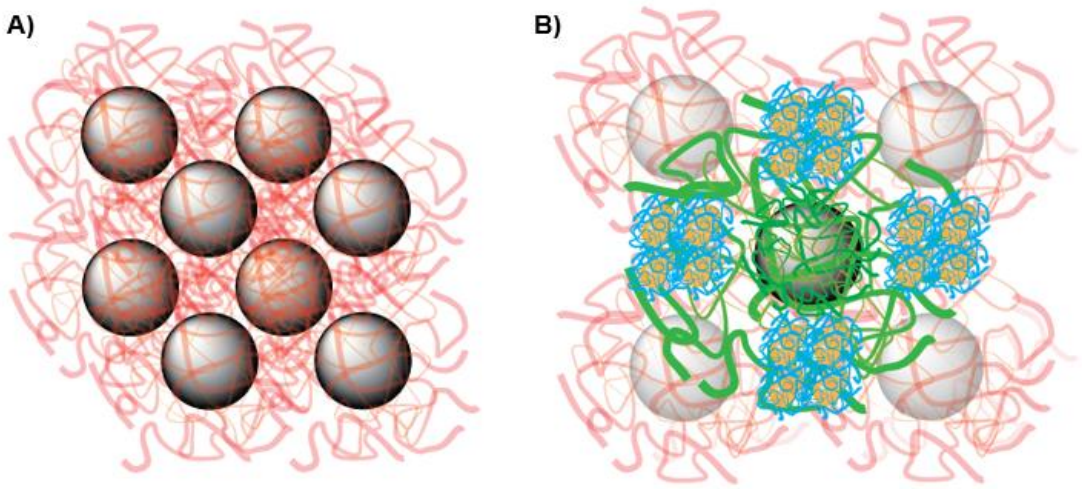

Figure 6. Illustration of HNP arrays and superlattice structure A) HNP 2D array through brush entanglement and B) Superlattice structures of HNPs using a variety of core sizes and selective brush interactions.

effective excluded volume parameter (Fig. 5). There are three main avenues to take in order to obtain HNP assemblies. Large assemblies can be held together through van der Waals, interactions on the outer surface of the corona[78–80] (e.g. chain entanglements, H-bonding) (Fig. 6), or chemical interactions (e.g. click-chemistry). The reinforcement of mechanical properties via corona entanglement was reported by Akcora *et al.*[82] and McEwan *et al.*[83] In their work, poly(methyl methacrylate) grafted HNPs in a matrix proved that mechanical reinforcement can occur as a result of corona bridging from neighboring particles. This bridging usually occurs when the polymer chains of the corona are in the SPDB regime. The entangled brushes on neighboring particles can enhance the toughness and fracture resistance of HNP assemblies by dissipating the fracture energy through craze formation and plastic deformation.[84] HNPs can also form superlattice structures as seen in Fig. 6B, where different size HNPs can form a network through brush interactions.

1.3 Aqueous Synthetic Approaches to HNP Systems

Synthetic techniques for the large-scale production of HNPs has been limited due to the difficulties of achieving high through-put, monodisperse, high purity HNPs. Chain growth polymerizations are necessary in order to prevent cross-linking of adjacent brushes. However, ideal polymerization techniques, such as living ionic polymerizations, require extremely pure solvents, rendering these techniques impractical for HNP synthesis as nanoparticles inherently have trace impurities.[78] Another limitation of HNP synthesis is the transformation of the hydrophilic metal oxide surface to that with a hydrophobic shell. This synthesis requires the use of toxic organic solvents (i.e. dimethyl acetamide, methyl isobutyl ketone, methyl ethyl ketone) with a

high dielectric constant, Ɛ, for the stabilization of the metal oxides.

Aqueous dispersed methods (emulsion polymerization, miniemulsion polymerization, suspension polymerization) have recently been used for synthesis of HNPs with a polymeric core; however, little research has been implemented for synthetic approaches involving from beginning to end the synthesis of HNPs with an inorganic core. Two of the most widely used controlled/living radical polymerization techniques, atom transfer radical polymerization (ATRP)[85,86], and reversible addition fragmentation transfer (RAFT)[87] polymerization have also been implemented for the generation of HNPs. This section will bring attention to the concepts of various types of emulsion polymerizations and ATRP in aqueous dispersed systems for the production of HNPs.

1.3.1 Emulsion polymerization as a means to HNPs

Emulsion polymerization is a chemical process that is widely used in industry to produce water-borne resins with various colloidal and physicochemical properties. The heterogenous process is a free-radical polymerization that involves emulsification of hydrophobic monomers in water by an oil-in-water emulsifier. The initiation typically occurs in the water phase using a water-soluble initiator (e.g. sodium persulfate (NaPS)); however, oil-soluble initiators, such as 2-2'-azobisisobutyronitrile (AIBN) are sometimes used allowing initiation to occur in the oil phase.[88,89]

Typical monomers used in emulsion polymerization include butadiene, styrene, acrylonitrile, acrylates and methacrylates. Emulsion polymerization is characterized by emulsified monomer droplets (1-10 μm in diameter) dispersed in the continuous phase along with monomer swollen micelles (~ 5-20 nm in diameter).[89,90] For micelles to exist in the dispersed phase the concentration of surfactant needs to be above its critical

micelle concentration (CMC). A small amount of monomer can also be dissolved in the aqueous phase; however most of the monomer dwells in the large monomer droplets that act as reservoirs feeding monomer to the growing particles.

In general, monomer droplets are not effective in competing with micelles in capturing free radicals generated in the aqueous phase due to their relatively small surface area. However, monomer droplets can become the predominant particle nucleation loci if the droplet size is reduced to the submicron range. The droplet sizes may be reduced through high shear forces (e.g. probe-sonication) leading to droplet sizes below 500 nm in diameter. This technique is termed miniemulsion polymerization and has been used in laboratory settings to obtain small polymer particles. [91–93]

Waterborne free radicals are typically initiated in the aqueous phase with the monomer molecules dissolved there. As the molecular weight of the growing chain increases, the chain becomes more hydrophobic creating oligomeric radicals. When a critical chain length is achieved, these oligomeric radicals become so hydrophobic that they show a strong tendency to enter the monomer-swollen micelles and then continue to propagate by reacting with those monomer molecules therein. Consequently, monomer swollen micelles become the particle nuclei growing the particles until the monomer reservoirs have been exhausted.

Another type of emulsion polymerization is seeded emulsion polymerization. Unlike ab initio polymerizations (unseeded), where the nucleation of particles has to take place, seeded emulsion polymerizations avoids this nucleation step. The size of the seed latex particles can span a wide range from below 50 nanometers for industrial emulsion polymerizations up to micrometers for preparation of monodisperse latexes. In the latter,

the seed latexes are treated in a specific way to allow a high degree of swelling.[94] Ugelstad *et. al.*[95,96] developed a two-step process involving the addition of a low molecular weight water-soluble solvent, such as acetone, to "activate" or allow transport of monomer through the aqueous phase to swell a seed particle due to a designed-in increased entropy of mixing in the particles. Acetone was then removed, effectively trapping the water-insoluble monomer in the seed particles, thereby localizing the monomer where it could be polymerized in the oil phase (up to 100 times the initial seed volume) (see Fig. 7).[95] This idea of using acetone as a transport agent and allowing monomer to traverse through the aqueous phase will be highlighted in chapter 2.

1.3.2 ATRP in Emulsion Polymerizations

Atom transfer radical polymerization is the most widely used form of controlled/living radical polymerizations (CLRP) where polymers of predetermined a molecular weight and low dispersity (Đ) are obtained with it. The vital mechanism in ATRP is the reversible redox equilibrium between activator and deactivator, maintaining low concentration of radicals suppressing side reactions.[85,97] Over the last 30 years, ATRP been improved with new mechanisms such as activators regenerated by electron transfer (ARGET) ATRP and aqueous ARGET ATRP. ARGET ATRP allows the polymerization to be conducted with ppm levels of copper catalyst, thereby

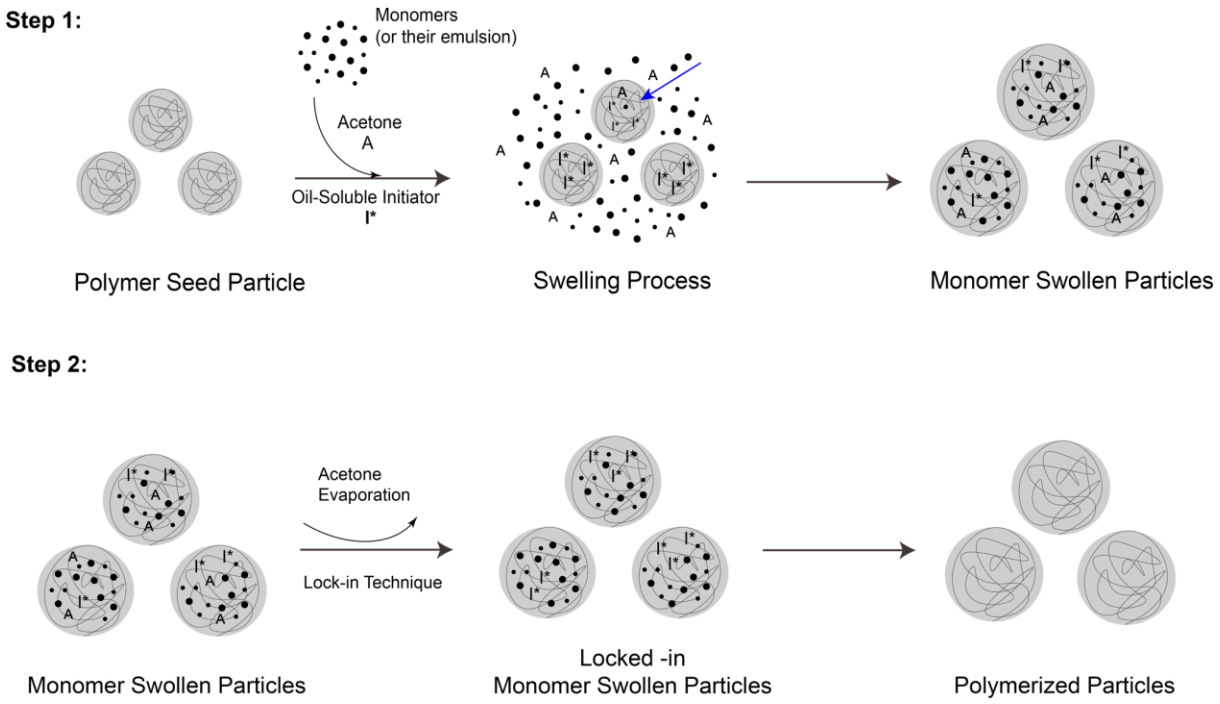

Figure 7. The two-step Ugelstad seeded emulsion polymerization process

reducing the amount of copper in the polymerization. ARGET ATRP also employs a reducing agent (e.g. ascorbic acid or tin(II) 2-ethylhexanoate) to reduce the oxidatively stable Cu^{II}-Br_2/Ligand species to Cu^{I}-Br/Ligand activator to create a reducing/reactivating cycle that eliminates radical traps (e.g. oxygen).[98,99]

Although ATRP offers controlled polymerizations within organic solvents, there is an inherent disadvantage with the mechanism when water is introduced to the system. The halide associated with the Cu^{II}-Br_2/ligand transition metal catalyst dissociates leaving an increased concentration of activators in solution. This causes a large number of radicals in the reaction which can undergo bimolecular termination yielding high dispersity polymers. Simakova et al. [98] have addressed issues of halogen dissociation with water -based ARGET-ATRP reactions by adding an excess of a monovalent halide salt to promote the reformation of the deactivator species.

For ATRP reactions in aqueous systems, a dispersed polymerization method is still preferred; its controlled/living characteristics may be best compared with those of emulsion polymerization and miniemulsion polymerization methods.[100] Min, Gao, and Matyjaszewski [101] first reported a miniemulsion ATRP via an activator generated by electron transfer (AGET) process starting from an oxidatively stable catalyst complex for the preparation of pure linear and star-shaped block copolymers. Wang *et al.* [102] were able to successfully conduct a miniemulsion using tris(2-pyridylmethyl)amine (TPMA) via the interaction between hydrophilic catalysts and an anionic surfactant sodium dodecyl sulfate (SDS).

Most recently, dispersed phase ATRP has also been employed for the production of HNPs. Bombalski et al. [94] reported the synthesis of hybrid materials via ATRP of butyl

acrylate on silica nanoparticles in an aqueous miniemulsion system. However, the ATRP initiator functionalized silica particles were first synthesized in methyl isobutyl ketone [103] prior to ATRP and not in an aqueous system. A straight-forward synthesis of hairy nanoparticles with an inorganic core has yet to be developed in the field, thus allowing us to probe significant questions regarding reaction localization and enhance current methods of emulsion ATRP to achieve HNPs.

Conclusions

This chapter has explored and outlined recent work being conducted in the field of polymer brushes on flat and spherical surfaces. Polymer brushes have demonstrated ease of synthesis on flat surfaces, the effective ability to alter surface properties and application to a number of advanced technologies. They can be bound to a large range of interfaces from gold to silica and attached using "grafting-to" and "grafting-from" techniques.

Polymer brushes on flat surfaces are used for many applications in the biomedical field. The anti-fouling properties of PEG polymer brushes are most desirable for biosensor platforms as they prevent non-specific binding of biomolecules. Although PEG polymer brushes show incredible fouling resistance, it was revealed that PEG decomposes in the presence of transition metal ions and oxygen, which are present in biochemically relevant solutions.

Polymer brushes of spherical surfaces are known as HNPs and are a family of materials that offer a unique combination of polymer processability and potential to scale novel organic-inorganic opto-electronic interfacial effects to the bulk. These new

hybrid materials, offer solutions for numerous applications ranging from quantum dots and chalcogenide-doped high-index lenses and gradient index optical elements for mid-wave IR (MWIR) photonics, to optimization of nanocomposite Faraday rotators, thermoelectrics, low-cost, low-dark-current, broadband PV-inspired IR photodetectors, plasmon-enhanced nonlinear optics for filters and limiters, and passive components (capacitors, resistors) for flexible hybrid electronics packaging.

This thesis consists of several projects that study the mechanism of obtaining low dispersity polymers in an aqueous dispersed system for the goal of obtaining polymer brushes grafted onto inorganic surfaces. Chapter 2 describes a new emulsion polymerization technique called mini monomer encapsulated emulsion polymerization (mini ME emulsions) using ARGET ATRP for the synthesis of PMMA. This emulsion polymerization technique uses acetone, an idea borrowed from seeded emulsion polymerization, to help monomer diffuse through the aqueous phase into the oil phase, while a phase transfer agent, tetrabutylammonium bromide (TBAB), shuttles the ATRP catalyst in the same manner.

In chapter 3, mini ME emulsion polymerization is used to achieve low dispersity polystyrene (PS). This polymerization presented a separate set of challenges that than the previous chapter as reaction localization shifted due to the increased hydrophobicity of PS. Effects such as compartmentalization are studied, and low dispersity PS is achieved through optimization of certain parameters such as initial monomer concentration, $[M]_{\circ}$, ATRP initiator, and ATRP ligand.

Chapters 4 and 5 go one step further and implement this new emulsion polymerization technique on the surface of SiO_2 nanoparticles. In chapter 4, the surface is modified with

PMMA while in chapter 5 it is modified with PS. This aqueous-based "grafting-from" technique generated hairy nanoparticles with a uniform polymer corona. Future studies need to be conducted to perfect this technique on the nanoparticle surface.

Chapter 6 describes a biosensor platform based on the antibody catalyzed water oxidation pathway (ACWOP) that directly detects captured primary antibodies by using their inherent catalytic activity. In this process, antibodies are used as catalysts in the reaction between singlet oxygen and water to generate hydrogen peroxide, which is then detected via colorimetric readout. Our sensor incorporates silica microparticles as an inexpensive substrate that is functionalized with Rose Bengal (photosensitizer), to generate singlet oxygen, and dinitrophenyl (antigen), to capture primary antibodies. We demonstrate specific capture of anti-DNP antibodies on our substrates followed by generation of an antibody-dependent colorimetric ACWOP signal.

In Chapter 7, a preliminary demonstration of a cellulose substrate that was functionalized with POEGMA polymer brushes shows that the ACWOP biosensor can be transformed onto a paper platform if the polymer brushes are present to repel any unwanted adsorption. Paper substrates are desirable as point-of-care devices for mass production. Furthermore, within this chapter mini ME emulsion polymerization is pushed further by using an iron catalyst, where PMMA was obtained with a moderate dispersity index. Future studies would involve the use of iron-mediate as well as metal-free mini ME emulsion polymerizations to continue to improve and span its applications for industry.

REFERENCE

(1) Ohm, C.; Welch, M. E.; Ober, C. K. Materials for Biosurfaces. *J. Mater. Chem.* **2012**, *22* (37), 19343.

(2) Zhao, B.; Brittain, W. J. Polymer Brushes: Surface-Immobilized Macromolecules. *Prog. Polym. Sci.* **2000**, *25* (5), 677–710.

(3) Matyjaszewski, K.; Miller, P. J.; Shukla, N.; Immaraporn, B.; Gelman, A.; Luokala, B. B.; Siclovan, T. M.; Kickelbick, G.; Vallant, T.; Hoffmann, H.; et al. Polymers at Interfaces: Using Atom Transfer Radical Polymerization in the Controlled Growth of Homopolymers and Block Copolymers from Silicon Surfaces in the Absence of Untethered Sacrificial Initiator. *Macromolecules* **1999**, *32* (26), 8716–8724.

(4) Hawker, C. J.; Bosman, A. W.; Harth, E. New Polymer Synthesis by Nitroxide Mediated Living Radical Polymerizations. *Chem. Rev.* **2001**, *101* (12), 3661–3688.

(5) Baum, M.; Brittain, W. J. Synthesis of Polymer Brushes on Silicate Substrates via Reversible Addition Fragmentation Chain Transfer Technique. *Macromolecules* **2002**, *35* (3), 610–615.

(6) Zhou, F.; Huck, W. T. S. Surface Grafted Polymer Brushes as Ideal Building Blocks for "Smart" Surfaces. *Phys Chem Chem Phys* **2006**, *8* (33), 3815–3823.

(7) Tovar, G.; Paul, S.; Knoll, W.; Prucker, O.; Rühe, J. Patterning Molecularly Thin Films of Polymers—New Methods for Photolithographic Structuring of Surfaces. *Supramol. Sci.* **1995**, *2* (2), 89–98.

(8) Ji, S.; Liu, C.-C.; Son, J. G.; Gotrik, K.; Craig, G. S. W.; Gopalan, P.; Himpsel, F. J.; Char, K.; Nealey, P. F. Generalization of the Use of Random Copolymers to Control the Wetting Behavior of Block Copolymer Films. *Macromolecules* **2008**, *41*

(23), 9098–9103.

(9) Senaratne, W.; Andruzzi, L.; Ober, C. K. Self-Assembled Monolayers and Polymer Brushes in Biotechnology: Current Applications and Future Perspectives. *Biomacromolecules* **2005**, *6* (5), 2427–2448.

(10) Welch, M. E.; Ober, C. K. Characterization of Polymer Brush Membranes via HF Etch Liftoff Technique. *ACS Macro Lett.* **2013**, *2* (3), 241–245.

(11) Ji, H.; De Gennes, P. G. Adhesion via Connector Molecules.Pdf. *Macromolecules* **1993**, *26*, 520–525.

(12) Raphael, E.; De Gennes, P. G. Rubber-Rubber Adhesion with Connector Molecules. *J. Phys. Chem.* **1992**, *96* (10), 4002–4007.

(13) Milner, S. . Polymer Brushes. *Science* **1991**, *251*, 905–914.

(14) Chen, X.; Armes, S. P. Surface Polymerization of Hydrophilic Methacrylates from Ultrafine Silica Sols in Protic Media at Ambient Temperature: A Novel Approach to Surface Functionalization Using a Polyelectrolytic Macroinitiator. *Adv. Mater.* **2003**, *15* (18), 1558–1562.

(15) Husemann, M.; Mecerreyes, D.; Hawker, C. J.; James L. Hedrick; Shah, R.; Abbott, N. L. Surface-Initiated Polymerization for Amplification of Self-Assembled Monolayers Patterned by Microcontact Printing. *Angew. Chem. Int. Ed.* **1999**, *38* (5), 647–649.

(16) von Werne, T. A.; Germack, D. S.; Hagberg, E. C.; Sheares, V. V.; Hawker, C. J.; Carter, K. R. A Versatile Method for Tuning the Chemistry and Size of Nanoscopic Features by Living Free Radical Polymerization. *J. Am. Chem. Soc.* **2003**, *125* (13), 3831–3838.

(17) Singhvi, R.; Kumar, A.; Lopez, G. P.; Stephanopoulos, G. N.; Wang, D. I. C.; Whitesides, G. M.; Ingber, D. E. Engineering Cell Shape and Function. *Science* **1994**, *264*, 696–698.

(18) Chen, C. S.; Mrksich, M.; Huang, S.; Whitesides, G. M.; Ingber, D. E. Geometric Control of Cell Life and Death. *Science* **1997**, *276*, 1425–1428.

(19) Aksay, I. A.; Trau, M.; Manne, S.; Honma, I.; Yao, N.; Zhou, L.; Fenter, P.; Eisenberger, P. M.; Gruner, S. M. Biomimetic Pathways for Assembling Inorganic Thin Films. *Science 273*, 872–898.

(20) Balazs, A. C.; Singh, C.; Zhulina, E.; Gersappe, D.; Pickett, G. Patterned Polymer Films. *MRS Bull.* **1997**, *22* (1), 16–21.

(21) Amiji, M.; Park, K. Surface Modification of Polymeric Biomaterials with Poly(Ethylene Oxide), Albumin, and Heparin for Reduced Thrombogenicity. *J. Biomater. Sci. Polym. Ed.* **1993**, *4* (3), 217–234.

(22) Houbenov, N.; Minko, S.; Stamm, M. Mixed Polyelectrolyte Brush from Oppositely Charged Polymers for Switching of Surface Charge and Composition in Aqueous Environment. *Macromolecules* **2003**, *36* (16), 5897–5901.

(23) Welch, M.; Rastogi, A.; Ober, C. Polymer Brushes for Electrochemical Biosensors. *Soft Matter* **2011**, *7* (2), 297–302.

(24) Kim, M.; Schmitt, S. K.; Choi, J. W.; Krutty, J. D.; Gopalan, P. From Self-Assembled Monolayers to Coatings: Advances in the Synthesis and Nanobio Applications of Polymer Brushes. *Polymers* **2015**, *7* (7), 1346–1378.

(25) Krishnan, S.; Weinman, C. J.; Ober, C. K. Advances in Polymers for Anti-Biofouling Surfaces. *J. Mater. Chem.* **2008**, *18* (29), 3405.

(26) Lee, K. S.; Ram, R. J. Plastic–PDMS Bonding for High Pressure Hydrolytically Stable Active Microfluidics. *Lab. Chip* **2009**, *9* (11), 1618.

(27) Chen, C.; Wang, J.; Chen, Z. Surface Restructuring Behavior of Various Types of Poly(Dimethylsiloxane) in Water Detected by SFG. *Langmuir* **2004**, *20* (23), 10186–10193.

(28) Chen, S.; Li, L.; Zhao, C.; Zheng, J. Surface Hydration: Principles and Applications toward Low-Fouling/Nonfouling Biomaterials. *Polymer* **2010**, *51* (23), 5283–5293.

(29) Zolk, M.; Eisert, F.; Pipper, J.; Herrwerth, S.; Eck, W.; Buck, M.; Grunze, M. Solvation of Oligo(Ethylene Glycol)-Terminated Self-Assembled Monolayers Studied by Vibrational Sum Frequency Spectroscopy. *Langmuir* **2000**, *16* (14), 5849–5852.

(30) Kazunori Emoto; Van Alstine, J. M. Stability of Poly(Ethylene Glycol) Graft Coatings.Pdf. *Langmuir* **1998**, *14*, 2722–2729.

(31) Li, L.; Chen, S.; Zheng, J.; Ratner, B. D.; Jiang, S. Protein Adsorption on Oligo (Ethylene Glycol)-Terminated Alkanethiolate Self-Assembled Monolayers: The Molecular Basis for Nonfouling Behavior. *J. Phys. Chem. B* **2005**, *109* (7), 2934–2941.

(32) Galvin, C. J.; Genzer, J. Applications of Surface-Grafted Macromolecules Derived from Post-Polymerization Modification Reactions. *Prog. Polym. Sci.* **2012**, *37* (7), 871–906.

(33) Adamczyk, M.; Fishpaugh, J. R.; Mattingly, P. G. Preparation and Use OfN-Hydroxysuccinimidyl Active Ester Resins. *Tetrahedron Lett.* **1999**, *40* (3), 463–466.

(34) Roberts, M. J.; Bentley, M. D.; Harris, J. M. Chemistry for Peptide and Protein PEGylation. *Adv. Drug Deliv. Rev.* **2012**, *64*, 116–127.

(35) Bhat, R. R.; Chaney, B. N.; Rowley, J.; Liebmann-Vinson, A.; Genzer, J. Tailoring Cell Adhesion Using Surface-Grafted Polymer Gradient Assemblies. *Adv. Mater*. **2005**, *17* (23), 2802–2807.

(36) Desseaux, S.; Klok, H.-A. Fibroblast Adhesion on ECM-Derived Peptide Modified Poly(2-Hydroxyethyl Methacrylate) Brushes: Ligand Co-Presentation and 3D-Localization. *Biomaterials* **2015**, *44*, 24–35.

(37) Muszanska, A. K.; Rochford, E. T. J.; Gruszka, A.; Bastian, A. A.; Busscher, H. J.; Norde, W.; van der Mei, H. C.; Herrmann, A. Antiadhesive Polymer Brush Coating Functionalized with Antimicrobial and RGD Peptides to Reduce Biofilm Formation and Enhance Tissue Integration. *Biomacromolecules* **2014**, *15* (6), 2019–2026.

(38) Lavanant, L.; Pullin, B.; Hubbell, J. A.; Klok, H.-A. A Facile Strategy for the Modification of Polyethylene Substrates with Non-Fouling, Bioactive Poly(Poly(Ethylene Glycol) Methacrylate) Brushes. *Macromol. Biosci.* **2010**, *10* (1), 101–108.

(39) Murata, H.; Prucker, O.; Rühe, J. Synthesis of Functionalized Polymer Monolayers from Active Ester Brushes. *Macromolecules* **2007**, *40* (15), 5497–5503.

(40) Diamanti, S.; Arifuzzaman, S.; Elsen, A.; Genzer, J.; Vaia, R. A. Reactive Patterning via Post-Functionalization of Polymer Brushes Utilizing Disuccinimidyl Carbonate Activation to Couple Primary Amines. *Polymer* **2008**, *49* (17), 3770–3779.

(41) Andruzzi, L.; Hexemer, A.; Li, X.; Ober, C. K.; Kramer, E. J.; Galli, G.; Chiellini, E.; Fischer, D. A. Control of Surface Properties Using Fluorinated Polymer Brushes Produced by Surface-Initiated Controlled Radical Polymerization. *Langmuir* **2004**, *20* (24), 10498–10506.

(42) Pereira, A. de los S.; Rodriguez-Emmenegger, C.; Surman, F.; Riedel, T.; Alles, A. B.; Brynda, E. Use of Pooled Blood Plasmas in the Assessment of Fouling Resistance. *RSC Adv* **2014**, *4* (5), 2318–2321.

(43) Rastogi, A.; Nad, S.; Tanaka, M.; Mota, N. D.; Tague, M.; Baird, B. A.; Abruña, H. D.; Ober, C. K. Preventing Nonspecific Adsorption on Polymer Brush Covered Gold Electrodes Using a Modified ATRP Initiator. *Biomacromolecules* **2009**, *10* (10), 2750–2758.

(44) Rodriguez Emmenegger, C.; Brynda, E.; Riedel, T.; Sedlakova, Z.; Houska, M.; Alles, A. B. Interaction of Blood Plasma with Antifouling Surfaces. *Langmuir* **2009**, *25* (11), 6328–6333.

(45) Unsworth, L. D.; Sheardown, H.; Brash, J. L. Polyethylene Oxide Surfaces of Variable Chain Density by Chemisorption of PEO-Thiol on Gold: Adsorption of Proteins from Plasma Studied by Radiolabelling and Immunoblotting. *Biomaterials* **2005**, *26* (30), 5927–5933.

(46) Leckband, D.; Sheth, S.; Halperin, A. Grafted Poly(Ethylene Oxide) Brushes as Nonfouling Surface Coatings. *J. Biomater. Sci. Polym. Ed.* **1999**, *10* (10), 1125–1147.

(47) Riedel, T.; Riedelová-Reicheltová, Z.; Májek, P.; Rodriguez-Emmenegger, C.; Houska, M.; Dyr, J. E.; Brynda, E. Complete Identification of Proteins Responsible for Human Blood Plasma Fouling on Poly(Ethylene Glycol)-Based Surfaces. *Langmuir* **2013**, *29* (10), 3388–3397.

(48) Zhao, C.; Li, L.; Wang, Q.; Yu, Q.; Zheng, J. Effect of Film Thickness on the Antifouling Performance of Poly(Hydroxy-Functional Methacrylates) Grafted Surfaces. *Langmuir* **2011**, *27* (8), 4906–4913.

(49) Ibanescu, S.-A.; Nowakowska, J.; Khanna, N.; Landmann, R.; Klok, H.-A. Effects of Grafting Density and Film Thickness on the Adhesion of *Staphylococcus Epidermidis* to Poly(2-Hydroxy Ethyl Methacrylate) and Poly(Poly(Ethylene Glycol)Methacrylate) Brushes. *Macromol. Biosci.* **2016**, *16* (5), 676–685.

(50) Faulón Marruecos, D.; Kastantin, M.; Schwartz, D. K.; Kaar, J. L. Dense Poly(Ethylene Glycol) Brushes Reduce Adsorption and Stabilize the Unfolded Conformation of Fibronectin. *Biomacromolecules* **2016**, *17* (3), 1017–1025.

(51) Emilsson, G.; Schoch, R. L.; Feuz, L.; Höök, F.; Lim, R. Y. H.; Dahlin, A. B. Strongly Stretched Protein Resistant Poly(Ethylene Glycol) Brushes Prepared by Grafting-To. *ACS Appl. Mater. Interfaces* **2015**, *7* (14), 7505–7515.

(52) Yandi, W.; Mieszkin, S.; Martin-Tanchereau, P.; Callow, M. E.; Callow, J. A.; Tyson, L.; Liedberg, B.; Ederth, T. Hydration and Chain Entanglement Determines the Optimum Thickness of Poly(HEMA- *Co* -PEG $_{10}$ MA) Brushes for Effective Resistance to Settlement and Adhesion of Marine Fouling Organisms. *ACS Appl. Mater. Interfaces* **2014**, *6* (14), 11448–11458.

(53) Herold, D. A.; Keil, K.; Bruns, D. E. OXIDATION OF POLYETHYLENE CLYCOLS BY ALCOHOL Dehydrogenase.Pdf. *Biomed. Pharmacol.* **1989**, *38* (1), 73–76.

(54) Fan, X.; Lin, L.; Messersmith, P. B. Cell Fouling Resistance of Polymer Brushes Grafted from Ti Substrates by Surface-Initiated Polymerization: Effect of Ethylene Glycol Side Chain Length. *Biomacromolecules* **2006**, *7* (8), 2443–2448.

(55) Akiba, U.; Anzai, J. Recent Progress in Electrochemical Biosensors for Glycoproteins. *Sensors* **2016**, *16* (12), 2045.

(56) Putzbach, W.; Ronkainen, N. Immobilization Techniques in the Fabrication of Nanomaterial-Based Electrochemical Biosensors: A Review. *Sensors* **2013**, *13* (4), 4811–4840.

(57) Wiarachai, O.; Vilaivan, T.; Iwasaki, Y.; Hoven, V. P. Clickable and Antifouling Platform of Poly[(Propargyl Methacrylate)- *Ran* -(2-Methacryloyloxyethyl Phosphorylcholine)] for Biosensing Applications. *Langmuir* **2016**, *32* (4), 1184–1194.

(58) de los Santos Pereira, A.; Riedel, T.; Brynda, E.; Rodriguez-Emmenegger, C. Hierarchical Antifouling Brushes for Biosensing Applications. *Sens. Actuators B Chem.* **2014**, *202*, 1313–1321.

(59) Vaisocherová-Lísalová, H.; Surman, F.; Víšová, I.; Vala, M.; Špringer, T.; Ermini, M. L.; Šípová, H.; Šedivák, P.; Houska, M.; Riedel, T.; et al. Copolymer Brush-Based Ultralow-Fouling Biorecognition Surface Platform for Food Safety. *Anal. Chem.* **2016**, *88* (21), 10533–10539.

(60) Vaisocherová, H.; Mrkvová, K.; Piliarik, M.; Jinoch, P.; Šteinbachová, M.; Homola, J. Surface Plasmon Resonance Biosensor for Direct Detection of Antibody against Epstein-Barr Virus. *Biosens. Bioelectron.* **2007**, *22* (6), 1020–1026.

(61) Riedel, T.; Rodriguez-Emmenegger, C.; de los Santos Pereira, A.; Bědajánková, A.; Jinoch, P.; Boltovets, P. M.; Brynda, E. Diagnosis of Epstein–Barr Virus Infection in Clinical Serum Samples by an SPR Biosensor Assay. *Biosens. Bioelectron.* **2014**, *55*, 278–284.

(62) Welch, M. E.; Doublet, T.; Bernard, C.; Malliaras, G. G.; Ober, C. K. A Glucose Sensor via Stable Immobilization of the GOx Enzyme on an Organic Transistor Using a Polymer Brush. *J. Polym. Sci. Part Polym. Chem.* **2015**, *53* (2), 372–377.

(63) Welch, M. E.; Ritzert, N. L.; Chen, H.; Smith, N. L.; Tague, M. E.; Xu, Y.; Baird, B. A.; Abruña, H. D.; Ober, C. K. Generalized Platform for Antibody Detection Using the Antibody Catalyzed Water Oxidation Pathway. *J. Am. Chem. Soc.* **2014**, *136* (5), 1879–1883.

(64) Block, S.; Piermari, G. J. Paul Wentworth Jr., Lyn H. Jones, Anita D. Wentworth, Xueyong Zhu, Nicholas A. Larsen, Ian A. Wilson, Xin Xu, 2 William A. Goddard III, 2 Kim D. Janda, Albert Eschenmoser, Richard A. Lerner1. *Science* **2001**, *293* (5536), 1806–1811.

(65) Gandhi, A.; Paul, A.; Sen, S. O.; Sen, K. K. Studies on Thermoresponsive Polymers: Phase Behaviour, Drug Delivery and Biomedical Applications. *Asian J. Pharm. Sci.* **2015**, *10* (2), 99–107.

(66) Civantos, A.; Martinez-Campos, E.; Nash, M. E.; Gallardo, A.; Ramos, V.; Aranaz, I. Polymeric and Non-Polymeric Platforms for Cell Sheet Detachment. *Adv. Mater. Interfaces* **2016**, 463–495.

(67) Mandal, K.; Balland, M.; Bureau, L. Thermoresponsive Micropatterned Substrates for Single Cell Studies. *PLoS One* **2012**, *7* (5), e37548.

(68) Yamada, N.; Okano, T.; Sakai, H.; Karikusa, F.; Sawasaki, Y.; Sakurai, Y. Thermo-Responsive Polymeric Surfaces; Control of Attachment and Detachment of Cultured Cells. *Makromol. Chem. Rapid Commun.* **1990**, *11* (11), 571–576.

(69) Patel, N. G.; Zhang, G. Responsive Systems for Cell Sheet Detachment. *Organogenesis* **2013**, *9* (2), 93–100.

(70) Tang, Z.; Okano, T. Recent Development of Temperature-Responsive Surfaces and Their Application for Cell Sheet Engineering. *Regen. Biomater.* **2014**, *1* (1), 91–

102.

(71) Edmondson, S.; Osborne, V. L.; Huck, W. T. S. Polymer Brushes via Surface-Initiated Polymerizations. *Chem. Soc. Rev.* **2004**, *33* (1), 14.

(72) Xiao, D.; Zhang, H.; Wirth, M. Chemical Modification of the Surface of Poly(Dimethylsiloxane) by Atom-Transfer Radical Polymerization of Acrylamide. *Langmuir* **2002**, *18* (25), 9971–9976.

(73) Balamurugan, S.; Mendez, S.; Balamurugan, S. S.; O'Brien, M. J.; López, G. P. Thermal Response of Poly(N-Isopropylacrylamide) Brushes Probed by Surface Plasmon Resonance. *Langmuir* **2003**, *19* (7), 2545–2549.

(74) Xu, F. J.; Zhong, S. P.; Yung, L. Y. L.; Kang, E. T.; Neoh, K. G. Surface-Active and Stimuli-Responsive Polymer−Si(100) Hybrids from Surface-Initiated Atom Transfer Radical Polymerization for Control of Cell Adhesion. *Biomacromolecules* **2004**, *5* (6), 2392–2403.

(75) Cooperstein, M. A.; Canavan, H. E. Biological Cell Detachment from Poly(*N* -Isopropyl Acrylamide) and Its Applications. *Langmuir* **2010**, *26* (11), 7695–7707.

(76) Takahashi, H.; Nakayama, M.; Yamato, M.; Okano, T. Controlled Chain Length and Graft Density of Thermoresponsive Polymer Brushes for Optimizing Cell Sheet Harvest. *Biomacromolecules* **2010**, *11* (8), 1991–1999.

(77) Akiyama, Y.; Kikuchi, A.; Yamato, M.; Okano, T. Ultrathin Poly(N-Isopropylacrylamide) Grafted Layer on Polystyrene Surfaces for Cell Adhesion/Detachment Control. *Langmuir* **2004**, *20* (13), 5506–5511.

(78) Fernandes, N. J.; Koerner, H.; Giannelis, E. P.; Vaia, R. A. Hairy Nanoparticle Assemblies as One-Component Functional Polymer Nanocomposites: Opportunities

and Challenges. *MRS Commun.* **2013**, *3* (01), 13–29.

(79) Person, V. Structure Properties of Heterophase Hairy-Nanoparticles: Organic vs. Inorganic. 113.

(80) Koerner, H.; Drummy, L. F.; Benicewicz, B.; Li, Y.; Vaia, R. A. Nonisotropic Self-Organization of Single-Component Hairy Nanoparticle Assemblies. *ACS Macro Lett.* **2013**, *2* (8), 670–676.

(81) Grabowski, C. A.; Koerner, H.; Meth, J. S.; Dang, A.; Hui, C. M.; Matyjaszewski, K.; Bockstaller, M. R.; Durstock, M. F.; Vaia, R. A. Performance of Dielectric Nanocomposites: Matrix-Free, Hairy Nanoparticle Assemblies and Amorphous Polymer–Nanoparticle Blends. *ACS Appl. Mater. Interfaces* **2014**, *6* (23), 21500–21509.

(82) Akcora, P.; Kumar, S. K.; Moll, J.; Lewis, S.; Schadler, L. S.; Li, Y.; Benicewicz, B. C.; Sandy, A.; Narayanan, S.; Ilavsky, J.; et al. "Gel-like" Mechanical Reinforcement in Polymer Nanocomposite Melts. *Macromolecules* **2010**, *43* (2), 1003–1010.

(83) McEwan, M. E.; Egorov, S. A.; Ilavsky, J.; Green, D. L.; Yang, Y. Mechanical Reinforcement of Polymer Nanocomposites: Theory and Ultra-Small Angle X-Ray Scattering (USAXS) Studies. *Soft Matter* **2011**, *7* (6), 2725.

(84) Choi, J.; Hui, C. M.; Pietrasik, J.; Dong, H.; Matyjaszewski, K.; Bockstaller, M. R. Toughening Fragile Matter: Mechanical Properties of Particle Solids Assembled from Polymer-Grafted Hybrid Particles Synthesized by ATRP. *Soft Matter* **2012**, *8* (15), 4072.

(85) Matyjaszewski, K.; Xia, J. Atom Transfer Radical Polymerization. *Chem. Rev.*

2001, *101* (9), 2921–2990.

(86) Bombalski, L.; Min, K.; Dong, H.; Tang, C.; Matyjaszewski, K. Preparation of Well-Defined Hybrid Materials by ATRP in Miniemulsion. *Macromolecules* **2007**, *40* (21), 7429–7432.

(87) Tumnantong, D.; Rempel, G. L.; Prasassarakich, P. Synthesis of Polystyrene-Silica Nanoparticles via RAFT Emulsifier-Free Emulsion Polymerization. *Eur. Polym. J.* **2016**, *80*, 145–157.

(88) Asua, J. M. Emulsion Polymerization: From Fundamental Mechanisms to Process Developments. *J. Polym. Sci. Part Polym. Chem.* **2004**, *42* (5), 1025–1041.

(89) Chern, C. S. Emulsion Polymerization Mechanisms and Kinetics. *Prog. Polym. Sci.* **2006**, *31* (5), 443–486.

(90) Chern, C.-S. *Emulsion Polymerization*; John Wiley & Sons, Inc, 2008.

(91) Crespy, D.; Landfester, K. Miniemulsion Polymerization as a Versatile Tool for the Synthesis of Functionalized Polymers. *Beilstein J. Org. Chem.* **2010**, *6*, 1132–1148.

(92) Schork, F. J.; Luo, Y.; Smulders, W.; Russum, J. P.; Butté, A.; Fontenot, K. Miniemulsion Polymerization. In *Polymer Particles*; Okubo, M., Ed.; Springer Berlin Heidelberg: Berlin, Heidelberg, 2005; Vol. 175, pp 129–255.

(93) Aizpurua, I.; Amalvy, J.; Barandiaran, M. J.; De La Cal, J. C.; Asua, J. M. Recent Developments in Miniemulsion Polymerization. In *Macromolecular Symposia*; Wiley Online Library, 1996; Vol. 111, pp 121–131.

(94) Frank Caruso. *Colloids and Colloide Assemblies*; WILEY-VCH Verlag GmbH & Co. KGaA: Weinheim, Germany, 2004.

(95) Ugelstad, J.; Kaggerud, K. H.; Hansen, F. K.; Berge, A. Absorption of Low

Molecular Weight Compounds in Aqueous Dispersions of Polymer-Oligomer Particles, 2. A Two Step Swelling Process of Polymer Particles Giving an Enormous Increase in Absorption Capacity. *Macromol. Chem. Phys.* **1979**, *180* (3), 737–744.

(96) J. Ugelstad; H.R. Mfutakamba; P.C. Mork; T. Ellington; A. Berge; R. Schmid; L. Holm; J. Jorgedal; F.K. Hansen; K. Nustad. Prepartation and Application of Monodisperse Polymer Particle. *J. Polym. Sci. Polym. Symp.* **1985**, *72*, 225–240.

(97) Ayres, N. Atom Transfer Radical Polymerization: A Robust and Versatile Route for Polymer Synthesis. *Polym. Rev.* **2011**, *51* (2), 138–162.

(98) Simakova, A.; Averick, S. E.; Konkolewicz, D.; Matyjaszewski, K. Aqueous ARGET ATRP. *Macromolecules* **2012**, *45* (16), 6371–6379.

(99) Kwak, Y.; Matyjaszewski, K. ARGET ATRP of Methyl Methacrylate in the Presence of Nitrogen-Based Ligands as Reducing Agents. *Polym. Int.* **2009**, *58* (3), 242–247.

(100) Charleux, B.; D'Agosto, F.; Delaittre, G. Preparation of Hybrid Latex Particles and Core–Shell Particles Through the Use of Controlled Radical Polymerization Techniques in Aqueous Media. In *Hybrid Latex Particles*; van Herk, A. M., Landfester, K., Eds.; Springer Berlin Heidelberg: Berlin, Heidelberg, 2010; Vol. 233, pp 125–183.

(101) Min, K.; Gao, H.; Matyjaszewski, K. Preparation of Homopolymers and Block Copolymers in Miniemulsion by ATRP Using Activators Generated by Electron Transfer (AGET). *J. Am. Chem. Soc.* **2005**, *127* (11), 3825–3830.

(102) Wang, Y.; Lorandi, F.; Fantin, M.; Chmielarz, P.; Isse, A. A.; Gennaro, A.; Matyjaszewski, K. Miniemulsion ARGET ATRP via Interfacial and Ion-Pair Catalysis: From Ppm to Ppb of Residual Copper. *Macromolecules* **2017**, *50* (21), 8417–8425.

(103) Pyun, J.; Jia, S.; Kowalewski, T.; Patterson, G. D.; Matyjaszewski, K. Synthesis and Characterization of Organic/Inorganic Hybrid Nanoparticles: Kinetics of Surface-Initiated Atom Transfer Radical Polymerization and Morphology of Hybrid Nanoparticle Ultrathin Films. *Macromolecules* **2003**, *36* (14), 5094–5104.

CHAPTER 2

MINI MONOMER ENCAPSULATED EMULSION POLYMERIZATION OF PMMA USING AQUEOUS ARGET ATRP

Abstract

A new emulsion polymerization based on Activators Regenerated by Electron Transfer Atom Transfer Radical Polymerization (ARGET ATRP) has been developed to produce polymethyl methacrylate (PMMA). The critical components of single-pot synthesis via a mini Monomer Encapsulated ARGET ATRP emulsion polymerization will be discussed. In this method, monomer is isolated in a micelle by pre-emulsification in a non-ionic surfactant through high power stirring while acetone is introduced to the polymerization to aid in reactant transport and tetrabutyl ammonium salts are used as phase transfer agents. Polymerizations using tetrabutylammonium bromide (TBAB) were more controlled and demonstrated low Đ (M_w/M_n<1.17), where those using tetrabutylammonium chloride (TBAC) exhibited higher Đ (M_w/M_n >1.50). First-order linear kinetics for MMA polymerizations at 100 mM TBAB was demonstrated, while the reactions deviated from linearity at higher concentrations of TBAB and all concentrations of TBAC.

Introduction

Dispersed phase controlled radical polymerization has recently advanced in such water-borne systems as microemulsion, miniemulsion and emulsion polymerization due to the development of living polymerization options.[1–6]

---

*This chapter was published by R. Cordero, A. Jawaid, M.S. Hsiao, Z. Lequeux, R.A. Vaia, and C.K. Ober in *ACS Macro Lett.*, **2018**, *7* (4), pp 459–463. DOI: 10.1021/acsmacrolett.8b00038.

These aqueous dispersed reactions use mild conditions, are eco-friendly and provide a high safety margin for industrial scale-up due to effective heat dissipation.[7] Miniemulsion polymerization, for example, has recently been the preferred method for co-polymerizing highly water-insoluble monomers that are difficult to polymerize in emulsion due to limited transport though the aqueous phase.[1] By coupling atom transfer radical polymerization (ATRP), for instance, with an aqueous dispersed polymerization we gain the ability to create narrow dispersity polymers.[8–10]

ARGET ATRP has been previously implemented in miniemulsion and emulsion polymerization offering controlled polymerizations in environmentally benign systems.[11–13] ARGET ATRP typically uses parts per million levels of catalyst suppressing any side reactions between the chain end and the catalyst, thereby allowing the formation of high molecular weight polymers with low dispersity. [14,15] ARGET ATRP also employs a reducing agent (e.g. ascorbic acid or tin(II) 2-ethylhexanoate) to reduce the oxidatively stable Cu^{II}-Br_2/Ligand species to Cu^{I}-Br/Ligand activator to create a reducing/reactivating cycle that eliminates radical traps (e.g. oxygen). Although ARGET ATRP in emulsion systems has many advantages, commercially available ATRP ligands (e.g. TPMA and Me_6TREN) which perform well in low catalyst concentrations are not useful in aqueous dispersed media because of their higher affinity toward water than the oil-phase, leading to uncontrolled polymerizations. [13]

Recently, Wang *et al.* [11] were able to successfully conduct a miniemulsion using TPMA via the interaction between hydrophilic catalysts and an anionic surfactant sodium dodecyl sulfate (SDS); however, emulsion polymerizations with TPMA and a non-ionic surfactant still remains a challenge. Another challenge of water based ATRP is controlling localization of the reaction, something that takes place naturally in

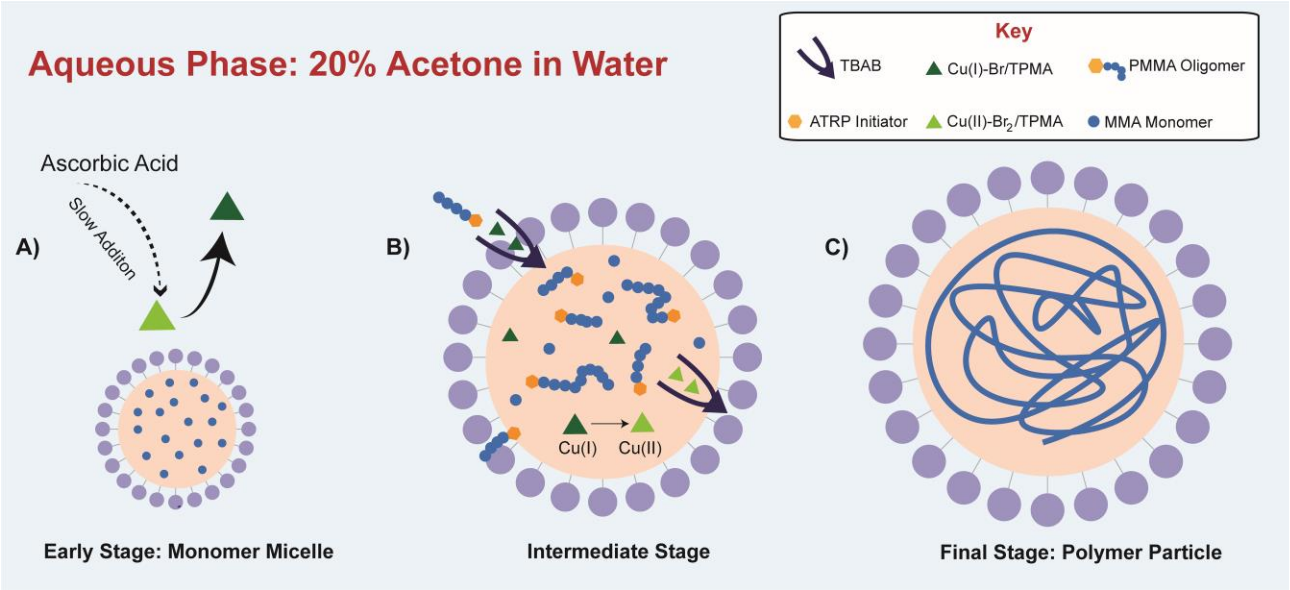

Scheme 1. Depiction of proposed mechanism of mini Monomer Encapsulated (mini ME) ARGET ATRP emulsion polymerization. The polymerization begins with A) a monomer encapsulated micelle and ATRP catalyst, ligand, TBAB, and initiator dissolved in the aqueous phase. Slow addition of ascorbic acid into the reaction reduces the Cu^{II}-Br_2/TPMA deactivator to the Cu^{I}-Br/TPMA activator species with initiation occurring in the aqueous phase. B) These ATRP components are transported in and out of the micelle by TBAB. Polymerization occurs within the micelle until C) polymeric nanoparticles are formed. The aqueous phase is composed of 20% acetone and 80% water.

conventional emulsion polymerization, but is often complex in other dispersed polymerization reactions.

In this report, our intention is to use some of the recent ideas of ARGET ATRP in emulsion and miniemulsion polymerization, combined with ideas of reaction localization first developed by Ugelstad,[16–18] to create an emulsion polymerization method for methyl methacrylate that addresses the limitations of traditional miniemulsion and emulsion polymerizations. We introduce here mini monomer encapsulated (mini Me) ARGET ATRP emulsion polymerization that side-steps many of the issues of monomer transport through an aqueous phase by shifting the limiting step of the polymerization.[19] The incorporation of acetone to aid solubility of several components in the aqueous phase, the use of a phase transfer agent such as tetrabutylammonium bromide (TBAB) or tetrabutylammonium chloride (TBAC) to shuttle into the micelle halogen ion, a water-soluble initiator, and a transition metal catalyst are key aspects to this polymerization system.

This combination allows the use of commercially available ligand (TPMA) affording controlled polymerizations with low Đ (<1.17) and molecular weights over 70,000 g/mol. The halide associated with the phase transfer agent is crucial as it will dictate the rate of polymerization as well as the dispersity. A faster rate and lower dispersities are observed when TBAB is used as the phase transfer agent due to faster exchange of the halide at the chain end.

Scheme 1 outlines a proposed mechanism to our emulsion system. There are two major differences between prior work in this area and mini Me ARGET ATRP emulsion polymerizations. The first is the introduction of acetone to the aqueous continuous phase and the second is the use of a tetrabutylammonium halide salt whose purpose is two-fold. First, it serves as the source of extra halide in ARGET ATRP to form the stable deactivator and increase control of the polymerization.[15] Second, it is used as a phase

transfer agent to aid in the transport of transition metal catalyst into the micelle. Ascorbic acid is slowly fed into the reaction vessel reducing Cu^{II}-Br_2/TPMA (deactivator) to Cu^{I}-Br/TPMA (activator) allowing for the polymerization to commence once it enters the monomer swollen micelle. The ratio of monomer to initiator was chosen according to a similar ratio used by Simakova *et al.* in aqueous ARGET ATRP.[15] Pluronic® F127 was the nonionic surfactant of choice with an HLB of 22 showing optimal results over other nonionic surfactants. Five halide salts were tested in this system: TBAB, TBAC, tetramethylammonium bromide (TMAB), sodium chloride (NaCl), potassium bromide (KBr).

Materials

Methyl methacrylate (MMA), stabilized, 99%, aluminum oxide (basic), L (+)-ascorbic acid, tetrabutylammonium bromide (99%), tetrabutylammonium chloride (98%), and copper (II) bromide (99%, extra pure, anhydrous) were all purchased from Acros Organics and used as received. Tris (2-pyridyl methyl) amine (TPMA, >98%), was purchased from TCI, while triethylamine, Pluronic®F-127, tetramethylammonium bromide, and 33% HBr in acetic acid were purchased from Sigma-Aldrich and used as received. ^{1}H NMR spectra were obtained with an INOVA 400 MHz spectrometer. Polymer conversions were obtained using ^{1}H NMR Mercury 300 MHz. Polymer molecular weights and dispersities were obtained using a Waters ambient temperature GPC in THF (polystyrene standards). The GPC is equipped with triple-detection capability: A Waters 410 differential refractive index detector; a Waters 486 UV-Vis detector; and a Wyatt Technologies TREOS three-angle light-scattering detector, useful for absolute molecular weight determination. The GPC columns are 3 PSS SDV (Polymer Standards Service); 8 mm x 300 mm with porosities of 1,000 angstroms; 10,000 angstroms, and Linear M. Optical microscope images were taken with an

Olympus BX51 with crosses polarization.

Experimental Procedure

Synthesis of N-(2-aminoethyl)-2-bromo-2-methylpropanamide (OBr) ATRP Initiator

A solution of α-bromoisobutyryl bromide (19.72 g, 85.8 mmol) in 40 mL of THF was slowly added at 0˚C to a solution of N-Boc-Ethylenediamine (9.16g, 57.2 mmol), in THF (150 mL) in the presence of triethylamine (11.58 g, 114.4 mmol) over a period of 2 hours. After 2 hours, the reaction was stirred at room temperature for 24 hours. Triethylammonium bromide was formed as a white precipitate and filtered off. The solvent was removed under vacuum resulting in a yellow solid. The yellow solid was dissolved in dichloromethane (DCM) and extracted twice with an aqueous solution saturated with Na_2CO_3. The organic phase was dried over sodium sulfate anhydrous, and DCM was evaporated under vacuum. Column chromatography was performed in a 95:5 solution of DCM: methanol. The resulting solid was washed with ethyl ether and a white solid was obtained as the Boc-protected product. Subsequently, 5g of the Boc-protected initiator was dissolved in 40 mL of ethyl acetate in a 400-mL beaker equipped with a stir bar. To this solution, 33% HBr in acetic acid (6 mL) was added dropwise until it formed a white precipitate. The precipitate was collected, dissolved in ethanol and re-precipitated in ethyl ether yielding a white solid corresponding to the initiator in its ammonium form (yield= 90%). ^{1}H NMR spectrum of initiator is given in Appendix A, Figure 5.

Synthesis of PMMA Homopolymer using Mini-ME ARGET Emulsion ATRP

In a 100-mL round-bottom flask, TBAB (1.934g, 6 mmol), OBr initiator (12.6 mg, 0.06 mmol), $CuBr_2$ (1 mg, 4.48 μmol), and Tris(2-pyridylmethyl) amine (TPMA) (10.45 mg, 36 μmol) were added to a mixture of acetone (12 mL, 20% v/v) and water (34.4 mL), then purged with argon for 30 min. In a separate vial, a surfactant mixture of pluronics

F127 (0.80 g) in water (10 mL) was then added to MMA (3.09 g, 30.85 mmol) and vortexed until it formed a milky white solution. This solution was then added to the contents of the 100-mL round-bottom forming a cloudy white solution and purged with argon for 30 mins. Lastly, in a separate vial, a stock solution of ascorbic acid (2.27 mM, 5 mL) was prepared and purged with argon for 30 min before being fed to the reaction using a syringe pump at a rate of 10 μL/min (3.6 mL). The polymerization was stopped by opening the reaction to air and PMMA was precipitated with methanol. The polymer was centrifuged and dissolved in THF and re-precipitated in hexanes. The polymer was collected and washed with water before oven drying. Purified polymer was dissolved in THF at 1mg/mL for GPC analysis.

Results and Discussion

The tetraalkylammonium salts demonstrated higher activity in shuttling the transition metal ligand due to their finite solubility in both phases, thus allowing it to shuttle between phases. On the other hand, the inorganic salts exhibited inactivity due to their failure to penetrate the micelle, making them ineffective. Polymerizations performed with TBAB demonstrated higher molecular weights and lower Đ (<1.20). The polymerization starts with a monomer-swollen micelle in a solution of 1:4 acetone: water, a ratio that offered optimal results. The ATRP transition metal catalyst (Cu^{II}-Br_2/TPMA), TBAB, and hydrophilic ATRP initiator N-(2-aminoethyl)-2-bromo-2-methylpropanamide (OBr) are also dissolved in the aqueous continuous solvent. Initiation of OBr is thought to occur in the aqueous phase producing oligomeric PMMA which is then absorbed into the micelle or transported via the phase transfer agent.

Molecular weights for polymerizations with both TBAC and TBAB are very similar in the lower concentration range with M_n for 30 mM and 50 mM being 68,000 g/mol and 73,000 g/mol, respectively (Figure 1A). Although the final molecular weights are

similar within this lower range of salt concentrations, the polymer dispersities were significantly different with TBAC displaying Đ above 1.6, while Đ with TBAB was below 1.2 (Figure 1B). When salt concentrations reached 100 mM, MMA polymerization rates for TBAB continued within the same molecular weight range (~74,000 g/mol) as the lower concentration TBAB reactions (Figure 1A). The dispersities of the resulting polymers with 100 mM TBAB remained quite low (Đ ≈ 1.14-1.17) throughout the polymerization, indicative of a fast exchange between active sites and the dormant species (Figure 1B). On the contrary, at 100 mM TBAC, the rate dramatically decreased giving a final molecular weight of ~ 55,000 g/mol after a 6-hr polymerization time.

The high stability of the C-Cl bond at the chain end produces an inefficient propagator in mini ME emulsion polymerization compared to the C-Br bond. Because of this slower rate, not all the chain ends are available to propagate simultaneously, thus broadening the dispersity. On the other hand, because the C-Br bond is less stable, propagation is faster and the accessibility of the monomer to the chain end is higher leading to fast but simultaneous propagation of the chain ends. The dispersity is thus controlled by the availability of monomer to the chain end where propagation occurs. If the chain end is inaccessible to monomer, not only does a reduced reaction rate occur, but control will be lost during the polymerization.

As salt concentrations were increased from 100 mM to 300 mM, the polymerization rates decreased giving a final molecular weight of ~55,000 g/mol for MMA polymerizations at 300 mM TBAB with a slightly higher Đ (< 1.34) (Figure 1B, Table 1). Alternatively, rates steadily decreased with a more dramatic effect in polymerizations with TBAC showing a final molecular weight of ~ 48,000 g/mol at 300 mM TBAC with a Đ > 3.0 (Figure 1B, Table 1). De Paoli *et al.*[20] observed a similar phenomenon of a decrease in rate of polymerization with increasing

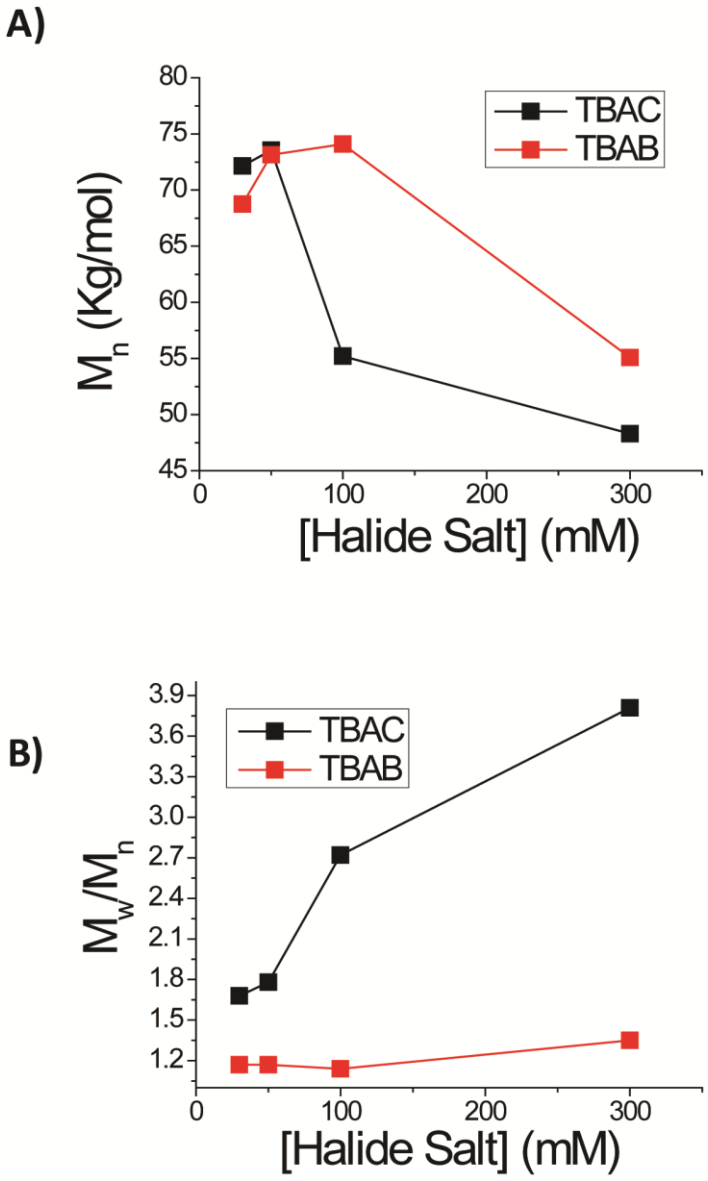

Figure 1. A) Effect of halide salt concentration (30 mM, 50 mM, 100 mM, and 300 mM) on molecular weight of PMMA (ascorbic acid feeding rate= 23 nmoles/min) B) Dispersity of MMA polymerization as a function of TBAC and TBAB concentrations. $[M]_0$ = 0.518 M, $[I]_0$ = 1 mM, $[CuBr_2]$ = 0.075 mM. All polymerizations were conducted at 30˚C for 6 hrs.

Halide Salt	Concentration (mM)	Đ	$M_n^{(SEC)}$ (g/mol)
TBAB	100	1.14	74,088
TBAC	100	2.72	55,006
TMAB	100	1.34	57,513
TBAB	300	1.35	55,087
TBAC	300	3.81	48,356

Table 1. Data table of MMA polymerizations at 6 hrs. with halide salts at 100 and 300 mM concentrations, their dispersity (Đ), and molecular weights. $[M]_0$ = 0.518 M, $[I]_0$ = 1 mM, [Cu]= 0.075 mM, and ascorbic acid feeding rate at 23 nmoles/min. All polymerizations were performed at 30˚C.

concentration of either Cl- and Br- in their ATRP polymerizations. It was shown that the real activator in ATRP is the $Cu^{I}L+$ species and Cl- and Br- have different affinities to this activator. They explained that the effect of Br- on K_{act} is smaller than the effect of Cl- and is related to the speciation of Cu^{I}, which, for any given concentration of X-, produces a higher fraction of the activator in the presence of Br- than Cl-.[20] The overall decrease in rates with increasing X- concentrations are attributed to the production of inactive species (Figure 1A).

To assess the effect the cation has on the reaction mechanism, two inorganic halide salts were utilized, KBr and NaCl. When these salts were employed, polymerization did not occur (Table 2). Figure 2 (inset: left) illustrates an image of a reaction mixtures when NaCl was used and its appearance did not change from when the reaction commenced. Figure 2 (inset: right) illustrates when the polymerization was conducted with TBAB. The solution transforms from cloudy and colorless to blue and transparent. This blue scattering is due to the Tyndall effect as the dispersed phase remains extremely small. The inability to produce PMMA when the inorganic salts are used is likely due to the localization of these salts in the aqueous phase and their limited ability to enter the micellar phase. As there is a large excess of salt compared to the $CuBr_2$, ligand and initiator ATRP components, these components will also likely remain in the aqueous phase with the salt, therefore, impeding the polymerization.

Figure 2 further confirms the ineffectiveness of the inorganic salts (KBr and NaCl) in the polymerization of PMMA with mini ME emulsions. The carbonyl peak at 1728 cm^{-1} associated with PMMA is not present after purification when mini ME emulsions are done with NaCl. When TBAB is utilized, the strong carbonyl peak is apparent after purification. Unswollen micelles were measured to have a diameter of 11 nm using dynamic light scattering measurements (DLS) (Figure 3A), while monomer

Halide Salt	Acetone	Result
KBr	Yes	No polymer
NaCl	Yes	No polymer
TBAB	None	No polymer
None	Yes	Polymer with Đ > 2.0
TBAB	Evaporated	M_n: 40,427 g/mol Đ: 1.37
TBAB	Yes	$M_{n:}$ 74,088 g/mol Đ: 1.14

Table 2. Data table of MMA polymerizations at 6 hrs. with halide salts at 100 mM. $[M]_0$ = 0.518 M, $[I]_0$ = 1 mM, $[CuBr_2]$ = 0.075 mM, and ascorbic acid feeding rate at 23 nmoles/min. All polymerizations were performed at 30˚C.

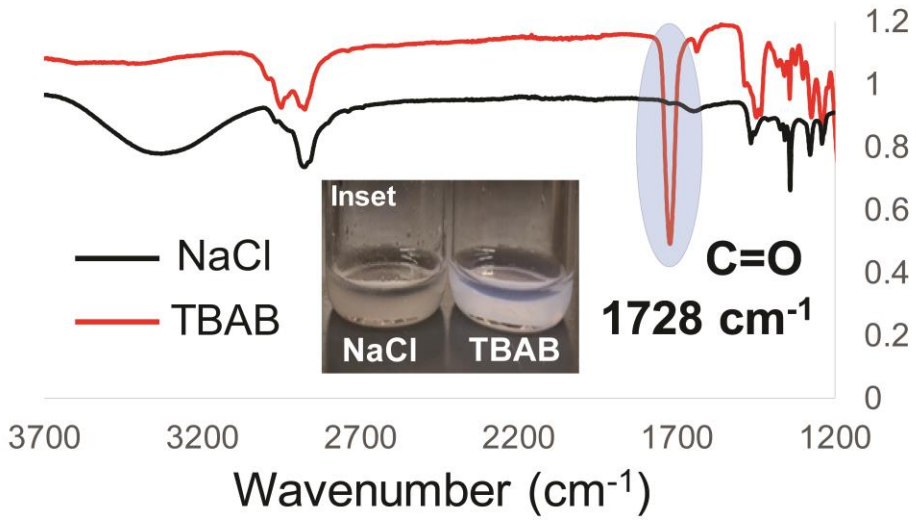

Figure 2. Fourier Transform Infrared Spectroscopy (FTIR) of polymerizations of MMA with TBAB or NaCl as halide salt in Pluronics F-127 surfactant. (Inset: mini ME emulsion with NaCl (Left) and TBAB (Right))

swollen micelles were measured to be 21 nm (Figure 3B). The final particle size was measured as 54 nm using DLS (Figure 3C). Emulsions were viewed under an optical microscope before the start of the polymerization revealing small monomer droplets (~2 μm) sparsely dispersed (Figure 4). This indicates that although monomer droplets exist in this emulsion system, most of the monomer is in the aqueous phase and in the monomer swollen micelles.

To compare the diffusion rate of the phase transfer catalyst in mini ME emulsion reactions, a less bulky cation on the phase transfer salt, TMAB, was employed. Polymerizations in which TMAB was utilized as the halide salt produced polymer with lower molecular weights and higher Đ than those done with TBAB; however, the polymerizations were more controlled than those with TBAC (Table 1). Plots of $\ln([M]_0/[M])$ vs time were obtained and used to compare phase transfer salts at 100 mM concentrations (Figure 5). This plot demonstrates the relative linearity of polymerizations with TBAB as also shown in Figure 6A, and the non-linear nature of the polymerizations in 100 mM TBAC and TMAB. The bulkiness of the cation is pivotal as the diffusion into the micelle appears to be faster with TBAB than with TMAB. This rate of diffusion becomes the limiting step of the polymerization. If the diffusion of the halide into the micelle is slow, such as in the case of TMAB, the overall polymerization rate slows and is associated with higher dispersity.

Figure 6B demonstrates a plot of $\ln([M]_0/[M])$ for MMA polymerizations with 100 and 300 mM TBAB and TBAC. The linearity of MMA polymerizations with TBAB indicates that the number of propagating species remains constant as described by the persistent radical effect (PRE).[21] This linearity starts to deviate as the concentration of the salt increases; a very similar mechanism to that mentioned previously with TBAC. These plots demonstrate that faster polymerization rates and exchange result in polymers with Đ lower than 1.2 in a mini ME ARGET ATRP emulsion system.

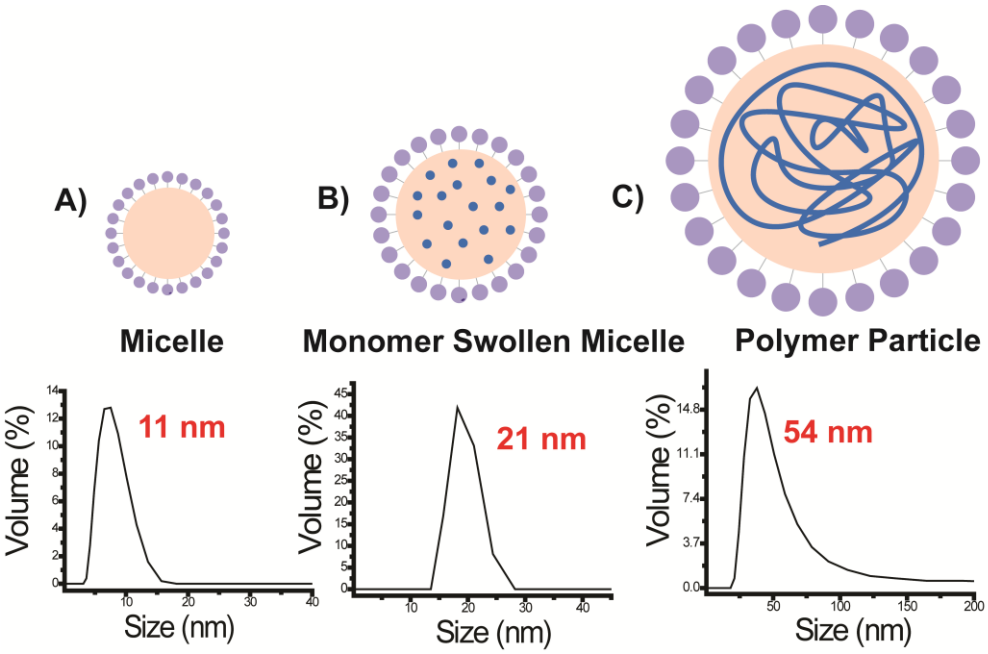

Figure 3. Particle size distribution of A) Pluronics F-127 micelle alone, B) monomer swollen micelle, and C) polymer particle after mini Me emulsion polymerization occurred. Ascorbic acid feeding rate= 23 nmoles/min, $[M]_0$ = 0.518 M, $[I]_0$ = 1 mM, $[CuBr_2]$ = 0.075 mM, [TBAB] = 100 mM. All polymerizations were conducted at 30˚C for 6 hr.

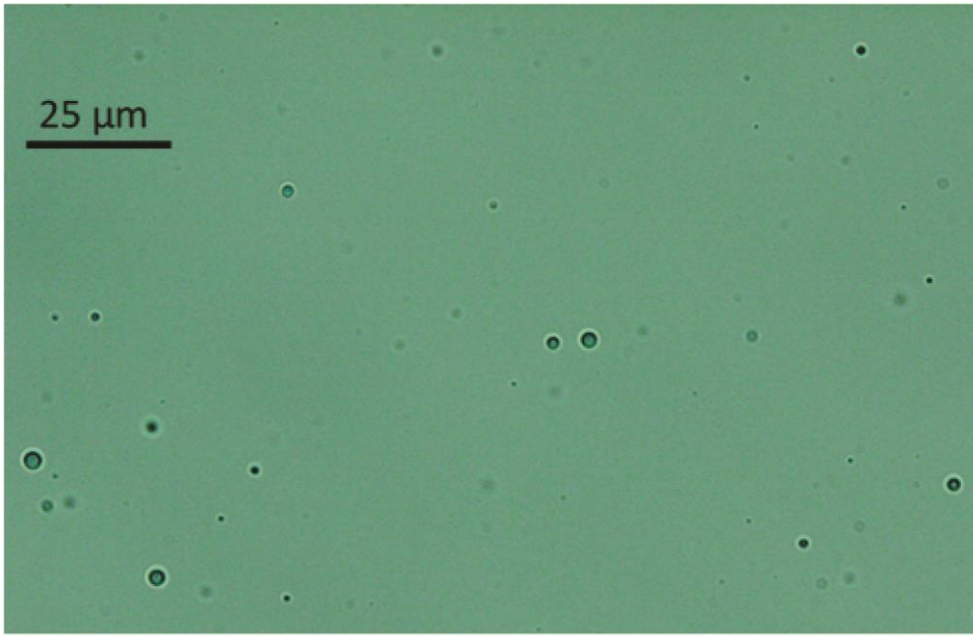

Figure 4. Optical microscope image of mini ME emulsion before the start of polymerization. Nominal magnification 40x

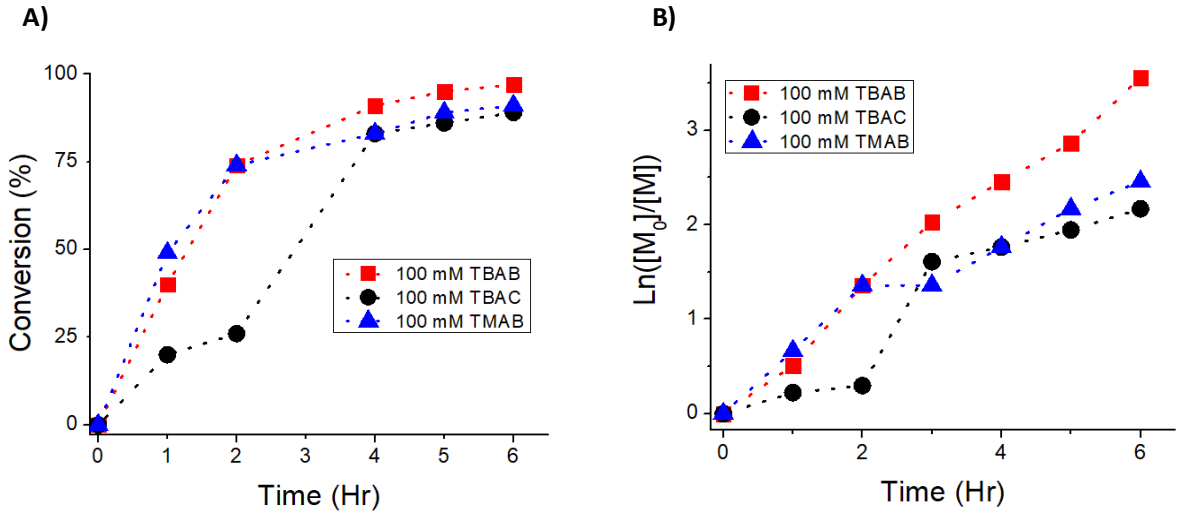

Figure 5. A) Conversion of PMMA versus time using mini-ME ARGET ATRP emulsions polymerizations with 100 mM TBAB, TMAB, and TBAC. B) First-order kinetic plot of mini-ME ARGET ATRP emulsions with TBAB, TBAC, and TMAB at 100 mM. $[M]_0$ = 0.518 M, $[I]_0$ = 1 mM, $[CuBr_2]$ = 0.075 mM, and ascorbic acid feeding rate at 23 nmoles/min. All polymerizations were performed at 30˚C. Note: dotted lines are provided to guide the eye.

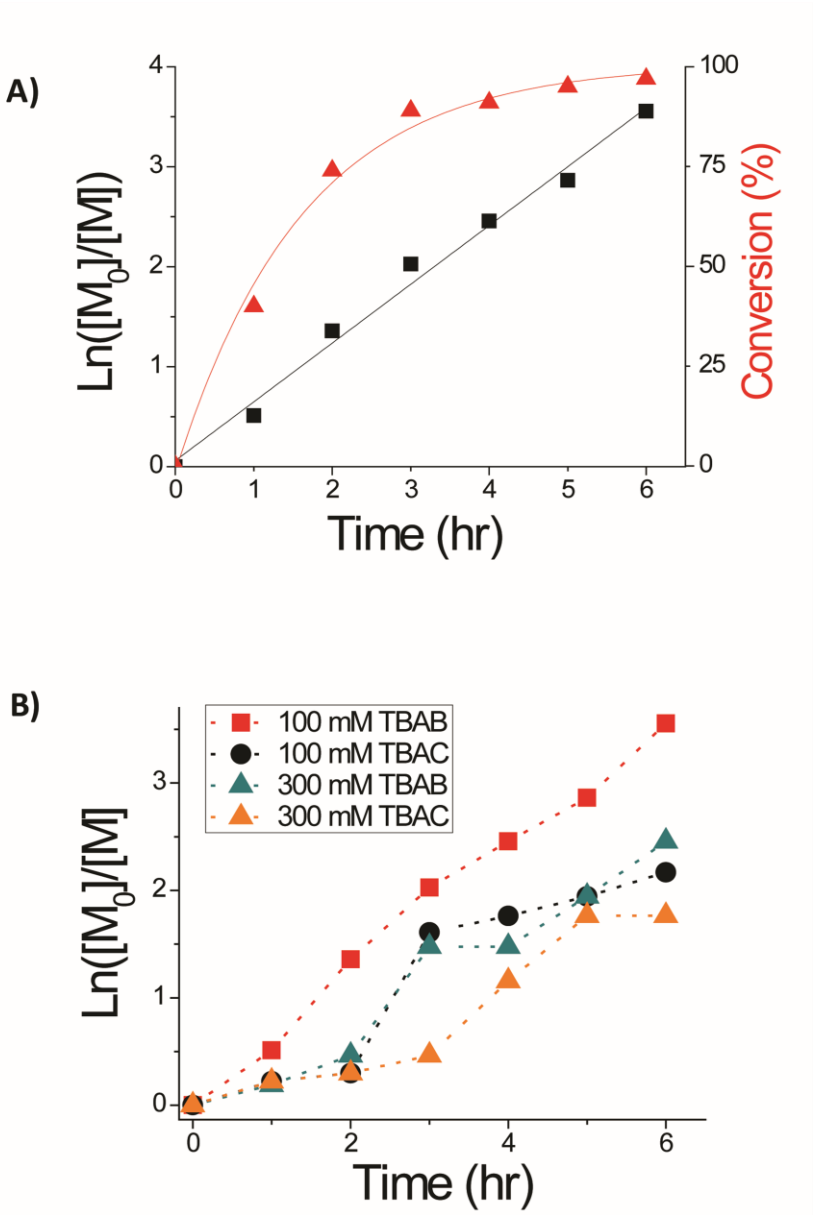

Figure 6. A) First-order kinetic plot for polymerization of MMA in mini ME ARGET emulsion ATRP with 100 mM and 300 mM TBAB and TBAC. B) Kinetic plot for polymerization of MMA with mini-ME ARGET ATRP emulsion conducted with 100 mM of TBAB. $[M]_0$ = 0.518 M, $[I]_0$ = 1 mM, [CuBr2] = 0.075 mM and ascorbic acid feeding rate at 23 nmoles/min. All polymerizations were conducted at 30˚C. Note: Lines were provided to guide the eye.

Finally, the effect of acetone on the polymerization was evaluated and the results are summarized in Table 2. In 1979, John Ugelstad developed a seeded emulsion polymerization involving the addition of a low molecular weight water-soluble solvent, such as acetone, to "activate" or allow transport of monomer through the aqueous phase to swell a seed particle due to a designed-in increased entropy of mixing in the particles. Acetone was then removed, effectively trapping the water-insoluble monomer in the seed particles, thereby localizing the monomer where it could be polymerized in the oil phase (up to 100 times the initial seed volume).[16]

As a control experiment in our studies using TBAB, acetone was not added to the reaction vessel at the start of the polymerization resulting in no polymer production. Another experiment was performed under the same conditions except acetone was added to the reaction vessel along with the pre-emulsified monomer swollen micelles. This mixture was stirred for 10 mins and then acetone was evaporated under argon for an hour. This experiment resulted in a lower molecular weight polymer (~40,000 g/mol) and a higher Đ (1.37) than under preferred conditions with TBAB, confirming the importance of using acetone as a shuttle system throughout the entire polymerization. Another control experiment involved the utilization of a hydrophobic initiator, methyl α-bromoisobutyrate, in lieu of the hydrophilic OBr initiator. The results of this experiment were similar to the previous control experiment with acetone evaporation. Polymer conversion was lower resulting in a molecular weight of 41,281 g/mol with a dispersity of 1.41 indicating that the location of initiation is pivotal to overall control of the polymerization.

Conclusions

In this work, an emulsion polymerization method based on ARGET ATRP was developed to polymerize MMA in an aqueous dispersion. Mini ME ARGET ATRP emulsion polymerization resulted in well-defined PMMA with dispersities as low as

1.14. By localizing the propagation and controlling the availability of monomer, we provide a framework that addresses the challenges of traditional miniemulsion and emulsion polymerizations. This was done by a) the incorporation of acetone and b) using a phase transfer agent. Acetone was used as an aid for reaction localization that helped lower molecular weight dispersity. The presence and choice of halide in the phase transfer catalyst was also pivotal in the reaction rate and overall control of the polymerization. Introduction of bromide anion to the oil phase using TBAB was shown to provide excellent polymerization results with dispersities as low as 1.14 and M_n as high as 74,088 g/mol. A linear kinetic plot was obtained with polymerizations using TBAB thus suggesting a constant number of propagating species, proving it to be a facile method of PMMA polymerization.

Polymerizations using TBAC as phase transfer agent generated polymer with much higher dispersities (Đ >1.5) and slower polymerization rates. The use of inorganic salts in the emulsion process impeded polymerization due to a lack of transport into the oil phase micelle, while a less bulky cation (TMAB) offered weaker partitioning into the micelle, thus lowering the rate and increasing Đ. It was concluded that faster rates of polymerization are associated with lower dispersities and higher molecular weights; these rates strongly depended on the phase transfer catalyst, the halide used and the nature of the cation.

ACKNOWLEDGMENTS

The authors would like to thank the Air Force Office of Scientific Research (AFOSR FA9550-17-1-0038), and for prior support the Air Force Research Laboratory (AFRL). This work made use of the Cornell Center for Materials Research Shared Facilities which are supported through the NSF MRSEC program (DMR-1719875). Experiments were conducted at both Cornell University and at AFRL. Contributing members include Zoe Lequeux who is an undergraduate student in the Ober group and ran the kinetic experiments for this paper, Dr. Ali Jawaid from AFRL who initially helped with the concept of mini ME emulsion polymerization through brain-storming, Dr. Ming-Siao Hsiao from AFRL who provided TEM images of the mini ME emulsions and Dr. Richard Vaia from AFRL whose lab mini ME emulsion polymerization was first developed in during my internship with AFRL (UES subcontracted).

REFERENCES

(1) Cunningham, M. F. Controlled/Living Radical Polymerization in Aqueous Dispersed Systems. *Prog. Polym. Sci.* **2008**, *33* (4), 365–398.

(2) Asua, J. M. Emulsion Polymerization: From Fundamental Mechanisms to Process Developments. *J. Polym. Sci. Part Polym. Chem.* **2004**, *42* (5), 1025–1041.

(3) Aizpurua, I.; Amalvy, J.; Barandiaran, M. J.; De La Cal, J. C.; Asua, J. M. Recent Developments in Miniemulsion Polymerization. In *Macromolecular Symposia*; Wiley Online Library, 1996; Vol. 111, pp 121–131.

(4) Min, K.; Matyjaszewski, K. Atom Transfer Radical Polymerization in Aqueous Dispersed Media. *Open Chem.* **2009**, *7* (4).

(5) Wei, Y.; Liu, P.; Wang, W.-J.; Li, B.-G.; Zhu, S. Well-Controlled and Stable Emulsion ATRP of MMA with Low Surfactant Concentration Using Surfactant–ligand Design as the Copper Capture Agent. *Polym. Chem.* **2015**, *6* (15), 2837–2843.

(6) Kagawa, Y.; Zetterlund, P. B.; Minami, H.; Okubo, M. Atom Transfer Radical Polymerization in Miniemulsion: Partitioning Effects of Copper(I) and Copper(II) on Polymerization Rate, Livingness, and Molecular Weight Distribution †. *Macromolecules* **2007**, *40* (9), 3062–3069.

(7) Schork, F. J.; Luo, Y.; Smulders, W.; Russum, J. P.; Butté, A.; Fontenot, K. Miniemulsion Polymerization. In *Polymer Particles*; Okubo, M., Ed.; Springer Berlin Heidelberg: Berlin, Heidelberg, 2005; Vol. 175, pp 129–255.

(8) Fantin, M.; Park, S.; Wang, Y.; Matyjaszewski, K. Electrochemical Atom Transfer Radical Polymerization in Miniemulsion with a Dual Catalytic System.

Macromolecules **2016**, *49* (23), 8838–8847.

(9) Bombalski, L.; Min, K.; Dong, H.; Tang, C.; Matyjaszewski, K. Preparation of Well-Defined Hybrid Materials by ATRP in Miniemulsion. *Macromolecules* **2007**, *40* (21), 7429–7432.

(10) Rusen, E.; Mocanu, A. Atom Transfer Radical Emulsion Polymerization (Emulsion ATRP) of Styrene with Water-Soluble Initiator. *Colloid Polym. Sci.* **2013**, *291* (9), 2253–2257.

(11) Wang, Y.; Lorandi, F.; Fantin, M.; Chmielarz, P.; Isse, A. A.; Gennaro, A.; Matyjaszewski, K. Miniemulsion ARGET ATRP via Interfacial and Ion-Pair Catalysis: From Ppm to Ppb of Residual Copper. *Macromolecules* **2017**, *50* (21), 8417–8425.

(12) Cheng, C.; Shu, J.; Gong, S.; Shen, L.; Qiao, Y.; Fu, C. Synthesis and Use of a Surface-Active Initiator in Emulsion Polymerization under AGET and ARGET ATRP Conditions. *New J Chem* **2010**, *34* (1), 163–170.

(13) Elsen, A. M.; Burdyńska, J.; Park, S.; Matyjaszewski, K. Activators Regenerated by Electron Transfer Atom Transfer Radical Polymerization in Miniemulsion with 50 Ppm of Copper Catalyst. *ACS Macro Lett.* **2013**, *2* (9), 822–825.

(14) Kwak, Y.; Magenau, A. J. D.; Matyjaszewski, K. ARGET ATRP of Methyl Acrylate with Inexpensive Ligands and Ppm Concentrations of Catalyst. *Macromolecules* **2011**, *44* (4), 811–819.

(15) Simakova, A.; Averick, S. E.; Konkolewicz, D.; Matyjaszewski, K. Aqueous ARGET ATRP. *Macromolecules* **2012**, *45* (16), 6371–6379.

(16) Ugelstad, J.; Kaggerud, K. H.; Hansen, F. K.; Berge, A. Absorption of Low Molecular Weight Compounds in Aqueous Dispersions of Polymer-Oligomer Particles,

2. A Two Step Swelling Process of Polymer Particles Giving an Enormous Increase in Absorption Capacity. *Macromol. Chem. Phys.* **1979**, *180* (3), 737–744.

(17) Ugelstad, J.; El-Aasser, M. S.; Vanderhoff, J. W. Emulsion Polymerization: Initiation of Polymerization in Monomer Droplets. *J. Polym. Sci. Part C Polym. Lett.* **1973**, *11* (8), 503–513.

(18) J. Ugelstad; H.R. Mfutakamba; P.C. Mork; T. Ellington; A. Berge; R. Schmid; L. Holm; J. Jorgedal; F.K. Hansen; K. Nustad. Prepartation and Application of Monodisperse Polymer Particle. *J. Polym. Sci. Polym. Symp.* **1985**, *72*, 225–240.

(19) Schork, F. J.; Luo, Y.; Smulders, W.; Russum, J. P.; Butté, A.; Fontenot, K. Miniemulsion Polymerization. In *Polymer Particles*; Okubo, M., Ed.; Springer Berlin Heidelberg: Berlin, Heidelberg, 2005; Vol. 175, pp 129–255.

(20) De Paoli, P.; Isse, A. A.; Bortolamei, N.; Gennaro, A. New Insights into the Mechanism of Activation of Atom Transfer Radical Polymerization by Cu(i) Complexes. *Chem. Commun.* **2011**, *47* (12), 3580.

(21) Matyjaszewski, K.; Xia, J. Atom Transfer Radical Polymerization. *Chem. Rev.* **2001**, *101* (9), 2921–2990.

CHAPTER 3

SYNTHESIS OF POLYSTYRENE USING MINI MONOMER ENCAPSULATED EMULSION POLYMERIZATION WITH AQUEOUS ARGET ATRP

Abstract

Polystyrene was successfully polymerized using Mini Monomer Encapsulated Emulsion polymerization (mini ME) based on activators regenerated by electron transfer atom transfer radical polymerization (ARGET ATRP). In this system, styrene monomer and the hydrophobic initiator, ethyl 2-bromoisobutyrate (EBIB), are pre-emulsified using Pluronic F127 surfactant. A phase transfer agent, tetrabutyl ammonium bromide (TBAB), acetone (20% v/v), and ATRP catalyst are dissolved in the aqueous phase while ascorbic acid is slowly fed into the reaction vessel at a constant rate. At an initial monomer concentration of 260 mM, using the $CuBr_2$/TPMA (1:8) ATRP catalyst, a controlled polymerization of polystyrene ($Đ < 1.2$) was obtained where $M_n \approx M_{n,theo}$. The effects of initiator, monomer concentration and ligand type were studied. Compartmentalization effects were observed when $[M]_\circ$ was increased to 518 mM using CuB_2/TPMA as the catalyst as well as when varying the ATRP ligand when $[M_\circ]$ was 260 mM.

---

*This chapter was submitted at the time of graduation by R. Cordero, Z. Lequeux, R.A. Vaia, and C.K. Ober to *Macromolecules*.

Introduction

Controlled/living radical polymerizations (CLRP) is a well-established area of research providing innovative routes to designing polymers with controlled microstructures.[1] Within recent years, the implementation of CLRP with aqueous dispersed phase polymerizations has seen increased interest, providing control over emulsion based systems that is desirable for a plethora of applications, including the manufacture of polymer-grafted nanoparticles.[2,3] Activators regenerated by electron transfer (ARGET) ATRP is the most common CLRP technique used in conjunction with emulsion systems in which a reducing agent, such as ascorbic acid, is used to convert *in situ* the less air-sensitive Cu(II) into Cu(I) allowing the polymerization to occur in the presence of a limited amount of oxygen. ARGET ATRP is also well suited to lower catalyst concentrations, reducing the amount of residual transition metal in the final product and suppressing many side reactions.[4] This bodes well for industry as emulsion polymerizations using ARGET ATRP, given the interesting properties discussed below, are more amenable to large-scale production of hydrophobic polymers.

The key to controlling radical polymerizations is to maintain a rapid equilibrium between the growing radicals and dormant species.[5] Due to the complex localization of monomer and transition metal catalyst in a heterogeneous system, for example emulsion polymerization, the unbalanced partitioning of the ligand and catalyst causes a shift in the equilibrium, thus generating poorly controlled polymerizations. Our group has recently reported the development of a new emulsion polymerization (mini ME), producing poly(methyl methacrylate) with distinctly low dispersity.[6] In this system, a tetraalkylammonium bromide phase transfer agent was used to shuttle the water-soluble

transition metal catalyst, Cu(I)Br/tris(2-pyridylmethyl)amine (TPMA), from the aqueous phase into the micelle.

Most recently, Lorandi *et al.*[7] used this idea to create an *ab initio* emulsion ATRP polymerization of methacrylate monomers using an amphiphilic catalyst system based on the hydrophilic complex (Cu/TPMA) and an anionic surfactant, sodium dodecyl sulfate (SDS).[8,9] In 2013, Rusen and Mocanu [10] had a similar idea for the polymerization of styrene in an emulsion system with a water-soluble initiator. They executed this concept by employing a dual-ligand technique using 2,2′-bipyridine (Bpy) as the water-soluble ligand and N, N, N′, N′, N″-pentamethyldiethylenetriamine (PMDETA) as the hydrophobic ligand soluble in the organic phase. However, this method will typically generate polymers with high Đ since introducing different ligands to the same polymerization can lead to different polymerization rates. A number of these effects are consistent with the known phenomenon of compartmentalization.

Compartmentalization and reactant partitioning involve the physical isolation of reactants within a confined locus.[11] Compartmentalization in CLRP can become complex specifically when deactivator species are sufficiently low in concentration and if they are sufficiently insoluble in the aqueous phase.[12] In our previous study,[6] localization of the monomer and transition metal catalyst was a valuable tool in gaining control of an ARGET ATRP polymerization. Our use of acetone in the aqueous phase further enabled the solubility and transport of monomer in both phases, allowing initiation to occur in the aqueous phase and polymer growth to take place in the monomer rich oil phase. Polymerization rates were consistent with the persistent radical effect [13] and compartmentalization did not seem to play a significant role in the

polymerization. However, localization of a monomer throughout the polymerization may be significantly more pronounced with the hydrophobic monomer, styrene, described in this study.

In the study reported herein, mini ME emulsion polymerization was carried out for the polymerization of polystyrene. Parameters such as the ligand type, initiator, monomer concentration, ascorbic acid feed rate, and copper:ligand ratio were varied to adjust the polymerization conditions. The ATRP ligand, TPMA, was observed to have desirable polymerization rates and Đ as low as 1.14 with initial monomer concentrations of 260 mM using the hydrophobic initiator, ethyl 2-bromoisobutyrate (EBIB) was achieved. As $[M]_0$ was increased to 518 mM, polymerization rates were decreased; however, the molecular weight distribution (MWD) remained low (Đ <1.2), indicative of compartmentalization effects. Ascorbic acid feed rates and copper:ligand ratios both had significant effects on the polymerization rates and molecular weight dispersity. Higher ascorbic acid feed rates and higher copper:ligand ratios produced the most uniform molecular weight and highest yields when TPMA was used as the ligand, while a lower copper:ligand ratio was more effective for the more active tris[2-(dimethylamino) ethyl] amine (Me_6TREN) ligand. PDMETA ligand provided the least control while generating polymers with Đ >1.9.

Experimental Section

Materials

Styrene, stabilized, 99%, aluminum oxide (basic), L (+)-ascorbic acid, tetrabutylammonium bromide (99%), and copper (II) bromide (99%, extra pure,

anhydrous) were all purchased from Acros Organics and used as received. Tris (2-pyridyl methyl) amine (TPMA, >98%), tris[2-(dimethylamino) ethyl] amine (Me_6TREN), and N, N, N′, N′, N″-pentamethyldiethylenetriamine (PMDETA) were purchased from TCI, while triethylamine, Ethyl 2-bromoisobutyrate (EBIB), 2-hydroxyethyl-2-bromoisobutyrate (HEBIB), Pluronic®F-127, and 33% HBr in acetic acid were purchased from Sigma-Aldrich and used as received.

Instrumentation

Polymer molecular weights and dispersities were obtained using a Waters ambient temperature GPC in THF (polystyrene standards). The GPC is equipped with triple-detection capability: A Waters 410 differential refractive index detector; a Waters 486 UV-Vis detector; and a Wyatt Technologies TREOS three-angle light-scattering detector, useful for absolute molecular weight determination. The GPC columns are 3 PSS SDV (Polymer Standards Service); 8 mm x 300 mm with porosities of 1,000 angstroms; 10,000 angstroms, and Linear M. Optical microscope images were taken with an Olympus BX51 with crosses polarization. Polymer particle size distribution was measured using dynamic light scattering (DLS) with the Zetasizer Nano ZS at 25˚C (Malvern Instruments).

Synthesis of N-(2-aminoethyl)-2-bromo-2-methylpropanamide (OBr) ATRP Initiator

OBr was prepared using a previously reported method.[6] Briefly, a solution of α-bromoisobutyryl bromide (19.72 g, 85.8 mmol) in 40 mL of THF was slowly added at 0˚C to a solution of N-Boc-Ethylenediamine (9.16g, 57.2 mmol), in THF (150 mL) in the presence of triethylamine (11.58 g, 114.4 mmol) over a period of 2 hours. After 2

hours, the reaction was stirred at room temperature for 24 hours. Triethylammonium bromide was formed as a white precipitate and filtered off. The solvent was removed under vacuum resulting in a yellow solid. The yellow solid was dissolved in dichloromethane (DCM) and extracted twice with an aqueous solution saturated with Na_2CO_3. The organic phase was dried over sodium sulfate anhydrous, and DCM was evaporated under vacuum. Column chromatography was performed in a 95:5 solution of DCM: methanol. The resulting solid was washed with ethyl ether and a white solid was obtained as the Boc-protected product. Subsequently, 5g of the Boc-protected initiator was dissolved in 40 mL of ethyl acetate in a 400-mL beaker equipped with a stir bar. To this solution, 33% HBr in acetic acid (6 mL) was added dropwise until it formed a white precipitate. The precipitate was collected, dissolved in ethanol and re-precipitated in ethyl ether yielding a white solid corresponding to the initiator in its ammonium form (yield= 90%).

General Procedure for Synthesis of Polystyrene Homopolymer using Mini ME ARGET Emulsion ATRP

In a three-neck 100-mL round-bottom flask equipped with a stir-bar, TBAB (1.934g, 6 mmol), initiator (1mM), $CuBr_2$ (2 mg, 8.96 μmol), and Tris(2-pyridylmethyl) amine (TPMA) (20.80 mg, 71.63 μmol) or Me_6TREN (4.78 μL, 0.018 mmol) or PMDETA (3.74 μL, 0.018 mmol) were added to a mixture of acetone (12 mL, 20% v/v) and water (33.2 mL). In a separate vial, a surfactant mixture of Pluronics F127 (0.80 g) in water (10 mL) was added to styrene (1.62 g, 15.54 mmol) (if EBIB was used as initiator, it was added directly to the monomer) and vortexed until it formed a milky white suspension. This solution was then added to the contents of the three-neck 100-mL

round-bottom flask forming a cloudy white suspension. The flask was then equipped with a reflux condenser sealed with a septum and an argon filled balloon attached to the condenser. The solution was purged with argon for 30 mins. Lastly, in a separate vial, a stock solution of ascorbic acid (18 mM, 5 mL) was prepared and purged with argon for 30 min before being fed to the reaction using a syringe pump at a rate of 1.67 μL/min (4.8 mL) at 80˚C. The polymerization was stopped by opening the reaction to air and polystyrene was precipitated with methanol. The polymer was centrifuged and dissolved in THF and re-precipitated in hexanes. The polymer was collected and washed with water before oven drying. Purified polymer was dissolved in THF at 1mg/mL for GPC analysis.

Results and Discussion

The ATRP ligand, Me_6TREN, was utilized for the mini ME emulsion polymerization of styrene at a Cu/ligand ratio of 1:2, unless otherwise indicated. Cu/ligand ratios and ascorbic acid feeding rates were varied in select experiments and discussed in below.

Effect of Initiator

N-(2-aminoethyl)-2-bromo-2-methylpropanamide (OBr) as ATRP Initiator

Formerly, with mini ME emulsion polymerization of PMMA, the hydrophilic OBr amine initiator was successfully used with excellent initiator efficiency.[6] For this study, OBr was originally employed along with Cu(II)/Me_6TREN at 80˚C while varying the Cu/ligand ratios and ascorbic acid feeding rates as illustrated in Fig. 1 (A and B). The plot in Fig. 1A shows an initial sharp decline in Đ from 1.82 (M_n=75,868 g/mol) using a 1:1 mole ratio of Cu(II)/Me_6TREN to a Đ of 1.53 (M_n=85,913g/mol) using a 1:2

Cu(II)/Me_6TREN ratio. This reduction was followed by an increase reaching a Đ of 1.64 (M_n=277, 886 g/mol) at 1:4 mole ratio of Cu(II)/Me_6TREN. Initiator efficiency dramatically decreased from ~ 71% at 1:1 Cu(II)/Me_6TREN to ~19 % at 1:4 Cu(II)/Me_6TREN, consistent with fast propagation due to a low concentration of deactivator species in solution.[13,14] When the ascorbic acid feeding rates were varied at a Cu(II)/Me_6TREN mole ratio of 1:2, no detectable trend in molecular weight was observed as seen in Fig. 1B. A sharp rise in molecular weight was detected when doubling the feed rate from 5 nmoles/min to 10 nmoles/min; however, the polymer's dispersity remained above 1.80. As ascorbic acid feeding rates continued to rise from 30 nmoles/min to 50 nmoles/min, a growth in dispersity was observed. Nevertheless, the experimental molecular weights ($M_{n,GPC}$) were substantially higher than theoretical molecular weights, which was calculated by using equation (1) where $[M]_\circ$ is the initial monomer concentration, $[I]_\circ$ is the initial initiator concentration, $MW_{monomer}$ is the monomer molecular weight, and $MW_{initiator}$ is the molecular weight of the initiator:

$$Mn, theoretical = ([M]_\circ \div [I]_\circ) \times MWmonomer \times Conversion + MWinitiator \quad (1)$$

There are several possible reasons why mini ME emulsion polymerization of styrene using the OBr initiator produced such uncontrolled polymerizations. First, the initiator itself could be reducing the oxidation state of the Cu(II)/Me_6TREN catalyst. Ethylene diamine is a known reducing agent having previously been employed to reduce Cu(II)/TPMA ATRP complexes in the past.[15]

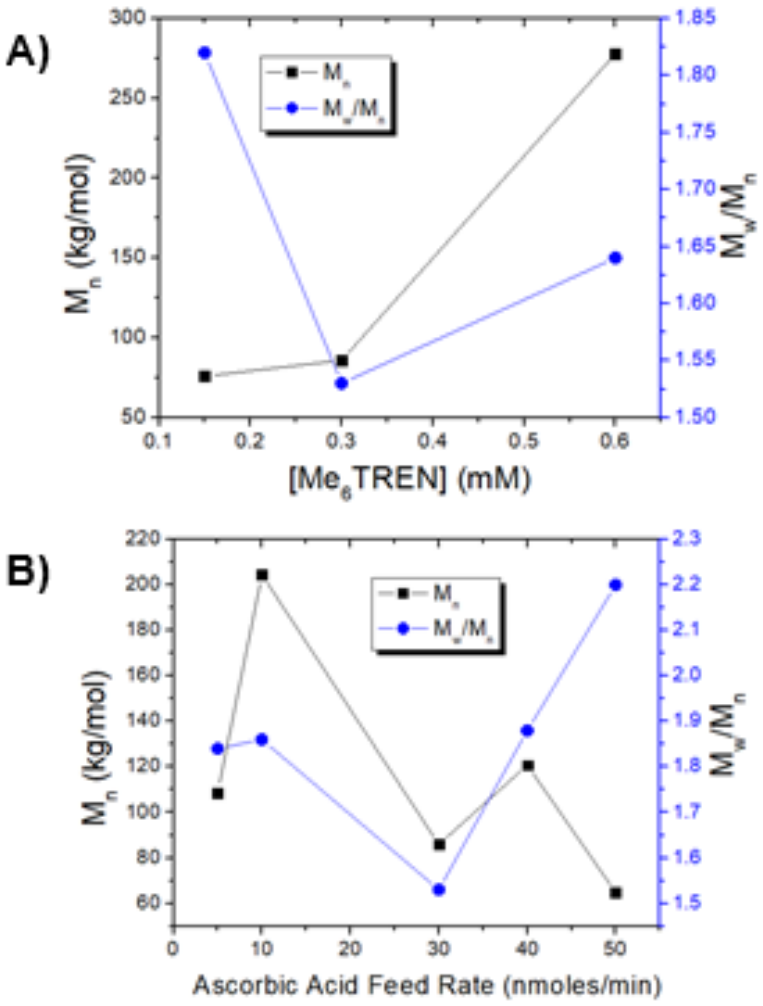

Figure 1. Using OBr initiator, (A) Effect of copper: Me_6TREN ratio (ascorbic acid feeding rate = 30 nmol/min) on M_n and dispersity. (B) Effect of ascorbic acid feeding rate on M_n and dispersity ($[Me_6TREN]$ = 0.30 mM). $[M]_\circ$ = 0.518 M, $[I]_\circ$ = 1 mM, $[CuBr_2]$ = 0.150 mM. All polymerizations were conducted at 80°C for 48 hrs.

Although OBr proved to be an efficient initiator for mini ME of PMMA, Me_6TREN is a more active ligand than TPMA. Consequently, the constant reduction of the transition metal ligand along with the high activity of Me_6TREN, led to higher molecular weight polymers with a broad MWD. Lastly, ethylenediamine is often used as a simple chelating agent, thus displacing the ATRP ligand as the ratio of initiator to ligand increases from ~1.7:1 for mini ME of PMMA to 3:1 for mini ME of polystyrene. This displacement causes an imbalance of radicals in the polymerization rendering OBr an ineffective initiator for mini ME emulsion polymerization of polystyrene. The commercially available HEBIB initiator subsequently replaced OBr as the water-soluble initiator.

2-Hydroxyethyl 2-bromoisobutyrate (HEBIB) as ATRP Initiator

Copper to ligand mole ratios were varied while utilizing the hydrophilic HEBIB ATRP initiator with initial monomer concentration of 518 mM in an effort to increase control of the polymerization. As illustrated in Fig. 2, an acute decrease in both the molecular weight and dispersity is seen as Me_6TREN concentrations are increased from 0.150 mM (1:1 Cu/L) (M_n= 116,479 g/mol, Đ = 2.04) to 0.30 mM (1:2 Cu/L) (M_n= 72,186, Đ = 1.76). Further increasing the ligand concentration from 0.30 mM to 0.60 mM (1:4 Cu/L), dramatically increased the dispersity to 2.22. All polymerizations at $[M]_\circ$=518 mM using Me_6TREN as the ligand and a hydrophilic initiator remained

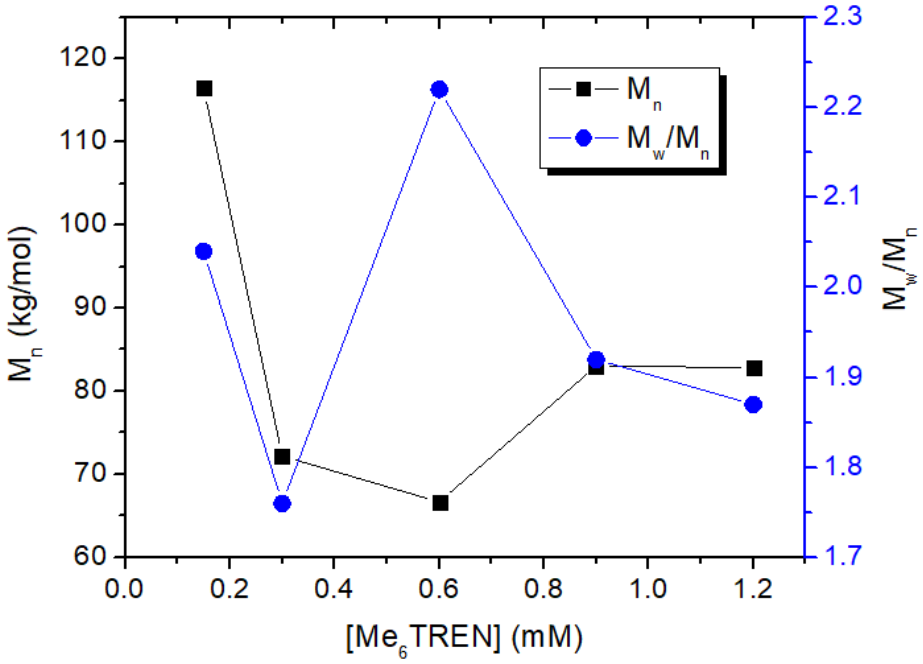

Figure 2. Using HEBIB initiator, (A) Effect of copper: Me_6TREN ratio (ascorbic acid feeding rate = 30 nmol/min) on M_n and dispersity. (B) Effect of ascorbic acid feeding rate on M_n and dispersity ([Me_6TREN] = 0.30 mM). $[M]_\circ$ = 0.518 M, $[I]_\circ$= 1 mM, [$CuBr_2$] = 0.150 mM. All polymerizations were conducted at 80°C for 48 hrs.

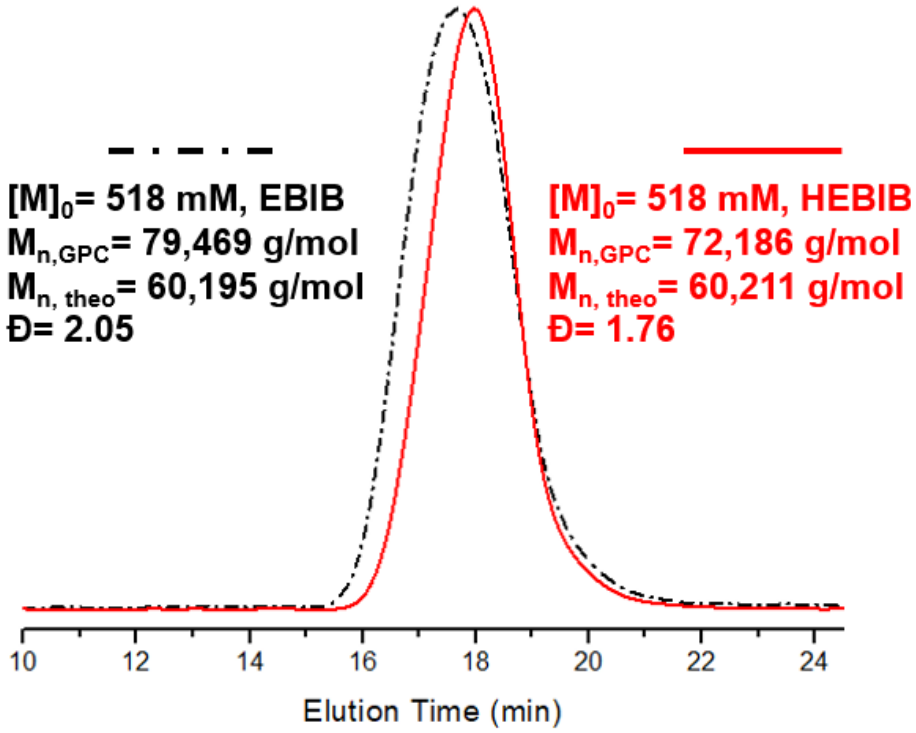

Figure 3. GPC curve of polystyrene from mini ME emulsion polymerization using EBIB and HEBIB as initiators. $[M]_{\circ}$= 518 mM, $[I]_{\circ}$= 1 mM, $[Me_6TREN]$ = 0.30 mM, $[CuBr_2]$ = 0.150 mM. Ascorbic acid feeding rate= 30 nmoles/min. All polymerizations were conducted at 80˚ C

poorly controlled. For comparison, the oil-soluble ethyl 2-bromoisobutyrate (EBIB), was used at a 1:2 Cu/L ratio and resulted in a polymer with a molecular weight of ~79,000 g/mol with Đ = 2.05 (Fig. 3).

Effect of Monomer Concentration

Styrene monomer is more hydrophobic than MMA monomer; therefore, polymer initiation and localization of the ATRP components will differ under the same surfactant and dispersion conditions used in the emulsion polymerization. This in part controls the initial size of the monomer droplets in solution and ultimately affects micelle formation and the nature of the reaction site.

In comparison, our prior studies of mini ME emulsion polymerization of PMMA a combination of micelles and monomer droplets were observed. The monomer droplets with a maximum size of ~ 2 μm looked sparse in population under the optical microscope.[6]. However, optical microscope images of the mini ME emulsion of PS under the conditions described above displayed many droplets with a large size distribution ranging from ~5 μm – 50 μm before the start of the polymerization (Fig. 4A). The disparate size of these monomer droplets leads to reaction inhomogeneity as the loci of the polymerization can occur in multiple environments ranging from micelles to the larger monomer droplets. The presence of multiple reaction environments may also lead to differences in local catalyst deactivator concentration which adds to broadening of MWD. To remedy this issue, the initial monomer concentration was reduced from 518 mM to 260 mM enabling smaller and more uniform micelle and droplet sizes much below ~ 2 μm (Fig. 4B). Polymerization was

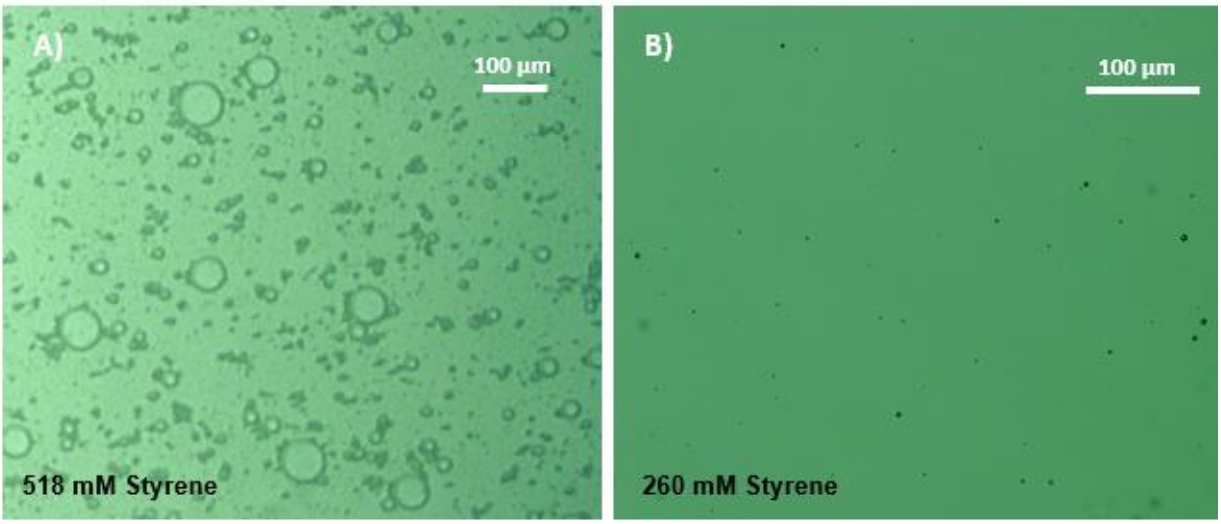

Figure 4. Optical microscope images of mini ME emulsion monomer droplets before the start of the polymerization at A) $[M]_{\circ}$= 518 mM (nominal magnification 50X) and B) $[M]_{\circ}$= 260 mM (nominal magnification 100X).

carried out with an initial monomer concentration at 260 mM using both EBIB and HEBIB initiators.

The reduction in initial monomer concentration significantly reduced the MWD, leading to a Đ of 1.35 for polymerizations using HEBIB and Đ of 1.30 with those using the water-insoluble EBIB initiator (Fig. 5). The EBIB initiator provided a lower dispersity indicating the importance of reaction locus. Nevertheless, the molecular weight for both polymerizations were ~ double the theoretical molecular weight. This was indicative of coupling between chains or the use of an over-active ligand, thus, TPMA and PDMETA ligands were analyzed for the optimization of mini ME emulsion of polystyrene.

Effect of Ligand

$CuBr_2$/ Me_6TREN complexes are ~10,000 times more active than the originally used $CuBr_2$/Bpy for conventional ATRP. Based on the relative K^0 values for activation of EBIB initiator by CuBr complexed with select ATRP ligands, the activity of the complexes decreases in the following order of ligand [16]

$K^0_{(relative)}$ Me_6TREN (39,000) > TPMA (2400) > TPEN (500) > PMDETA (20) > Bpy (1)

However, too large K^0 or K results in high radical concentration causing irreversible termination. Although Me_6TREN is exceptional as it not only makes a very active Cu based activator, but it is also an efficient deactivator and side reactions and cross-linking do occur as the deactivation step in the ATRP equilibrium can be too slow when Me_6TREN is used as the ligand.[16] TPMA offers control of ATRP

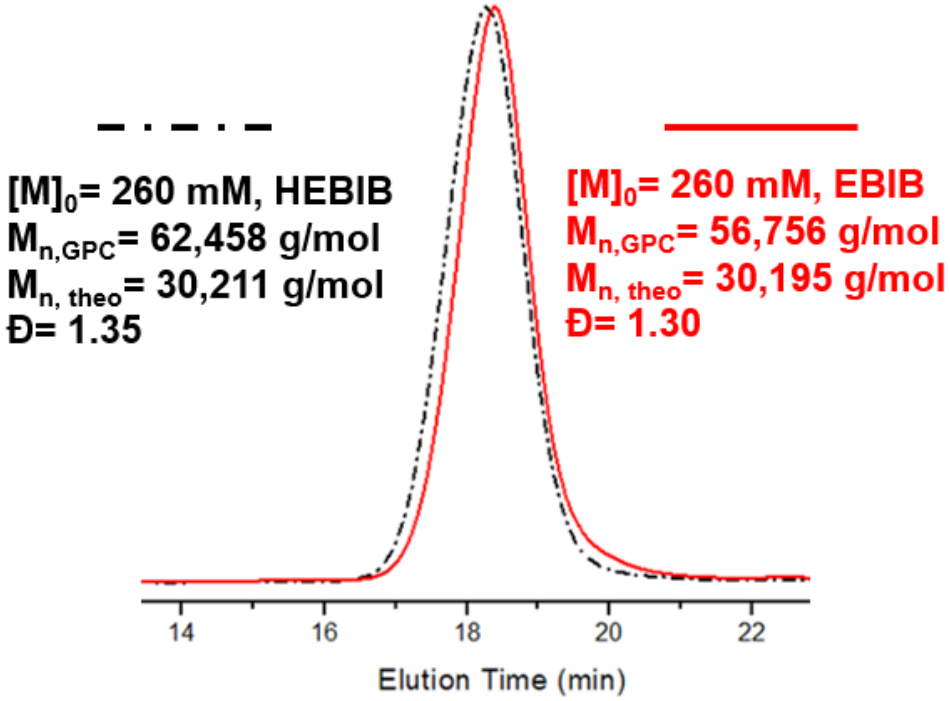

Figure 5. GPC curve of polystyrene from mini ME emulsion polymerization using EBIB and HEBIB as initiators. $[M]_{\circ}$= 260 mM, $[I]_{\circ}$= 1 mM, $[Me_6TREN]$ = 0.30 mM, $[CuBr_2]$ = 0.150 mM. Ascorbic acid feeding rate= 30 nmoles/min. All polymerizations were conducted at 80˚ C for 48 hrs.

polymerizations specifically at low catalyst concentrations as well as having a stronger binding constant to copper than Me_6TREN and PMDETA.[17]

Mini ME emulsion polymerization of polystyrene was performed using TPMA and, for comparison, the hydrophobic PMDETA ligand was also used as a control. Fig. 6 displays the GPC curves of each polymerization using EBIB as the initiator at a monomer concentration of 260 mM. Utilizing PMDETA ATRP ligand led to polymerizations with Đ > 1.90 and an experimental molecular weight over 3 times the theoretical molecular weight. This control result was consistent with our expectations as at high dilution and elevated temperatures, PMDETA displays a stability constant, β^I, below 10^8,[18] and consequently is not suitable for ARGET ATRP. Significant dissociation of the CuBr and $CuBr_2$/PMDETA complexes ultimately result in a lower absolute value of deactivator concentration (and poor control over the polymerization).[15,18]

Polymerizations using TPMA instead generated polymer with Đ < 1.40 and an experimental molecular weight ($M_{n,GPC}$= 28,501 g/mol, Đ = 1.35) close to the theoretical molecular weight (Fig. 6). Dynamic light scattering (DLS) measurements of the polymer particles with mini ME emulsion polymerization of PS using Me_6TREN, TPMA, and PMDETA are seen in Fig. 7. A bimodal particle distribution is observed in all three polymerizations with varying volumes of particle sizes. Within the larger size range (200 nm – 1.3 μm), PS particles made using Cu/Me_6TREN as ATRP catalyst displayed the largest volume fraction of larger particles, while the volume fraction of particles within the 200nm – 1.3 μm range was significantly decreased when Cu/TPMA was used as the ATRP catalyst. The volume fraction of

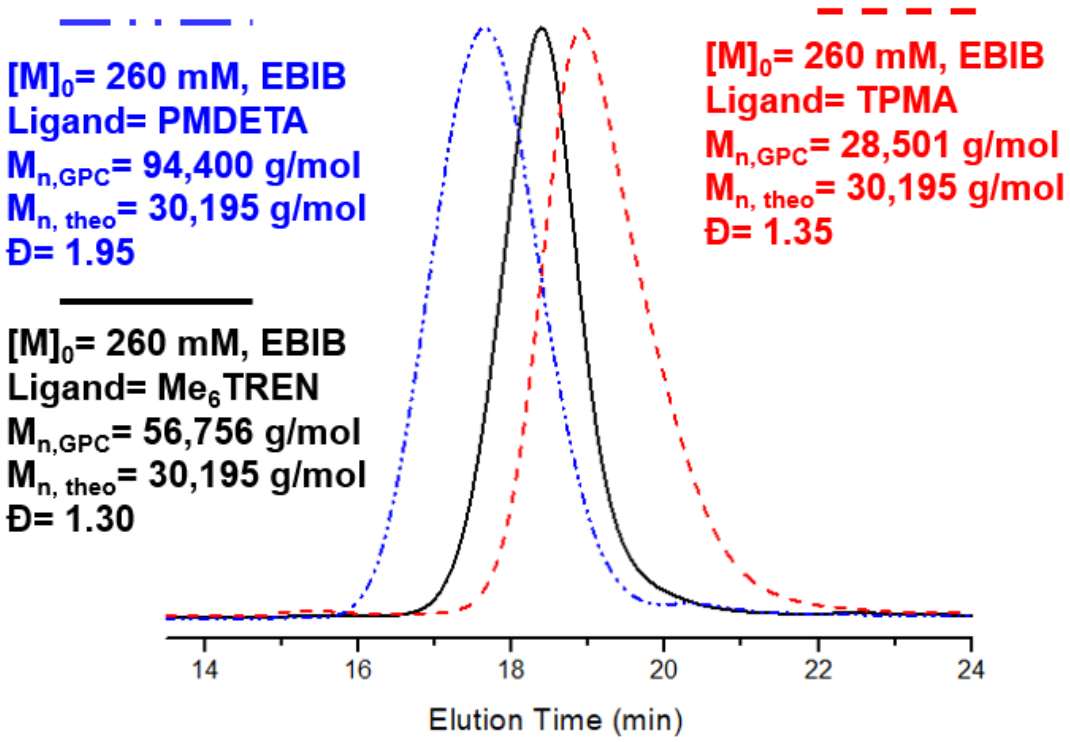

Figure 6. GPC curve of polystyrene from mini ME emulsion polymerization varying the ligand using EBIB as initiator. [Ligand]= 0.30 mM, $[M]_{\circ}$= 260 mM, $[I]_{\circ}$= 1 mM, $[CuBr_2]$ = 0.150 mM. Ascorbic acid feeding rate= 30 nmoles/min. All polymerizations were conducted at 80˚ C for 48 hrs.

particles within this larger size range was the lowest for PS particles made using Cu/PMDETA. However, when focusing on the smaller size range (20 nm-180 nm) (Inset: Fig. 7), PS particles made using PMDETA as ligand displayed the broadest overall size distribution, whereas resulting PS particles using TPMA as ligand showed the smallest size distribution offering PS particles of ~ 50 nm. The bimodal results observed from the DLS measurements coupled with the molecular weight and dispersity of these experiments can be best explained by compartmentalization effects.

Compartmentalization Effects

Compartmentalization is a term that refers to the physical confinement of reactants to a very small volume (usually in particles under 100 nm). This effect is primarily observed in heterophase polymerizations (e.g. miniemulsion polymerization) and depending on a number of factors, this confinement can alter the local polymerization rates compared to an uncompartmentalized system.[11] Compartmentalization comprises a *confined space effect,*[19] which acts to improve control over MWD, a *segregation effect,*[19] which results in increased livingness, a *fluctuation effect,*[11] whereby an uneven distribution of deactivator species between particles exists, and *a monomer concentration variation (MCV) effect,*[11] which refers to a reduction in R_p due to monomer concentrations varying between particles. [11,19]

The confined space effect primarily leads to lower R_p and narrower MWD in smaller particles whereby deactivation occurs more rapidly as the radicals are closer in space. When physical separation of the propagating radicals occurs as in the case of the

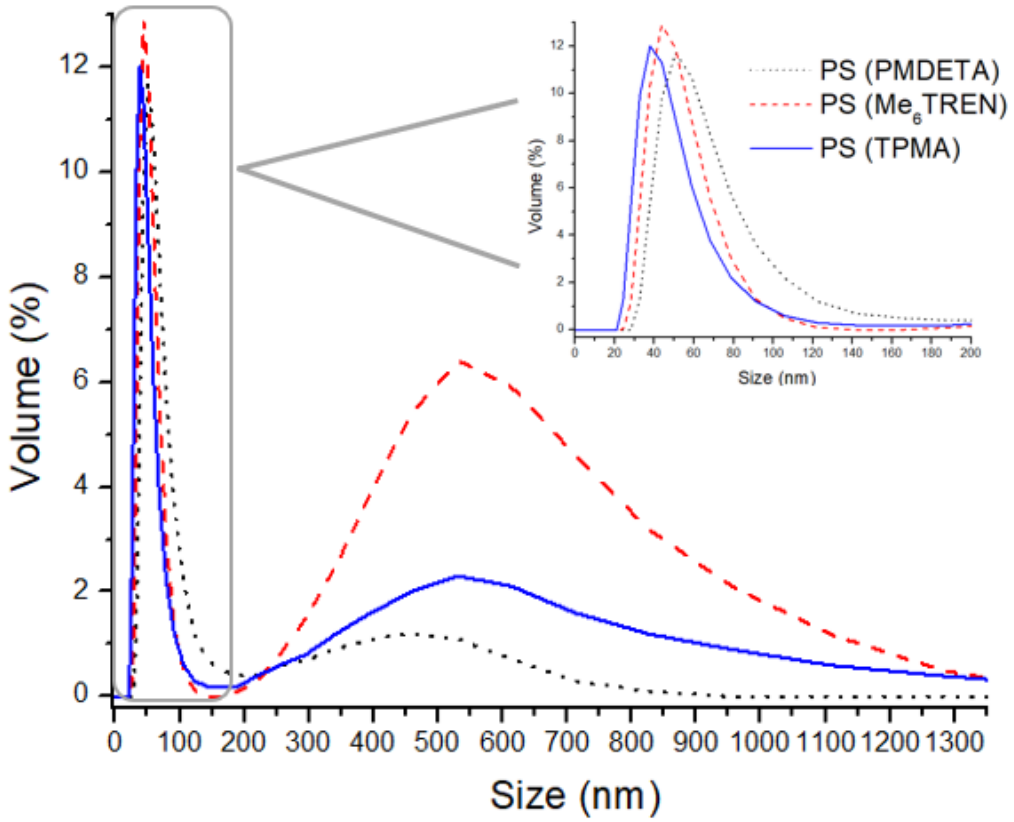

Figure 7. Dynamic light scattering measurements of polystyrene polymer particles manufactured using mini ME emulsion polymerization using PDMETA, Me_6TREN, or TPMA ATRP ligand. [Ligand]= 0.30 mM, $[M]_o$= 260 mM, $[I]_o$= 1 mM, [$CuBr_2$] = 0.150 mM. Ascorbic acid feeding rate= 30 nmoles/min. All polymerizations were conducted at 80˚ C for 48 hrs.

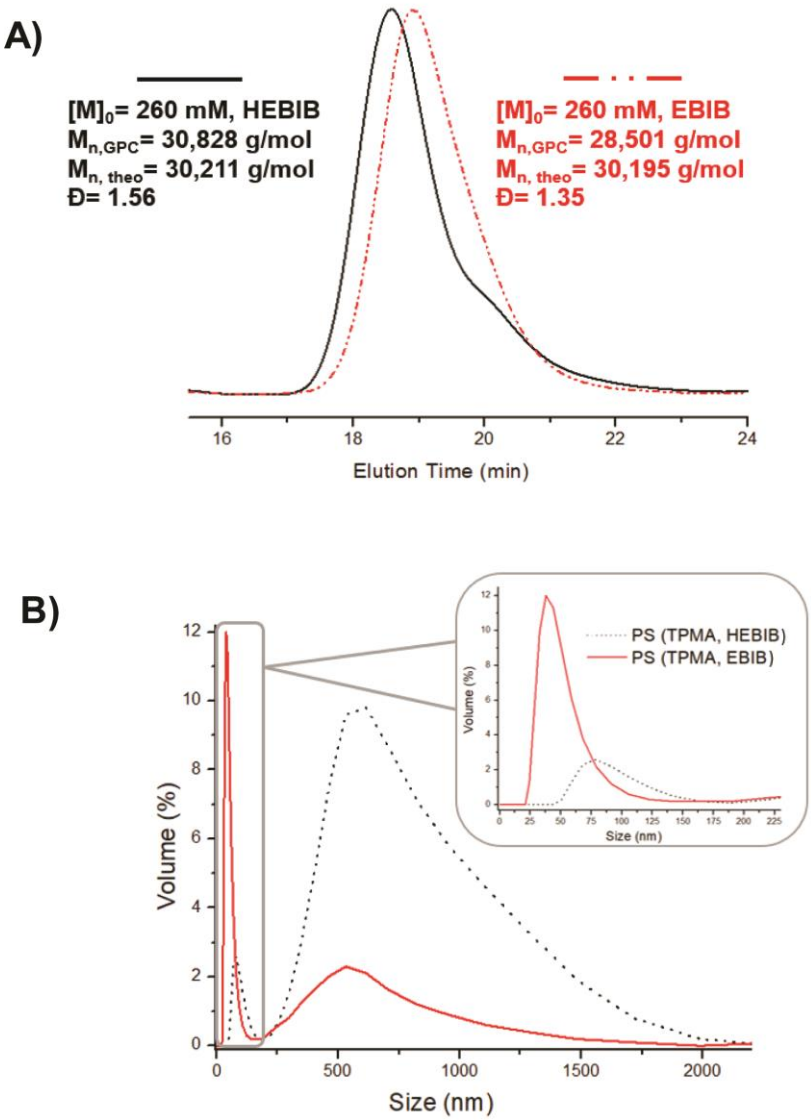

Figure 8. A) GPC curve of polystyrene from mini ME emulsion polymerization using either HEBIBB or EBIBB initiator. B) DLS measurements for particle sizes using HEBIBB or EBIBB as initiator. $[M]_\circ$= 260 mM, $[I]_\circ$= 1 mM, [TPMA]= 0.30 mM, $[CuBr_2]$ = 0.150 mM, ascorbic acid feeding rate = 30 nmoles/min. All polymerizations were conducted at 80˚C for 48 hrs.

segregation effect, their termination rate is significantly decreased leading to higher R_p, broader MWD, and an increase in livingness. The fluctuation effect leads to an increase in R_p, broadening of the MWD and a decrease in livingness as a result of having different concentrations of deactivator species per particle. Finally, the *MCV effect* occurs when some particles contain very little monomer. Theoretically, as a radical enters said particle, the radical is "wasted" due to a low level of accessible monomer, thus this effect is more pronounced at higher conversions. However,

experimentally, monomer transfer between droplets reduces this effect. What is also seen experimentally is the R_p decreasing as the diameter is reduced beyond a certain minimum diameter. The MCV effect becomes stronger than the segregation effect in this case, reducing bimolecular termination.[11,19,20]

In the recent literature, *M.E. Thomson and M. F. Cunningham* [1], theoretically investigated compartmentalization effects in ATRP in aqueous dispersed phase systems to understand the effects of particle size on the rate of polymerization and degree of control for the n-butyl methacrylate/CuBr/EHA_6TREN system. They concluded that for the highly active catalyst CuBr/EHA_6TREN, the rate of polymerization increases with increasing particle size to a maximum and levels out to the rate in an equivalent bulk system. For small particle sizes, both the rate of polymerization and the number of units added per activation decreased proportionally to the volume of the particles, attributed to the confined space effect. This effect is consistent with the results seen in Fig. 7 with the PS particles using CuBr/TPMA and CuBr/Me_6TREN catalysts. The higher volume of large particles associated with the CuBr/Me_6TREN system is consistent with the literature as the polymerization is faster resulting in higher molecular weight polymers.

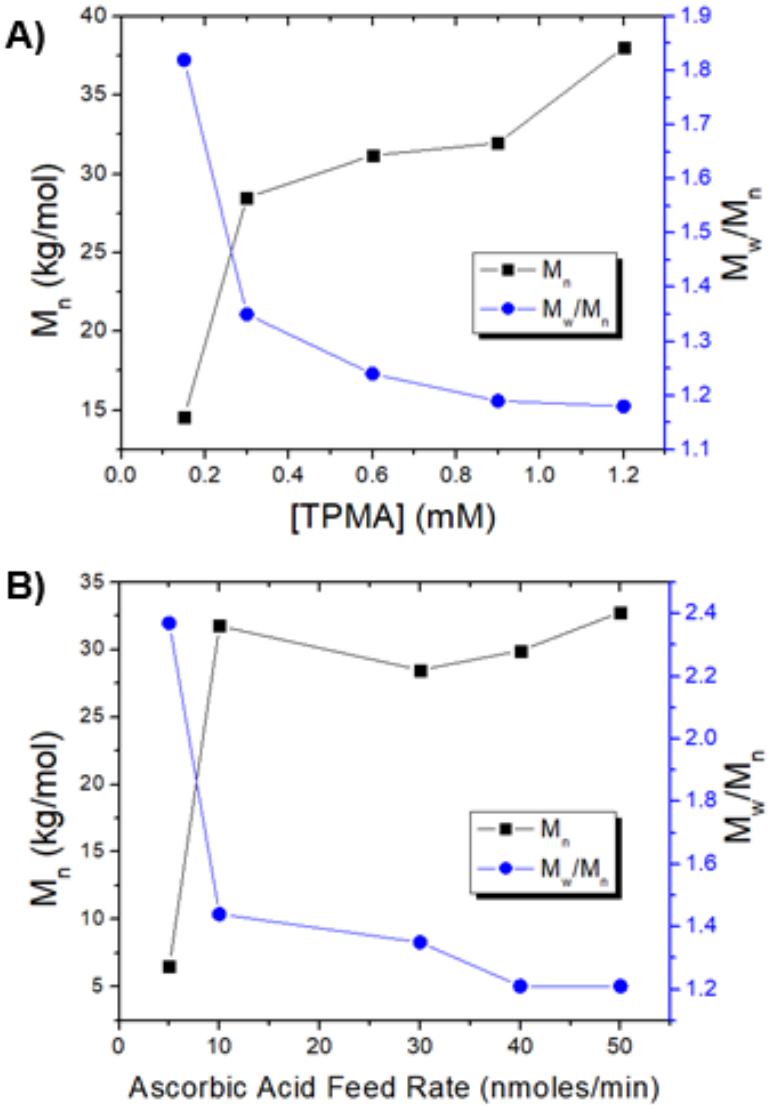

Figure 9. Using TPMA as ATRP ligand (A) Effect of copper: TPMA ratio (ascorbic acid feeding rate = 30 nmol/min) on M_n and dispersity. (B) Effect of ascorbic acid feeding rate on M_n and dispersity ([TPMA] = 0.30 mM). $[M]_\circ$ = 0.260 M, $[EBIBB]_\circ$ = 1 mM, $[CuBr_2]$ = 0.150 mM. All polymerizations were conducted at 80°C for 48 hrs.

The lower volume of large particles and lower size distribution within the smaller particle size range using CuBr/TPMA further agrees with a confined space effect, where lower molecular weight polymer was generated suggesting a slower rate of polymerization.

Utilizing TPMA Ligand

Use of the TPMA ATRP ligand generated polymers with the lowest dispersity and $M_{n,gpc}$ closest to the theoretical molecular weight of ~ 30,000 g/mol. At a Cu/TPMA ratio of 1:2, mini ME emulsion polymerization of PS using EBIB was compared to that of a polymerization using HEBIB. As shown in Fig. 8A, the hydrophilic initiator produced polymer with a high dispersity (Đ = 1.56), while the hydrophobic initiator yielded a polymer with lower dispersity.

The GPC curve illustrated in Fig. 8A also exhibits a shoulder on PS with HEBIB as initiator. This shoulder is symptomatic of lower molecular weight chains being produced as a result of the aqueous location of initiation. Since styrene monomer is far more hydrophobic than MMA, initiation is more efficient in the organic phase, thus, the EBIB is the more efficient initiator for mini ME emulsion polymerization of polystyrene. The polymerizations using HEBIB also produced much larger polymer particles (~ 800 nm) compared to the polymer particles generated using the EBIB initiator (Fig. 8B). Due to a shift in the location of initiation and reaction loci (fluctuation effect)[11], the concentration of deactivator species may vary between particles causing a broadening of the MWD.

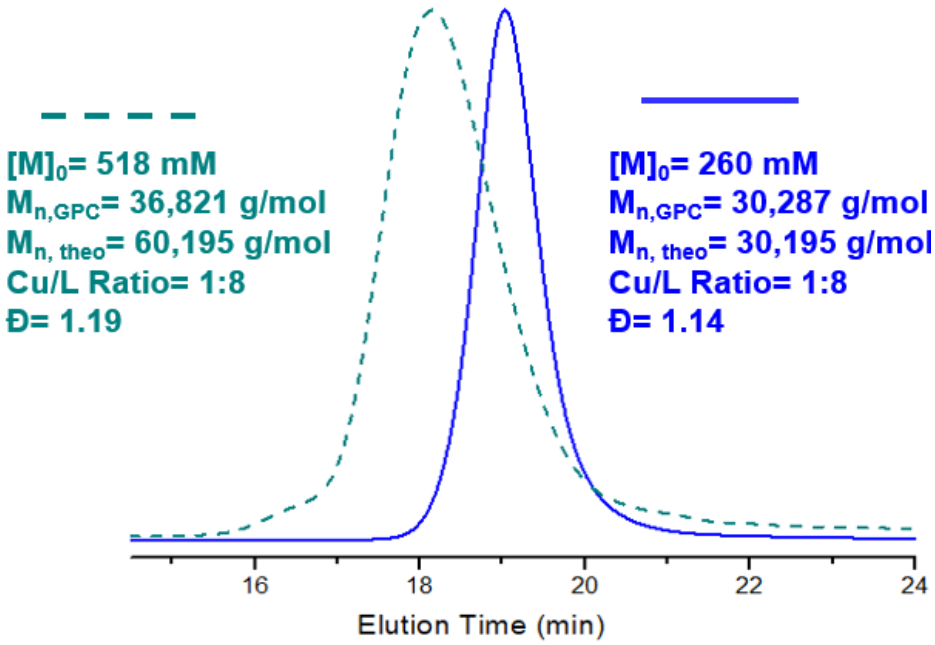

Figure 10. GPC curve of PS using mini ME emulsion polymerization when $[M]_{\circ}$= 518 mM or $[M]_{\circ}$= 260 mM. [EBIBB]= 1 mM, [$CuBr_2$] = 0.150 mM, [TPMA]= 1.2 mM, ascorbic acid feeding rate= 40 nmoles/min. All polymerizations were conducted at 80˚C for 48 hrs.

The copper to TPMA ratios were systematically varied for polystyrene polymerization. Fig. 9A displays a graph of molecular weight, M_n, and dispersity at increasing concentrations of TPMA. A clear trend is observed as TPMA is increased; M_n also increases, while the dispersity decreases. Higher Cu/TPMA ratios produce polymers with controlled polymerizations with Đ as low as 1.14. Ascorbic acid feed rates were also varied as a function of molecular weight and dispersity, producing similar effects (Fig. 9B). Higher ascorbic acid feed rates allow the polymerization to go to almost full conversion while the MWD decreases.

Ascorbic acid feed rate of 40 nmoles/min with a Cu/TPMA ratio of 1:8, and $[M]_\circ$= 260 mM were determined to be the optimal parameters for this particular polymerization. This polymerization yielded a Đ as low as 1.14 and a molecular weight close to theoretical (Fig. 10). For assessment, these optimum parameters were then employed at an initial monomer concentration of 518 mM and the results observed may be attributed to compartmentalization effects as described in References 1 and 11. When compartmentalization effects are dominant, both control (narrower MWD) and livingness are increased, but this is at the expense of a lower rate of polymerization. As $[M]_\circ$ increased to 518 mM, the theoretical molecular weight also

increased to ~ 60,000 g/mol. However, the $M_{n,GPC}$ for this polymerization shows a lower molecular weight with a conversion of 61% at 48 hours; nonetheless, the dispersity remained below 1.2. It is not possible to obtain a simultaneous increase in control/livingness and rate of polymerization as a result of compartmentalization.

Conclusions

In conclusion, mini ME emulsion polymerization of polystyrene was successfully implemented yielding a Đ as low as 1.14. Initiator, ligand, ascorbic acid feed rates, and Cu/Ligand ratio were essential for successful polymerization of PS. TPMA was the most efficient ATRP ligand at a Cu/Ligand ratio of 1:8 and ascorbic acid feed rate of 40 nmoles/min. TPMA has a $K^0_{(relative)}$ value of 2,400 versus Me_6TREN whose value is over 16 times that. Nonetheless, TPMA is still considered a very active ligand, and can withstand low catalyst loadings essential for ARGET ATRP. Employing the hydrophobic initiator, EBIB, with polymerizations using Cu/TPMA, improved the control of the system; while the hydrophilic initiator, HEBIB, led the polymerizations that formed PS with high Đ (> 1.50). This was attributed to efficient initiation only occurring within the organic phase due to the hydrophobicity of the styrene monomer partitioning within the micelle and/or monomer droplets. Me_6TREN ATRP ligand was an unsuccessful deactivator in this heterogenous system offering polymer molecular weights over two times $M_{n,theo}$, while the PMDETA control provided little catalyst stability rendering it inefficient.

Compartmentalization effects were prominent as the ATRP ligand was varied from most active Me_6TREN ligand to the more stable TPMA ligand offering slower and more controlled polymerizations. The PS dispersed phase using the catalyst Cu/Me_6TREN was located in the large micelle/droplet regime and formed a broad size distribution (200 nm –1.3 μm). The polymer dispersed phase generated using the Cu/TPMA catalyst possessed a narrower size distribution with species of ~ 50 nm, while a PS dispersed phase produced using the Cu/PMDETA catalyst had the largest size distribution with

the most uncontrolled polymerization (M_n= 94,400 g/mol, Đ = 1.95). Effects due to compartmentalization were also seen when the $[M]_\circ$ was increased from 260 mM to 518 mM using $CuBr_2$/TPMA as the catalyst in a ratio of 1:8, with an ascorbic acid feed rate of 40 nmoles/min. Although increasing the initial monomer concentration still offered a controlled polymerization (Đ < 1.2), the rate of polymerization was significantly decreased with a polymer conversion of 61% at 48 hours. This is typical of compartmentalization as increasing the control/livingness, and degree of polymerization, often comes at the expense of rate of polymerization.

ACKNOWLEDGEMENTS

The authors would like to thank the Air Force Office of Scientific Research (AFOSR FA9550-17-1-0038), and for prior support the Air Force Research Laboratory (AFRL). This work made use of the Cornell Center for Materials Research Shared Facilities which are supported through the NSF MRSEC program (DMR-1719875). Experiments were conducted at both Cornell University and at AFRL under Dr. Richard Vaia's supervision whom helped with the concept of mini ME emulsion polymerization. I would like to acknowledge Zoe Lequeux, an undergraduate in the Ober group, as a contributing member of this work. She ran some of the mini ME emulsion polymerizations varying copper and ligand types for this study.

REFERENCES

(1) Cunningham, M. F. Controlled/Living Radical Polymerization in Aqueous Dispersed Systems. *Prog. Polym. Sci.* **2008**, *33* (4), 365–398.

(2) Ding, X.; Zhao, J.; Liu, Y.; Zhang, H.; Wang, Z. Silica Nanoparticles Encapsulated by Polystyrene via Surface Grafting and in Situ Emulsion Polymerization. *Mater. Lett.* **2004**, *58* (25), 3126–3130.

(3) Tumnantong, D.; Rempel, G. L.; Prasassarakich, P. Synthesis of Polystyrene-Silica Nanoparticles via RAFT Emulsifier-Free Emulsion Polymerization. *Eur. Polym. J.* **2016**, *80*, 145–157.

(4) Kwak, Y.; Magenau, A. J. D.; Matyjaszewski, K. ARGET ATRP of Methyl Acrylate with Inexpensive Ligands and Ppm Concentrations of Catalyst. *Macromolecules* **2011**, *44* (4), 811–819.

(5) Tian, B. Y.; Hu, P. J.; Yuan, M.; Tang, E. J.; Liu, S. J.; Zhao, X. Y.; Zhao, D. S. Effect of Different Ligands on the Controlled Polymerization of Monodisperse Polystyrene Nanospheres by Atom Transfer Radical Polymerization in an Aqueous Emulsion. *Express Polym. Lett.* **2012**, *6* (10), 837–846.

(6) Cordero, R.; Jawaid, A.; Hsiao, M.-S.; Lequeux, Z.; Vaia, R. A.; Ober, C. K. Mini Monomer Encapsulated Emulsion Polymerization of PMMA Using Aqueous ARGET ATRP. *ACS Macro Lett.* **2018**, *7* (4), 459–463.

(7) Lorandi, F.; Wang, Y.; Fantin, M.; Matyjaszewski, K. Ab Initio Emulsion Atom-Transfer Radical Polymerization. *Angew. Chem.* **2018**, *130* (27), 8402–8406.

(8) Fantin, M.; Chmielarz, P.; Wang, Y.; Lorandi, F.; Isse, A. A.; Gennaro, A.; Matyjaszewski, K. Harnessing the Interaction between Surfactant and Hydrophilic

Catalyst to Control *e* ATRP in Miniemulsion. *Macromolecules* **2017**, *50* (9), 3726–3732.

(9) Wang, Y.; Lorandi, F.; Fantin, M.; Chmielarz, P.; Isse, A. A.; Gennaro, A.; Matyjaszewski, K. Miniemulsion ARGET ATRP via Interfacial and Ion-Pair Catalysis: From Ppm to Ppb of Residual Copper. *Macromolecules* **2017**, *50* (21), 8417–8425.

(10) Rusen, E.; Mocanu, A. Atom Transfer Radical Emulsion Polymerization (Emulsion ATRP) of Styrene with Water-Soluble Initiator. *Colloid Polym. Sci.* **2013**, *291* (9), 2253–2257.

(11) Zetterlund, P. B.; Thickett, S. C.; Perrier, S.; Bourgeat-Lami, E.; Lansalot, M. Controlled/Living Radical Polymerization in Dispersed Systems: An Update. *Chem. Rev.* **2015**, *115* (18), 9745–9800.

(12) Zetterlund, P. B.; Kagawa, Y.; Okubo, M. Compartmentalization in Atom Transfer Radical Polymerization of Styrene in Dispersed Systems: Effects of Target Molecular Weight and Halide End Group †. *Macromolecules* **2009**, *42* (7), 2488–2496.

(13) Fischer, H. The Persistent Radical Effect: A Principle for Selective Radical Reactions and Living Radical Polymerizations. *Chem. Rev.* **2001**, *101* (12), 3581–3610.

(14) Ayres, N. Atom Transfer Radical Polymerization: A Robust and Versatile Route for Polymer Synthesis. *Polym. Rev.* **2011**, *51* (2), 138–162.

(15) Matyjaszewski, K.; Jakubowski, W.; Min, K.; Tang, W.; Huang, J.; Braunecker, W. A.; Tsarevsky, N. V. Diminishing Catalyst Concentration in Atom Transfer Radical Polymerization with Reducing Agents. *Proc. Natl. Acad. Sci.* **2006**, *103* (42), 15309–15314.

(16) Broja M. Mandal. *Fundamentals of Polymerization*; World Scientific: India,

2013.

(17) Bai, L.; Zhang, L.; Cheng, Z.; Zhu, X. Activators Generated by Electron Transfer for Atom Transfer Radical Polymerization: Recent Advances in Catalyst and Polymer Chemistry. *Polym. Chem.* **2012**, *3* (10), 2685.

(18) Woodruff, S. R.; Davis, B. J.; Tsarevsky, N. V. Selecting the Optimal Reaction Conditions for Copper-Mediated Atom Transfer Radical Polymerization at Low Catalyst Concentration. In *Progress in Controlled Radical Polymerization: Mechanisms and Techniques*; Matyjaszewski, K., Sumerlin, B. S., Tsarevsky, N. V., Eds.; American Chemical Society: Washington, DC, 2012; Vol. 1100, pp 99–113.

(19) Zetterlund, P. B. Controlled/Living Radical Polymerization in Nanoreactors: Compartmentalization Effects. *Polym Chem* **2011**, *2* (3), 534–549.

(20) Zetterlund, P. B.; Okubo, M. Compartmentalization in Nitroxide-Mediated Radical Polymerization in Dispersed Systems. *Macromolecules* **2006**, *39* (26), 8959–8967.

CHAPTER 4

MINI MONOMER ENCAPSULATED EMULSION POLYMERIZATION FOR THE SYNTHESIS OF HAIRY NANOPARTICLES

Abstract

Hairy nanoparticles with an SiO_2 core and PMMA brushes (SiO_2-PMMA) were synthesized utilizing mini monomer encapsulated emulsion polymerization (mini ME emulsion) with ARGET ATRP. Ludox-TM 40 particles (27 nm) were initially modified with a hydrophobic ATRP initiator in ethanol, then dispersed in methyl methacrylate monomer before carrying out the new emulsion polymerization technique. Mini ME emulsion polymerization allows ATRP catalyst and ligand to be delivered to the micelle employing the phase transfer agent, TBAB. Lower concentrations (5.56×10^{-4} M) of the surfactant, Pluronic F127, were found to facilitate the polymerization on the nanoparticle surface offering a larger polymer canopy while the samples were devoid of excess surfactant. The effect of initial monomer concentrations was also examined showing a uniform polymer shell of ~ 5 nm and ~ 10 nm when $[M]_\circ$ was 0.670 M and 1.340 M, respectively.

Introduction

Surface modification of nanoparticles with polymeric chains has been prevalent in engineering hybrid materials to enable new technologies with well-controlled microstructures. Polymer-grafted nanoparticles (PGNs) or "hairy" nanoparticles (HNPs) have been the focus of research over recent years due to their ability to produce a wide range of advanced materials.[1] HNPs possess unique properties due to their

versatility and capacity to entangle with the brushes on neighboring polymer grafted nanoparticles, giving them enhanced thermal, mechanical and electrical properties compared to their micro and macroscale counterparts.[2] Their unique combination of polymer processability and the potential to scale-up novel organic-inorganic hybrid material is of interest to the successful development of new hybrid materials for numerous applications such as gradient index optical material (GRIN) for midwave-IR photonics, faraday rotators, as well as "nano-inks" for flexible hybrid electronics packaging. Owing to the improvement of synthetic techniques within the past decade, it has become possible to methodically address topics such as NP-based organic-inorganic materials for not only opto-electronics, but for biological applications as well.[3]

Nevertheless, several challenges persist with the assembly of HNPs limiting the ability to produce them at a large-scale (grams). These challenges involve the control of initiator density, control of brush molecular weight and dispersity of longer chains, as well as aggregation of functionalized particles and purification. Several synthetic strategies exist to produce these polymer-inorganic hybrids. Matyjaszewski *et al.* synthesized poly(methyl methacrylate) (PMMA) and polystyrene (PS) grafted SiO_2 nanoparticles using atom transfer radical polymerization (ATRP) with Nissan nanoparticles dispersed in methyl isobutyl ketone (MIBK).[4] Chevigny *et al.* synthesized PS-SiO_2 particles using the commercially available Ludox TM-40 and through a solvent-transfer technique, successfully dispersed the particles in N'N'-dimethylacetamide (DMAc) and later functionalized the particles with an ATRP initiator.[5] Ludox-TM particles are supplied dispersed in an aqueous solution as

hydrophilic bare SiO_2 nanoparticles and are not stable in organic solvents unless they are dispersed in high boiling point/high dielectric solvents such as MIBK or DMAc. Several other groups have synthesized SiO_2 particles using the Stöber method, attaching an ATRP initiator to the surface and then dispersing them into an organic solvent such as anisole or toluene before polymerizing PMMA or PS on the surface.[6] However, large-scale production of these nano-hybrids in such conditions is difficult and comes with a potential negative environmental impact.

Water-based polymerization methods offer many advantages for the direct, one pot synthesis of HNPs, particularly for large-scale production, since water is readily available and eco-friendly. A successful water-based method for HNP synthesis could transform the availability of HNPs and enable implementation of many future applications. To date no straightforward, aqueous HNP synthesis, using a metal oxide core, has been carried out.

Previously, this group has discovered and successfully carried out a new emulsion polymerization technique, mini monomer encapsulated emulsion polymerization (mini ME emulsions) using ARGET-ATRP.[7] Low dispersity PMMA was formed ($Đ < 1.2$) in the presence of a phase-transfer agent, tetrabutyl ammonium bromide, and acetone. Herein, we report the application of mini ME emulsion polymerization to generate a PMMA canopy on the surface of silica nanoparticles to produce SiO_2-PMMA HNPs. First, the commercially available Ludox-TM 40 SiO_2 particles are conditioned with ion-exchange resin, transferred to ethanol, then functionalized with a hydrophobic ATRP initiator. Second, the particles are purified and dispersed in MMA monomer before

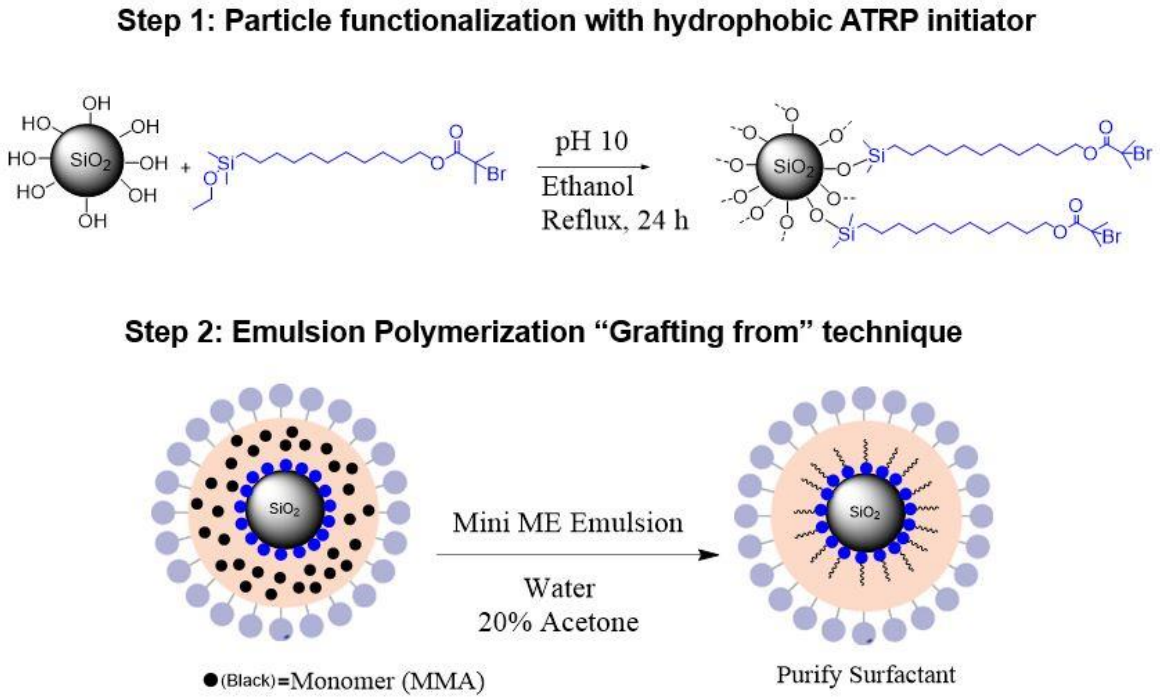

Figure 1. Two-step synthetic procedure for SiO_2-PMMA HNPs where in Step 1) the particle surface is initially functionalized with the hydrophobic initiator EDMP in ethanol at basic pH and refluxed for 24 hours. After initial particle functionalization and removal of excess initiator, Step 2) requires the particles to be dispersed in MMA monomer and pre-emulsified using Pluronic F-127 surfactant before carrying out mini ME emulsion in 20% acetone in water.

carrying out mini ME emulsion polymerization using ARGET-ATRP. Finally, the HNPs are purified and washed before their final dispersion in a good solvent for characterization and analysis. This method generated HNPs with uniform polymer canopies that can be fine-tuned by varying initial monomer and surfactant concentrations.

Experimental Section

Materials:

MMA, stabilized, 99%, aluminum oxide (basic), L (+)-ascorbic acid, tetrabutylammonium bromide (99%), and copper (II) bromide (99%, extra pure, anhydrous) were all purchased from Acros Organics and used as received. Tris (2-pyridyl methyl) amine (TPMA, >98%), was purchased from TCI, while triethylamine, 2-bromoisobutyryl bromide (BIBB), Pluronic®F-127, 28% NH_3 in water, and Karstedt catalyst were purchased from Sigma-Aldrich and used as received. Ludox-TM 40 was also purchased from Sigma-Aldrich and treated with an ion exchange procedure. Dowex 1X8-200 mesh and Dowex 50W X8 100-200 mesh ion-exchange resin, ammonium hydroxide and Snakeskin dialysis tubing, 10k MW cut-off, 35 mm, were all purchased through Fisher Scientific. Dimethylethoxysilane was purchased through GELEST and used as received.

Instrumentation:

Polymer molecular weights and dispersities were obtained using a Waters ambient temperature GPC in THF (polystyrene standards). The GPC is equipped with triple-detection capability: A Waters 410 differential refractive index detector; a Waters 486

UV-Vis detector; and a Wyatt Technologies TREOS three-angle light-scattering detector, useful for absolute molecular weight determination. The GPC columns are 3 PSS SDV (Polymer Standards Service); 8 mm x 300 mm with porosities of 1,000 angstroms; 10,000 angstroms, and Linear M. Powder x-ray diffraction (XRD) characterization was carried out on Bruker-AXS D8 Discover Diffractometer using Cu Kα radiation at λ = 1.54 Å by depositing powder on glass substrate. Fourier transform-infrared (FT-IR) (Vertex V80V vacuum FT-IR; Bruker, Billerica, MA, USA) spectroscopy was used to confirm production of PMMA-SiO_2 HNPs using mini ME emulsion technique. Samples for FT-IR analysis were ground into fine powder using a mortar and pestle. Sample morphologies were observed using a field-emission scanning electron microscope (Zeiss Ultra SEM; Zeiss) at an accelerating voltage of 3 kV. Thermogravimetric analysis (TGA) was performed on a TGA Q500 instrument (TA Instruments Inc.) at a heating rate of 10°C /min to 700°C under a nitrogen atmosphere with a sample size of 8–10 mg. Transmission electron microscope (TEM) images were collected on a corrected FEI Talos TEM with an accelerating voltage of 200 kV.

Synthesis of 11-(ethoxydimethylsilyl) undecyl 2-bromo-2-methylpropanoate (EDMP) ATRP Initiator

Step 1: Bromination

In a 100 mL round-bottom flask equipped with a stir bar, 10-undecen-1-ol (4.257 g, 5mL, 0.025 mol) and pyridine (2.1 mL, 0.026 mol) were dissolved in 30 mL of anhydrous tetrahydrofuran (THF). Then, at 0˚C, 2-bromoisobutyryl bromide (BIBB) (5.760 g, 3.1 mL, 0.024 mol) in 10 mL of THF was added dropwise to the solution in the round-bottom flask over a period of 2 hours with stirring. After 2 hours, the solution

was warmed to room temperature and stirred for 24 hours. Triethylammonium bromide salt was formed as a white precipitate and filtered out. The solvent was removed under vacuum resulting in a yellow oil. The yellow oil was dissolved in dichloromethane (DCM) and extracted twice with an aqueous solution saturated with Na_2CO_3. The organic phase was dried over sodium sulfate anhydrous, and DCM was evaporated under vacuum. Column chromatography was performed in a 100% dichloromethane resulting in a pale-yellow oil (yield = 95%).

Step 2: Hydrosilylation

Dimethylethoxysilane (0.04 mol) and Karstedt catalyst (6 μL) were added to the product from step 1 (0.004 mol), and the mixture was stirred for over-night at room temperature in a nitrogen environment. Excess dimethylethoxysilane was then removed under vacuum and the residual liquid was then stored at -20˚ C until needed.

Addition of EDMP ATRP Initiator to Ludox-TM 40 particles

Conditioning of Dowex Resin

Dowex 50W X8 and Dowex 1X8 resin (50 g each) were each transferred to a 600 mL beaker (separate beakers). Each resin was washed with 3N NaOH, hot water, methanol, and cold water. After each individual wash, the resins were recollected via filtration, added back into the beaker and washed again with the subsequent solvent. This cycle was repeated 5 times with each resin. After the last wash cycle of Dowex 50W X8, the resin was converted to the hydrogen form with a final wash using excess 3N HCl. Likewise, Dowex 1X8 was converted to the hydroxy form with 3N NaOH. This must be converted shortly before use. Resins were then rinsed with copious amounts of doubly distilled water and mixed under stirring. The resins were recollected via

filtration.

Ion-exchange of Ludox-TM 40

Ludox-TM 40 (100 mL) was diluted with 100 mL of Millipore water, stirred and added to Dowex 50W X8 resin in a beaker under agitation over-night. Ludox-TM 40 particles were then collected via filtration and then added to Dowex 1X8 resin in a beaker and subsequently stirred over-night. The particles were then collected via filtration (large aggregates were centrifuged down at 3000 rpm), then dialyzed against ethanol for 1 week.

Addition of EDMP to Ludox-TM 40 in Ethanol

Ludox particles dispersed in ethanol (1 g, 50 mL) was added to a 200 mL round-bottom flask. Then, 28% NH_3 in water was slowly added to the ethanol dispersion until the pH was 10. The ATRP initiator, EDMP (0.860 g, 0.002 mol) was then slowly added to the suspension and sonicated for 1 hour before refluxing the solution at 85˚C for a period of 24 hours. After 24 hours, the solution was cooled to room temperature and centrifuged at 4000 rpm to separate out any aggregates. The solution was then dialyzed against ethanol for 1 week.

Synthesis of PMMA-SiO_2 Hairy Nanoparticles using ARGET-ATRP Mini ME Emulsion Polymerization

EDMP-SiO_2 particles in ethanol (200 mg) were added to MMA monomer (4.3 mL, 0.040 mol) in a 20 mL scintillation vial and mixed. The ethanol was then evaporated leaving the particles dispersed in the MMA monomer. A surfactant mixture of Pluronics F-127 (0.40 g) in water (10 mL) was then added to the MMA-particle suspension and vortexed until it formed a milky white solution. In a 100-mL round-bottom flask, TBAB

(1.934g, 6 mmol), $CuBr_2$ (1 mg, 4.48 μmol), and Tris(2-pyridylmethyl) amine (TPMA) (10.45 mg, 36 μmol) were added to a mixture of acetone (12 mL, 20% v/v) and water (34.4 mL). The pre-emulsified solution of MMA with particles and surfactant was then added to the contents of the 100-mL round-bottom flask forming a cloudy white solution and purged with argon for 30 mins. Lastly, in a separate vial, a stock solution of ascorbic acid (2.27 mM, 5 mL) was prepared and purged with argon for 30 min before being fed to the reaction using a syringe pump at a rate of 10 μL/min (3.6 mL). The polymerization was stopped by opening the reaction to air. The hairy nanoparticles were separated from free polymer by centrifugation (4400 rpm for 20 mins). The particles were then dispersed in THF and precipitated in hexanes before being washed with water to get rid of any residual surfactant. They were then oven dried at 80˚C for several hours before being re-dispersed in THF.

Results and Discussion

Ludox-TM 40 SiO_2 particles (25 nm) are commercial aqueous dispersions of negatively charged silica particles. Ludox was chosen as the inorganic core due to its relative monodispersity in solution and extensive literature on surface functionalization and treatment of these particles. According to suppliers (DuPont), the counter-ion is Na^+ while the co-ion is OH^-. The particles must be pretreated to remove Na^+ ions and any other additives that may be adsorbed onto the surface of the particles hindering efficient modification. It was previously observed that ethanol addition to Ludox TM particles flocculates the suspension because of the presence of soluble silica.[8] Consequently, the particles were conditioned via an ion-exchange technique using Dowex resin (detailed

in experimental section), and later dispersed in ethanol. The particles were then modified with the EDMP hydrophobic ATRP initiator in an ethanol dispersion that was basified to a pH 10 using and aqueous solution of 28% NH_3 and refluxed for 24 hours (Fig. 1A). The particles decorated with EDMP ATRP initiator were then transferred to MMA monomer ($[M]_\circ = 0.670$ M) before performing mini ME emulsion polymerization to obtain SiO_2-PMMA HNPs.

Effect of Surfactant Concentration

The concentration of Pluronic F-127 surfactant was varied in initial experiments to gauge its effect on polymer canopy growth. The TGA graph is illustrated in Fig. 2, showing that as surfactant concentrations increase from 5.56×10^{-4} M (sample A) to 1.59×10^{-3} M (sample B), there is an increase in % weight change from 50% to 22%, respectively. PMMA undergoes a two-step degradation process evidenced by the TGA curves in Fig.2. The first stage, which can be divided up into two steps, represents decomposition of weak head-to-head linkages and impurities for the range between 160-240˚C (and decomposition of PMMA chain ends at ~ 290˚C). The second stage, between 300-400˚C, represents random scission of the polymer chains.[9] Free polymer generated from each polymerization was measured using GPC, sample A resulted in an M_n of 51,275 g/mol (Đ = 1.37), while sample B was measured to have an M_n of 24,828 (Đ = 1.38) (Inset: Fig. 2). These molecular weights are inconsistent with the TGA curves as sample B displays a higher polymer content,

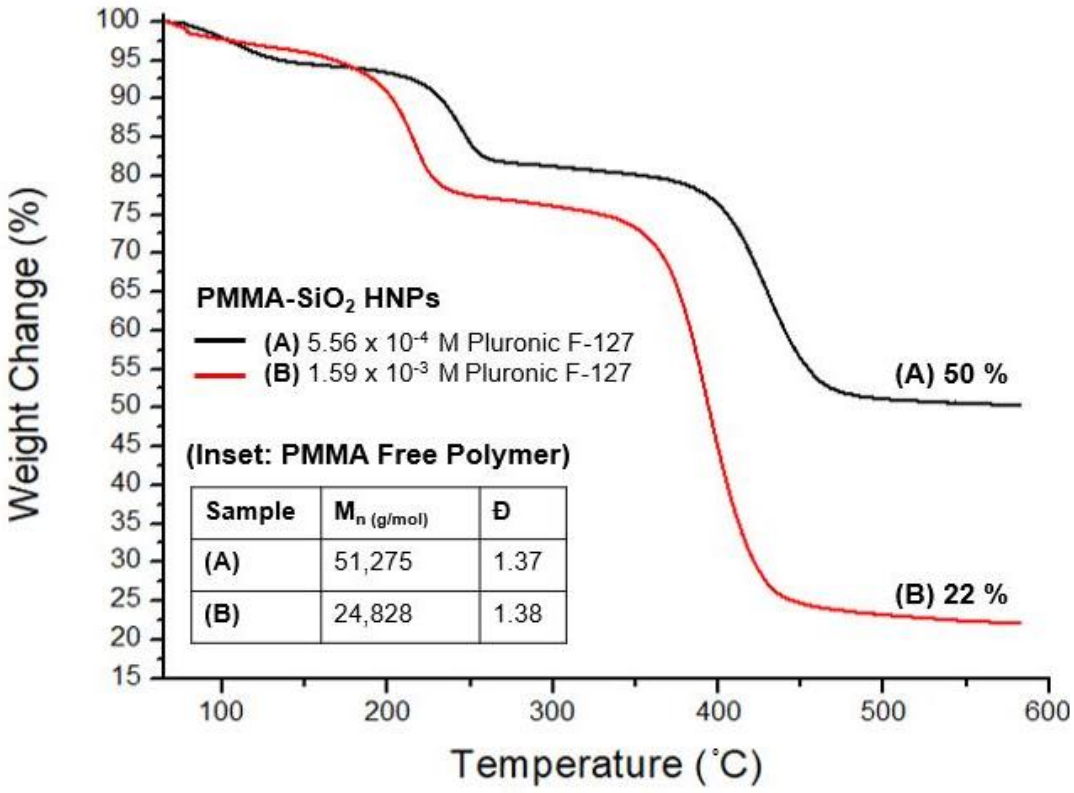

Figure 2. TGA of SiO_2-PMMA hairy nanoparticles synthesized via mini ME emulsion polymerization. Pluronic F127 surfactant concentrations were varied from 1.59 x 10^{-3}M for sample B to 5.56 x 10^{-4} M for sample A, displaying a 22% and 50% weight change, respectively. Free polymer (Inset) formed in the aqueous phase was measured to have molecular weights of 51,275 g/mol (Đ = 1.37) and 24, 828 g/mol (Đ = 1.37) for samples A and B, respectively. $[M]_\circ$= 0.670 M, $[CuBr_2]$ = 0.075 mM, [TBAB]= 100 mM, and ascorbic acid feeding rate is 23 nmoles/min. All polymerizations were conducted in 20% acetone in water at 30˚C for 6 hrs.

but the free polymer was measured to have a lower molecular weight than sample A.

To address this apparent contradiction, scanning electron microscopy (SEM) was performed on samples A and B to view their surface morphologies. As shown in Fig. 3A, the particle sizes for sample A range from 40-50 nm and do not appear to be aggregated nor embedded in polymer or surfactant. However, sample B (Fig. 3B) displays the particles embedded in what was concluded to be excess surfactant. The individual particles sizes are still ~40 nm, therefore, the % weight change on sample B from the TGA was skewed by unremoved surfactant. Furthermore, sample A exhibits higher degradation temperatures than that of sample B, which can be attributed to the surfactant present in the polymer emulsion powder in sample B. Sample B required extensive washing steps to fully rid the powder of any surfactant.

Further analysis of the polymer canopies on both samples using dark-field transmission electron microscope (TEM), demonstrates a clear polymer shell with a size of ~ 5 nm and uniform coverage (Fig. 4B and 4C). High-resolution TEM was performed on sample A and illustrated in Fig.4A, displaying the HNPs interacting via their polymer canopies. The dark-field TEM images of sample B (Fig. 4E and 4F) show faint and smaller polymer canopies than those of sample A, affirming a lower molecular weight PMMA shell on the surface of the inorganic core. This verifies that higher concentrations of surfactant lead to lower molecular weight polymers in solution and, under such conditions, on the nanoparticle surface as well.

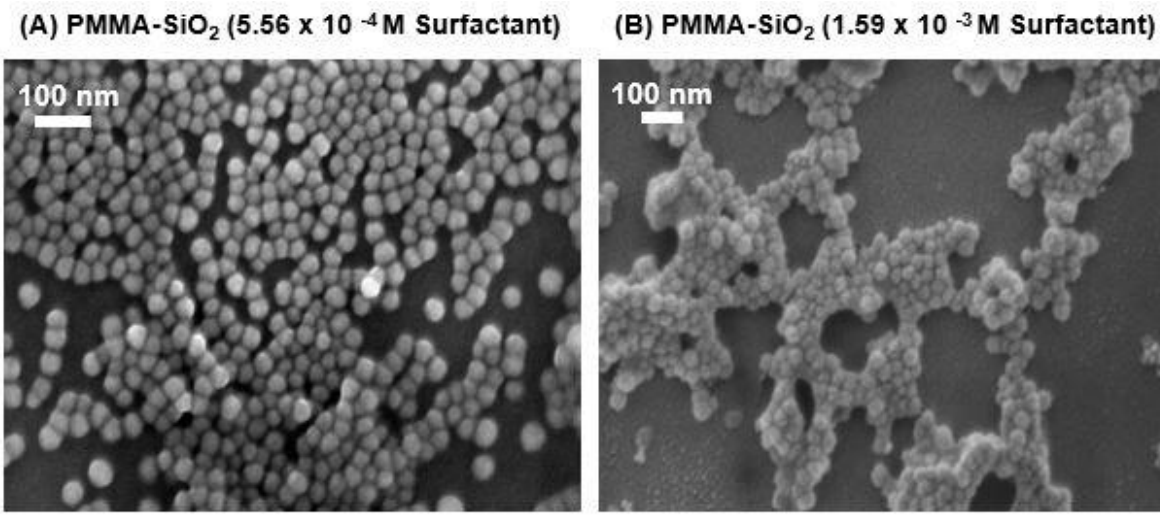

Figure 3. SEM images of SiO_2-PMMA hairy nanoparticles synthesized via mini ME emulsion polymerization using A) sample A, surfactant concentration of 5.56 x 10^{-4} M and B) sample B, surfactant concentration of 1.59 x 10^{-3} M. $[M]_\circ$ = 0.670 M, $[CuBr_2]$ = 0.075 mM, [TBAB]= 100 mM, and ascorbic acid feeding rate is 23 nmoles/min. All polymerizations were conducted in 20% acetone in water at 30˚C for 6 hrs.

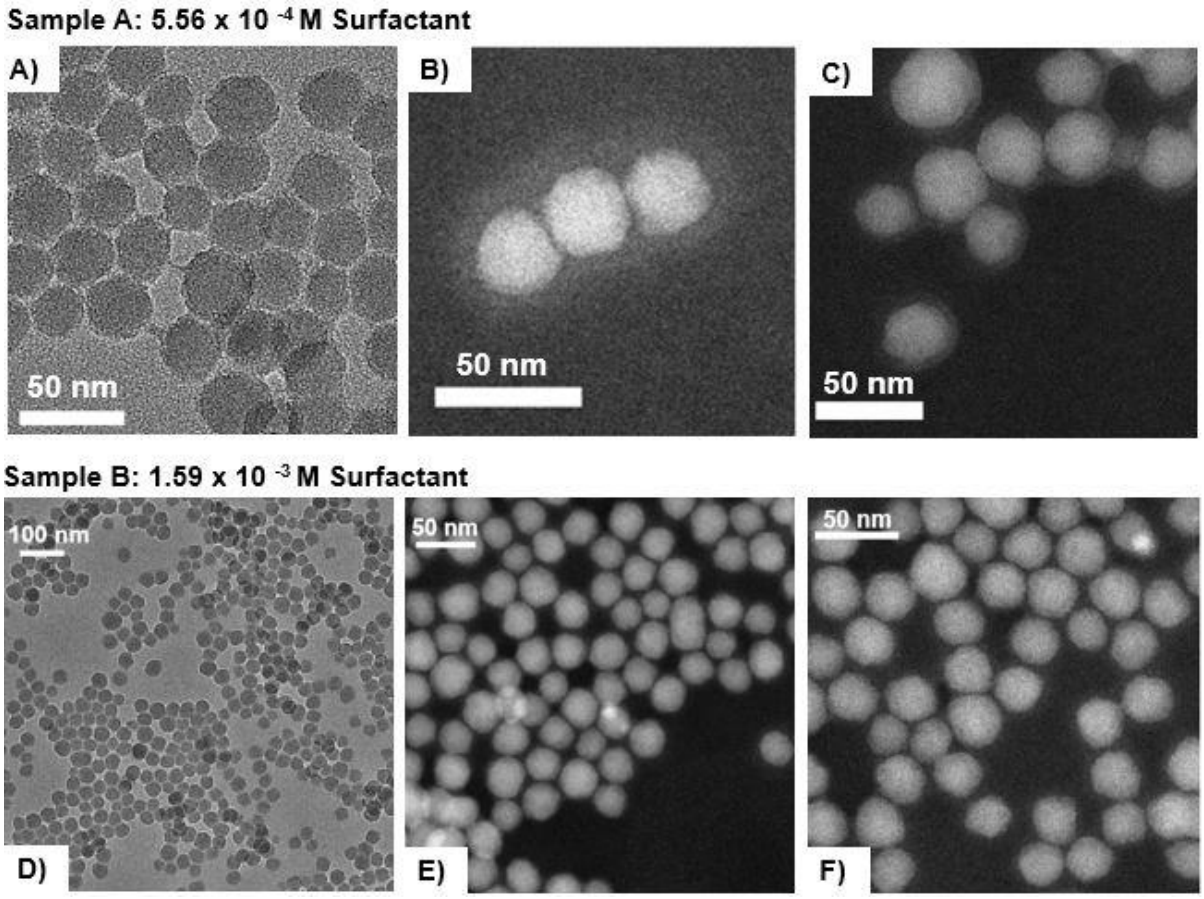

Figure 4. TEM images (high-resolution and dark-field) of sample A generated utilizing mini ME emulsion polymerization with a surfactant concentration of 5.56 x 10^{-4} M (top row) displaying a PMMA corona and sample B with a surfactant concentration of 1.59 x 10^{-3} M (bottom row) exhibiting a smaller polymer corona. $[M]_{\circ}$= 0.670 M, $[CuBr_2]$ = 0.075 mM, [TBAB]= 100 mM, and ascorbic acid feeding rate is 23 nmoles/min. All polymerizations were conducted in 20% acetone in water at 30˚C for 6 hrs.

This observation agrees with the confined space effect, as when the concentration of surfactant is increased, particle sizes are smaller, thus, leading to lower rates of polymerization (R_p) with higher degrees of livingness.[10] To further confirm the attachment of PMMA to the SiO_2 surface, Fourier transform infrared spectroscopy (FTIR) was performed using sample A, comparing bare SiO_2 to SiO_2-PMMA HNPs. The C=O stretch at ~ 1730 cm^{-1} and -CH_2 peaks from ~ 2952-2997 cm^{-1} signature of the PMMA polymer are present along with the Si-O-Si peak at ~ 1100 cm^{-1} from the SiO_2 nanoparticle (Fig. 5A). Depicted in Fig. 5B is the TGA of sample A compared to that of bare silica and SiO_2-Initiator, showing a 40% weight difference between the particles grafted with only initiator and SiO_2-PMMA particles; the remainder 50% of the weight its due to the inorganic portion of the HNPs.

XRD Characterization of SiO_2-PMMA HNPs, Pure PMMA and Bare SiO_2

To further investigate structures of PMMA, SiO_2, and SiO_2-PMMA HNPs (sample A), X-ray diffraction patterns at 10–70° (2θ) were examined. The data shows three characteristic peaks at 2θ= 13.8° (a very broad peak) and 2θ= 30.3° and 42.1° (two bands of lower intensity) in the XRD pattern of unmodified PMMA (Fig. 6), which is similar to Bergamonti et al.[11] In comparison, an additional peak at 2θ= 22.3° appears on the XRD pattern of SiO_2-PMMA nanoparticles. This can be assigned to the SiO_2 functional group in the SiO_2-PMMA nanoparticles as this peak aligns with the reference bare SiO_2.[12] However, the addition of the SiO_2 nanoparticles to a PMMA shell via mini ME emulsion does not induce changes in the XRD pattern of PMMA and there is no evidence of crystalline phases as the HNPs appear to be completely amorphous.

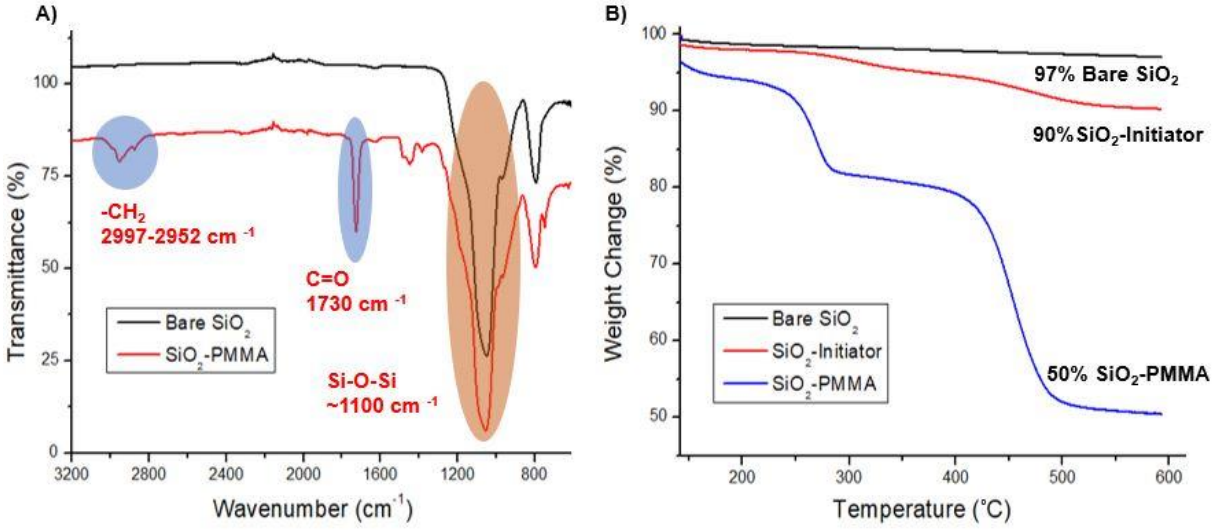

Figure 5. A) FTIR of sample A SiO_2-PMMA hairy nanoparticle compared to bare SiO_2 and B) TGA of sample A compared to bare SiO_2 and SiO_2-Initiator. $[M]_\circ$ = 0.670 M, $[CuBr_2]$ = 0.075 mM, [TBAB]= 100 mM, and ascorbic acid feeding rate is 23 nmoles/min. All polymerizations were conducted in 20% acetone in water at 30˚C for 6 hrs.

Effect of Monomer Concentration

As evidenced above, utilizing lower concentrations of Pluronic F-127 surfactant for the synthesis of SiO_2-PMMA HNPs is optimal, because 1) it allows the polymer to grow at a faster R_p providing higher molecular weight polymers on the surface of SiO_2 and 2) the cleaning procedure of surfactant from the HNPs is made easier and less extensive. Going forward, varied monomer concentrations and their effect on the molecular weight and surface functionalization of the particle was studied using the surfactant concentration implemented on sample A (5.56×10^{-4} M Pluronic F-127). At an initial monomer concentration of 0.343 M (sample C), the HNPs obtained from this synthesis only displayed a 73% polymer content through TGA analysis. This was compared to the 50% polymer content on sample A which had an initial monomer concentration of 0.670 M and the 41% polymer content on the HNPs with $[M]_\circ$= 1.340 M (sample D).

The TGAs demonstrate that as $[M]_\circ$ is increased, the polymer content is also increased in the sample (Fig. 7). This is supported by the molecular weight of the free polymer in solution generated during each synthesis (Fig. 7: Inset). The molecular weight of the free polymer from sample D ($[M]_\circ$= 1.340 M) was 81,279 g/mol with a Đ of 1.66, while the molecular weight of sample A ($[M]_\circ$= 0.670 M) was 51,275 g/mol with a Đ of 1.37. No free polymer was generated with the polymerization that produced sample C ($[M]_\circ$= 0.343 M) as it was assumed that most of the monomer was polymerized on the surface of the nanoparticle. Interestingly, the livingness of the polymerization decreased as $[M]_\circ$ was doubled from 0.670 M to 1.340M.

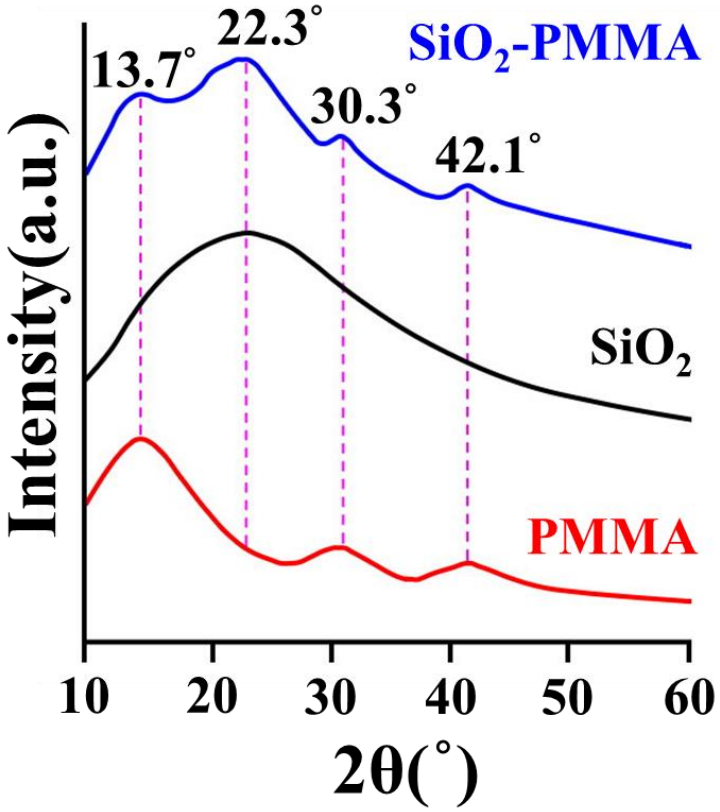

Figure 6. XRD of sample A hairy nanoparticle in reference to pure PMMA and bare SiO_2. $[M]_\circ$= 0.670 M, $[CuBr_2]$ = 0.075 mM, [TBAB]= 100 mM, and ascorbic acid feeding rate is 23 nmoles/min. All polymerizations were conducted in 20% acetone in water at 30˚C for 6 hrs.

Nevertheless, there was only a 9% weight difference between sample A ($[M]_{\circ}$= 0.670 M) and sample D ($[M]_{\circ}$= 1.340 M) HNPS. It was unexpected to see such a small increase in polymer content as, theoretically, a higher initial monomer concentration should lead to a higher degree of polymerization, thus, an increase in polymer content on the nanoparticles was expected.

Although a slight increase in % weight change is still observed, the weight difference was expected to be larger (~ 20%). SEM images of samples C and D HNPs are displayed in Fig. 8 and show extreme differences. Sample C, having the lowest initial monomer concentration, is assumed to also have the lowest molecular weight and grafting density, σ, on the particle surface. This is evidenced by the "raspberry-like" morphology adopted by the polymer on the particles. When the distance, D, between the grafting points is larger than twice the radius of gyration, R_g, the polymers assume the "mushroom" conformation.[2,13] These mushroom-like conformations can appear as globular structures as it seems in Fig. 8A. On the other hand, Fig. 8B exhibits the SEM image of sample D where the particles have aggregated. It was unclear whether the organic material on the surface was just the PMMA polymer or a mixture of excess MMA monomer that was incorporated within the sample causing the particles to aggregate during sample preparation.

To further examine samples C and D, TEM analysis was performed and illustrated in Fig.9. The polymer shell on sample C was difficult to see under TEM; however, looking closely, a slight polymer shell of ~ 1-2 nm was observed (Fig. 9A-C). The image in Fig. 9D shows the particles from sample D embedded in polymer or excess

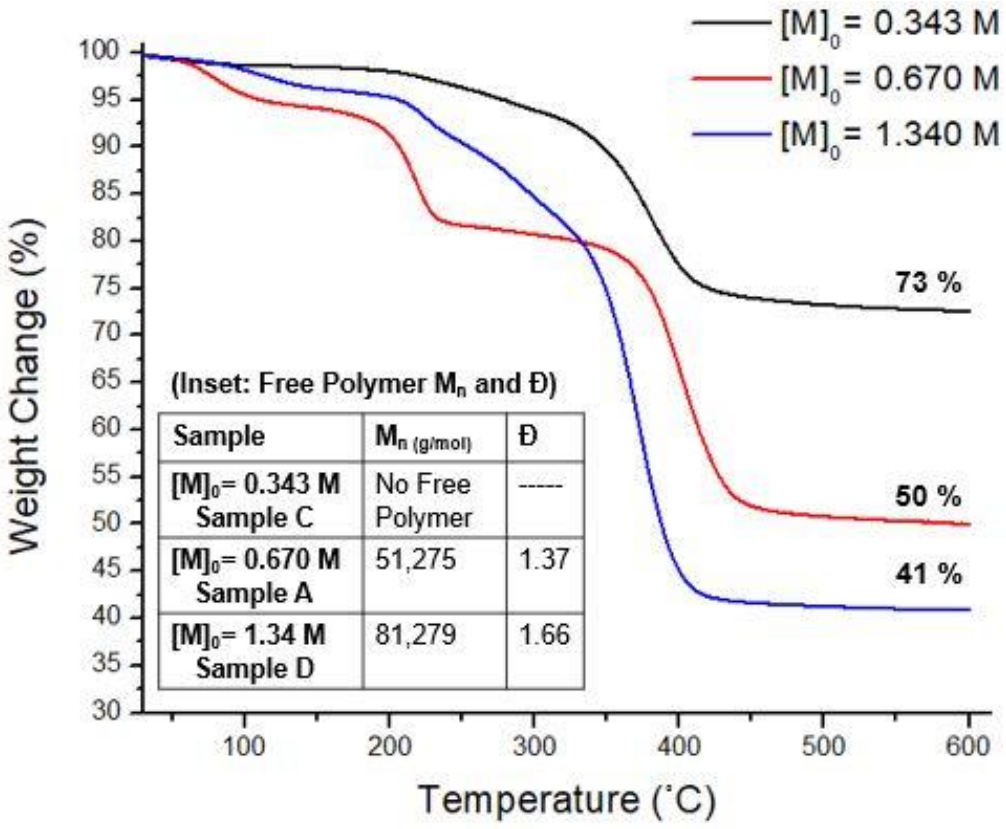

Figure 7. TGA of SiO_2-PMMA hairy nanoparticles synthesized via mini ME emulsion polymerization. Initial monomer concentration was varied ($[M]_o$ = 0.343 M, 0.670 M, and 1.340 M). Free polymer (Inset) formed in the aqueous phase was measured to have molecular weights of 51,275 g/mol (Đ = 1.37) and 81,279 g/mol (Đ = 1.66) for samples A and D, respectively. Sample C did not produce free polymer. [$CuBr_2$] = 0.075 mM, [TBAB]= 100 mM, [Pluronic F127] = 5.56 x 10^{-4} M and ascorbic acid feeding rate is 23 nmoles/min. All polymerizations were conducted in 20% acetone in water at 30˚C for 6 hrs.

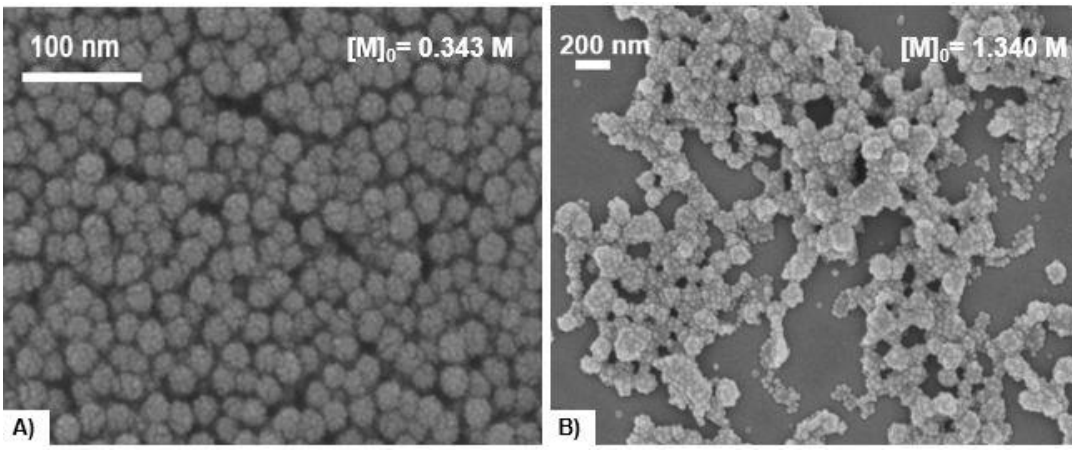

Figure 8. SEM images of SiO_2-PMMA hairy nanoparticles synthesized via mini ME emulsion polymerization A) sample C ($[M]_\circ$= 0.343 M) and B) sample D ($[M]_\circ$= 1.340 M). [$CuBr_2$] = 0.075 mM, [TBAB]= 100 mM, [Pluronic F127] = 5.56 x 10^{-4} M and ascorbic acid feeding rate is 23 nmoles/min. All polymerizations were conducted in 20% acetone in water at 30˚C for 6 hrs.

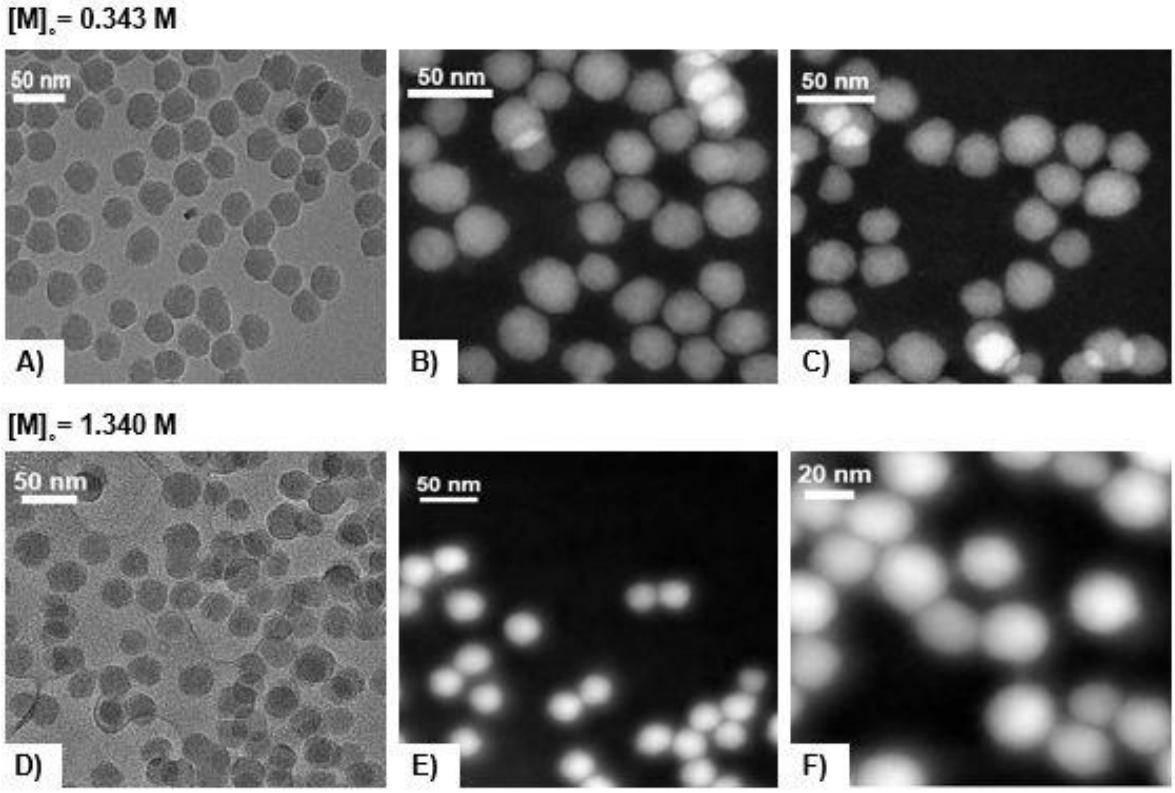

Figure 9. TEM images (high-resolution and dark-field) of sample C generated utilizing mini ME emulsion polymerization with $[M]_o$ = 0.343 M (top row) and sample B with $[M]_o$ = 1.340 M (bottom row) displaying a corona of ~ 10 nm. $[CuBr_2]$ = 0.075 mM, [TBAB]= 100 mM, [Pluronic F127] = 5.56 x 10^{-4} M and ascorbic acid feeding rate is 23 nmoles/min. All polymerizations were conducted in 20% acetone in water at 30˚C for 6 hrs.

monomer, still, to definitively see the polymer canopy covering the particle surface, dark-field images were taken (Fig. 9E-F).

These TEM images of sample D show a clear polymer shell ~ 8-10 nm around the nanoparticle, confirming that mini ME emulsion polymerization can be applied to a nanoparticle surface. Nevertheless, although SiO_2-PMMA HNPs were produced, there seems to be some barrier to efficient surface brush growth as initial monomer

concentrations are increased. There is also a large amount of free polymer generated as $[M]_\circ$ is increased (~ 80 wt.%). One possible explanation for the polymerization to produce such a large amount of free polymer is that perhaps as a few polymer chains come off the surface throughout the polymerization, they are polymerized within new loci in the dispersed phase. The monomer within reservoirs or in the aqueous phase are feeding into these new reaction loci and are no longer feeding into the micelles containing the SiO_2 particles with initiator. This feeding of monomer into new loci is more pronounced as monomer concentrations are increased. Production of free polymer in the aqueous phase can be diminished by the addition of a water-soluble polymerization inhibitor. This would inhibit further polymerizations in the aqueous phase and only allow them to occur where the nanoparticles functionalized with initiator are present.

Another way to prevent free polymer formation is by changing the initiator. The current initiator that is functionalized on the surface has an ester linkage. Esters are known to hydrolyze in aqueous solutions making them unstable. Amide linkages are far more stable in aqueous dispersed systems, therefore free polymer will not form if initiators do not hydrolyze off the nanoparticle surface. Mini ME polymerizations of

SiO_2-PMMA will address this issue in a future paper.

Conclusions

Hairy nanoparticles of SiO_2-PMMA were synthesized using a novel aqueous synthetic method. Ludox-TM SiO_2 nanoparticles were initially functionalized with a hydrophobic ATRP initiator, EDMP, in ethanol. A uniform polymer shell was successfully formed on the surface of these SiO_2 nanoparticles forming SiO_2-PMMA HNPs via mini ME emulsion polymerization using ARGET ATRP. The effect of surfactant concentration was examined, and it was observed that synthesis in the presence of lower concentrations (5.56×10^{-4}M Pluronic F127) of surfactant was beneficial to the manufacture of SiO_2-PMMA HNPs. It allowed polymer to grow on the surface with a faster R_p and purification excess surfactant from the HNPs was made easier. Initial monomer concentrations, $[M]_\circ$ were varied using a surfactant concentration of 5.56×10^{-4} M and initial monomer concentrations of 0.343 M, 0.670 M, and 1.340 M. HNPs produced using $[M]_\circ = 0.343$ M, the lowest monomer concentration studied, the particles were observed via SEM to adopt a "raspberry"-like morphology on the inorganic surface. These SEM images showed evidence that the polymer brush shell fell into the "mushroom" regime assuming these globular structures. The polymer canopy was difficult to detect under TEM as a faint polymer canopy was present.

As initial monomer concentrations increased from 0.343 M to 0.670 M, the polymer content was also increased; however, polymerization on the nanoparticle surface was dramatically reduced as the initial monomer concentration was increased from 0.670 M to 1.340 M. Although the monomer concentration was doubled, there was only a 9 %

weight difference between samples, compared to the 23% weight difference between HNPs produced when $[M]_{\circ}$= 0.343 M and $[M]_{\circ}$= 0.670 M, respectively.

Nevertheless, TEM images of HNPs produced using an initial monomer concentration of 1.340 M displayed a clear polymer corona of ~ 8- 10 nm. It was expected to produce a much larger polymer canopy. Another observation during this study was that as initial monomer concentrations increased, a larger volume of free polymer was produced in the dispersed phase (as high as 80 wt. %). This large amount of free polymer may have been formed from chains coming off the particle surface and polymerizing in a different locus. As initial monomer concentrations were increased, the polymerizations occurring in the aqueous phase would expend the monomer, thus not allowing all the monomer to enter the micelles containing the nanoparticles. Future work will address this issue by diminishing polymerization in the aqueous phase, therefore, allowing the main loci to be within nanoparticle-containing micelles.

ACKNOWLEDGEMENTS

The authors would like to thank the Air Force Office of Scientific Research (AFOSR FA9550-17-1-0038), and for prior support the Air Force Research Laboratory (AFRL). This work made use of the Cornell Center for Materials Research Shared Facilities which are supported through the NSF MRSEC program (DMR-1719875). Experiments were conducted at both Cornell University and at AFRL under Dr. Richard Vaia's supervision. Contributing members include Zoe Lequeux who is my undergraduate student and helped me run the mini ME emulsion experiments on the nanoparticle surface, and Dung Yi Wu who is a master's student in the Ober group at Cornell University and characterized the particles using SEM imaging, FTIR spectroscopy, and XRD. Dr. Ali Jawaid, and Dr. Lawrence Drummy from AFRL both further characterized the hairy nanoparticles using TEM imaging.

REFERENCES

(1) Fernandes, N. J.; Koerner, H.; Giannelis, E. P.; Vaia, R. A. Hairy Nanoparticle Assemblies as One-Component Functional Polymer Nanocomposites: Opportunities and Challenges. *MRS Commun.* **2013**, *3* (01), 13–29.

(2) Fernandes, N. J.; Koerner, H.; Giannelis, E. P.; Vaia, R. A. Hairy Nanoparticle Assemblies as One-Component Functional Polymer Nanocomposites: Opportunities and Challenges. *MRS Commun.* **2013**, *3* (01), 13–29.

(3) Cagno, V.; Andreozzi, P.; D'Alicarnasso, M.; Jacob Silva, P.; Mueller, M.; Galloux, M.; Le Goffic, R.; Jones, S. T.; Vallino, M.; Hodek, J.; et al. Broad-Spectrum Non-Toxic Antiviral Nanoparticles with a Virucidal Inhibition Mechanism. *Nat. Mater.* **2017**, *17* (2), 195–203.

(4) Pyun, J.; Jia, S.; Kowalewski, T.; Patterson, G. D.; Matyjaszewski, K. Synthesis and Characterization of Organic/Inorganic Hybrid Nanoparticles: Kinetics of Surface-Initiated Atom Transfer Radical Polymerization and Morphology of Hybrid Nanoparticle Ultrathin Films. *Macromolecules* **2003**, *36* (14), 5094–5104.

(5) Chevigny, C.; Gigmes, D.; Bertin, D.; Jestin, J.; Boué, F. Polystyrene Grafting from Silica Nanoparticles via Nitroxide-Mediated Polymerization (NMP): Synthesis and SANS Analysis with the Contrast Variation Method. *Soft Matter* **2009**, *5* (19), 3741.

(6) Li, D.; Sheng, X.; Zhao, B. Environmentally Responsive "Hairy" Nanoparticles: Mixed Homopolymer Brushes on Silica Nanoparticles Synthesized by Living Radical Polymerization Techniques. *J. Am. Chem. Soc.* **2005**, *127* (17), 6248–6256.

(7) Cordero, R.; Jawaid, A.; Hsiao, M.-S.; Lequeux, Z.; Vaia, R. A.; Ober, C. K. Mini Monomer Encapsulated Emulsion Polymerization of PMMA Using Aqueous

ARGET ATRP. *ACS Macro Lett.* **2018**, *7* (4), 459–463.

(8) Raşa, M.; Philipse, A. P.; Meeldijk, J. D. Heteroaggregation, Repeptization and Stability in Mixtures of Oppositely Charged Colloids. *J. Colloid Interface Sci.* **2004**, *278* (1), 115–125.

(9) Meneghetti, P.; Qutubuddin, S. Synthesis, Thermal Properties and Applications of Polymer-Clay Nanocomposites. *Thermochim. Acta* **2006**, *442* (1–2), 74–77.

(10) Zetterlund, P. B.; Okubo, M. Compartmentalization in Nitroxide-Mediated Radical Polymerization in Dispersed Systems. *Macromolecules* **2006**, *39* (26), 8959–8967.

(11) Bergamonti, L.; Bondioli, F.; Alfieri, I.; Alinovi, S.; Lorenzi, A.; Predieri, G.; Lottici, P. P. Weathering Resistance of PMMA/SiO 2 /ZrO 2 Hybrid Coatings for Sandstone Conservation. *Polym. Degrad. Stab.* **2018**, *147*, 274–283.

(12) Tański, T.; Matysiak, W.; Krzemiński, Ł.; Jarka, P.; Gołombek, K. Optical Properties of Thin Fibrous PVP/SiO 2 Composite Mats Prepared via the Sol-Gel and Electrospinning Methods. *Appl. Surf. Sci.* **2017**, *424*, 184–189.

(13) Chen, W.-L.; Cordero, R.; Tran, H.; Ober, C. K. 50th Anniversary Perspective: Polymer Brushes: Novel Surfaces for Future Materials. *Macromolecules* **2017**, *50* (11), 4089–4113.

CHAPTER 5

SYNTHESIS OF SILICA-POLYSTYRENE HAIRY NANOPARTICLES USING MINI MONOMER ENCAPSULATED EMULSION POLYMERIZATION

Abstract

Mini ME emulsion polymerization using ARGET ATRP was employed for the synthesis of SiO_2-polystyrene hairy nanoparticles. Ludox particles were initially modified with a hydrophobic ATRP initiator in ethanol, then dispersed in styrene monomer with an initial monomer concentration, $[M]_o$ = 0.400 M before carrying out the emulsion polymerization technique. Mini ME emulsion polymerization allows ATRP catalyst and ligand to be delivered to the micelle using the phase transfer agent, TBAB. Spherical aggregates were formed during the polymerization with the sphere diameters ranging from 200 nm – 500 nm in size.

Introduction

Within recent decades, interest in the development of nanoparticle-filled polymer composites has been prevalent.[1–8] The combination of inorganic nanoparticles and organic polymers can result in various advanced materials with enhanced thermal, electronic, and optical properties, which are strongly dependent on the dispersion characteristics of the nanoparticle in the polymer matrix.[3] In the early 1950s, Van de Waarden introduced the idea of grafting organic molecules on inorganic particles which stabilized the particles in the matrix and this idea has been used for stabilization of particles since.[9] Hairy nanoparticles (HNPs), a subset of these composites, are an emerging family of material that possesses the combined properties of the core (i.e.

dielectric, band gap, dielectric properties) and the mechanical properties of the organic polymer (i.e., flexibility). [3,8]

Recently, many synthetic techniques have been developed to produce HNPs; however, low product yield, initiator instability, and use of toxic/high boiling point solvents has been an issue.[3,10] Aqueous synthetic techniques are the desired route to generate HNPs in a large-scale batch. Mini ME emulsion polymerization using ARGET ATRP, developed in this group, has recently proven to successfully manufacture SiO_2-PMMA HNPs.[11] This new emulsion technique uses acetone to facilitate the solubility of monomer in the aqueous phase, as well as aiding the transfer of several components within the aqueous phase to the micelle. The phase transfer agent, tetrabutylammonium bromide (TBAB), assisted to shuttle ATRP catalyst between phases and provided extra halide anions (Br^-). The extra halogen was used to compensate for Br^- anions that were dissociated from the ATRP transition metal catalyst in the aqueous phase, allowing for a more controlled polymerization.

In this thesis, Chapter 3 discussed the important challenges that were encountered when mini ME emulsion polymerization was used to produce low dispersity polystyrene. One of those challenges was the rate of polymerization being significantly decreased when initial monomer concentration, $[M]_\circ$, was increased due to compartmentalization effects. The initial monomer concentration was decreased by half to reduce the size of the monomer droplets, which led to controlled polymerizations ($Đ < 1.2$) and experimental molecular weights close to theoretical molecular weights.

This chapter will focus on the synthesis of SiO_2-PS hairy nanoparticles using mini ME emulsion polymerization via the procedure outlined in Chapter 3. The method for

nanoparticle modification was outlined in Chapter 4 and was also implemented to provide SiO_2-PS HNPs. Nanoparticles of ~ 200-500 nm were obtained from this procedure and were found to be highly aggregated. In future, further studies will be performed to obtain unaggregated SiO_2-PS HNPs.

Experimental Procedure

Synthesis of 11-(ethoxydimethylsilyl) undecyl 2-bromo-2-methylpropanoate (EDMP) ATRP Initiator

Step 1: Bromination

In a 100 mL round-bottom flask equipped with a stir bar, 10-undecen-1-ol (4.257 g, 5mL, 0.025 mol) and pyridine (2.1 mL, 0.026 mol) were dissolved in 30 mL of anhydrous tetrahydrofuran (THF). Then, at 0˚C, 2-bromoisobutyryl bromide (BIBB) (5.760 g, 3.1 mL, 0.024 mol) in 10 mL of THF was added dropwise to the solution in the round-bottom flask over a period of 2 hours with stirring. After 2 hours, the solution was warmed to room temperature and stirred for 24 hours. Triethylammonium bromide salt was formed as a white precipitate and filtered out. The solvent was removed under vacuum resulting in a yellow oil. The yellow oil was dissolved in dichloromethane (DCM) and extracted twice with an aqueous solution saturated with Na_2CO_3. The organic phase was dried over sodium sulfate anhydrous, and DCM was evaporated under vacuum. Column chromatography was performed in a 100% dichloromethane resulting in a pale-yellow oil (yield = 95%).

Step 2: Hydrosilylation

Dimethylethoxysilane (0.04 mol) and Karstedt catalyst (6 μL) were added to the

product from step 1 (0.004 mol), and the mixture was stirred for over-night at room temperature in a nitrogen environment. Excess dimethylethoxysilane was then removed under vacuum and the residual liquid was then stored at -20˚ C until needed.

Addition of EDMP ATRP Initiator to Ludox-TM 40 particles

Conditioning of Dowex Resin

Dowex 50W X8 and Dowex 1X8 resin (50 g each) were each transferred to a 600 mL beaker (separate beakers). Each resin was washed with 3N NaOH, hot water, methanol, and cold water. After each individual wash, the resins were recollected via filtration, added back into the beaker and washed again with the subsequent solvent. This cycle was repeated 5 times with each resin. After the last wash cycle of Dowex 50W X8, the resin was converted to the hydrogen form with a final wash using excess 3N HCl. Likewise, Dowex 1X8 was converted to the hydroxy form with 3N NaOH. This must be converted shortly before use. Resins were then rinsed with copious amounts of doubly distilled water and mixed under stirring. The resins were recollected via filtration.

Ion-exchange of Ludox-TM 40

Ludox-TM 40 (100 mL) was diluted with 100 mL of Millipore water, stirred and added to Dowex 50W X8 resin in a beaker under agitation over-night. Ludox-TM 40 particles were then collected via filtration and then added to Dowex 1X8 resin in a beaker and subsequently stirred over-night. The particles were then collected via filtration (large aggregates were centrifuged down at 3000 rpm), then dialyzed against ethanol for 1 week.

Addition of EDMP to Ludox-TM 40 in Ethanol

Ludox particles dispersed in ethanol (1 g, 50 mL) was added to a 200 mL round-bottom flask. Then, 28% NH_3 in water was slowly added to the ethanol dispersion until the pH was 10. The ATRP initiator, EDMP (0.860 g, 0.002 mol) was then slowly added to the suspension and sonicated for 1 hour before refluxing the solution at 85˚C for a period of 24 hours. After 24 hours, the solution was cooled to room temperature and centrifuged at 4000 rpm to separate out any aggregates. The solution was then dialyzed against ethanol for 1 week.

Synthesis of PS-SiO_2 Hairy Nanoparticles using ARGET-ATRP Mini ME Emulsion Polymerization

EDMP-SiO_2 particles in ethanol (200 mg) were added to styrene monomer (2.78 mL, 0.024 mol) in a 20 mL scintillation vial and mixed. The ethanol was then evaporated leaving the particles dispersed in the styrene monomer. A surfactant mixture of Pluronics F-127 (0.80 g) in water (10 mL) was then added to the styrene-particle suspension and vortexed until it formed a milky white dispersion. In a three-neck 100-mL round-bottom flask, TBAB (1.934g, 6 mmol), $CuBr_2$ (2 mg, 8.96 μmol), and Tris(2-pyridylmethyl) amine (TPMA) (20.90 mg, 72 μmol) were added to a mixture of acetone (12 mL, 20% v/v) and water (34.4 mL). The pre-emulsified dispersion of styrene with particles and surfactant was then added to the contents of the three-neck 100-mL round-bottom flask forming a cloudy white dispersion. The flask was then equipped with a reflux condenser and an argon-filled balloon. The flask was then purged with argon for 30 mins. Lastly, in a separate vial, a stock solution of ascorbic acid (2.27 mM, 5 mL) was prepared and purged with argon for 30 min before being fed to the reaction using a syringe pump at a rate of 1.67 μL/min (4.8 mL). The polymerization was stopped by

opening the reaction to air. A yellow solid containing the hairy nanoparticles was floating over the top of the reaction. This solid was dissolved in THF and precipitated in hexanes before being washed with water to get rid of any residual surfactant. The particles obtained from this solid was then oven dried at 80˚C for several hours before being re-dispersed in THF.

Results and Discussion

Compartmentalization is defined as the physical confinement of reactants to a very small space. This effect is primarily observed in two-phase polymerization systems (e.g. emulsion and miniemulsion polymerizations) and can alter the polymerization rates, molecular weights, and dispersities of the polymer compared to an uncompartmentalized system. Compartmentalization of radicals throughout the polymerization was observed in Chapter 3 to affect the final molecular weight and dispersity of the polymers for mini ME emulsion polymerizations of polystyrene. As $[M]_\circ$ concentration was decreased from 518 mM to 260 mM, the monomer droplets became smaller and sparsely dispersed and compartmentalization of the radicals was minimized. To that end, when applying mini ME emulsion polymerization procedure to manufacture SiO_2-PS HNPs, $[M]_\circ$ was reduced from 0.670 M (concentration used in chapter 4 for SiO_2-PMMA HNPs) to 0.400 M to evade complications due to compartmentalization.[12–14]

Particles modified with the hydrophobic initiator, EDMP, were dispersed in styrene via the procedure described in the experimental section. Once the polymerization was complete after 48 hours, the HNPs were observed to have precipitated out of the solution

indicative of aggregation. This precipitate was purified and analyzed with FTIR (Fig. 1A) showing the Si-O-Si (~1100 cm^{-1}) peak of the SiO_2 nanoparticle along with typical polystyrene peaks. A 44% weight difference is observed using TGA analysis (Fig. 1B) between SiO_2-Initiator (90% weight change) particles and SiO_2-PS HNPs (46% weight change).

XRD patterns of the pure PS and PS-SiO_2 nanoparticles were analyzed and are depicted in Fig. 2. The spectrum of PS revealed a broad peak at around $2\theta = 20^\circ$ shown in Fig. 2 (red line). The XRD result of PS-SiO_2 nanoparticles was similar to that of the PS alone. The results revealed SiO_2-PS do not have nanoparticles polymer crystallinity, and the spectrum is analogous to previously reported literature of SiO_2-PS HNPs.[15]

SEM images of the SiO_2-PS HNPs are shown in Fig. 3 and illustrate large, almost perfect spheres that range from ~ 200 nm – 500 nm. According to the TGA, the polymer content (46 wt. %) of these SiO_2-PS particles does not equate to the size of the spheres present in the SEM images as the spheres are too large for the polymer to only make up half of the weight of the entire sample. To further examine these spheres, TEM analysis was performed and the images are shown in Fig. 4. It was found that several particles formed large aggregates in the form of the spheres. These aggregates are atypical of what is usually seen with nanoparticle aggregation as they are perfectly spherical. One explanation for this outcome is having residual surfactant still present within the solid samples even after purification. Excess surfactant causes a reduction of the interfacial tension between the aggregated HNPs and the solvent, tetrahydrofuran (THF), allowing the formation of the large spheres.

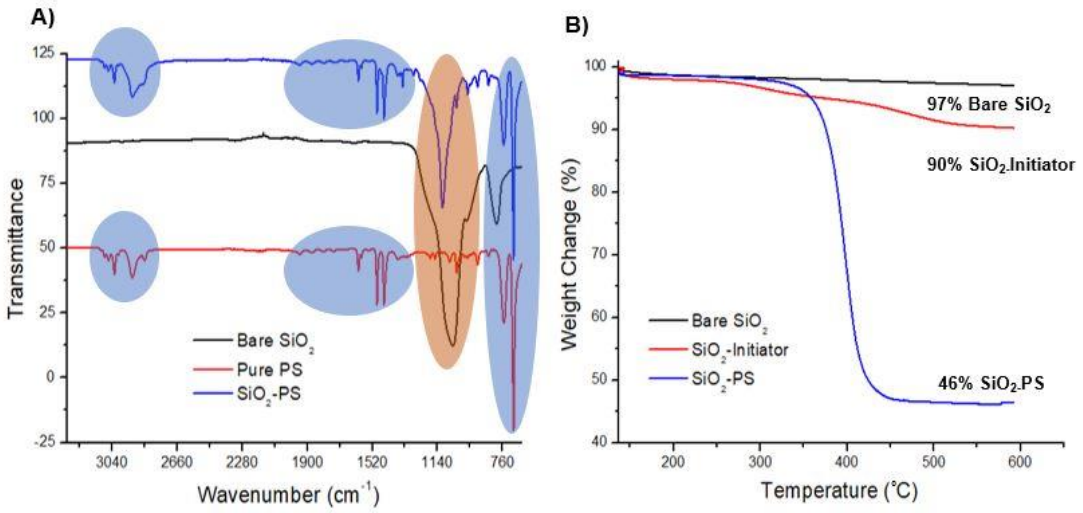

Figure 1. A) FTIR of SiO_2-PS hairy nanoparticles compared to to bare SiO_2 and pure PS and B) TGA of bare SiO_2, SiO_2-Initiator, and SiO_2-PS. $[M]_o$= 0.400 M, $[CuBr_2]$ = 0.150 mM, [TBAB]= 100 mM, and ascorbic acid feeding rate is 40 nmoles/min. All polymerizations were conducted in 20% acetone in water at 80˚C for 48 hrs.

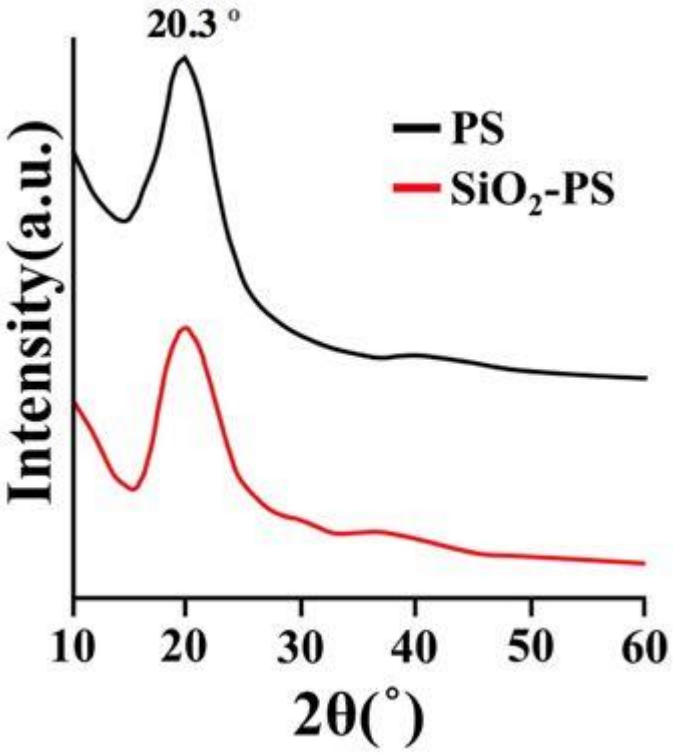

Figure 2. XRD of SiO_2-PS hairy nanoparticle compared to pure PS and bare SiO_2. $[M]_o$= 0.400 M, $[CuBr_2]$ = 0.150 mM, [TBAB]= 100 mM, and ascorbic acid feeding rate is 40 nmoles/min. All polymerizations were conducted in 20% acetone in water at 80˚C for 48 hrs.

To ascertain whether aggregation occurred during the polymerization or as a consequence of the purification procedure the reaction was repeated, and aliquots were removed every few hours. The 200 μL aliquots were then diluted with 800 μL of THF and drop casted on a clean silicon wafer chip before imaging with an SEM. At T=0 hours, the surfactant is the prominent material as polymer is yet to be formed (Fig. 5, row 1). Large spheres start to appear within the first hour of the polymerization with increasing size and concentration as time progresses (Fig. 5).

These large particles coalesced forming even greater aggregates at longer reaction times. However, at T=12 hours (Fig. 6, first row), the density of these spheres in solution begin to decrease. This decrease of spheres in the SEM images is happening because the aggregates began precipitating out of solution. As more particles are being formed, the cycle continues with larger aggregates precipitating out; however, as free polymer is formed, few particles become embedded in it as shown in Fig 6 and Fig. 7. After 48 hours, almost all the particles have precipitated out of solution leaving a small percentage within the free polymer (Fig. 7). These SEM images confirm that the particles aggregate during the polymerization and the aggregates are not the result of purification. Further research needs to be conducted to probe this issue and understand why this aggregation is occurring.

One possibility as to why the HNPs are aggregating during the polymerization is that localization of the reaction in this system was still not very well controlled. Firstly, because a high concentration of the Pluronic F127 surfactant was utilized (1.59×10^{-3} M) resulting in many, very small micelles, the SiO_2-initiator particles could be localized

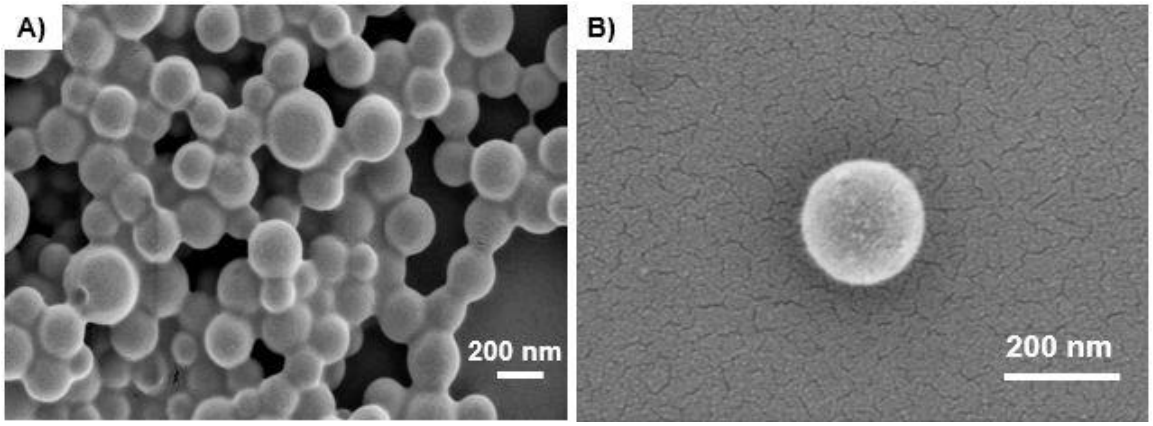

Figure 3. SEM images of SiO_2-PS hairy nanoparticles which are aggregates that have formed into "perfect" spheres. $[M]_o$ = 0.400 M, $[CuBr_2]$ = 0.150 mM, [TBAB]= 100 mM, and ascorbic acid feeding rate is 40 nmoles/min. All polymerizations were conducted in 20% acetone in water at 80˚C for 48 hrs.

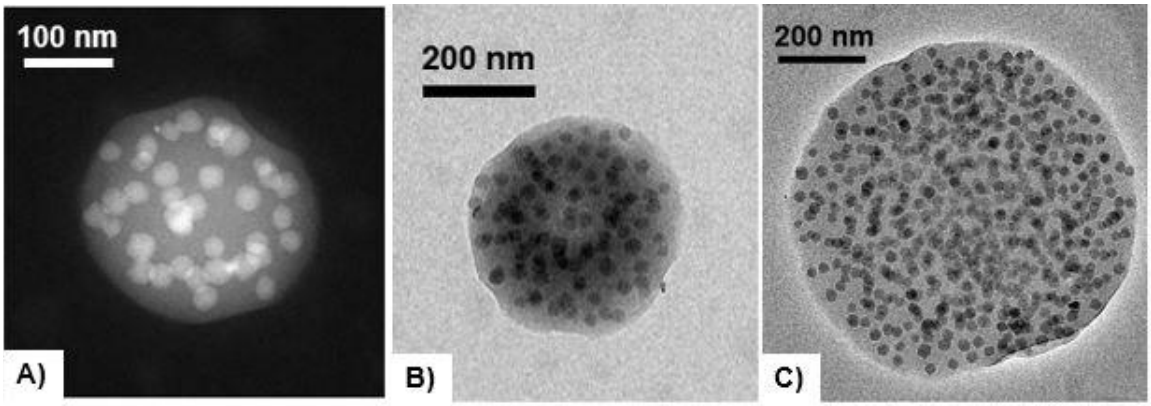

Figure 4. TEM images of SiO_2-PS hairy nanoparticles showing several aggregated particles that form the larger spheres. $[M]_\circ$= 0.400 M, $[CuBr_2]$ = 0.150 mM, [TBAB]= 100 mM, and ascorbic acid feeding rate is 40 nmoles/min. All polymerizations were conducted in 20% acetone in water at 80˚C for 48 hrs.

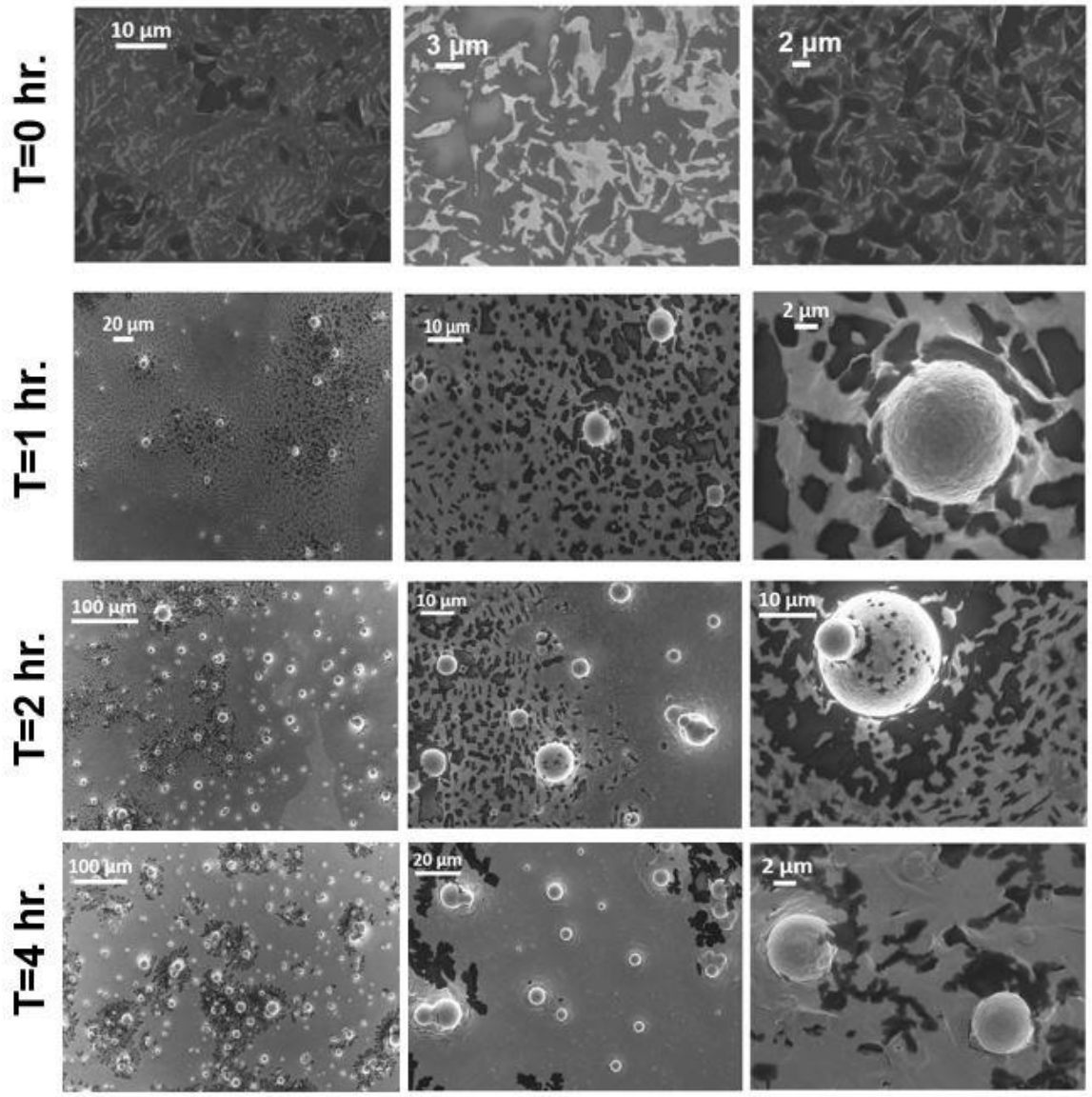

Figure 5. SEM images of the time study performed with mini ME emulsion polymerization to generate SiO_2-PS hairy nanoparticles. Aliquots were taking out at T=0, T= 1 hr., T= 2 hr., and T= 4 hr. Large spheres started to appear at T=1 hr. and became more concentrated as time progressed. $[M]_\circ$= 0.400 M, $[CuBr_2]$ = 0.150 mM, [TBAB]= 100 mM, and ascorbic acid feeding rate is 40 nmoles/min. All polymerizations were conducted in 20% acetone in water at 80˚C for 48 hrs.

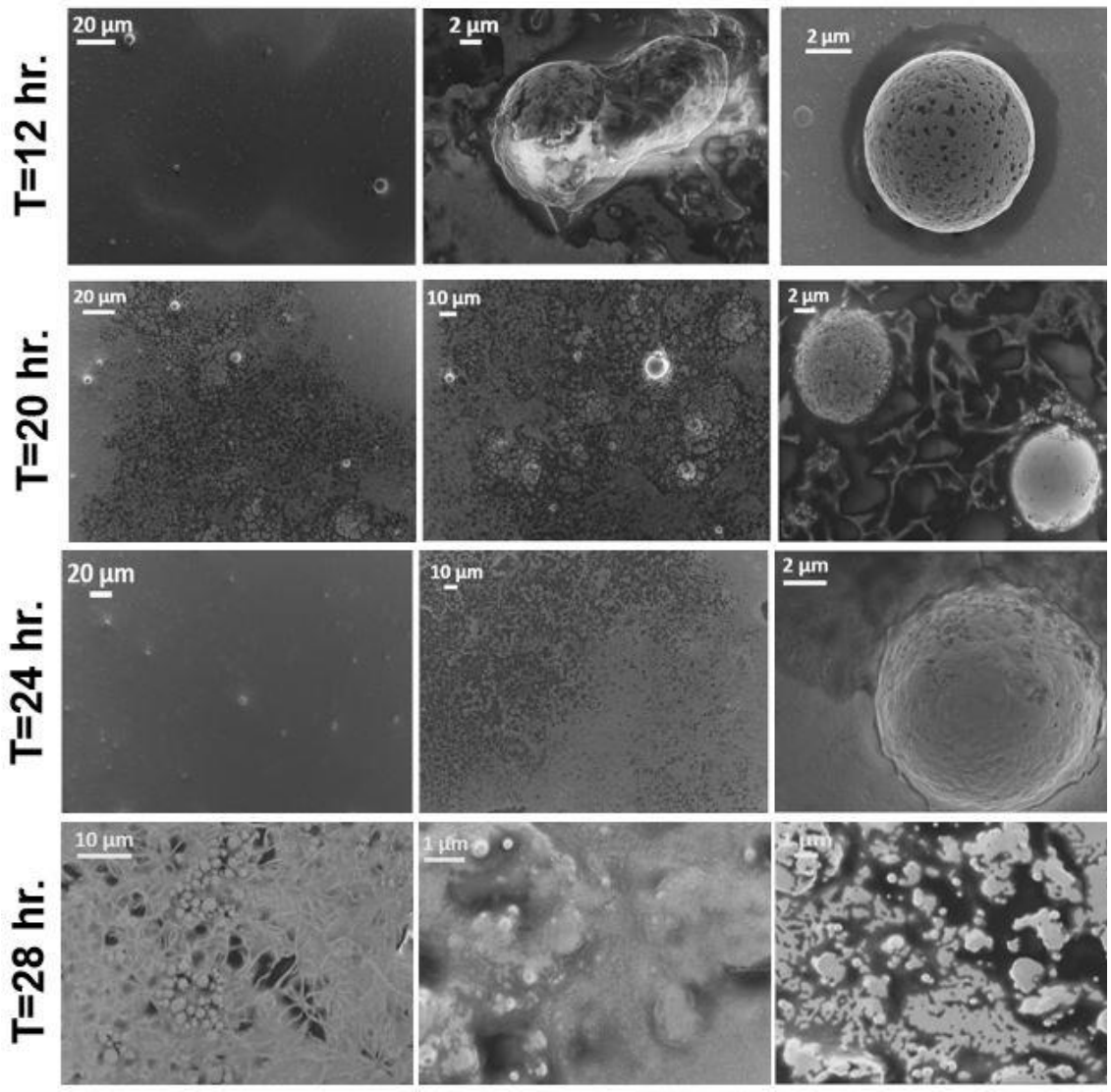

Figure 6. SEM images of the time study performed with mini ME emulsion polymerization to generate SiO_2-PS hairy nanoparticles. Aliquots were taking out at T=12, T= 20 hr., T= 24 hr., and T= 28 hr. The aggregates start to precipitate out of solution at T= 12 hr. and a lower density of large aggregates are viewed under the SEM. $[M]_\circ$= 0.400 M, $[CuBr_2]$ = 0.150 mM, [TBAB]= 100 mM, and ascorbic acid feeding rate is 40 nmoles/min. All polymerizations were conducted in 20% acetone in water at 80˚C for 48 hrs.

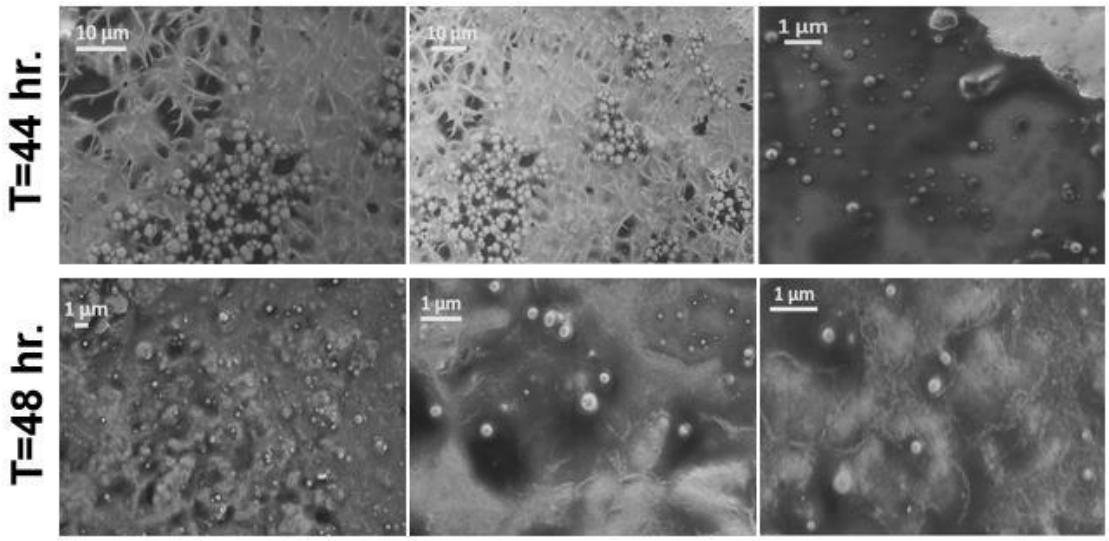

Figure 7. SEM images of the time study performed with mini ME emulsion polymerization to generate SiO_2-PS hairy nanoparticles. Aliquots were taking out at T=44, and T= 48 hr. Aggregates that have not precipitated out are embedded in free polymer. $[M]_\circ$= 0.400 M, $[CuBr_2]$ = 0.150 mM, [TBAB]= 100 mM, and ascorbic acid feeding rate is 40 nmoles/min. All polymerizations were conducted in 20% acetone in water at 80˚C for 48 hrs.

within the larger monomer droplets as these particles are ~ 30 nm. The larger droplets may be housing a number of these particles, thus causing them to coalesce and resulting in the large spheres. Secondly, because the polymerization is conducted at 80˚C, and is under reflux, the acetone would reflux and come back into the dispersion in a cycle. The concentration of acetone would be varied throughout the polymerization which can lead to complications with monomer localization. To avoid this issue, in the future, we would need to keep the concentration of both solvents relatively constant in the reaction.

Conclusions

SiO_2-PS hairy nanoparticles were synthesized using mini ME emulsion polymerization with ARGET ATRP. These hairy nanoparticles were aggregated and formed perfect spheres due to residual surfactant left after purification. This residual surfactant decreased the surface tension, thus allowed the large aggregated particles to form a network in the shape of these spheres. A polymerization time study was performed in order to determine whether the aggregates formed during the polymerization or as a result of the purification. The SEM images of the time study demonstrated that the aggregates formed within the first hour of the polymerization and continued to aggregate as time progressed. The aggregates precipitated out of the reaction leaving only a small percentage embedded in free polymer. The aggregates ranged from ~ 200 nm – 500 nm in size.

These masses may be forming because the larger droplets may be housing a number of these particles, thus causing them to coalesce and resulting in the large spheres. This aggregation can also be symptomatic of the inconsistent concentration of acetone

throughout the polymerization due to refluxing. The concentration of acetone would be varied throughout the polymerization which can lead to complications with monomer localization. Further researched will be conducted in the future to diminish the amount of aggregation that occurs throughout the polymerization.

ACKNOWLEDGMENTS

The authors would like to thank the Air Force Office of Scientific Research (AFOSR FA9550-17-1-0038), and for prior support the Air Force Research Laboratory (AFRL). This work made use of the Cornell Center for Materials Research Shared Facilities which are supported through the NSF MRSEC program (DMR-1719875). Experiments were conducted at both Cornell University and at AFRL under Dr. Richard Vaia's supervision. Contributing members include Zoe Lequeux, my undergraduate student who helped with the synthesis of the hairy nanoparticles and Dung Yi Wu, a master's student in the Ober group at Cornell University who helped with characterizing the hairy nanoparticles via SEM imaging, FTIR, and XRD. Dr. Ali Jawaid, and Dr. Lawrence Drummy from AFRL both further characterized the hairy nanoparticles via TEM imaging.

REFERENCES

(1) Krishnamoorti, R.; Vaia, R. A. Polymer Nanocomposites. *J. Polym. Sci. Part B Polym. Phys.* **2007**, *45* (24), 3252–3256.

(2) Kumar, S. K.; Krishnamoorti, R. Nanocomposites: Structure, Phase Behavior, and Properties. *Annu. Rev. Chem. Biomol. Eng.* **2010**, *1* (1), 37–58.

(3) Fernandes, N. J.; Koerner, H.; Giannelis, E. P.; Vaia, R. A. Hairy Nanoparticle Assemblies as One-Component Functional Polymer Nanocomposites: Opportunities and Challenges. *MRS Commun.* **2013**, *3* (01), 13–29.

(4) Grabowski, C. A.; Koerner, H.; Meth, J. S.; Dang, A.; Hui, C. M.; Matyjaszewski, K.; Bockstaller, M. R.; Durstock, M. F.; Vaia, R. A. Performance of Dielectric Nanocomposites: Matrix-Free, Hairy Nanoparticle Assemblies and Amorphous Polymer–Nanoparticle Blends. *ACS Appl. Mater. Interfaces* **2014**, *6* (23), 21500–21509.

(5) Winey, K. I.; Vaia, R. A. Polymer Nanocomposites. *MRS Bull.* **2007**, *32* (04), 314–322.

(6) Mezzenga, R.; Ruokolainen, J. Nanoparticles in the Right Place: Nanocomposites. *Nat. Mater.* **2009**, *8* (12), 926–928.

(7) Crosby, A. J.; Lee, J. Polymer Nanocomposites: The “Nano” Effect on Mechanical Properties. *Polym. Rev.* **2007**, *47* (2), 217–229.

(8) Person, V. Structure Properties of Heterophase Hairy-Nanoparticles: Organic vs. Inorganic. 113.

(9) van der Waarden, M. Stabilization of Carbon-Black Dispersions in Hydrocarbons. *J. Colloid Sci.* **1950**, *5* (4), 317–325.

(10) Chevigny, C.; Gigmes, D.; Bertin, D.; Jestin, J.; Boué, F. Polystyrene Grafting from Silica Nanoparticles via Nitroxide-Mediated Polymerization (NMP): Synthesis and SANS Analysis with the Contrast Variation Method. *Soft Matter* **2009**, *5* (19), 3741.

(11) Cordero, R.; Jawaid, A.; Hsiao, M.-S.; Lequeux, Z.; Vaia, R. A.; Ober, C. K. Mini Monomer Encapsulated Emulsion Polymerization of PMMA Using Aqueous ARGET ATRP. *ACS Macro Lett.* **2018**, *7* (4), 459–463.

(12) Zetterlund, P. B.; Kagawa, Y.; Okubo, M. Compartmentalization in Atom Transfer Radical Polymerization of Styrene in Dispersed Systems: Effects of Target Molecular Weight and Halide End Group †. *Macromolecules* **2009**, *42* (7), 2488–2496.

(13) Zetterlund, P. B.; Thickett, S. C.; Perrier, S.; Bourgeat-Lami, E.; Lansalot, M. Controlled/Living Radical Polymerization in Dispersed Systems: An Update. *Chem. Rev.* **2015**, *115* (18), 9745–9800.

(14) Zetterlund, P. B.; Okubo, M. Compartmentalization in Nitroxide-Mediated Radical Polymerization in Dispersed Systems. *Macromolecules* **2006**, *39* (26), 8959–8967.

(15) Haldorai, Y.; Lyoo, W. S.; Noh, S. K.; Shim, J.-J. Ionic Liquid Mediated Synthesis of Silica/Polystyrene Core–Shell Composite Nanospheres by Radical Dispersion Polymerization. *React. Funct. Polym.* **2010**, *70* (7), 393–399.

CHAPTER 6

A NOVEL BIOSENSOR FOR DIRECT ANTIBODY DETECTION BASED ON THE ANTIBODY-CATALYZED WATER OXIDATION PATHWAY

Abstract

Current clinical diagnosis of infectious diseases is performed using an Enzyme Linked Immunosorbent Assay (ELISA) that makes use of secondary reagents to detect primary antibodies captured from serum. These secondary reagents can cause limitations to the assay, such as false positives (due to non-specific binding), time-intensive incubation steps, species-dependence and increased cost. To overcome these limitations, we report a novel biosensor based on the antibody catalyzed water oxidation pathway (ACWOP) that directly detects captured primary antibodies by using their inherent catalytic activity. In this process, antibodies are used as catalysts in the reaction between singlet oxygen and water to generate hydrogen peroxide, which is then detected via colorimetric readout. Our sensor incorporates silica microparticles as an inexpensive substrate that is functionalized with rose bengal (photosensitizer), to generate singlet oxygen, and dinitrophenyl (antigen), to capture primary antibodies.

---

*Portions are adapted from Pranav Sundaram's master's thesis. This project was a collaboration between the groups of Prof. Brian Kirby and Prof. Christopher Ober.

We demonstrate specific capture of anti-DNP antibodies on our substrates followed by generation of an antibody-dependent colorimetric ACWOP signal. By eliminating the use of secondary reagents, we have developed a universal platform that detects antibodies in a species-independent manner with improved speed and inexpensive reagents, with the ultimate goal of transitioning to a point-of-care sensor that can be used for widespread monitoring of infectious diseases.

Introduction

Infectious diseases affect several hosts such as humans, livestock, pets and wildlife.[1] For example, the influenza virus resides in reservoir hosts, such as ducks, cranes and other wild birds, from which the pathogen then passes into transmission hosts, such as domestic poultry and bats and ultimately to spillover hosts such as humans, cows, cats and swine.[2,3] Infectious diseases spread rapidly and pose the threat of developing into epidemics that can cause large scale loss of lives.[4-6] Several key factors aid in the spread of infectious diseases: multiple species acting as transmission and spillover hosts, increased contact between humans and wildlife and other species, frequent travelling across nations and lack of global monitoring strategies.[7] Consequently it is important to develop novel sensitive tools that can achieve widespread monitoring of these diseases across several species in a timely manner.[8]

Currently, serology is the primary clinical tool used for detecting infectious pathogens in several hosts. In serology, antibodies that are developed as part of the host's immune response to the infection are detected in the patient's serum. These disease-specific antibodies have a unique function of binding to a specific molecule on the target

pathogen (i.e. the antigen), thus their presence in the patient's serum can indicate exposure to pathogen.

The Enzyme Linked Immunosorbent Assay or ELISA is the most commonly used in-vitro diagnostic test to detect antibody responses to infectious agents in the host. [9] In an ELISA, the host's serum is incubated in antigen-coated microwell plates. Antibodies specific to the coated antigen are captured from the patient's serum onto the plates through antigen-antibody binding.[10] These captured primary antibodies are then detected with secondary reagents. Based on the secondary reagent used, ELISAs are classified into two types: indirect ELISA and competitive ELISA. An indirect ELISA uses secondary antibodies that are tagged to an enzyme such as horseradish peroxidase (colorimetric detection) or a fluorophore (fluorometric detection). These secondary antibodies are species-specific, as they recognize the Fc fragment of the captured primary antibody. In contrast, a competitive ELISA, uses antibodies that compete with primary antibodies from serum for the antigen binding sites. These competitive antibodies are species-independent and are antigen-specific.

Use of secondary reagents present certain limitations: (a) non-specific binding of secondary reagents in the wells can lead to false positives and low sensitivity.[11], (b) additional incubation steps, which range from 2 hours at room temperature to overnight at 40˚C, are required for binding these secondary reagents, thereby increasing the total test time [10], (c) the use of secondary antibodies that are specific to the species being tested for prevents testing across several hosts with the same device [12] and (d) the use of secondary reagents increases the overall cost of the tests.[13]

To overcome these limitations, we eliminate use of secondary reagents by directly

detecting the captured primary antibodies using their intrinsic catalytic property. Wentworth *et. al.* showed that all antibodies, irrespective of antigenic specificity or source, can act as a catalyst in a specific reaction between singlet oxygen($^1O_2$) and water to form hydrogen peroxide (H_2O_2).[14] This process is termed the antibody-catalyzed water oxidation pathway, or ACWOP. They tested a panel of intact immunoglobulins and antibody fragments from a range of species, clones and isotypes and found this property to be conserved across all antibodies.[15]

We engineered a surface-based biosensor that uses porous silica microparticles as an inexpensive substrate for functionalizing cofactors required for the ACWOP and antigens required for capturing primary antibodies. The captured primary antibodies generate H_2O_2 via the ACWOP, which is detected and quantified using a colorimetric method. Our sensor successfully generates an antibody-dependent ACWOP signal with fewer incubation steps and cheaper reagents. Through the development of this universal platform, we demonstrate potential to transform our biosensor into a species-independent point-of-care device that can be used for rapid, cheap and sensitive monitoring of infectious diseases across a host of species.

Experimental Section

Materials

Hydrogen peroxide, Peroxidase from horseradish (HRP), 3,3′,5,5′-Tetramethylbenzidine (TMB), Hydrochloric acid, Toluene, N, N-Dimethylformamide, HATU, N,N-Diisopropylethylamine, DNP-ε-amino-n-caproic acid, 1,4-Dimethylpyridinium p-toluenesulfonate, DIC, TWEEN-20 and Citric Acid were

purchased from Millipore Sigma. Rose Bengal and porous silica gel were purchased from Alfa Aesar. 1x Dulbecco's Phosphate-Buffered Saline (DPBS), Methanol, Ethanol, L (+)-Ascorbic acid, Triethylamine, Sodium phosphate dibasic and Dimethyl sulfoxide were purchased from VWR International. 3-Aminopropyl (diethoxy) methylsilane was purchased from Gelest. Rose Bengal Disodium Salt was purchased from Fisher Scientific. Clear F-bottom 96-well microplate and Black F-bottom 96-well microplate were purchased from Greiner Bio-one. Normal Rat IgG, Azide free was purchased from R&D Biosystems, Goat anti-DNP IgG was purchased from Bethyl Laboratories and Donkey anti-goat IgG-Alexa Fluor 568 was purchased from ThermoFisher Scientific. Dinitrophenyl mouse IgG and Normal-mouse IgG were purchased from Santa Cruz Biotechnology.

TMB stock solution: Citrate Phosphate (CP Buffer, pH 5.0) was prepared by mixing 24.3mL of 0.1N citric acid, 25.7mL of 0.2N sodium phosphate and 50mL of DI water. TMB stock solution of 1.04mM was prepared by adding 5mg of TMB powder to 5mL DMSO and stirred gently until TMB dissolved. The prepared solution was then added to 15mL CP buffer.

Unless otherwise stated, all stock solutions were prepared by dilution or dissolution in 1x DPBS.

Instrumentation:

A Synergy H1 Hybrid plate reader from BioTek was used at default settings to measure absorbance intensity, absorbance spectra, and fluorescence intensity of samples. BioTek Gen5 data analysis software was used to analyze optical data collected from the plate reader. A Sorvall ST16 centrifuge from ThermoFisher Scientific fitted

with a swinging bucket rotor-Model: M20 for 96-well microplates and Model: TX-400 for Falcon tubes, was used to wash substrates. A Centrifuge 5424

from Eppendorf fitted with a fixed angle (45o) rotor - Model: FA-45-24-11 was used for microcentrifugation. A Select Series UV Crosslinker (XLE-1000A) from Spectroline was repurposed with four 12" green cold cathode tube lights from Logisys (CLK12GN2, brightness: 28000 to 30000 cd/m^2) to form a green-light illuminator. The green lights were controlled with an external HY3003 DC power supply at 12V and 1.25A with a toggle switch. The green light illuminates a region suitable for placing a 96-well microplate. A Vacuum filtration unit was designed by fitting vacuum tubing to an Erlenmeyer flask and attaching a 60 mL Pore-E buchner funnel.

Detection of singlet oxygen generated by photosensitization reaction in solution:

Rose Bengal was diluted in DPBS (pH 7.4, 100µL) to form the following concentrations: 6.25µM, 5µM, 4µM, 3.12µM, 2µM and 1.56µM and was added to wells 1-6 in Row A in a clear 96-well microplate. A negative control of DPBS (pH 7.4, 100 µL) was added to well 7 in Row A. Ascorbic Acid (100µL, 0.625mM stock) was added to all 7 wells. The plate was placed in the green-light illuminator and illuminated from above for 30 minutes. HRP (20µL, 0.171µM stock) and TMB (100µL, 1.04mM stock) were added to each well. The plate was covered with aluminum foil and incubated for 5 minutes. The absorbance intensity at 650nm was measured for each well in the plate reader. The above experiment was performed in triplicate and each data point is reported as the mean + S.E.M. The absorbance intensity at 650nm was converted to [H_2O_2] using the H_2O_2 standard curve.

Proof of concept ACWOP assay in solution - all reagents freely diffusing in solution:

Rat IgG, azide free, that was resuspended in DPBS (100μL, 20μM stock) was serially diluted in DPBS (pH 7.4, 100μL) with a dilution factor of 1/2 in 11 wells of a clear 96-well microplate. A well containing DPBS (pH 7.4, 100μL) was used as the negative control. RB (100μL, 0.01mM) was added to all 12 wells. The plate was placed in the green-light illuminator and illuminated from above for 30 minutes. HRP (20μL, 0.171μM stock) and TMB (100μL, 1.04mM stock) were added to each well. The plate was covered with aluminum foil and incubated for 5 minutes. The absorbance intensity at 650nm was measured for each well in a plate reader. The above experiment was performed in triplicate and each data point is reported as the mean + S.E.M. The absorbance intensity measured was converted to [H_2O_2] using the H_2O_2 standard curve.

Functionalization of Rose Bengal on silica microparticles:

Activation of Silica Microparticles:

12g of silica microparticles were mixed with 100 mL of 10% HCl (10 mL HCl to 90 mL water) and refluxed with continuous stirring for 24 hours at 110˚C. After 24 hours, the silica microparticles were collected by filtration and decantation, washed with pure water until the pH of the water was neutral, and dried at 60˚C for 24 hrs.

APDMES Conjugation on Silica Microparticles:

The dried particles (11g) were then added to a 300 mL round-bottom flask along with 100 mL of anhydrous toluene, 4.5mL of APDMES, and 2.5mL of triethylamine. This mixture was refluxed at 110˚C for 24 hours. Subsequently, the mixture was left to cool to room temperature and particles were collected by filtration. The silica microparticles were washed with methanol and ethanol 5 times each. The APDMES-silica microparticles were then dried in an oven for 24 hours.

Rose Bengal Conjugation on APDMES-Silica Microparticles:

The concentration of Rose Bengal used was 2 mM (Rose Bengal: 1 equivalent, HATU: 1 equivalent, DIPEA: 2 equivalents). APDMES-silica microparticles (2 g) was added to a 100 mL round-bottom flask along with 30 mL of amine-free anhydrous DMF and a stir bar. Rose Bengal sodium salt (61.06 mg), HATU (22.82 mg) (coupling agent) and N, N-Diisopropylethylamine (21μL) (DIPEA base) was added to the mixture and stirred manually for about 1 minute. This solution was stirred for 24 hours at room temperature, collected via filtration, and washed in a cycle with methanol, ethanol, and DPBS buffer solution until mother liquor was colorless.

Detection of singlet oxygen generated by photosensitization reaction on a surface: Detection with Ascorbic Acid:

RB-functionalized silica microparticles (RB-silica) were suspended in DPBS (pH 7.4) to obtain a concentration of 15 mg RB-silica per 100 μL of suspension. The same was done for APDMES-silica microparticles for the negative control. RB-silica suspension (100 μL, 15 mg per 100 μL of suspension) and APDMES-silica suspension (100 μL, 15 mg per 100 μL of suspension) was added wells in a clear 96-well microplate. Ascorbic acid (100 μL, 78 μM stock) was added to both wells. The plate was placed in the green-light illuminator and illuminated from the top for 30 minutes. 150 μL of the supernatant from each well was collected in individual microcentrifuge tubes. The tubes were centrifuged in a microcentrifuge at 18000xg for 5 minutes. 100 μL of the supernatant from the microcentrifuge tubes were then transferred to a new clear 96-well microplate. An absorption spectrum was performed for both wells to ensure that there was no freely diffusing RB in solution. HRP (20 μL, 0.171 μM stock) and TMB (100 μL, 1.04 mM

stock) were then added to each well. The plate was covered with aluminum foil and incubated for 5 minutes. The absorbance intensity at 650 nm was measured for each well. The above experiment was performed in triplicate and each data point is reported as the mean + S.E.M. The absorbance intensity at 650 nm was converted to [H_2O_2] using the H_2O_2 standard curve.

Detection with freely diffusing IgG:

RB-functionalized silica microparticles (RB-silica) was suspended in DPBS (pH 7.4) to obtain a concentration of 15mg RB-silica per 100μL of suspension. Rat IgG, azide free, resuspended in DPBS (100 μL, 15.87 μM stock) was serially diluted in DPBS (pH 7.4, 100 μL) with a dilution factor of 1/2 in 10 wells of a clear 96-well microplate. A well containing DPBS (pH 7.4, 100 μL) was used as the negative control. The remaining procedure was the same as described in detection with ascorbic acid above.

Functionalization of Dinitrophenyl on silica microparticles:

APDMES-silica microparticles (0.3 g) were added to a 50mL round-bottom flask equipped with a stir bar along with 10mL of amine-free anhydrous DMF. Then, 18.75 mg of DNP, 93.75 mg of 1,4-Dimethylpyridinium p-toluenesulfonate (DPTS), and 62.5 μL of N, N′-Diisopropylcarbodiimide (DIC) were added to the flask with the particles. This solution was stirred at 32˚C for 24 hours. The particles were then washed with ethanol and methanol using several centrifugation steps until the supernatant was clear. The washed particles were dried in the oven at 60˚C for two hours.

Capture of primary anti-DNP IgG on DNP functionalized silica microparticles - Readout with fluorophore-tagged secondary antibodies:

DNP-functionalized silica microparticles (DNP-silica) were suspended in DPBS (pH

7.4) to obtain a concentration of 30mg DNP-silica per 100 μL of suspension. Goat anti-DNP IgG (100 μL, 6.67 μM stock) was serially diluted in DPBS (pH 7.4, 100 μL) with a dilution factor of 1/2 in 11 wells of a clear 96-well microplate. A well containing DPBS (pH 7.4, 100 μL) was used as the negative control. DNP-silica suspension (100 μL, 30 mg per 100 μL of suspension) was added to all 12 wells. The plate was covered with aluminum foil and incubated for 4 hours at room temperature (25˚C). Wash buffer (200 μL, 0.05% (v/v) Tween-20 in DI) was added to each well. The plate was centrifuged at 3000xg for 3 minutes and the resulting supernatant was aspirated. The wash protocol described was performed 3 times. AlexaFluor 568 donkey anti-goat IgG (100 μL, 0.01 μM) was added to all 12 wells. The plate was covered with aluminum foil and incubated for 2 hours at room temperature (25˚C). The wash protocol described was performed 3 times. DPBS (100 μL, pH 7.4) was added to each well and all of the contents of each well were transferred to a black 96-well microplate. The fluorescence intensity (Ex: 568nm, Em: 603nm) was measured for each well using a plate reader. The above experiment was performed in duplicate and each data point is reported as the mean + S.E.M.

Demonstration of a surface-based antibody sensor that directly detects captured primary antibodies via the ACWOP:

ACWOP readout of captured primary anti-DNP antibodies:

DNP-functionalized silica microparticles (DNP-silica) were suspended in DPBS (pH 7.4) to obtain a concentration of 15 mg DNP-silica per 100 μL of suspension. RB functionalized silica microparticles (RB-silica) was suspended in DPBS (pH 7.4) to obtain a concentration of 15 mg RB-silica per 100μL of suspension. Mouse anti-DNP

IgG (100 μL, 1.33 μM stock) was serially diluted in DPBS (pH 7.4, 100 μL) with a dilution factor of 1/2 in 7 wells of a clear 96-well microplate. A well containing DPBS (pH 7.4, 100 μL) was used as the negative control. DNP-silica suspension (100 μL, 15 mg per 100 μL of suspension) was added to all 8 wells. The plate was covered with aluminum foil and incubated for 4 hours at room temperature (25˚C). Wash buffer (200μL, 0.05% (v/v) Tween-20 in DI) was added to each well. The plate was centrifuged at 3000xg for 3 minutes and the resulting supernatant was aspirated. The wash protocol described was performed 3 times. RB-silica suspension (100 μL, 15 mg per 100 μL of suspension) was added to all 8 wells. The plate was placed in the green-light illuminator and illuminated from the bottom for 45 minutes. The supernatant (150 μL) from each well was collected in individual microcentrifuge tubes. The tubes were centrifuged in a microcentrifuge at 18000xg for 5 minutes. 50 μL of the supernatant from the tubes were then transferred to a new clear 96-well microplate. An absorption spectrum was performed for all 8 wells using a plate reader to ensure there was no freely diffusing RB in solution. HRP (20 μL, 0.171 μM stock) and TMB (100 μL, 1.04 mM stock) were then added to each well. The plate was covered with aluminum foil and incubated for 5 minutes. The absorbance intensity at 650 nm was measured for each well in a plate reader.

ACWOP readout of captured primary control antibodies:

N-Mouse IgG (100 μL, 2.67 μM stock) was serially diluted in DPBS (pH 7.4, 100 μL) with a dilution factor of 1/2 in 6 wells of a clear 96-well microplate. Same procedure as *ACWOP readout of captured primary anti-DNP antibody* section above was followed and instead of Mouse anti-DNP IgG, a control antibody was used to determine non-

specific binding of IgG to silica microparticles.

Results and Discussion

The key components of our ACWOP biosensor include silica microparticles used as an inexpensive substrate to conjugate antigens and ACWOP cofactors, $^1O_2$ (reactant) generation on a surface and an optimized colorimetric detection system to detect the H_2O_2 generated via antibody catalysis.

We used a TMB-HRP based colorimetric detection system to detect the H_2O_2 that is generated in the ACWOP process. Upon oxidation by stock H_2O_2, TMB changes from colorless to blue in the presence of an enzyme HRP.[18] This change in color was detected and quantified by measuring the absorbance at 650 nm using absorbance spectroscopy with a plate reader. The colorimetric detection signal was expressed as the Absorbance intensity or OD at 650 nm/Path Length, with a linear trend against H_2O_2 concentration. We optimized the detection system for HRP and TMB to obtain a final H_2O_2 standard curve. Our system developed a colorimetric detection signal of H_2O_2 within 5 minutes, not shown previously in literature, with a sensitivity of 0.078 μM (data in Appendix B.1). We obtained a relationship between the measured colorimetric intensity signal and H_2O_2 concentration, which was used for conversion in all further experiments.

Singlet oxygen, the excited state of molecular oxygen, is a key reactant in the ACWOP reaction and was generated via a photosensitization reaction.[19] The process

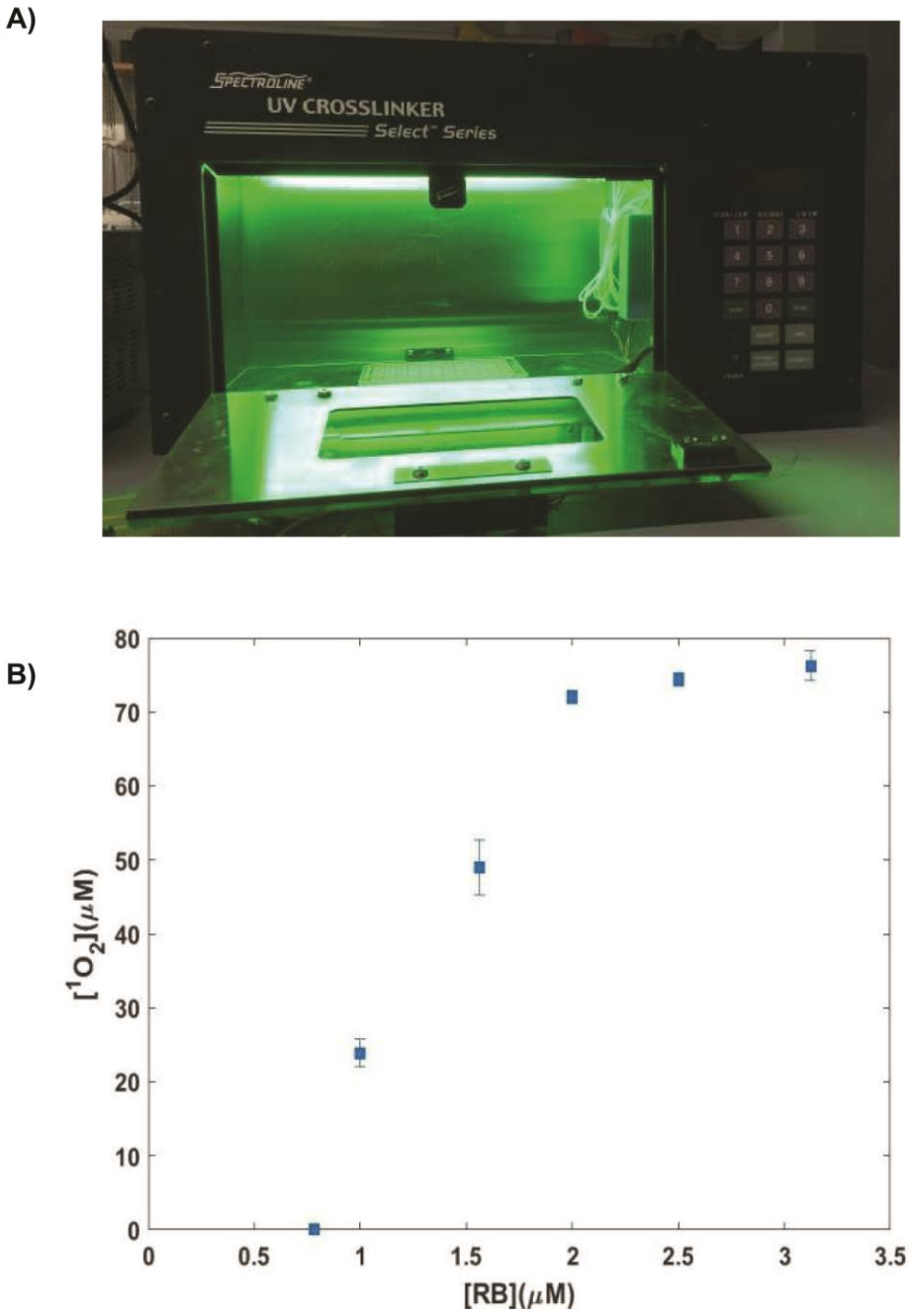

Figure 1. $^1O_2$ generation via photosensitization of RB in solution followed by detection using an optimized ascorbic acid system (**a**) Green-light illuminator fit with 4 cold cathode green tubes light and operated via an external DC power source. The illuminator provides a constant and uniform source of green light from the top (**b**) Generation of $^1O_2$ as a function of [RB] in solution. There is a linear increase in singlet oxygen generation with [RB] until 2μM beyond where the curve saturates as AA acts as the limiting reagent.

requires oxygen, light of a suitable wavelength and a photosensitizer that can absorb that light and excite triplet oxygen to its singlet state. We used the xanthene dye, rose bengal (RB) as the photosensitizer primarily for three reasons: (a) it has a high quantum yield of 0.76, (b) it is soluble and can be used to photosensitize in DPBS and (c) it is inexpensive.[19] RB has an absorption maximum at 550 nm (Fig. S1), (i.e. green light), so we designed an illuminator system (Fig. 1A) to provide a constant and uniform source of green light.

Although the final readout uses ACWOP, to initially quantify the $^1O_2$ generated by photosensitization of RB with green light, we used an ascorbic acid detection system. Ascorbic acid (AA) reacts with $^1O_2$ in a 1:1 mole ratio to generate H_2O_2 at a pH of 7.4.[20] The generated H_2O_2 was detected with our optimized TMB-HRP colorimetric detection system. AA dissolved in 1x DPBS (10mM phosphate/160 mM sodium chloride, pH 7.4) showed a decrease in pH below 7.4 for [AA] > 10 mM (Fig. S2). For [AA] < 10mM, the generation of $^1O_2$ as a function of [AA] showed an ascorbate dependent detection signal. There existed an optimal [AA] for both RB freely diffusing in solution and RB functionalized on silica microparticles (Fig. S3, S4). Detection of $^1O_2$ generated due to photosensitization reactions in solution, using the optimum [AA], showed a linear increase in $^1O_2$ generated with [RB] (Fig. 1B). A minimum of [RB] = 0.78 μM was required to generate detectable $^1O_2$ in solution for the given conditions. We developed an ACWOP proof-of-concept assay to confirm that our system can detect non-specific, freely diffusing antibodies in solution via ACWOP.

We chose 10μM as the concentration of RB for this assay, as Fig 1b showed that $^1O_2$ generation saturates for [RB]>2μM. Similarly, for that concentration of RB, the limit of

detection (LOD) of the generated H_2O_2 in solution is the lowest (Appendix B.2). Sodium azide, commonly used as a preservative, is known to be an inhibitor of $^1O_2$, so azide-free rat IgG was used.[21] The system, consisting of RB and IgG in solution, was placed in the green illuminator to generate $^1O_2$ followed by IgG catalysis via ACWOP to generate H_2O_2 (Fig. 2A). The H_2O_2 was detected colorimetrically and we obtained a reproducible non-linear antibody-dependent signal (Fig. 2B). Our result verifies proof-of-concept experiments that were performed by Wentworth et. al. using horse IgG and fluorescent detection, wherein they obtained a similar non-linear signal. They hypothesized that the curvature is due to the reduced lifetime of $^1O_2$ in solution due to reaction with the antibody.[15] This demonstration provides the basis for developing a biosensor that can detect antibodies based on the colorimetric H_2O_2 detection signal output produced due to ACWOP.

To develop a surface-based ACWOP biosensor that captures primary antibodies and detects them directly, we selected porous silica microparticles as the substrate for functionalizing the photosensitizer and the antigen. We have previously worked with silica surfaces and Welch *et. al.* demonstrated an electrochemical ACWOP biosensor using POEGMA brushes functionalized on silicon wafers.[22,23] APDMES was conjugated to activated-porous silica surfaces via a silanization reaction at elevated temperatures by modifying the protocol used by Wu et.al.[24] RB was functionalized to the APDMES-silica substrates via an amidation reaction between the carboxylic acid group of the dye and the amine groups on the substrate (Fig. 3A).[25]

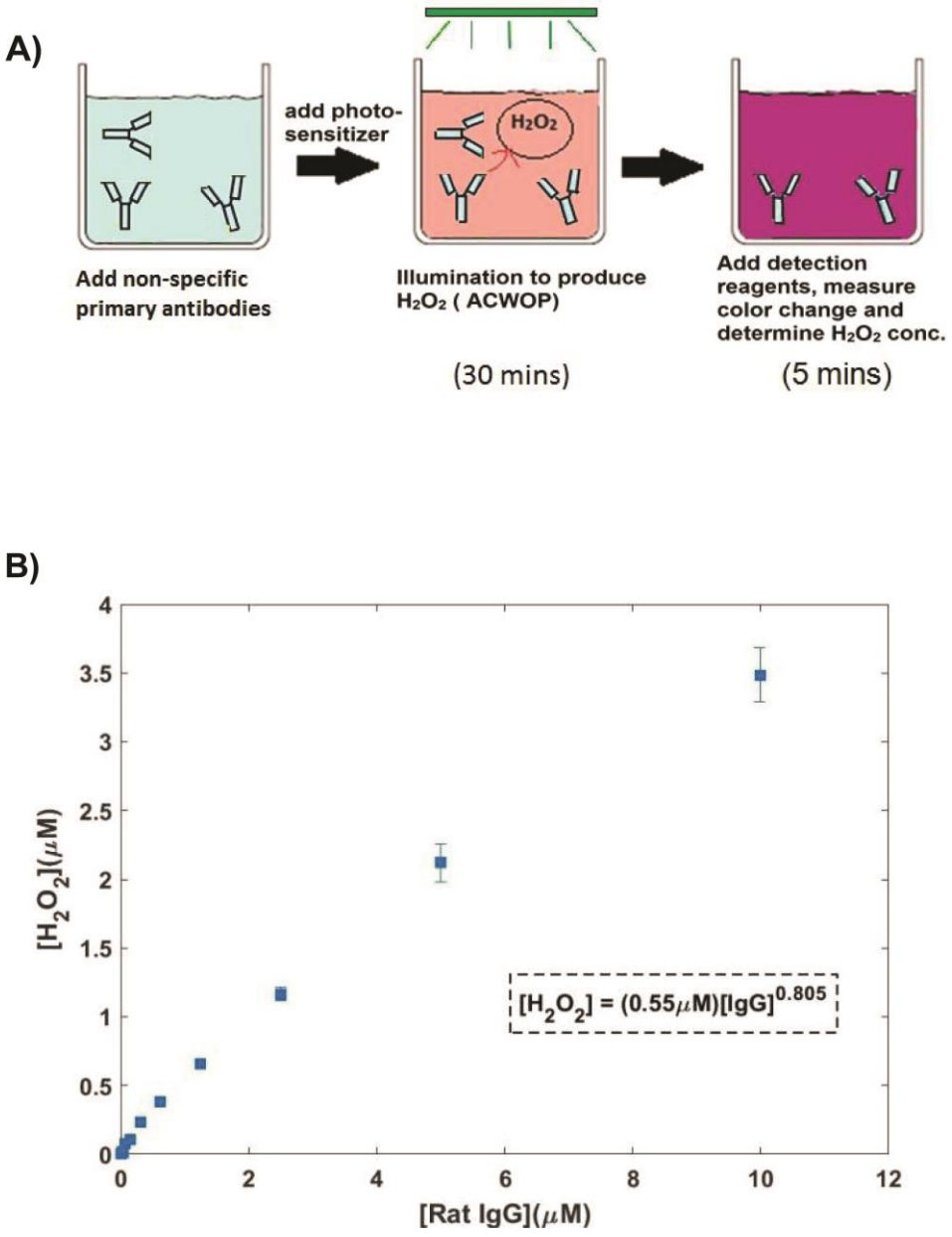

Figure 2. Demonstration of a proof-of-concept ACWOP assay that detects non-specific antibodies in solution. All reagents are freely diffusing in solution. (**a**) Process involved in developing a proof-of-concept assay. Non-specific rat IgG and RB were added to a well, illuminated with green light for 30mins to perform and the generate H_2O_2 was detected via a colorimetric readout (**b**) H_2O_2 generated via ACWOP as a function of non-specific rat IgG freely diffusing in solution. Obtained a repeatable antibody-dependent H_2O_2 generation.

The absorption spectrum of RB-silica (100μL, 15mg in DPBS) gave a sharp peak at 550nm, the absorption maximum of RB, thereby confirming successful functionalization (Fig. 3B).

RB-silica particles (15 mg) have a total outer surface area of 1.14×10^{-3} that can theoretically bind 2.3×10^{-9} moles of RB (Appendix C.1). This is roughly the same amount of RB that was in solution in the proof-of-concept assay. Hereafter, 15mg of RB-silica particles were illuminated with green light to generate $^1O_2$ on a surface that was detected with ascorbic acid in solution (Fig. 4A). Comparison of photosensitization reactions on a surface with the reactions in solution showed a 100-fold higher efficiency of $^1O_2$ generation by RB freely diffusing in solution (Appendix D). These findings agree with Schaap *et al.* when they compared the efficiency of $^1O_2$ production of free rose bengal with rose bengal immobilized on Merrifield polymer and found a 100-fold higher production rate of $^1O_2$ from the free photosensitizer.[26] To further confirm the generation of $^1O_2$ from the RB-silica substrate, we used freely diffusing azide-free rat IgG in solution to catalyze the reaction between the generated $^1O_2$ and water to produce H_2O_2. We obtained repeatable antibody-dependent H_2O_2 generation, thereby validating the RB-silica microparticles as reliable sources of $^1O_2$ (Fig. 4B).

DNP was utilized as a model antigen that is bound by anti-DNP antibodies from several species and classes for initial development of our ACWOP biosensor.[22] DNP ε-amino n-caproic acid was functionalized to the APDMES-silica microparticles in a manner similar to that for RB. An amidation reaction occurs between the carboxylic acid group of DNP and the free amine on the APDMES-silica microparticles.

We confirmed the capture of anti-DNP primary IgG on DNP-silica microparticles

using secondary fluorophore-tagged antibodies. 30mg of DNP-silica microparticles were used as that provided 71 times more surface area than the bottom of a well in an ELISA plate, thereby providing more binding sites for antibody capture (Appendix C.2). The process involved incubation of the DNP-silica microparticles with primary goat anti-DNP IgG, incubation with secondary donkey anti-goat IgG and fluorescence intensity measurement with a plate reader (Fig. 5A). We observed an increase in the fluorescence readout from the secondary antibody with increasing primary antibody concentration used for incubation (Fig. 5B). This confirms primary-antibody concentration dependent capture on DNP-silica particles that saturates at higher IgG concentrations possibly due to limited number of binding sites.

The generation of ACWOP signal from the surface-based biosensor involved the following process: (a) capture of primary antibodies on DNP-silica microparticles, (b) generation of $^1O_2$ from RB-silica microparticles and (c) antibody catalysis to generate H2O2 that is detected colorimetrically (Fig. 6A). DNP-silica microparticles were incubated with mouse anti-DNP IgG using the validated protocol used previously. Because the lifetime of $^1O_2$ in aqueous solutions is in the range of 1-10 μs, which

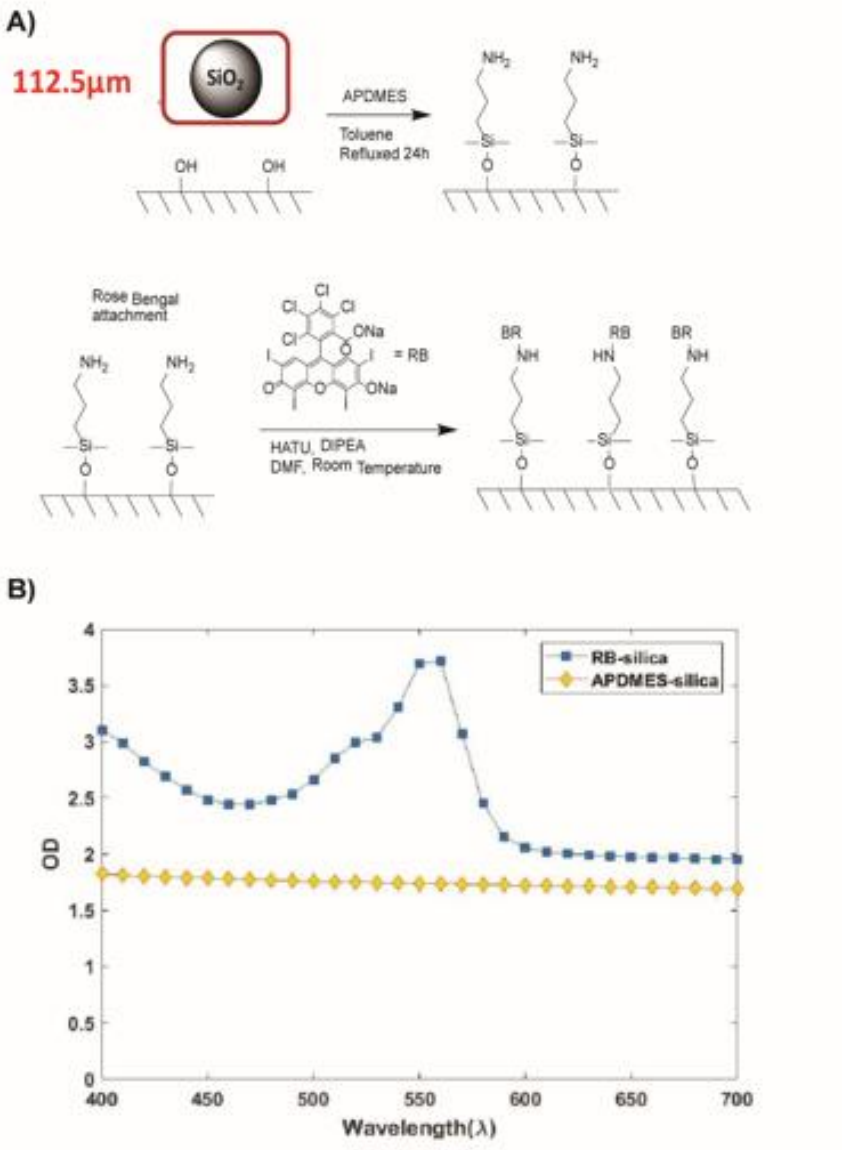

Figure 3. Functionalization of porous silica microparticles with RB (**a**) Chemistry and the process involved in functionalizing 112.5µM porous silica microparticles with RB. Activated silica microparticles are treated with APDMES via a silanization reaction to form APDMES-silica (top). RB is functionalized to APDMES-silica via an amidation reaction to form RB-silica (bottom) (**b**) Confirmation of the presence of RB on RB-silica microparticles using an absorption spectrum. RB-silica shows a peak at 550nm in its absorption spectrum (blue) when compared to APDMES-silica (yellow) confirming successful conjugation of RB.

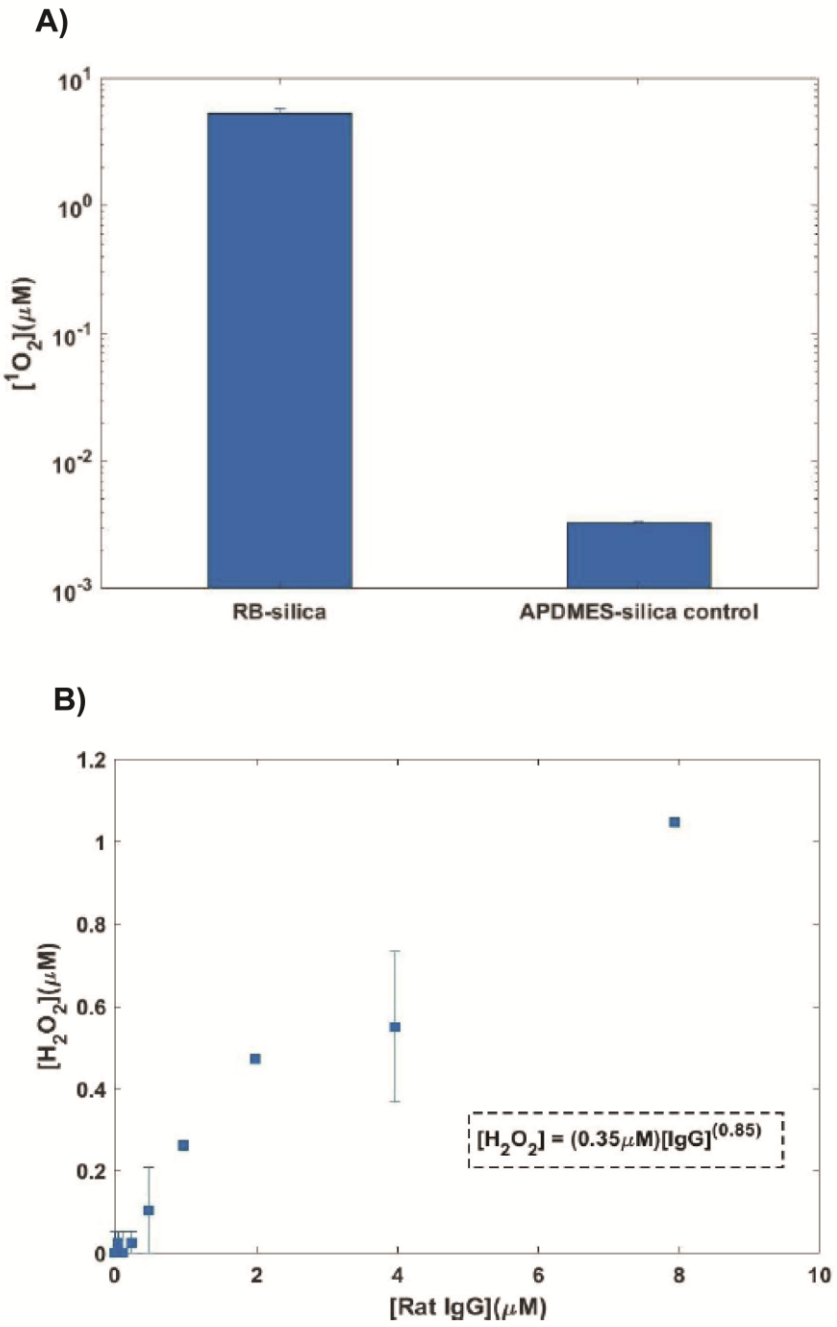

Figure 4. $^1O_2$ generation via photosensitization of RB on a surface followed by detection using two different methods (**a**) Ascorbic acid detection. 15mg of RB-silica microparticles generated $^1O_2$ on illumination with green light. APDMES-silica microparticles (control) that have no RB functionalized to the surface produced no $^1O_2$ (**b**) Freely diffusing non-specific antibodies in solution via ACWOP. $^1O_2$ generated by 15mg RB-silica microparticles reacted with water in the presence of rat IgG to generate H_2O_2. Obtained a repeatable antibody-dependent signal confirming generation of $^1O_2$ from RB surfaces.

corresponds to a mean square diffusion distance of less than 0.5μm (diffusion coefficient of O_2: 2 x 10^{-5} cm^2/sec), the DNP-silica and RB-silica microparticles were mixed well together to ensure close proximity of the $^1O_2$ to the antibody.[27] The system was illuminated with green light to generate $^1O_2$ that reacted with water in the presence of the captured antibodies to produce H_2O_2. We obtained a captured primary antibody-dependent H_2O_2 production (Fig. 6B). A negative control of normal-mouse IgG was performed using the same protocol to determine non-specific binding of IgG to silica surfaces. On comparison the H_2O_2 generation from the specific DNP-captured antibody was higher than the control. The curve for the ACWOP readout of primary anti-DNP antibodies exhibits a curvature with decreasing slope at higher concentrations of IgG, either because of saturation of primary antibody binding sites as seen in the previous section or because of the short lifetime of $^1O_2$ due to consumption as postulated by Wentworth in the proof of concept assay.[15]

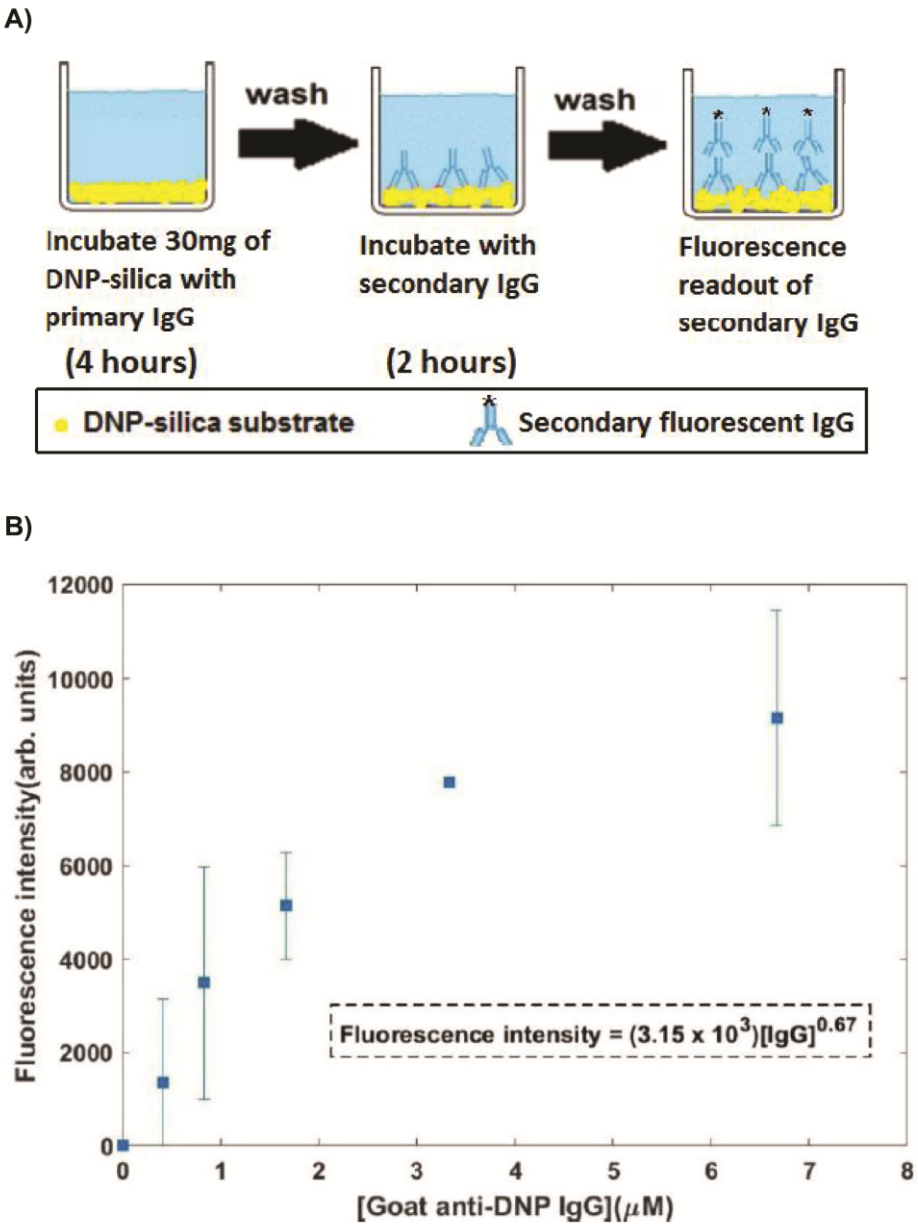

Figure 5. Confirmation of capture of primary anti-DNP antibodies on DNP-silica microparticles using fluorophore-tagged secondary antibodies (**a**) Process involved in developing a secondary readout from captured primary antibodies. Primary antibody: goat anti-DNP IgG, secondary antibody: AlexaFluor 568 donkey anti-goat IgG. (**b**) Fluorescence readout from secondary antibody bound to captured primary antibodies on DNP-silica. Obtained a repeatable primary-antibody dependent signal confirming successful capture.

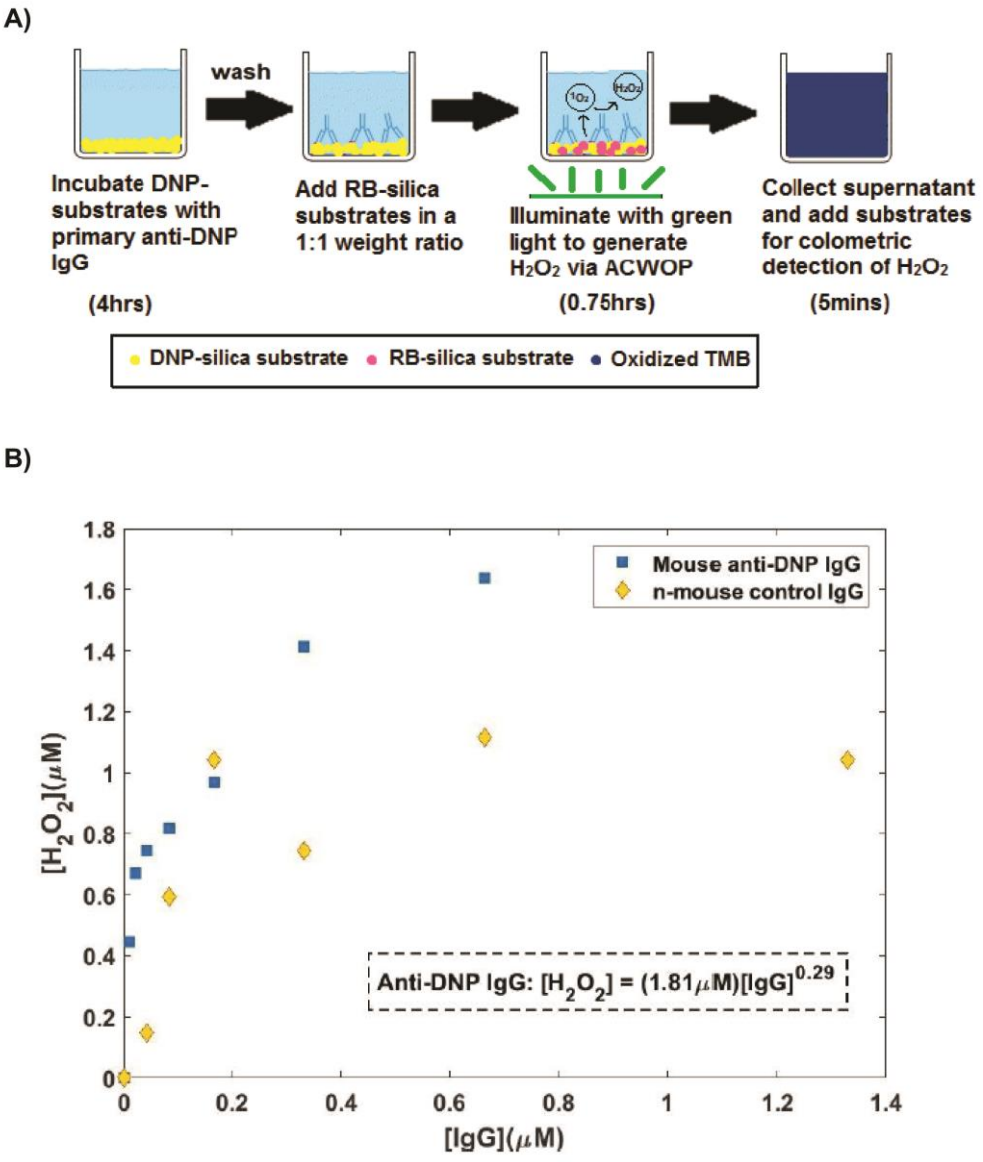

Figure 6. Demonstration of a novel surface-based ACWOP biosensor that can directly detect captured primary antibodies and generate a colorimetric readout (**a**) Process involved in capture and detection of anti-DNP primary antibodies using the ACWOP biosensor. Mouse anti-DNP IgG were captured on DNP-silica. $^1O_2$ generated by RB-silica reacts with water in presence of captured antibodies to generate H_2O_2 which is detected via a colorimetric readout (**b**) Obtained a primary antibody-dependent H_2O_2 generation (blue). A negative control with n-mouse IgG showed non-specific binding of IgG to silica substrates (yellow). The non-specific capture (yellow) occurred to a lesser extent than the specific DNP capture (blue).

Conclusions

In summary, we developed a silica-microparticle based biosensor that directly detects captured primary antibodies via the ACWOP and generates an antibody-dependent colorimetric signal. By eliminating the use of secondary antibodies that are specific to a given species, our ACWOP biosensor is capable of directly detecting antibodies from any species. The sensor improves testing time by eliminating the 2-hour incubation step required for binding secondary reagents in traditional ELISA kits. We have used relatively inexpensive substrates and reagents, which, coupled with the elimination of expensive, specially prepared secondary reagents, our sensor is more cost effective. The surface-based sensor provides a universal platform for direct antibody detection via a species-independent method. Future studies involve modification of this platform into a lateral flow test format for point-of-care monitoring of infectious diseases in multiple hosts via ACWOP.

ACKNOWLEDGEMENTS

The authors would like to thank the National Science Foundation grant for support of this work. This work made use of the Cornell Center for Materials Research Shared Facilities which are supported through the NSF MRSEC program (DMR-1719875). Experiments were conducted in Prof. Brian Kirby's and Prof. Christopher Ober's groups. Contributing members include Pranav Sundaram who tested my material and ran all the colorimetric detection experiments, Andrew Sanchez who used my surfaces and ran the fluorometric experiments, and Wei-Liang Chen who was able to cut my samples using the dicing blade at the Cornell Nanoscale Facility.

REFERENCES

1. Bean et. al.; Studying immunity to zoonotic diseases in the natural host - keeping it real; Nat Rev Immunol.; 2013 Dec; 13(12):851-61. doi: 10.1038/nri35.

2. Russell CJ et al.; Influenza Hemagglutinin Protein Stability, Activation, and Pandemic Risk.; Trends Microbiol.; 2018 Apr 19.; pii: S0966-842X(18)30068-4. doi: 10.1016/j.tim.2018.03.005.

3. Potter, C. W.; A history of influenza.; J. Appl. Microbiol.; 2001; 91, 572.

4. Sturm-Ramirez, K. M. et.al.; Reemerging H5N1 influenza viruses in Hong Kong in 2002 are highly pathogenic to ducks.; J. Virol.; 2004; 78, 4892.

5. Dye C.; After 2015: infectious diseases in a new era of health and development.; Philosophical Transactions of the Royal Society B: Biological Sciences.; 2014; 369(1645):20130426. doi:10.1098/rstb.2013.0426.

6. Simonds, Anita K.; Influenza News from the Frontline: What's Happening? ERJ Open Research 4.1; 2018; 00020–2018. PMC. Web. 5 June 2018.

7. Lashley et. al.; Factors Contributing to the Occurrence of Emerging Infectious Diseases; Biological Research for Nursing, Vol 4, Issue 4, pp. 258 – 267.

8. Velumani, S.; Ho, H.-T.; He, F.; Musthaq, S.; Prabakaran, M.; Kwang, J.; PLoS One 2011, 6, e20737.

9. Washington JA.; Principles of Diagnosis. In: Baron S, editor.; Medical Microbiology. 4th edition. Galveston (TX): University of Texas Medical Branch at Galveston; 1996. Chapter 10.

10. Yolken RH.; Enzyme-linked immunosorbent assay (ELISA): a practical tool for rapid diagnosis of viruses and other infectious agents.; The Yale Journal of Biology and

Medicine.; 1980; 53(1):85-92.

11. Stricker RB, Johnson L.; Let's tackle the testing; BMJ : British Medical Journal.; 2007; 335(7628):1008.

12. Manning, Colleen F., Angeliki M. Bundros, and James S. Trimmer.; Benefits and Pitfalls of Secondary Antibodies: Why Choosing the Right Secondary Is of Primary Importance.; Ed. Joy Sturtevant.; PLoS ONE 7.6 (2012): e38313. PMC. Web. 5 June 2018.

13. Voskuil J.; Commercial antibodies and their validation; Version 1.; F1000Res.; 2014; 3: 232.

14. Wentworth, P.; Jones, L. H.; Wentworth, A. D.; Zhu, X. Y.; Larsen, N. A.; Wilson, I. A.; Xu, X.; Goddard, W. A.; Janda, K. D.; Eschenmoser, A.; Lerner, R. A.; Science; 2001; 293, 1806.

15. Wentworth A D, Jones L H, Wentworth P, Janda K D, Lerner R A(2000); Proc Natl Acad Sci USA; 97:10930–10935. pmid:11005865.

16. Zhu, X. Y.; Wentworth, P.; Wentworth, A. D.; Eschenmoser, A.; Lerner, R. A.; Wilson, I. A.; Proc. Natl. Acad. Sci. U.S.A.; 2004; 101,2247.

17. Datta, D.; Vaidehi, N.; Xu, X.; Goddard, W. A.; Proc. Natl. Acad. Sci.; U.S.A.; 2002; 99 (5) 2636– 2641.

18. Josephy PD, et. al.; The horseradish peroxidase-catalyzed oxidation of 3,5,3',5'-tetramethylbenzidine. Free radical and charge-transfer complex intermediates.; J Biol Chem.; 1982 Apr 10; 257(7):3669-75.

19. M.C. DeRosa, R.J. Crutchley; Photosensitized singlet oxygen and its applications; Coordination Chemistry Reviews; 233/234 (2002) 351/371.

20. Kramarenko GG, Hummel SG, Martin SM, Buettner GR; Ascorbate Reacts with Singlet Oxygen to Produce Hydrogen Peroxide; Photochem Photobiol.; 2006; 82(6): 1634–1637.doi: 10.1562/2006-01-12-RN-774.

21. Bancirova, M. (2011); Sodium azide as a specific quencher of singlet oxygen during chemiluminescent detection by luminol and Cypridina luciferin analogues.; Luminescence; 26: 685-688. doi:10.1002/bio.1296.

22. M. Elizabeth Welch, Nicole L. Ritzert, Hongjun Chen, Norah L. Smith, Michele E. Tague, Youyong Xu, Barbara A. Baird, Héctor D. Abruña, and Christopher K. Ober; Journal of the American Chemical Society; 2014; 136 (5), 1879-1883. DOI: 10.1021/ja409598c.

23. Wei-Liang Chen, Roselynn Cordero, Hai Tran, and Christopher K. Ober; Macromolecules; 2017; 50 (11), 4089-4113. DOI: 10.1021/acs.macromol.7b00450

24. Wu N. et. al.; A novel surface molecularly imprinted polymer as the solid-phase extraction adsorbent for the selective determination of ampicillin sodium in milk and blood samples; J Pharm Anal.; 2016 Jun; 6(3):157-164. doi: 10.1016/j.jpha.2016.01.004.

25. Guo, Yanyan, Snezna Rogelj, and Peng Zhang.; Rose Bengal-Decorated Silica Nanoparticles as Photosensitizers for Inactivation of Gram-Positive Bacteria.; Nanotechnology 21.6 (2010): 065102. PMC. Web. 5 June 2018.

26. Schaap, A. P., A. L. Thayer, G. L. Faler, K. Coda and T. Kimura (1974) J. Am. Chem. Soc. 96, 4025-6.

27. Merkel, P. B.; Kearns, D. R.; Nilsson, R.; Deuterium effects on singlet oxygen lifetimes in solutions. New test of singlet oxygen reactions; J. Am. Chem. Soc.; 1972; 94, 1030.

CHAPTER 7
FUTURE DIRECTION

Mini ME Emulsion Polymerization of Free Polymer

Iron-Mediated Mini ME Emulsion Polymerization

Atom transfer radical polymerization (ATRP) is one of the most well-known forms of controlled/living radical polymerizations generating well-defined polymers with precise molecular weight and high end-group functionality.[1] The key to ATRP is the reversible redox equilibrium between activator and deactivator, maintaining low concentration of radicals suppressing side reactions.[1,2] However, a significant factor limiting the widespread industrial use of ATRP is copper contamination. Largely, the focus within the ATRP field in recent years has been directed toward lower catalyst loadings, such as those in ARGET ATRP. Nonetheless, even trace amounts of copper is problematic for microelectronics as it acts as a conductor, and in biological applications due to its toxicity.[3,4]

Although mini ME emulsion polymerization utilizes ARGET ATRP [5,6], it would still not be a viable method for industry as the presence of any amount of copper within the polymerization is undesirable. As an alternate ATRP method, Iron-mediated ATRP polymerizations has recently been studied in aqueous media and would be a good alternative to copper-mediated ATRP as iron (Fe) is widely available, has low toxicity, and has good biocompatibility.[7]

In their work, Bian *et. al.* used photoinduced Fe-mediated ATRP in aqueous media for the well-controlled polymerizations of $PEGMA_{500}$ and $PEGA_{480}$ using $FeBr_3$ as the catalyst and triphenylphosphine-3,3',3''-trisulfonic acid trisodium (TPPSA) as

the ATRP ligand achieving polymers with Đ < 1.4.[7] Inspired by their work, we briefly conducted preliminary experiments using Fe-mediated mini ME emulsion polymerization. The results are summarized in Table 1.

Two concentrations of TBAB were utilized (100 mM and 50 mM) and compared to the control experiment where no TBAB was added. Although a low temperature (30˚C) was used for the mini ME emulsion polymerization of PMMA with copper as the catalyst, the temperature needed to be increased to 80˚C over a 20-hour period as the rate of polymerization (R_p) of Fe-mediated ATRP is much slower than the R_p in ATRP with Cu. The ligand that was used was tris[2-(2-methoxyethoxy) ethyl] amine (TDA) and TBAB was employed as the phase transfer agent; however, TBAB has also been known to serve as an ATRP ligand for Fe-mediated polymerizations.

At 100 mM TBAB, the polymerization reached full conversion, but the polymer dispersity was high (Đ = 1.96), thus the polymerization was still poorly controlled. As [TBAB] was decreased, the molecular weight and dispersity decreased as well (M_n= 13,060 g/mol, Đ = 1.41). The controlled experiment excluding TBAB from the polymerization continued to lower the molecular weight of PMMA (M_n= 7,896 g/mol), but the dispersity increased from Đ = 1.41 at 50 mM TBAB to Đ = 1.74 with no TBAB. This indicated that a small amount of TBAB is still required in the polymerization for shuttling of the catalyst. Too much TBAB causes a poorly controlled polymerization because TBAB can also be used as a ligand, therefore, it may well be competing with TDA causing an imbalance of radicals in solution. In the future, a systematic study

[TBAB] (mM)	**M_n (g/mol)**	**Đ**
100	88,314	1.96
50	13,060	1.41
None	7,896	1.74

Table 1. Iron-mediated mini ME emulsion polymerization of PMMA. $[M]_\circ$= 500 mM, [I]= 1 mM, [TDA]= 3 mM, [ascorbic acid] = 2 mM. All polymerizations were conducted at 80˚C for 20 hours.

must be performed to obtain the optimal amount of ligand: Fe ratio and TBAB: ligand ratio.

Metal-Free ATRP Mini ME Emulsion Polymerization

An alternate ATRP technique that eliminates the use of any metal was developed by Hawker *et. al.* with a photomediated process using an organic-based catalyst, such as 10-phenylphenothiazine (PTH). The photoexcited PTH* reduces alkyl bromide chain end to generate a propagating radical and a corresponding PTH radical cation which subsequently can deactivate the propagating chain to regenerate a ground state PTH and a dormant polymer chain end allowing controlled polymerizations of methyl methacrylate under 380 nm light (Scheme 1). [8] A broad range of monomers from methacrylate, acrylate to styrene can be polymerized with this catalyst. The polymerization could be switched on/off by light. They found that the conversion increased under exposure of light and stopped after the removal of light. The conversion went up again after re-exposure to light. High chain end functionality like traditional ATRP was observed for the PTH mediated, metal free system, indicating by the formation of a diblock copolymer. [8]

Combining this method with mini ME emulsion polymerization could have vital implications to the large-scale industrial use of this technique. Because this method would allow ATRP to be conducted without the use of any metals and applying what we learned about reaction localization in mini ME emulsions to achieve low dispersity polymers, it can lead to widespread use for future applications like in the manufacture of hairy nanoparticles.

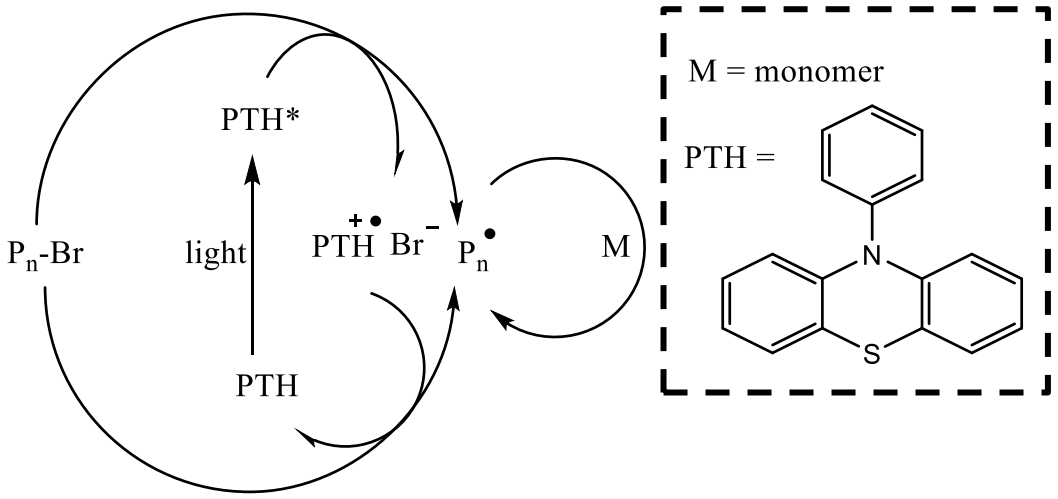

Scheme 1. Proposed mechanism of metal-free photomediated ATRP with 10-phenylphenothiazine (PTH).

Hairy Nanoparticles Arrays

Opportunities to harness controlled enthalpic and entropic interactions (e.g. hydrogen bonds, entanglements) between particle canopies have been largely unexplored. These interactions can affect mechanical, optical and electrical properties of HNP assemblies; however, they are rarely studied. In large part this was due to the lack of synthetic diversity, limited quantities of materials available and poor control of lattice symmetry because of limited HNP canopy design.[9] Implementing mini ME emulsion polymerization for the production HNPs offers an easier route to obtaining complex polymer canopies due to its unique control of reactant localization, which can be finely-tuned with various initiators, monomers, and phase transfer agents.

One clear direction for this project would be increasing the complexity of the canopy, including multiphase mixed HNP structures which can exploit the power of polymer processing including directed self-assembly to tailor these emerging materials in ways not before achieved (Fig. 1). NP arrays, made using tailored complementary interparticle (IP) interactions, are an important goal of this research program and these NP arrays can be generated using complementary HNP pairs (Fig. 2).

Complementary (mutually attractive) HNPs would allow the production of binary arrays while combination of large and small HNPs would permit the formation of more complex superlattices (Fig. 2). The control of brush chemistry and size to enable weak (e.g. chain entanglement) or strong interactions (e.g. hydrogen bonding) between nanoparticles can also be studied. In addition to brush interaction through entanglements, triggering interactions by means of photoactivated H-bonding

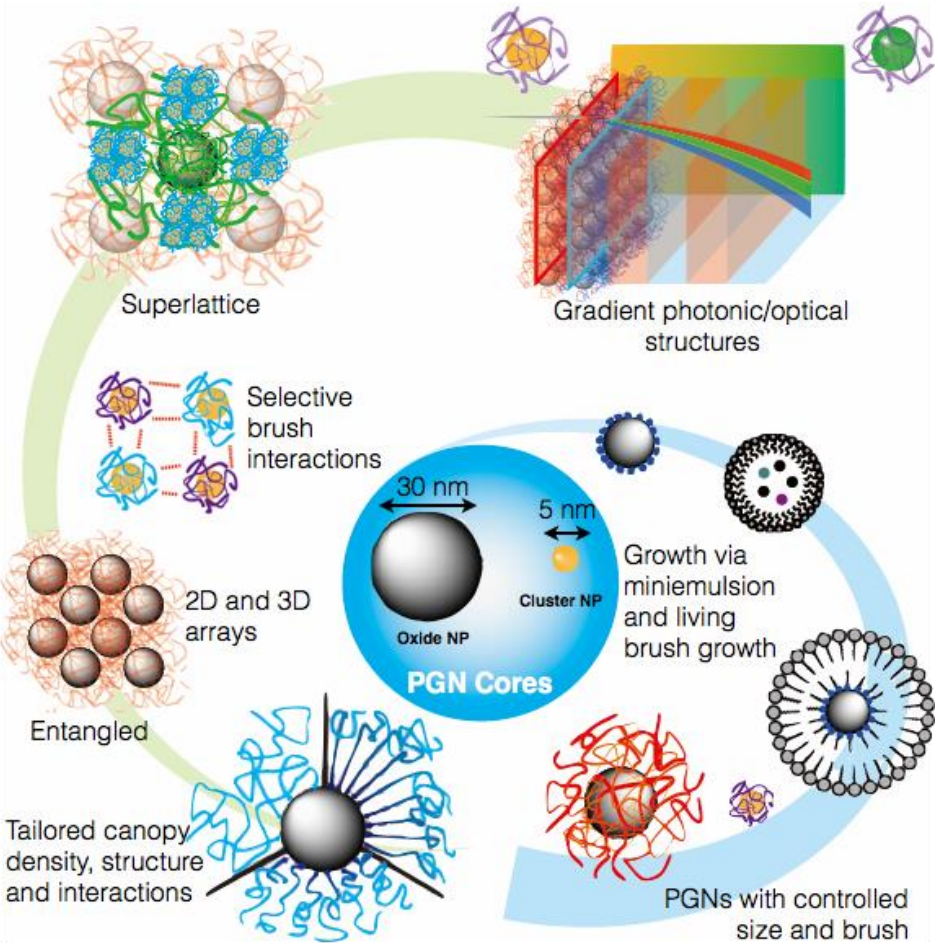

Fig. 1. Research pathway. Starting with growing HNP by aqueous seeded polymerization. HNPs will be prepared with specific brush size and architecture. Subsequent exploration with brush canopy / entanglement/ selective interactions will lead to formation of novel superlattice/array which leads to enhanced performance in optical materials, such a GRIN or Faraday rotator devices.

complexes would allow the creation of HNP superlattices as well as 2D arrays. [10–15]. Entanglement, ionic interactions between acids and bases, and hydrogen bonding between neighboring HNP pairs can also be explored, while research in the use of small metal oxide clusters (MOC) would provide tailored superlattice structures. Metal oxide cluster compounds offer precise size, composition and graft density but need a shorter graft length to balance composition and require alternatives to chain entanglement due to their short brush length.

Future research can also probe the use of light activation to control the very short brushes needed for: 1) small HNPs and 2) polymer grafted MOC units. Since these NPs are below the wavelength of activating radiation, simple exposures will be enough to turn on these polymerizations. These smaller diameter materials will enable the production of interesting two component NP arrays and introduce units with very specific compositions. Ye *et al.* have shown that selecting the proper size difference and volume content of the different NP populations, will possibly allow the creation of very unusual structures which is anticipated to have beneficial optical properties.[16]

Hydrogen bonding HNPs

Further effort can also be directed to forming more controlled and stable superlattices by using hydrogen bonding (Fig. 3). Hydrogen bonding between HNPs to accomplish several objectives would be of great interest. First, in short chain brush canopies needed for very small diameter NPs and in MOCs, finding an alternative for entanglement to create strong interactions between NPs. Hydrogen bonding can do that. Second, hydrogen bonds between short ligands or long polymer chains on a

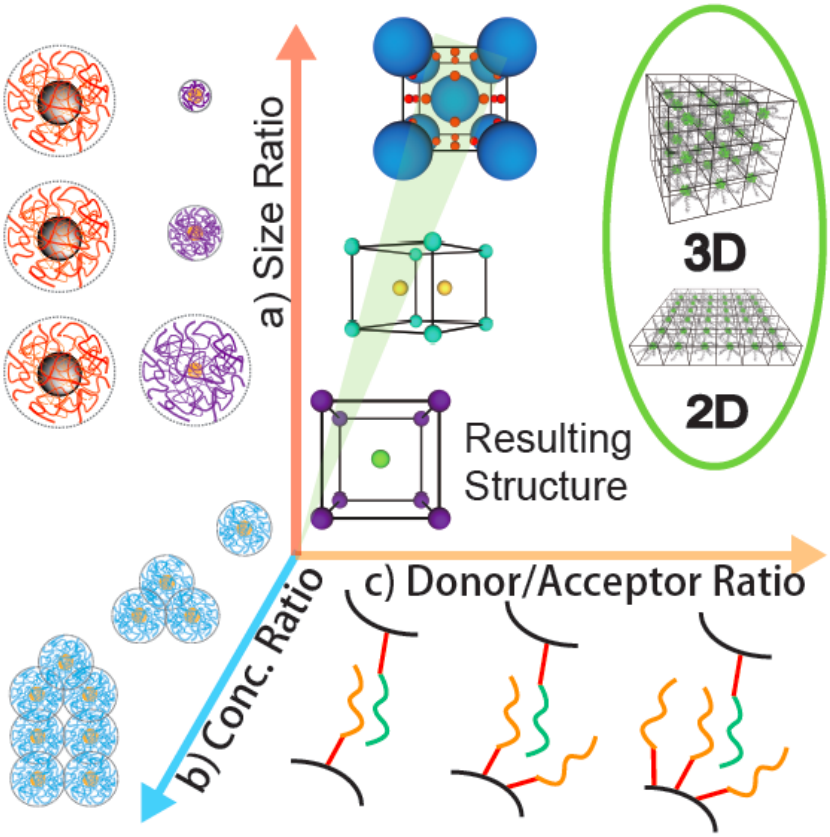

Figure 2. Strategies for controlling superlattice structure. The direction of the arrows for each strategy corresponds to formation of more asymmetric superlattice. Strategies include: a) size ratio between HNPs. c) Concentration ratio added in the blend between HNPs. c) H-bond donor / acceptor ratio between HNPs. Derived superlattice could be either 2D / 3D array depending on the specific tuning.

particle surface may also assist in the self-assembly of particles into non-close packed or closely packed one-dimensional or two-dimensional superlattices[17], to enable new collective physicochemical properties which are remarkably different from either the individual NPs or their bulk materials, and further extend their application capabilities.[18–22] Moreover, hydrogen bonding offers a flexible and controllable pathway for structural manipulation of assembly.[23] Mini ME emulsion polymerization can be used to create different polymer brushes containing hydrogen bond donor sites, such as poly (acrylic acid) (PAA), poly (methacrylic acid) (PMAA), and poly(4-vinylphenol) or hydrogen bond acceptor sites, such as poly(4-vinylpyridine) (PVPy) and poly(vinylpyrrolidone). By selecting complementary hydrogen bonding canopies, it will be possible to provide interparticle interactions that replace those lost as the chains become shorter than the entanglement molecular weight.

Hidden/latent hydrogen bonding

One of the challenges of creating NP arrays is the need for mobility in the HNPs during the assembly process. By their very nature, the hydrogen bonding groups are designed to create strong inter-canopy interactions, which if present may hinder ordering of an array. Should this prove to be an obstacle, latent photochemically accessible H-bonding groups can be used. By introducing a latent H-bonding moiety into the polymer brush, dynamic and switchable superlattices can be achieved and regulated by external stimuli such as pH value, temperature and UV light.

The Ober group has expertise in the chemistry of photoresists and can imagine at least two methods for masking an H-bonding group and then turning it on using light. For

example, an o-nitrobenzyl-containing photoreactive moiety on a polymer brush was reported by our group in 2011.[24] This structure upon exposure to UV radiation releases a masked carboxylic acid which would then bind to a hydrogen acceptor. Such a group could be incorporated with the first group of HNPs, whose polymer brushes contain acid groups, while the second type of HNP canopy is functionalized with polymer brushes containing hydrogen bond acceptor sites. After two types of HNPs are mixed, UV light can be applied to the superlattice upon which the nitrobenzyl moieties will be cleaved from the brushes and hydrogen bonding between donor brushes and acceptor brushes will be activated as shown in Fig. 3, bottom. Locking up of HNPs may be minimized during annealing and this interaction may even aid array formation by favoring a partnering of donor and acceptor HNPs in the array.

Once more, applying concepts from photoresist chemistry, groups such as t-butyl esters on carboxylic acids represent nonpolar groups that can be easily processed and mixed with hydrogen bond acceptors without strong interactions. However, when heated especially in the presence of catalytic amounts of acid, the ester groups cleave to reveal proton donating acid groups. This chemistry can be activated by exposing these groups to acid from an external source (blanket conversion) or with the addition of a photoacid generator (photo defined activation). Combined with the cleavage of photosensitive o-nitrobenzyl-containing groups we have two methods for photo defining H-bond formation that we will explore as we study NP array formation.

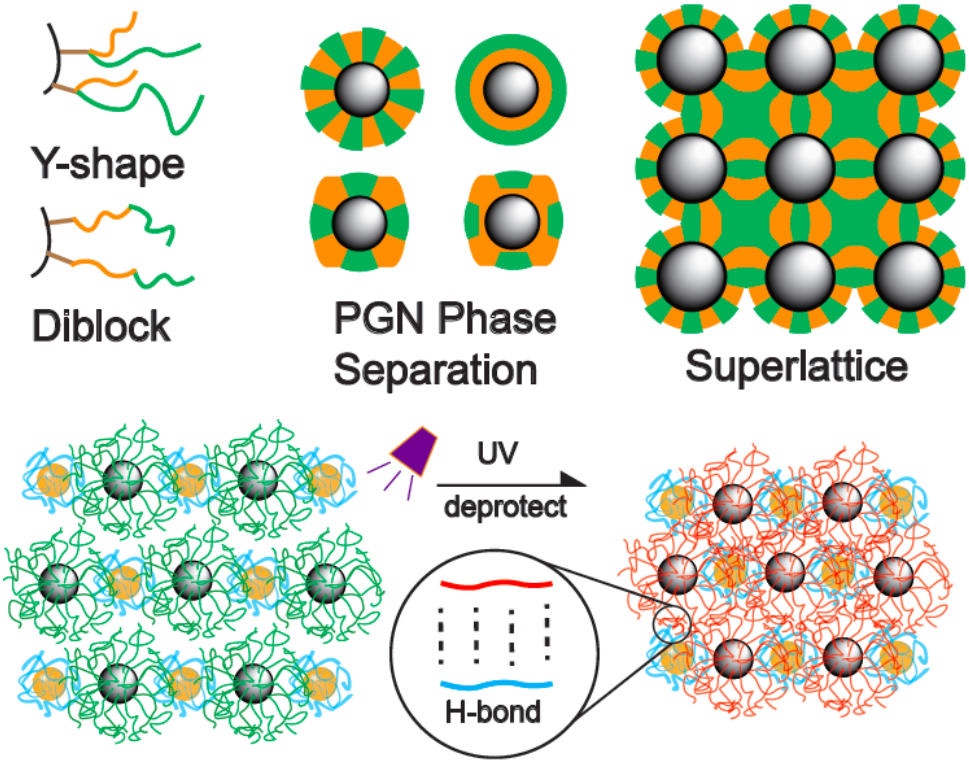

Figure 3. Superlattice film coating strategy and selected brush structures. Top: Left – Two-phase brush structures. Middle - Phase separated HNP. Right - Phase separated superlattice. Bottom: binary superlattice "locked" by H-bonding following UV light exposure.

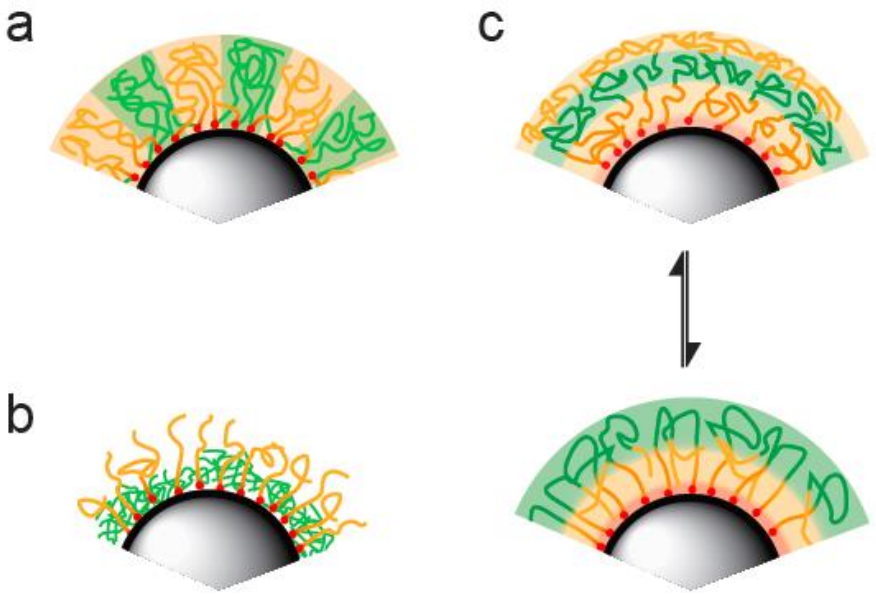

Figure. 4. Phase separated NP canopies and interesting surface architecture. a) Lateral phase separation. b) Inner shell and outer "antenna" c) Reversible phase shift in triblock copolymer canopy.

Phase separated mixed brush canopies

Moreover, another future direction for HNPs would be constructing multifunctional brush canopies both from both block copolymer brushes and by using binary initiators with the goal of making active phase separated canopies along the circumference of the HNP. By controlling different ratios and concentrations of the phase separated zones it can provide brush canopies that select for HNP array symmetry, multiple attachments sites between large and small HNPs and the creation of generally more versatile HNP canopies (Fig. 4).

ACWOP Biosensor

This project has evolved tremendously over the past 5 years as it was once an electrochemical based biosensor [25] and today's generation is based on a colorimetric readout with a microparticle platform. Although the microparticles allowed us to easily functionalize the surface for testing and optimization, the particles themselves would need to be tethered to a microfluidic platform to get to a point-of-care device. One way to do this would be to use a cellulose surface rather than a particle-based one as most current point-of-care device platforms are paper-based (e.g. pregnancy tests, glucose monitoring devices). The modification of cellulose strips with POEGMA polymer brushes post-functionalized with a specific antigen would be an ideal platform for mass production.

I conducted preliminary experiments to demonstrate that cellulose is a viable substrate for specific antigen detection. As illustrated in Fig. 5, a paper substrate (Whatman's filter paper) was functionalized with POEGMA

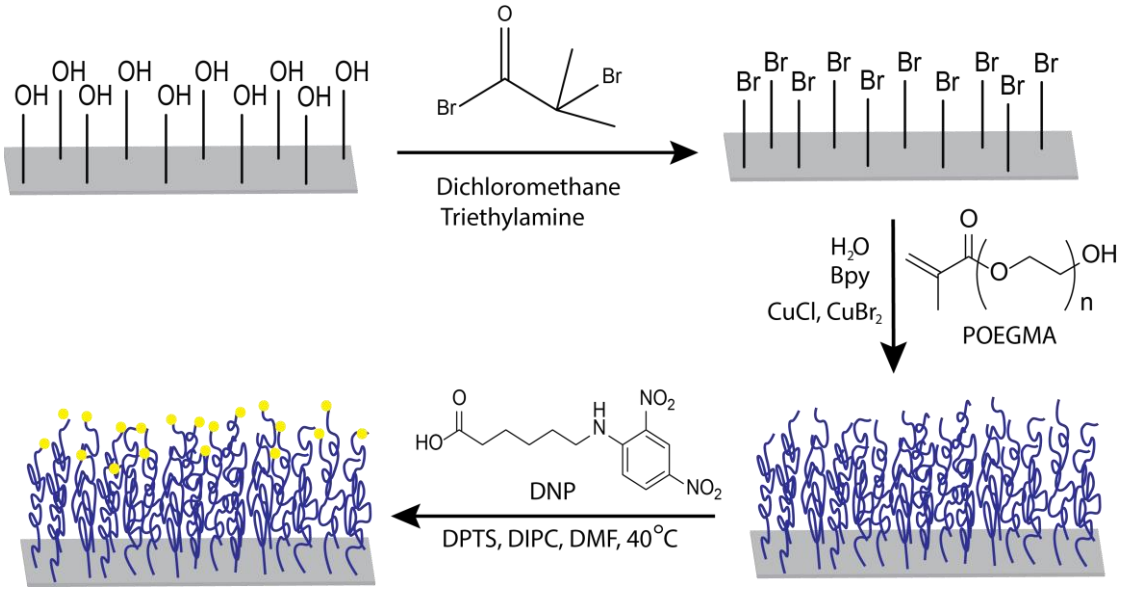

Figure 5. Depiction of polymer brush synthesis on a paper surface (Whatman's filter paper) and subsequent DNP post-functionalization.

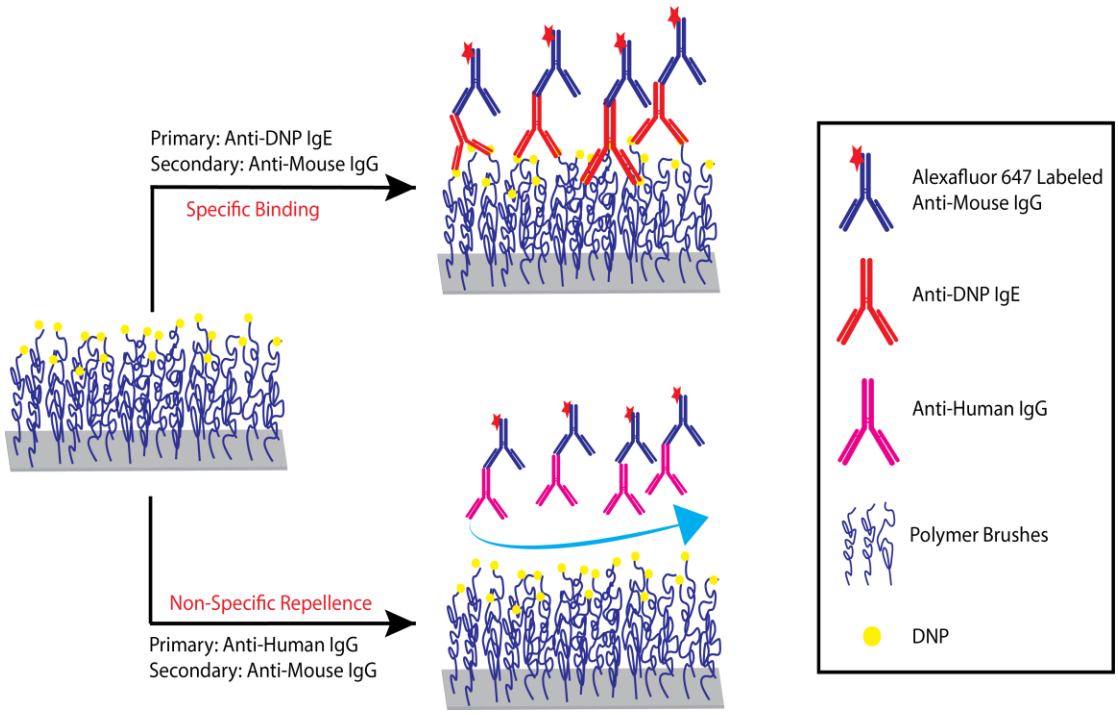

Figure 6. Illustration of specific binding and non-specific repellence of anti-DNP IgE and anti- human IgG antibodies, respectively, to the DNP antigen tethered to POEGMA polymer brushes on a paper substrate.

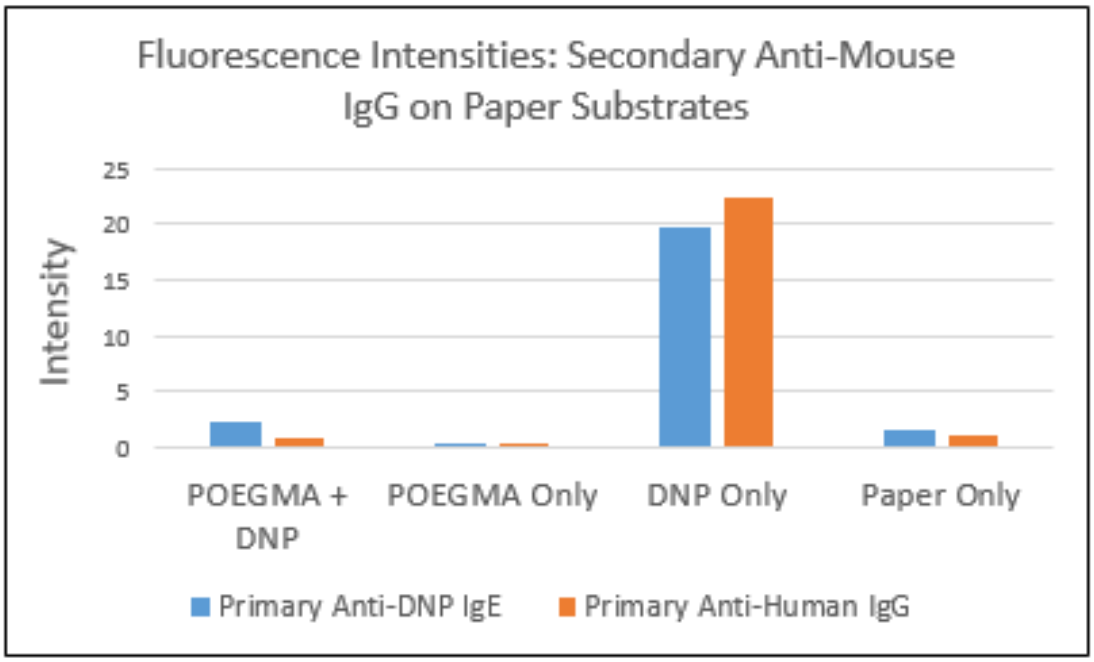

Figure 7. Graph of fluorescence intensities of paper substrates functionalized with POEGMA + DNP, POEGMA only, and DNP only compared with the paper only control experiment.

polymer brushes via an ATRP polymerization. Dinitrophenyl (DNP) antigens were then covalently tethered to the POEGMA polymer brush (procedure in Appendix B). Figure 6 illustrates the specific binding of anti-DNP IgE to the DNP on the polymer brushes using AlexaFluor 647 labeled anti-mouse IgG as the secondary antibody.

As a control experiment, an anti-human IgG primary was used to promote non-specific repellence, thus demonstrating the need for polymer brushes to prevent non-specific binding. Figure 7 shows a bar graph comparing the fluorescence intensities of the POEGMA-DNP brushes functionalized on the paper substrate, as well as the control experiments, POEGMA only, DNP only and paper only. What was observed was a large amount of non-specific binding to the DNP only substrates and a small amount of non-specific binding to the paper only substrates. POEGMA polymer brushes allowed these substrates to obtain higher specificity by reducing the amount of non-specific adsorption on the paper substrate.

These preliminary experiments demonstrated that paper is a feasible platform for an antibody detection system if polymer brushes are used to prevent non-specific adsorption. As mentioned in chapter 1, POEGMA polymer brushes are not the only brush system that is able to prevent fouling.[26] In future studies, brush systems such as zwitterionic brushes can also be polymerized on paper and have their anti-fouling behavior compared with those of POEGMA based substrates. This shift would bring the ACWOP biosensor closer to a point-of-care device.

ACKNOWLEDGEMENTS

I would like to acknowledge Prof. Barbara Baird and Prof. David Holowka for their contributions to the preliminary work of antibody detection using a paper substrate. Contributing members for this work include Dr. Eshan Mitra who helped me with the preliminary experiments of detecting anti-DNP antibodies on the surfaces. His fluorescently labeled anti-mouse IgG was used for this experiment. Jordan Mohr, and Dr. Nirmalya Bag both helped with imaging of the paper substrates using the fluorescent microscope.

REFERENCES

(1) Matyjaszewski, K.; Xia, J. Atom Transfer Radical Polymerization. *Chem. Rev.* **2001**, *101* (9), 2921–2990.

(2) Ayres, N. Atom Transfer Radical Polymerization: A Robust and Versatile Route for Polymer Synthesis. *Polym. Rev.* **2011**, *51* (2), 138–162.

(3) He, D.; Xue, Z.; Khan, M. Y.; Noh, S. K.; Lyoo, W. S. Phosphorus Ligands for Iron(III)-Mediated ATRP of Styrene via Generation of Activators by Monomer Addition. *J. Polym. Sci. Part Polym. Chem.* **2010**, *48* (1), 144–151.

(4) Fu, L.; Simakova, A.; Fantin, M.; Wang, Y.; Matyjaszewski, K. Direct ATRP of Methacrylic Acid with Iron-Porphyrin Based Catalysts. *ACS Macro Lett.* **2018**, *7* (1), 26–30.

(5) Cordero, R.; Jawaid, A.; Hsiao, M.-S.; Lequeux, Z.; Vaia, R. A.; Ober, C. K. Mini Monomer Encapsulated Emulsion Polymerization of PMMA Using Aqueous ARGET ATRP. *ACS Macro Lett.* **2018**, *7* (4), 459–463.

(6) Simakova, A.; Averick, S. E.; Konkolewicz, D.; Matyjaszewski, K. Aqueous ARGET ATRP. *Macromolecules* **2012**, *45* (16), 6371–6379.

(7) Bian, C.; Zhou, Y.-N.; Guo, J.-K.; Luo, Z.-H. Photoinduced Fe-Mediated Atom Transfer Radical Polymerization in Aqueous Media. *Polym. Chem.* **2017**, *8* (47), 7360–7368.

(8) Treat, N. J.; Sprafke, H.; Kramer, J. W.; Clark, P. G.; Barton, B. E.; Read de Alaniz, J.; Fors, B. P.; Hawker, C. J. Metal-Free Atom Transfer Radical Polymerization. *J. Am. Chem. Soc.* **2014**, *136* (45), 16096–16101.

(9) Fernandes, N. J.; Koerner, H.; Giannelis, E. P.; Vaia, R. A. Hairy Nanoparticle

Assemblies as One-Component Functional Polymer Nanocomposites: Opportunities and Challenges. *MRS Commun.* **2013**, *3* (01), 13–29.

(10) Camera, K. L.; Gómez-Zayas, J.; Yokoyama, D.; Ediger, M. D.; Ober, C. K. Photopatterning of Indomethacin Thin Films: A Solvent-Free Vapor-Deposited Photoresist. *ACS Appl. Mater. Interfaces* **2015**, *7* (42), 23398–23401.

(11) Jacobs, A. G.; Jung, B.; Jiang, J.; Ober, C.; Thompson, M. O. Control of Polystyrene-Block-Poly (Methyl Methacrylate) Directed Self-Assembly by Laser-Induced Millisecond Thermal Annealing. *J. MicroNanolithography MEMS MOEMS* **2015**, *14* (3), 031205.

(12) Chavis, M. A.; Smilgies, D.-M.; Wiesner, U. B.; Ober, C. K. Widely Tunable Morphologies in Block Copolymer Thin Films Through Solvent Vapor Annealing Using Mixtures of Selective Solvents. *Adv. Funct. Mater.* **2015**, *25* (20), 3057–3065.

(13) Jung, B.; Satish, P.; Bunck, D. N.; Dichtel, W. R.; Ober, C. K.; Thompson, M. O. Laser-Induced Sub-Millisecond Heating Reveals Distinct Tertiary Ester Cleavage Reaction Pathways in a Photolithographic Resist Polymer. *ACS Nano* **2014**, *8* (6), 5746–5756.

(14) Wieberger, F.; Neuber, C.; Ober, C. K.; Schmidt, H.-W. Tailored Star Block Copolymer Architecture for High Performance Chemically Amplified Resists. *Adv. Mater.* **2012**, *24* (44), 5939–5944.

(15) Wieberger, F.; Kolb, T.; Neuber, C.; Ober, C.; Schmidt, H.-W. Combinatorial Techniques to Efficiently Investigate and Optimize Organic Thin Film Processing and Properties. *Molecules* **2013**, *18* (4), 4120–4139.

(16) Ye, X.; Zhu, C.; Ercius, P.; Raja, S. N.; He, B.; Jones, M. R.; Hauwiller, M. R.;

Liu, Y.; Xu, T.; Alivisatos, A. P. Structural Diversity in Binary Superlattices Self-Assembled from Polymer-Grafted Nanocrystals. *Nat. Commun.* **2015**, *6*, 10052.

(17) Luo, D.; Yan, C.; Wang, T. Interparticle Forces Underlying Nanoparticle Self-Assemblies. *Small* **2015**, *11* (45), 5984–6008.

(18) Pileni, M. P. Inorganic Nanocrystals Self Ordered in 2D Superlattices: How Versatile Are the Physical and Chemical Properties? *Phys. Chem. Chem. Phys.* **2010**, *12* (38), 11821.

(19) Fendler, J. H. Chemical Self-Assembly for Electronic Applications. *Chem. Mater.* **2001**, *13* (10), 3196–3210.

(20) Lee, J.; Govorov, A. O.; Kotov, N. A. Nanoparticle Assemblies with Molecular Springs: A Nanoscale Thermometer. *Angew. Chem.* **2005**, *117* (45), 7605–7608.

(21) Brust, M. Nanoparticle Ensembles: Nanocrystals Come to Order. *Nat. Mater.* **2005**, *4* (5), 364–365.

(22) Agarwal, A.; Lilly, G. D.; Govorov, A. O.; Kotov, N. A. Optical Emission and Energy Transfer in Nanoparticle−Nanorod Assemblies: Potential Energy Pump System for Negative Refractive Index Materials. *J. Phys. Chem. C* **2008**, *112* (47), 18314–18320.

(23) Bhattacharjee, R. R.; Mandal, T. K. Polymer-Mediated Chain-like Self-Assembly of Functionalized Gold Nanoparticles. *J. Colloid Interface Sci.* **2007**, *307* (1), 288–295.

(24) Xu, Y.; Hoshi, Y.; Ober, C. K. Photo-Switchable Polyelectrolyte Brush for Dual Protein Patterning. *J. Mater. Chem.* **2011**, *21* (36), 13789.

(25) Welch, M. E.; Ritzert, N. L.; Chen, H.; Smith, N. L.; Tague, M. E.; Xu, Y.;

Baird, B. A.; Abruña, H. D.; Ober, C. K. Generalized Platform for Antibody Detection Using the Antibody Catalyzed Water Oxidation Pathway. *J. Am. Chem. Soc.* **2014**, *136* (5), 1879–1883.

(26) Chen, W.-L.; Cordero, R.; Tran, H.; Ober, C. K. 50th Anniversary Perspective: Polymer Brushes: Novel Surfaces for Future Materials. *Macromolecules* **2017**, *50* (11), 4089–4113.

APPENDIX A

Chapter 2: Mini ME Emulsion Polymerization of PMMA using ARGET ATRP

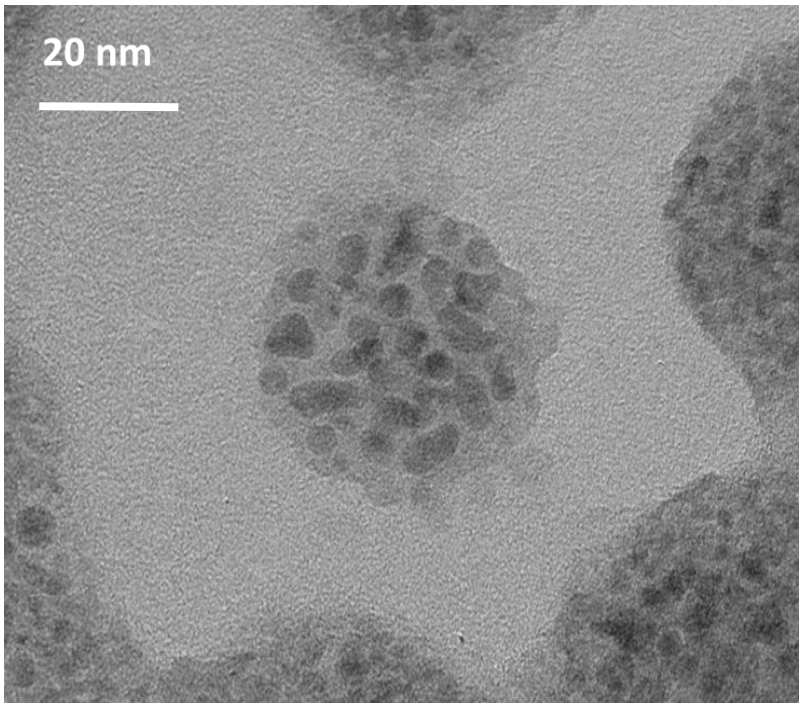

Figure A1. TEM image of micelles after polymerization using 100 mM NaCl. $[M]_0$ = 0.518 M, $[I]_0$ = 1 mM, [CuBr2] = 0.075 mM and ascorbic acid feeding rate at 23 nmoles/min. All polymerizations were conducted at 30˚C.

Figure A1 displays a micelle of ~ 21 nm after attempting mini ME polymerization using NaCl as the halide salt. The micelle size did not increase from before the polymerization as the DLS results in chapter 2 show that the monomer swollen micelles are ~ 21 nm. The nodules that are observed in the TEM image could be crystalized salt that formed during the reaction or small pockets of low molecular weight polymer. It was clear that

an inorganic halide salt would not facilitate the polymerization.

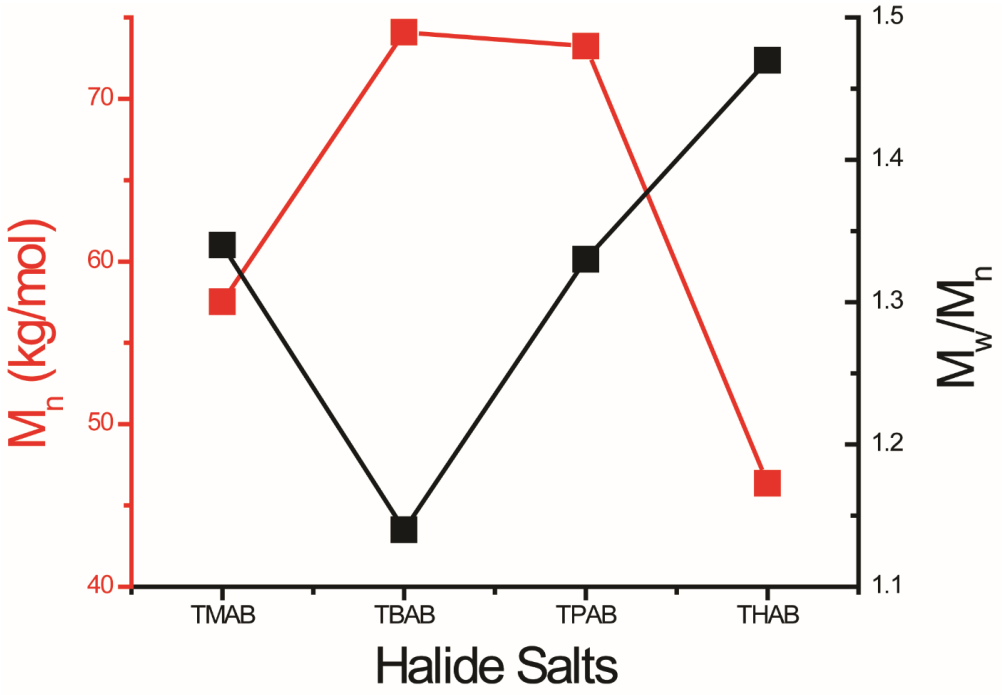

Figure A2. Graph of phase transfer agents against molecular weight and dispersity. [Halide salt] = 100 mM, $[M]_0$ = 0.518 M, $[I]_0$ = 1 mM, [CuBr2] = 0.075 mM and ascorbic acid feeding rate at 23 nmoles/min. All polymerizations were conducted at 30˚C.

Figure A2 shows a comparison between four phase transfer agents, Tetramethylammonium bromide (TMAB), tetrabutylammonium bromide (TBAB), tetrapentylammonium bromide (TPAB), tetraheptylammonium bromide (THAB). What was observed was a "Goldilocks" effect where the optimal phase transfer agent was TBAB. TMAB was unable to diffuse into the micelle at an appropriate diffusion rate to deliver the halide to the chain end, while TPAB and THAB were unable to diffuse out of the micelle, thus the Cu^I-Br/TPMA (activator) cannot get shuttled into the organic phase.

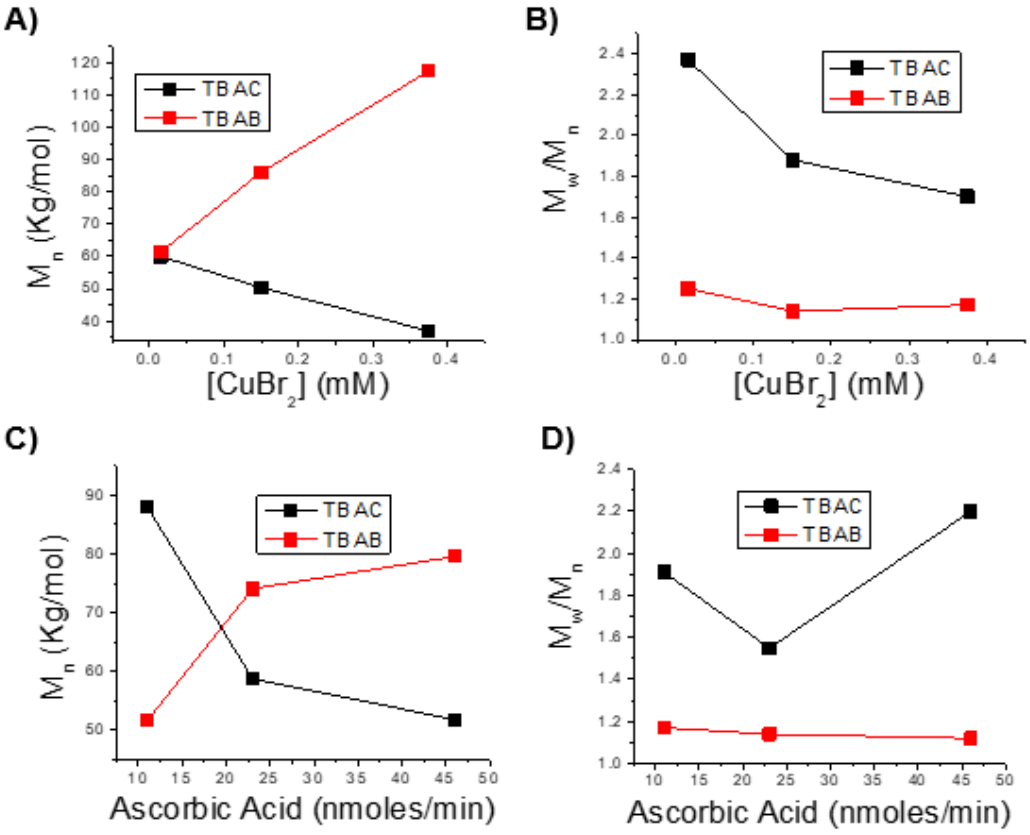

Figure A3. Comparing the effects of varying $CuBr_2$ concentrations and ascorbic acid feeding rate on molecular weight of PMMA when using either TBAB or TBAC.

Figure A3 demonstrates the dramatic effect that mini ME emulsion polymerization undergoes when tetrabutylammonium chloride is used as the phase transfer agent. Complete opposite trends of molecular weight and polymer dispersity are seen when varying $CuBr_2$ concentrations ascorbic acid feeding rates. Further investigation needs to be conducted in the future to fully understand these effects.

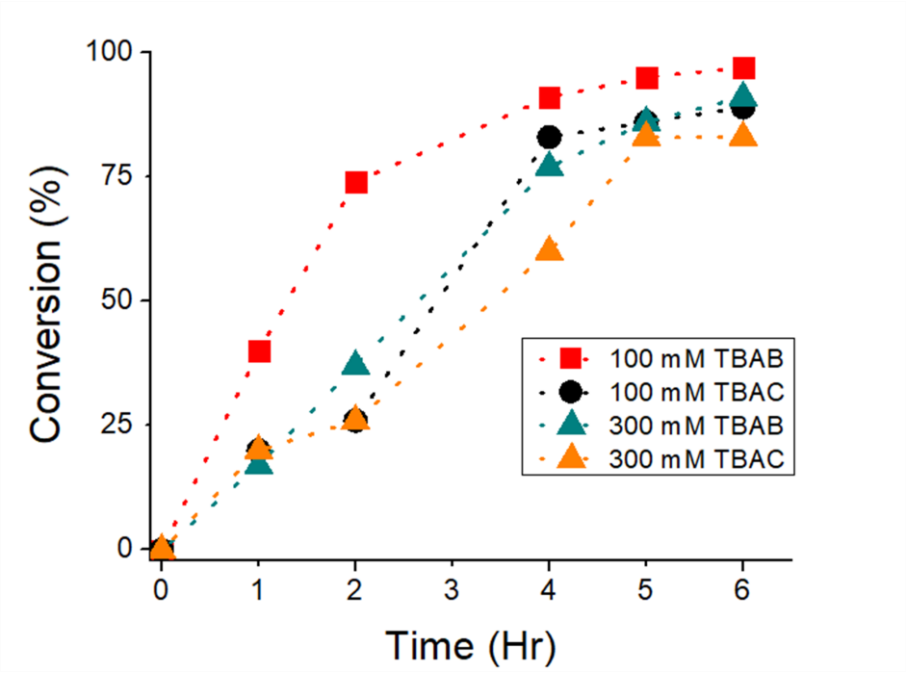

Figure A4. Conversion of PMMA versus time using mini-ME ARGET ATRP emulsion polymerization with TBAB and TBAC at 100 and 300 mM. $[M]_0$ = 0.518 M, $[I]_0$ = 1 mM, $[CuBr_2]$ = 0.075 mM, and ascorbic acid feeding rate at 23 nmoles/min. All polymerizations were performed at 30˚C. Note: dotted lines were provided to guide the eye.

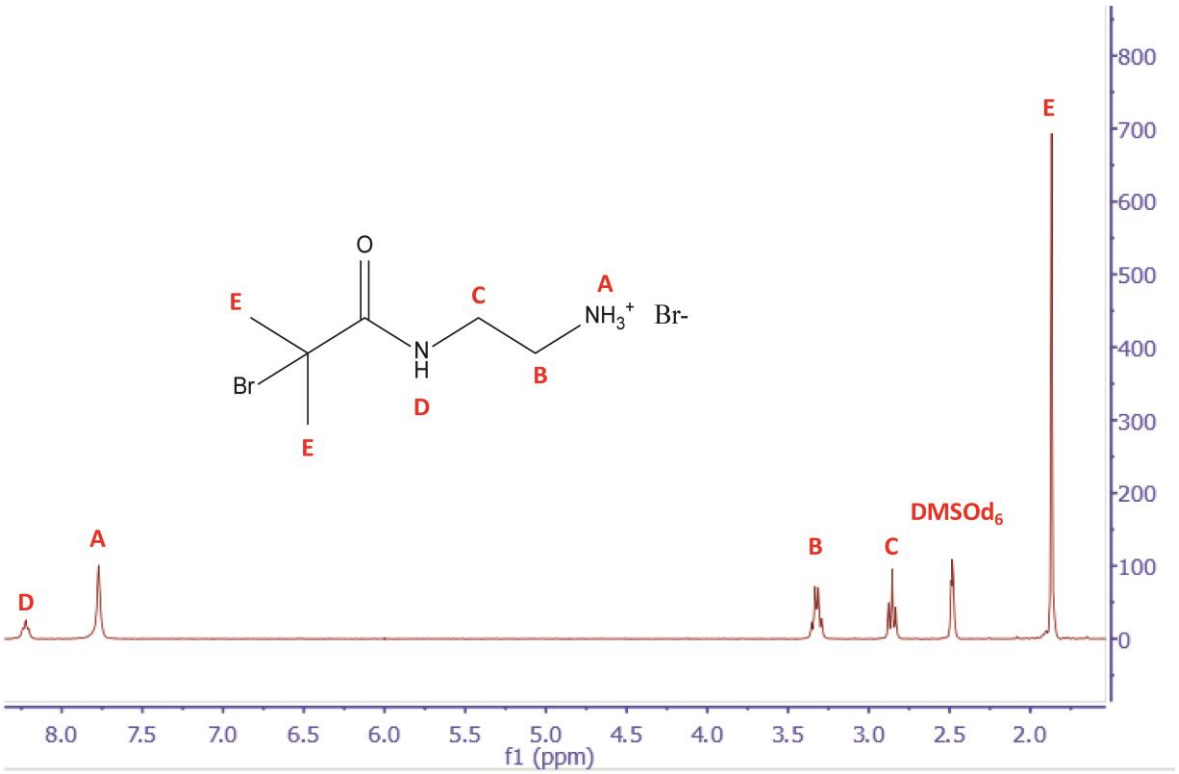

Figure A5. ^{1}H NMR spectra of N-(2-aminoethyl)-2-bromo-2-methylpropanamide ATRP initiator in its ammonium form in $DMSOd_6$.

APPENDIX B

Chapter 6. ACWOP Biosensor. B.1 Development and optimization of a hydrogen peroxide colorimetric detection system

[HRP] optimization:

HRP (100µL, 11µM) was serially diluted in DPBS (pH 7.4, 100µL) with a dilution factor of 1/2 in 11 wells of a clear 96-well microplate. A well containing DPBS (pH 7.4, 100µL) was used as the negative control. H_2O_2 (100µL, 20µM) and TMB (100µL, 1.04mM) was added to each well. The plate was covered with aluminum foil and incubated for 5 minutes. The absorbance intensity at 650nm was measured using a plate reader for all the wells. The above experiment was performed in triplicate and each data point is reported as the mean + S.E.M.

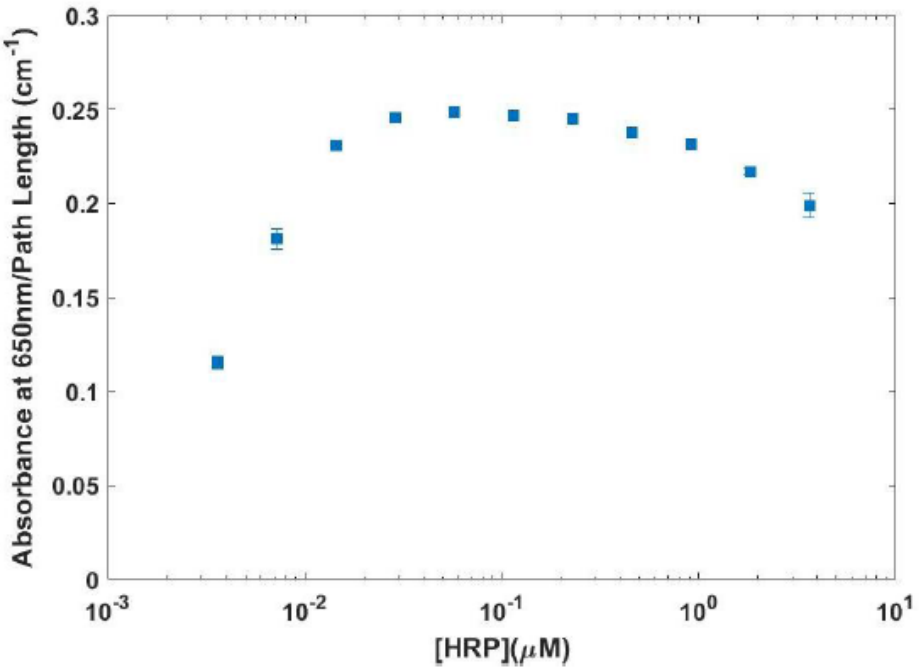

Figure B1. Optimization of [HRP] to obtain maximum colorimetric H_2O_2 detection signal. [H_2O_2] = 20µM, [TMB] = 1.04mM and time = 5 minutes.

The optimum [HRP] was chosen to be **0.171µM**.

[TMB] optimization:

TMB (100µL, 1.04mM) was serially diluted in DPBS (pH 7.4, 100µL) with a dilution factor of 1/2 in 11 wells of a clear 96-well microplate. A well containing DPBS (pH 7.4, 100µL) was used as the negative control. H_2O_2 (100µL, 44µM) and HRP (20µL, 0.171µM) was added to each well. The plate was covered with aluminum foil and incubated for 5 minutes. The absorbance intensity at 650nm was measured using a plate reader for all the wells. The above experiment was performed in triplicate and each data point is reported as the mean + S.E.M.

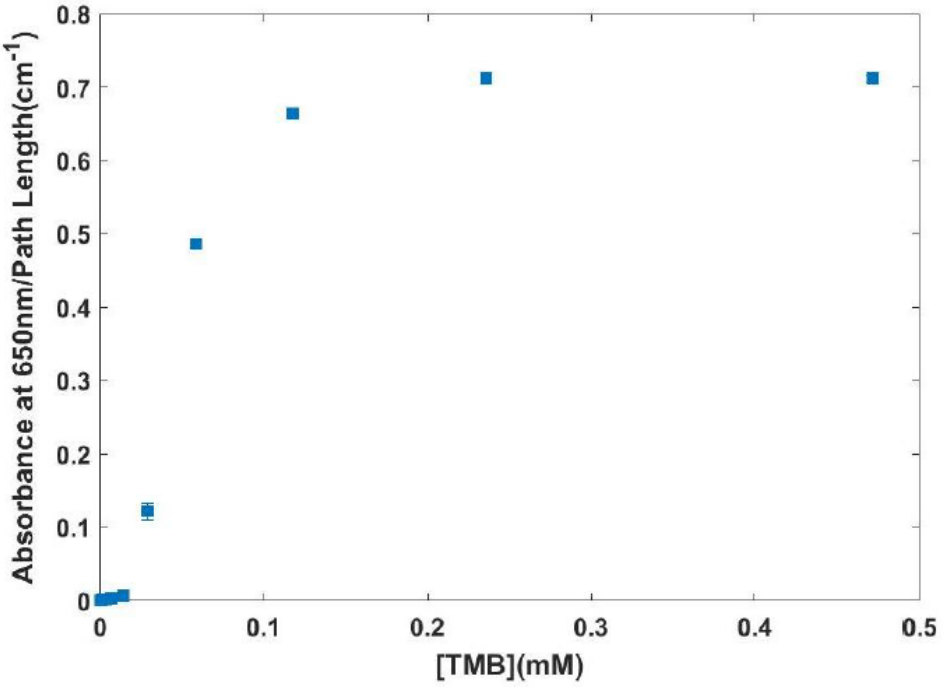

Figure B2. Optimization of [TMB] to obtain maximum colorimetric H_2O_2 detection signal. [H_2O_2] = 44µM, [HRP] = 0.171mM and time = 5 minutes.

The blue color change takes place when $[H_2O_2] \leq [TMB]$ and at equimolar concentration the color is most intense. Based on this observation, an optimum [TMB] of **1.04mM** was chosen as the stock solution.

Hydrogen peroxide standard curve for proof-of-concept assay:

H_2O_2 was detected by the oxidative color change of TMB in the presence of HRP. H2O2 (100µL, 64µM stock) was serially diluted in DPBS (pH 7.4, 100µL) with a dilution factor of 1/2 in 11 wells of a clear 96-well microplate. A well containing DPBS (pH 7.4, 100µL) was used as the negative control. RB (100µL, 0.01mM stock), HRP (20µL, 0.171µM stock) and TMB (100µL, 1.04mM stock) were added to all 12 wells. The plate was covered with aluminum foil and incubated for 5 minutes. The absorbance intensity

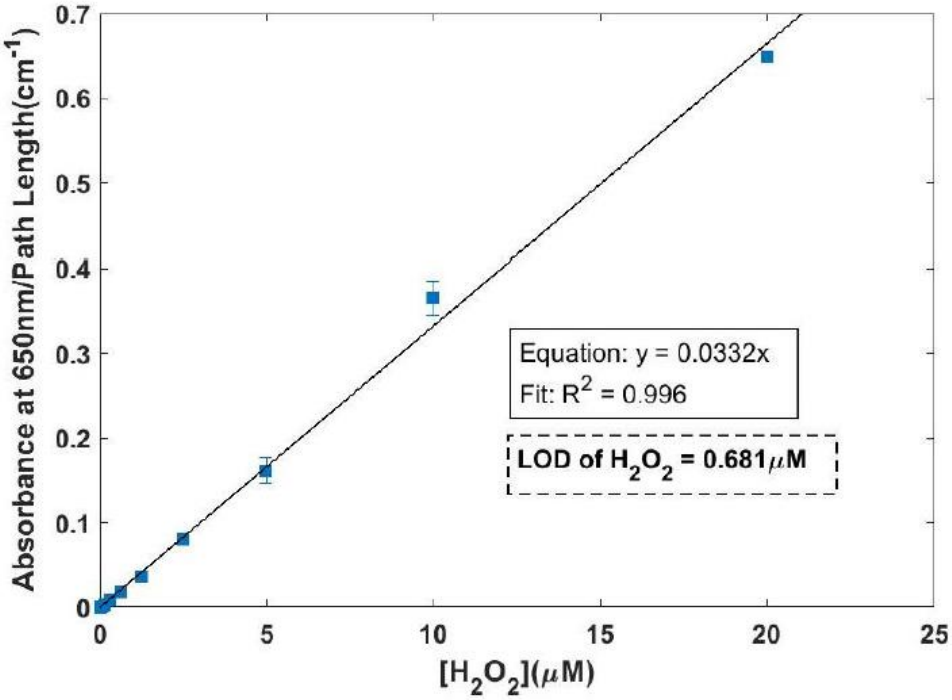

Figure B3. H_2O_2 standard curve for the proof-of-concept assay. Colorimetric signal obtained from the plate reader is converted to $[H_2O_2]$ based on the relation provided in the inset. [HRP] = 0.171µM, [TMB] = 1.04mM, [RB] = 0.01mM and time = 5 minutes.

at 650nm was measured using a plate reader for all the wells. The above experiment was performed in triplicate and each data point is reported as the mean + S.E.M.

Hydrogen peroxide standard curve for RB-silica microparticle based experiments:

H_2O_2 was detected by the oxidative color change of TMB in the presence of HRP. H_2O_2 (100µL, 64µM stock) was serially diluted in DPBS (pH 7.4, 100µL) with a dilution factor of 1/2 in 11 wells of a clear 96-well microplate. A well containing DPBS (pH 7.4, 100µL) was used as the negative control. HRP (20µL, 0.171µM stock) and TMB (100µL, 1.04mM stock) were added to all 12 wells. The plate was covered with aluminum foil and incubated for 5 minutes. The absorbance intensity at 650nm was

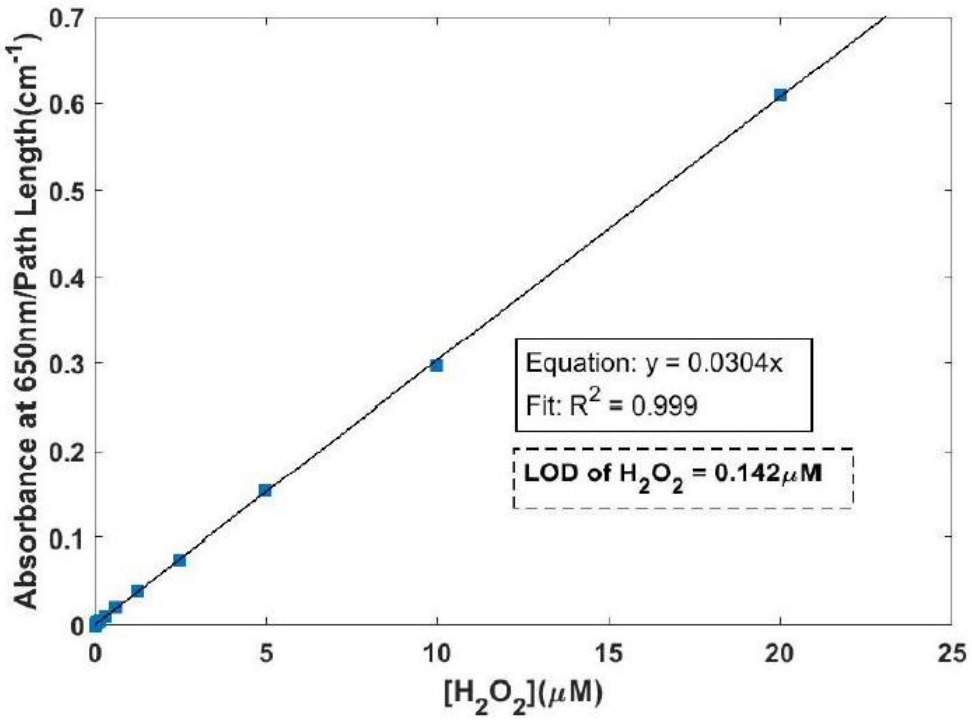

Figure B4. H_2O_2 standard curve for surface-based sensor experiments. Colorimetric signal obtained from the plate reader is converted to [H_2O_2] based on the relation provided in the inset. [HRP] = 0.171µM, [TMB] = 1.04mM and time = 5 minutes.

measured using a plate reader for all the wells. The above experiment was performed in

triplicate and each data point is reported as the mean + S.E.M.

B.2 Limit of detection of hydrogen peroxide in different Rose Bengal concentrations in solution

H_2O_2 (100µL, 64µM stock) was serially diluted in DPBS (pH 7.4, 100µL) with a dilution factor of 1/2 in 11 wells of a clear 96-well microplate. A well containing DPBS (pH 7.4, 100µL) was used as the negative control. RB (100µL, 0.01M stock), HRP (20µL, 0.171µM stock) and TMB (100µL, 1.04mM stock) were added to all 12 wells. The plate was covered with aluminum foil and incubated for 5 minutes. The absorbance intensity at 650nm was measured using a plate reader for all the wells. Four other RB stock

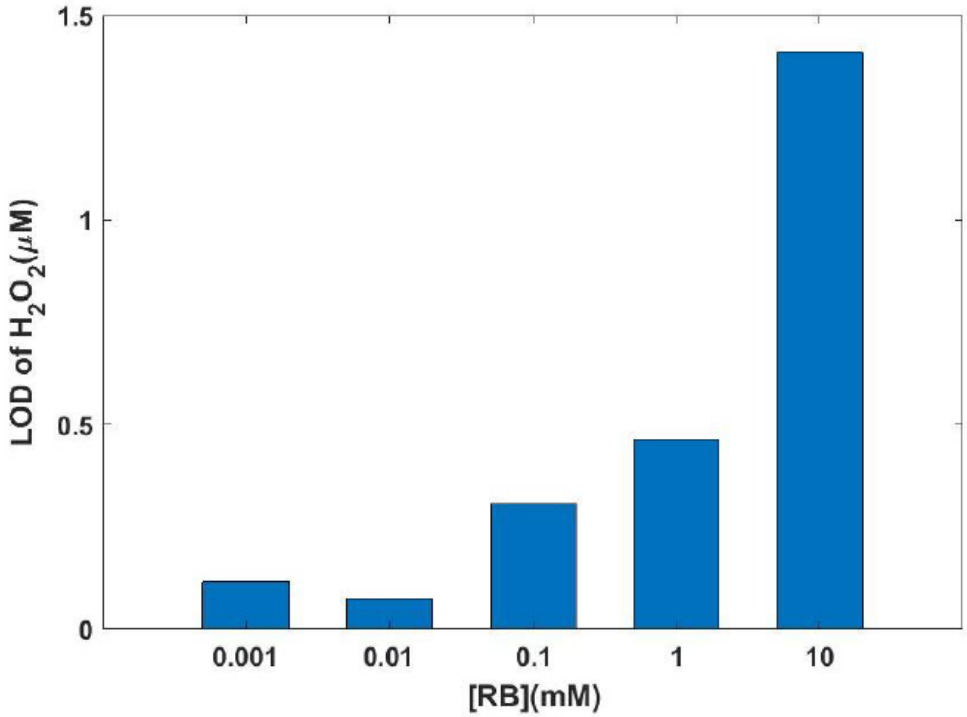

Figure B5. Analysis of LOD of H_2O_2 for different [RB] in solution. RB = 0.01mM provided the best (lowest) LOD and hence was chosen as the RB concentration in the ACWOP proof-of-concept assay.

conditions - 1mM, 0.1mM, 0.01mM and 1µM were tested following the same protocol

as above. All experiments were performed in triplicate and each data point is reported as the mean + S.E.M.

RB=0.01mM gave the lowest limit of detection and was chosen as the optimum [RB] for the proof-of-concept ACWOP assay

Dinitrophenyl (DNP) conjugation on APDMES-Silica Particles (also on cellulose substrate)

0.3g of APDMES-Silica particles (or Whatman's filter paper (1 cm x 2 cm) was added to a 50-mL round-bottom flask equipped with a stir bar along with 10 mL of amine-free anhydrous DMF. Then, 18.75 mg of DNP, 93.75 mg of 1,4-Dimethylpyridinium *p*-toluenesulfonate (DPTS), and 62.5 μL of *N,N′*-Diisopropylcarbodiimide (DIC) were added to the flask with the particles. This solution was stirred at 32˚C for 24 hours. The particles were then washed with ethanol and methanol using several centrifugation steps until the supernatant was completely clear. Likewise, the functionalized filter paper was washed with ethanol, methanol and then DCM, taking care not to tear it. The particles were then dried in the oven at 60˚C for two hours while the filter paper was air dried overnight. Separately, an ATRP initiator (α-bromoisobutyryl bromide) was reacted with the amine functional groups of APDMES on the silica gel and used as a macroinitiator to grow poly(oligoethylene glycol) methacrylate (POEGMA) polymer brushes on the surface. POEGMA polymer brushes have been proven in the past to decrease the amount of non-specific binding of biomolecules, increasing the specificity and sensitivity of a previous version of this biosensor on a silicon chip. The experimental procedure for polymer brush synthesis on the silica gel surfaced will be highlighted below.

Addition of ATRP initiator to APDMES-Silica to make Silica-Br (also on cellulose substrate)

APDMES-Silica gel (or APDMES-Cellulose) (2.50g) was dispersed in 150 ml of anhydrous toluene. After cooling solution to 0˚C, triethylamine (4 mL) was added and stirred for 5 mins. In a separate 10 mL Erlenmeyer flask, 10 mL of anhydrous toluene and 3 mL of α-bromoisobutyryl bromide (BIBB) was added. This solution was stirred manually and placed in a 50-mL dropper funnel equipped with a septum and a needle. The BIBB solution was added dropwise to the particles in toluene at 0˚C over a 2-hour period and stirred for an additional 2 hours at this temperature. Then, the solution was warmed to room temperature and stirred overnight. The next day, the particles were collected via filtration and washed with methanol and dichloromethane before being dried in the oven at 60˚C for several hours giving a product with a slight brown color to it. The cellulose substrate was washed similarly and dried in air overnight.

Polymer brush synthesis on Silica-Br to make Silica-POEGMA

Once the Silica-Br particles were dried, activators regenerated electron transfer (ARGET) ATRP was performed with 1 gram of the particles. ATRP components such as 0.05 mM of $CuBr_2$, 500 mM of POEGMA monomer (M_n Average is 360), 100 mM NaCl, and 0.4 mM of TPMA (ATRP ligand) were dissolved in 58.2 mL of water and degassed with argon for 30 mins. Subsequently, a 0.5 mM stock solution of ascorbic acid was prepared in a total volume of 5 mL and degassed with argon for 30 mins as well. A syringe pump was set at a rate of 10 μL/min to add a total volume of 1.8 mL of ascorbic acid solution to the main round-bottom flask with the ATRP components at

30˚C. After the ascorbic acid solution was fulling added, the particles with polymer brush were collected via filtration and washed with water, ethanol, and methanol 5 times each. It was dried in an oven at 60˚C overnight. The filter paper was dried overnight in air.

Addition of DNP to Silica-POEGMA to make Silica-POEGMA-DNP

DNP was added to the Silica-POEGMA surfaces with the same procedure as described in the section labeled "*Dinitrophenyl (DNP) conjugation on APDMES-Silica Particles*" above. The particles were then washed with methanol and ethanol over several centrifugation steps until the supernatant was clear.

APPENDIX C

C.1 Calculation of number of moles of RB present on 15mg of RB-silica microparticles

Bulk density of silica gel = 700kg/m^3

Hence 15mg of silica gel has a total volume = 2.142 x 10^{-8} m^3

From the manufacturer's specification, porous silica gel corresponds to -100+200 mesh which means the size of a particle lies between 75 to 150 µm.

Assuming an average of 112.5µm, the radius of a single particle = R = 56.25µm.

$$\text{Volume of a particle} = \frac{4 \times \pi \times R^3}{3} = 7.45 \times 10^{-13}\ m^3$$

Number of silica microparticles in 15mg = Total volume/Volume of a particle = 28752 particles

Outer surface area of one particle = $4 \times \pi \times R^2 = 3.97 \times 10^{-8}\ m^2$

Total outer surface area of all particles =

Number of particles x Outer surface area of a particle = 1.14 x 10^{-3} m^2

Molar volume of Rose Bengal = 338 x 10^{-6} m^3

Volume of single RB molecule = Molar volume/N_A(Avagadro number) = 5.611 x 10^{-28} m^3

$$\text{Radius of a single RB molecule} = \sqrt[3]{\frac{\text{Volume of a single molecule x 3}}{4 \text{ x } \pi}} = 0.511 \text{ nm}$$

Cross sectional area of a single molecule = $\pi \text{ x } R^2 = 8.22 \text{ x } 10^{-19} \text{ m}^2$

Total number of RB molecules that can fit on the silica surface =

Total outer surface area / Cross sectional area of an RB molecule = $1.38 \text{ x } 10^{15}$ molecules.

Total moles of RB that can be functionalized on the outer surface of 15mg of silica microparticles = Total number of RB molecules/N_A = **$2.3 \text{ x } 10^{-9}$ moles**

C.2 Comparison of Total Surface Area(TSA) provided by 30mg DNP-silica particles with the TSA of the bottom of a well in a 96-well ELISA microplate:

Bulk density of silica gel = $700 kg/m^3$

Hence 30mg of silica gel has a total volume = $4.285 \times 10^{-8} m^3$

From the manufacturer's specification, porous silica gel corresponds to -100+200 mesh. This means the size of a particle lies between 75 to 150 µm.

Assuming an average of 112.5µm, the radius of a single particle = R = 56.25µm.

$$\text{Volume of a particle} = \frac{4 \times \pi \times R^3}{3} = 7.45 \times 10^{-13} \ m^3$$

Number of silica microparticles in 30mg = Total volume/Volume of a particle = 57517 particles

Outer surface area of one particle = $4 \times \pi \times R^2 = 3.97 \times 10^{-8} \ m^2$

Total outer surface area of all particles = Number of particles x Outer surface area of a particle = $2.28 \times 10^{-3} \ m^2$

Radius of the bottom of a F-bottom well from greiner bio-one, R = 3.195×10^{-3} m

Total surface area of the bottom of the well = $\pi \times R^2 = 3.2 \times 10^{-5} \ m^2$

Ratio of Surface areas = Total Surface area of 30mg DNP-silica particles/Total surface area of the bottom of an ELISA well = **71**

APPENDIX D

Comparison of the singlet oxygen generation efficiency between Rose Bengal freely diffusing in solution and RB functionalized to silica microparticles

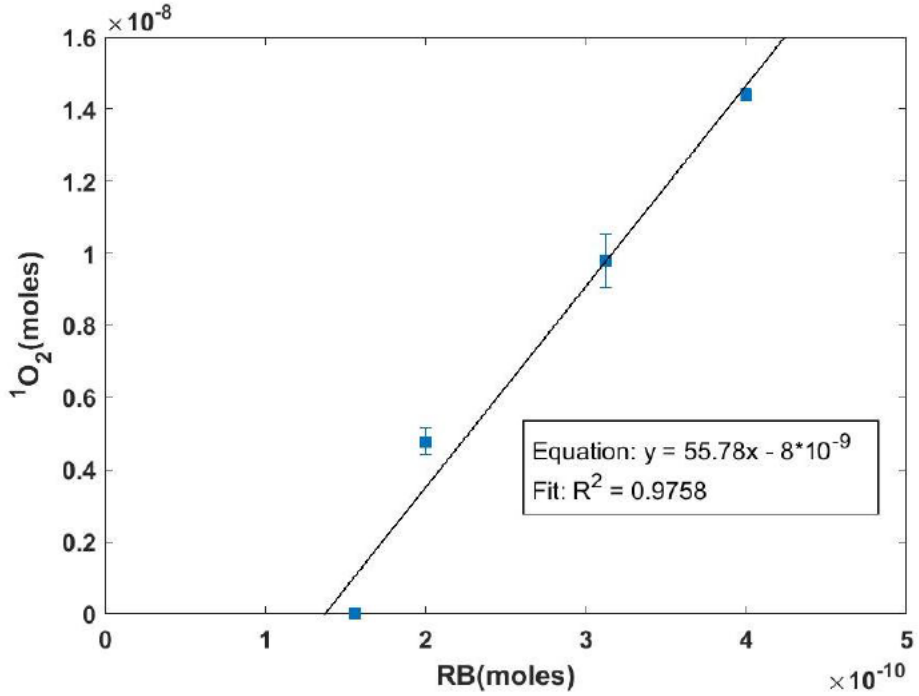

Figure D. Comparison between photosensitization reactions in solution and on a surface (**a**) Analysis of number of moles of $^1O_2$ generated per mole of RB in solution (**b**) Analysis of number of moles of $^1O_2$ generated per moles of RB on a surface

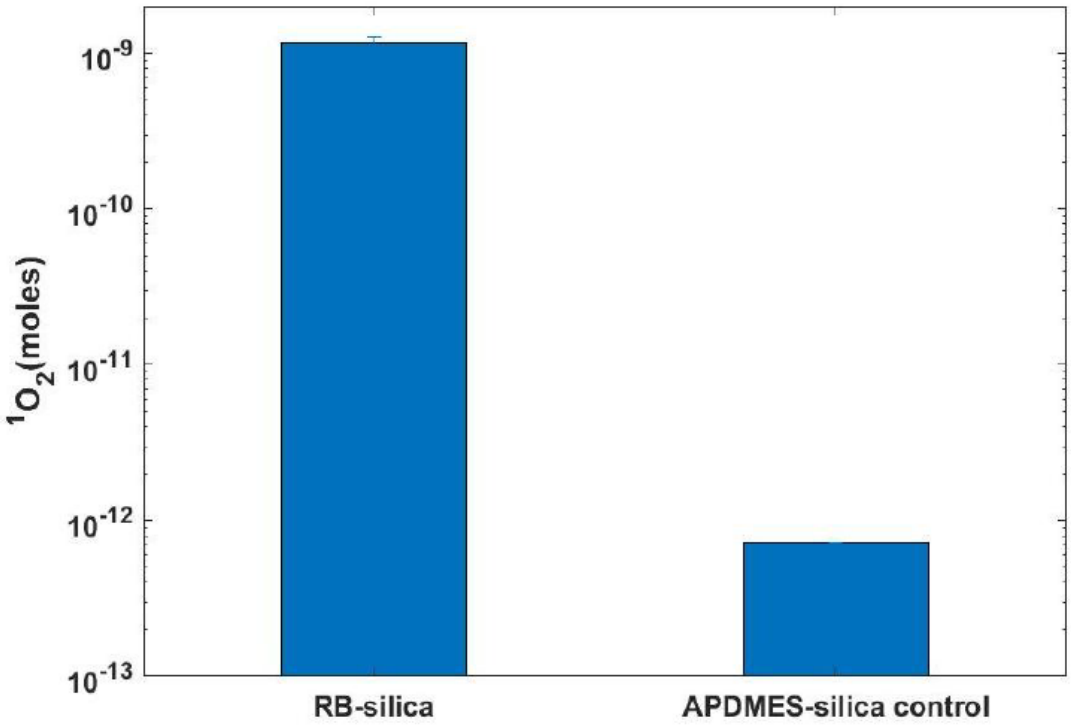

Figure D. Comparison between photosensitization reactions in solution and on a surface (**a**) Analysis of number of moles of $^1O_2$ generated per mole of RB in solution (**b**) Analysis of number of moles of $^1O_2$ generated per moles of RB on a surface

Rose Bengal in solution:

From Fig C(a), $^1O_2$ moles generated/RB moles in solution = 55.78

Therefore, 1 mole of RB in solution generates 55.78 moles of $^1O_2$ in 30 minutes.

Rose Bengal functionalized to silica microparticles:

From Appendix B.1, moles of RB on 15mg silica particles = 2.3×10^{-9} moles.

From Fig C, $^1O_2$ moles generated from 15mg RB-silica = 1.15×10^{-9} moles

$^1O_2$ moles generated/RB moles on surface = 0.5

Therefore 1 mole of RB on the surface generates 0.5 moles of $^1O_2$ in 30 minutes

Ratio of (1)/(2) = 55.78/0.5 = **111.56**

RB in solution generates 111.56 more moles of $^1O_2$ than RB on surface.

Hence RB freely diffusing in solution is 100 times more efficient in generating $^1O_2$ than RB functionalized on silica particles.

Supplementary Information

1. Absorption spectrum of RB in solution:

RB (100µL, 0.01mM) in DPBS (pH 7.4, 1x) was taken in a well and the absorbance spectrum was performed using a plate reader. The spectrum showed that the photosensitizer has an absorption maximum at 550nm i.e. green light.

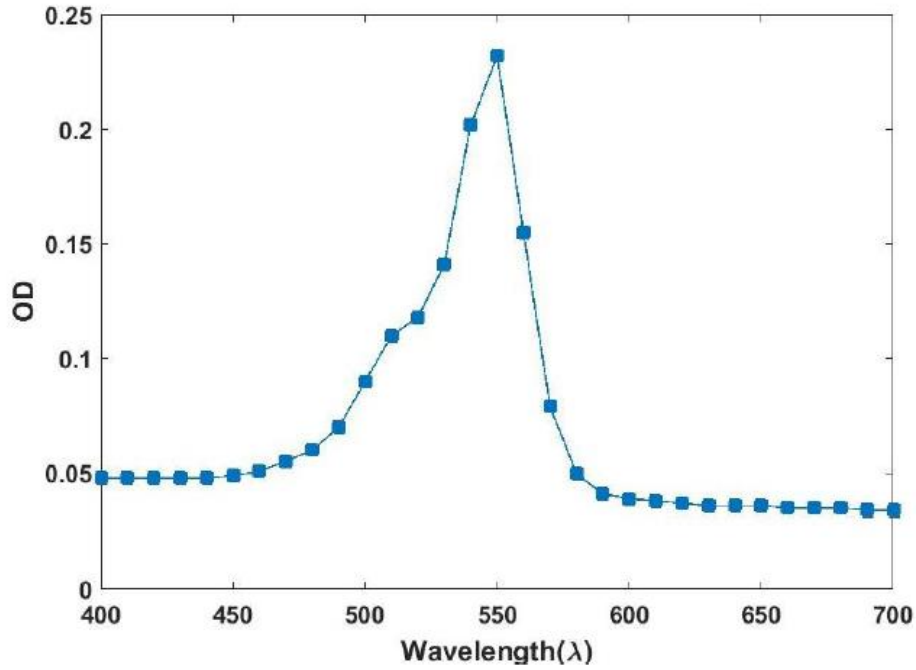

Figure S1. Absorption spectrum of 0.01mM RB in solution. Absorption maximum occurs at 550nm i.e. green light.

2. pH as a function of Ascorbic Acid concentration:

Ascorbic Acid (5mL, 0.07M) was serially diluted in 1x DPBS (phosphate 10mM/sodium chloride 160mM, pH 7.4, 5mL) with a dilution factor of ½ in 11 scintillation vials. A control of 1x DPBS (pH 7.4, 5mL) was taken in a separate vial. The pH was measured using a Mettler Toledo 7 pH/conductivity meter.

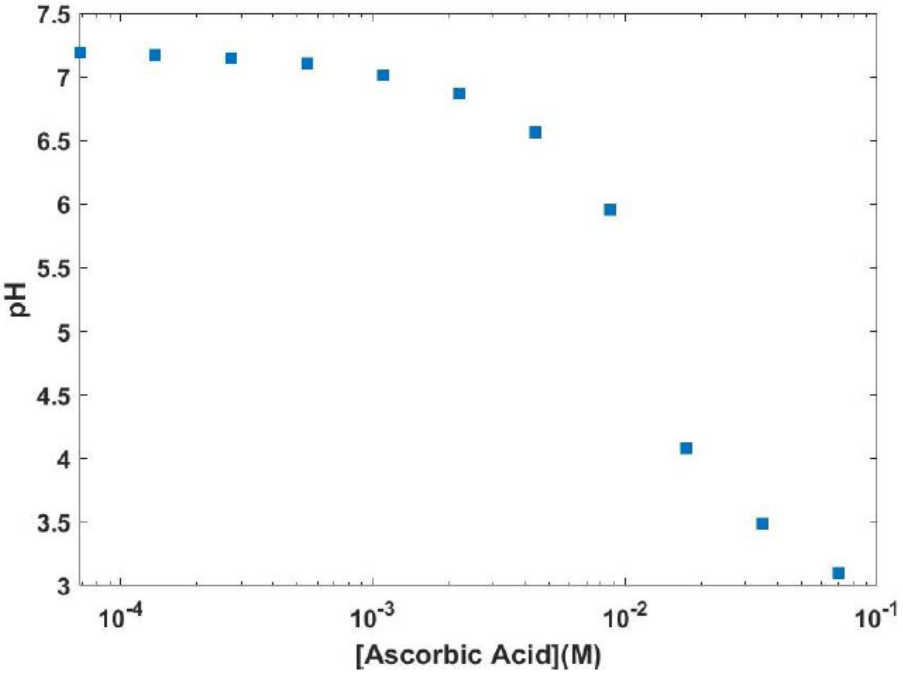

Figure S2. pH of ascorbic acid dissolved in DPBS as a function of [ascorbic acid]. For AA>10mM (buffering capacity of DPBS), the pH drops steeply.

For AA>10mM, there was a sharp drop in pH below 7.4 because the buffering capacity of 1x DPBS was 10mM. 4 7

3. Optimization of Ascorbic Acid for various concentrations of Rose Bengal in solution: Ascorbic Acid (100µL, 10mM stock) was serially diluted in DPBS (pH 7.4, 100µL) with a dilution factor of 1/2 in 11 wells of a clear 96-well microplate. A well containing DPBS (pH 7.4, 100µL) was used as the negative control. RB (100µL, 0.01M stock) was added to each well. The plate was placed in the green-light illuminator and illuminated from the top for 60 minutes. HRP (20µL, 0.171uM stock) and TMB (100µL, 1.04mM stock) were added to each well. The plate was covered with aluminum foil and incubated for 5 minutes.

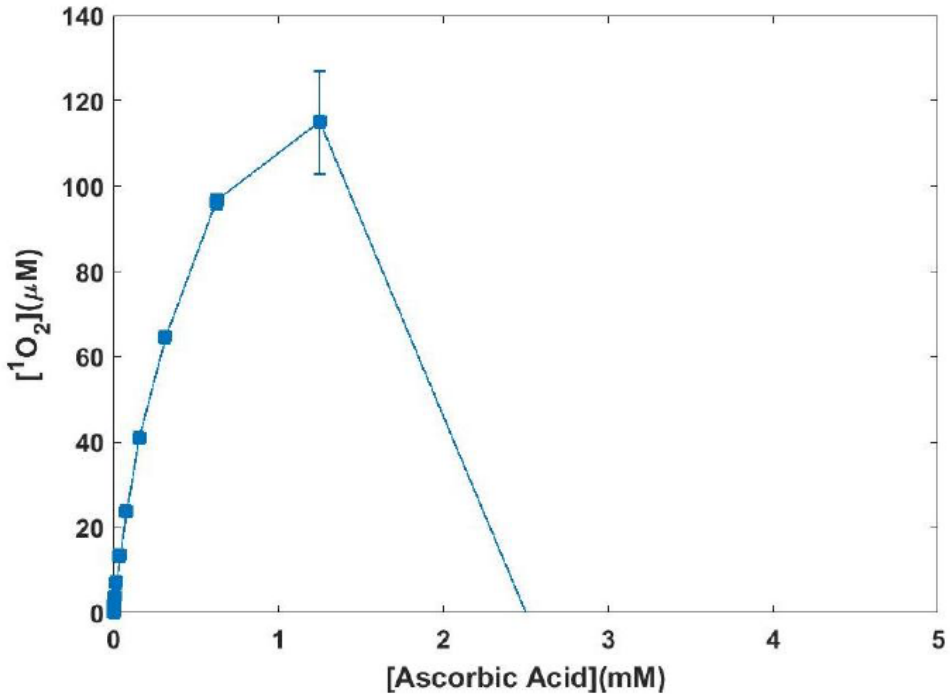

Figure S3. Determining the optimum [AA] for obtaining maximum $^1O_2$ detection signal. $^1O_2$ is generated via photosensitization reactions in solution.

4 other RB stock conditions - 1mM, 0.1mM, 0.01mM and 1µM were tested for following the

same protocol as above. All of the experiments for different RB conditions were performed in triplicate and each data point is reported as the mean + S.E.M. The absorbance intensity at 650nm was converted to [H2O2] using the H2O2 standard curve.

4. Optimization of Ascorbic Acid for 15mg of RB-silica microparticles:

RB functionalized silica microparticles (RB-silica) was suspended in 1x DPBS (pH 7.4) to obtain a concentration of 15mg RB-silica per 100μL of suspension. Ascorbic acid (100μL, 10mM stock) was serially diluted in DPBS (pH 7.4, 100μL) with a dilution factor of 1/2 in 11 wells of a clear 96-well microplate. A well containing DPBS (pH 7.4, 100μL) was used as the negative control. RB-silica suspension (100μL, 15mg per 100μL of suspension) was added to all 12 wells. The plate was placed in the green-light illuminator and illuminated from the top for 30 minutes. 150μL of the supernatant from each well was collected in individual microcentrifuge tubes. The tubes were centrifuged in a microcentrifuge at 18000xg for 5 minutes. 100μL of the supernatant from the tubes were then transferred to a new clear 96-well microplate. An absorption spectrum was performed for all 11 wells using a plate reader to ensure there was no freely diffusing RB in solution. HRP (20μL, 0.171μM stock) and TMB (100μL, 1.04mM stock) were then added to each well. The plate was covered with aluminum foil and incubated for 5 minutes. The absorbance intensity at 650nm was measured for each well in a plate reader. The above experiment was performed in triplicate and each data point is reported

as the mean + S.E.M. The absorbance intensity at 650nm was converted to [H_2O_2] using the H_2O_2 standard curve.

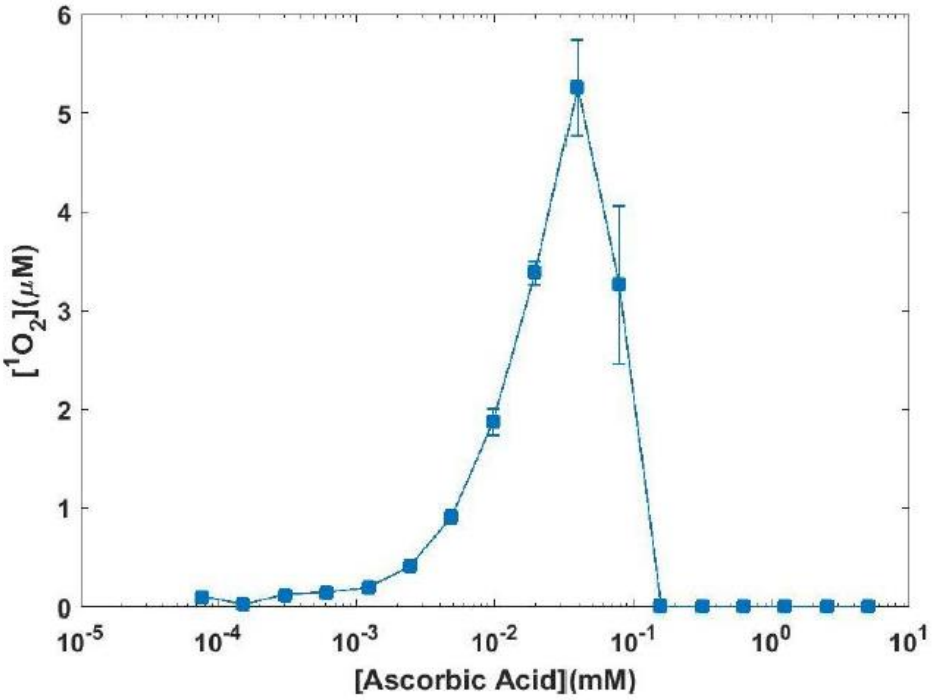

Figure S4. Determining the optimum [AA] for obtaining maximum $^1O_2$ detection signal. $^1O_2$ is generated via photosensitization reactions on a surface.